

**Role of Molecular Orientations in Structural Evolution of
Organic Molecular Solids – Spectroscopic Studies under
Extreme Conditions**

By

NAINI BAJAJ

PHYS01201504010

BHABHA ATOMIC RESEARCH CENTRE, MUMBAI

A thesis submitted to the

Board of Studies in Physical Sciences

In partial fulfilment of requirements

for the Degree of

DOCTOR OF PHILOSOPHY

of

HOMI BHABHA NATIONAL INSTITUTE

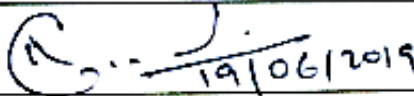
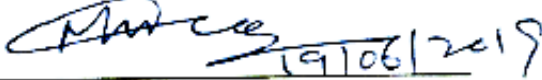
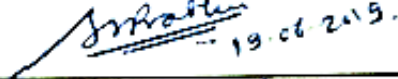
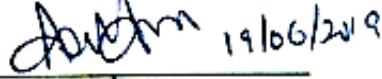
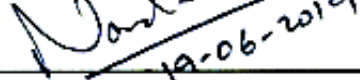


February 2019

Homi Bhabha National Institute¹

Recommendations of the Viva Voce Committee

As members of the Viva Voce Committee, we certify that we have read the dissertation prepared by "Naini Bajaj" entitled "Role of Molecular Orientations in Structural Evolution of Organic Molecular Solids – Spectroscopic Studies Under Extreme Conditions" and recommend that it may be accepted as fulfilling the thesis requirement for the award of Degree of Doctor of Philosophy.

Chairman – Dr. R.C. Rannot	 19/06/2019
Guide / Convener – Dr. M. N. Deo	 19/06/2019
Examiner – Prof. Shriganesh Prabhu	 19.06.2019.
Member 1 – Dr. Ashok K. Arya	 19/06/2019
Member 2 – Prof. S. Wategaonkar	 19/06/2019
Member 3 – Dr. D.K. Aswal	 19/06/2019
Technical Advisor – Dr. Nandini Garg	 19-06-2019

Final approval and acceptance of this thesis is contingent upon the candidate's submission of the final copies of the thesis to HBNI.

I/We hereby certify that I/we have read this thesis prepared under my/our direction and recommend that it may be accepted as fulfilling the thesis requirement.

Date: 19/06/2019

Place: Mumbai

Signature

Co-guide (if any)

Signature

Guide


19/06/2019

¹ This page is to be included only for final submission after successful completion of viva voce.

STATEMENT BY AUTHOR

This dissertation has been submitted in partial fulfilment of requirements for an advanced degree at Homi Bhabha National Institute (HBNI) and is deposited in the Library to be made available to borrowers under rules of the HBNI.

Brief quotations from this dissertation are allowable without special permission, provided that accurate acknowledgement of source is made. Requests for permission for extended quotation from or reproduction of this manuscript in whole or in part may be granted by the Competent Authority of HBNI when in his or her judgment the proposed use of the material is in the interests of scholarship. In all other instances, however, permission must be obtained from the author.

NAINI BAJAJ

DECLARATION

I, hereby declare that the investigation presented in the thesis has been carried out by me. The work is original and has not been submitted earlier as a whole or in part for a degree / diploma at this or any other Institution / University.

NAINI BAJAJ

List of Publications arising from the thesis

Journals:

1. “Orientational Adaptations Leading to Plausible Phase transitions in L-Leucine at Low Temperatures : revealed by Infrared Spectroscopy”, **Naini Bajaj**, Himal Bhatt, S.R. Vishwakarma, and M.N. Deo, *The Journal of Physical Chemistry B*, 2019, 123, 3, 561-570.
2. “Phase transition in metal–organic complex $\text{trans-PtCl}_2(\text{PEt}_3)_2$ under pressure: insights into the molecular and crystal structure”, **Naini Bajaj**, Himal Bhatt, K. K. Pandey, H. K. Poswal, A. Arya, P. S. Ghosh, N. Garg, and M. N. Deo, *CrystEngComm*, 2018, 20, 3728-3740.
3. “Perceptible isotopic effect in 3D-framework of α -glycine at low temperatures”, **Naini Bajaj**, Himal Bhatt, Chitra Murli, S.R. Vishwakarma, R. Chitra, T.R. Ravindran, and M.N. Deo, *Spectrochimica Acta Part A: Molecular and Biomolecular Spectroscopy*, 2018, 204, 495–507.
4. “Spectroscopic Studies of Temperature Induced Phase Transitions in Metal-Organic Complex $\text{trans-PtCl}_2(\text{PEt}_3)_2$ ”, **Naini Bajaj**, Himal Bhatt, H.K. Poswal, and M.N. Deo – Under Review.

Conferences:

1. “Phase transition in L-Asparagine Monohydrate at Low Temperatures”, **Naini Bajaj**, Himal Bhatt, S.R. Vishwakarma, R. Chitra, and M.N. Deo, 7th International

- Conference on Perspective in Vibrational Spectroscopy, November 25-29, 2018, Mumbai, India.
2. “Distinct High Pressure Behavior of Metal-Organic Platinum(II) Isomers in $\text{PtCl}_2(\text{PEt}_3)_2$ ”, **Naini Bajaj**, Himal Bhatt, H.K. Poswal, Nandini Garg, and M.N. Deo, 7th International Conference on Perspective in Vibrational Spectroscopy, November 25-29, 2018, Mumbai.
 3. “Low temperature IR spectroscopic study of torsional vibrations of taurine”, **Naini Bajaj**, Himal Bhatt, S. R. Vishwakarma, Susy Thomas, C. Murli, and M. N. Deo, AIP Conference Proceedings 1942, 030017 (2018).
 4. “High pressure infrared spectroscopy of Pt(II) complex *cis*- $\text{PtCl}_2(\text{PEt}_3)_2$ ”, **Naini Bajaj**, Himal Bhatt, Nandini Garg, and M. N. Deo, AIP Conference Proceedings 1832, 030012 (2017).
 5. “Deuterated α -glycine up to 4.2 K – a far IR absorption study”, **Naini Bajaj**, Himal Bhatt, S.R. Vishwakarma, R.Chitra, C.Murli, and M.N. Deo, 6th International Conference on Perspective in Vibrational Spectroscopy, November 5-8, 2016, Lucknow.
 6. “High pressure Raman spectroscopic studies of Pt(II) complex *trans*- $\text{PtCl}_2(\text{PEt}_3)_2$ ”, **Naini Bajaj**, H. K. Poswal, Himal Bhatt, M. N. Deo, and Surinder M. Sharma, AIP Conference Proceedings 1731, 090031 (2016).
 7. “FT-Raman spectroscopy of structural isomers of Pt(II) complex $\text{PtCl}_2(\text{PEt}_3)_2$ ”, Himal Bhatt, M. N. Deo, S. R. Vishwakarma, **Naini Bajaj**, and Surinder M. Sharma, AIP Conference Proceedings 1665, 090045 (2015).

NAINI BAJAJ

Dedicated to my family

ACKNOWLEDGEMENTS

Firstly, I would like to express my sincere gratitude to my supervisor Prof. M.N. Deo for the continuous support of my Ph.D. study and related research, for his patience, motivation, and immense knowledge. His guidance helped me in all the time of research and writing of this thesis. I could not have imagined having a better advisor and mentor for my Ph.D. study. I am very grateful to my mentor, Dr. Himal Bhatt for enlightening me the first glance of research. This feat was possible because of the unconditional supported provided by him. Despite his busy schedules, with positive disposition, he has always made himself available to discussions and useful suggestions, which provided me an opportunity to learn from his research expertise. His constant support, guidance, inspiration, motivation has always kept me going ahead. I owe a lot to him and feel privileged to be associated with a person like him during my life. I would like to thank the doctoral committee members: Dr. S.M. Sharma, Dr. N.K. Sahoo, Prof. S. Wategaonkar, Dr. A.K. Arya, Dr. D.K. Aswal, and Dr. Nandini Garg, for their insightful comments and encouragement, but also for the hard question which incented me to widen my research from various perspectives. My sincere thanks to Dr. H.K. Poswal, who introduced me to the field of high pressure Raman spectroscopy and Dr. K.K. Pandey who introduced me to the high pressure x-ray diffraction technique and its analysis. I would like to thanks Dr. K.K. Pandey and Dr. V. Shrihari, for collection of the high pressure x-ray diffraction data at INDUS-2, BL-11, RRCAT, Indore. I would also like to thank Mr. S.R. Vishwakarma for helping in low temperature IR spectroscopic measurements and cryogenic section of RRACT, Indore, for providing the cryogens for the low temperature experiments. I would like to thank Dr. R. Chitra for the amino acids sample and Dr. V.K. Jain for the platinum complexes. I acknowledge Dr. H.K. Poswal and Dr. C. Murli for helping

with the low temperature Raman data collection. Thanks to Dr. R. Rajul for the useful discussions on the single crystal x-ray diffraction data analysis.

Special thanks to Dr. Susy Thomas, Dr. D. Lahari, Dr. Sunanda Mam, and Mr. Naveen Sir for helping me in numerous ways during various stages of my PhD. And a big thank to Rahul Kumar and Anuj Sharma for the task of doing final formatting of this thesis. I thank my friend as well as my Roommates, Preeta Kumari and Shruti Pandey, for constant source of positive energy, providing moral and emotional support and always standing by my side supporting me during the hardships of life. I will always cherish the warmth shared by us. Thanks to Debashish Sarkar, for always listening and suggesting me the solutions during the tough times in Ph.D. I also acknowledge my old pals, Vivek Sharma, Sunita Kalita, Kirti Bara and Mansi for their well wishes and support. Last but not the least, I would like to thank my family: my Father, Rajesh Kumar Bajaj, mother, Amita Bajaj and my brother, Abhishek Bajaj for eternal support and understanding my goals and aspirations.

NAINI BAJAJ

SUMMARY

Studies of molecular conformations, distortions in the inter/intra-molecular bonds and transitions in the crystal structures of organic molecular solids under varying thermodynamic conditions of temperature and pressure are of current research interest due to their applications in the fields of biology, pharmaceutical industry, molecular electronics, non-linear optical materials, ferroelectricity, and crystal engineering. Each molecular moiety can have a diverse response to the change of thermodynamic parameters which have a profound effect on its physical, structural, and bonding properties. Further, weakly interacting forces like hydrogen bonds, which are ubiquitous and are among fundamental non-covalent interactions, can easily undergo a change under such conditions, thereby influencing the properties of the material under consideration. The changes in inter-atomic distances, intra-molecular interactions, non-covalent bond lengths and molecular conformations may result in new structural assemblies with novel properties. Therefore, one can invoke the “structure-property” correlations to evaluate the mechanism of structural transformations.

This thesis reports the study of organic and metal-organic complexes under varying thermodynamic conditions of temperature and pressure. Both the techniques produce compression of the materials, but the origin of resulting changes may be different, thus leading to varying effects. Vibrational spectroscopy (IR and Raman) along with complementary x-ray diffraction technique have been used to probe these systems. While spectroscopic techniques probe the information on molecular motions, x-ray diffraction has been used to characterize the crystal structure and associated transitions. Thus, the work presented in this thesis describes the properties of hydrogen bonds in the simplest as well as in complex organic molecular solids under varying thermodynamic conditions, where

molecular orientations and conformations play a substantial role to trigger the structural phase transitions.

The results of the present thesis can be utilized to understand the signatures and microscopic mechanism of the possible phase transitions upon varying the thermodynamic conditions and thus the realization of new useful structural motifs and paves the way towards better understanding of fundamental systems like glycine, framing a general trend of hydrogen bonding networks in amino acids under varying conditions to harness the properties of technologically important organic systems, other macro-molecular systems such as proteins and for their molecular modelling.

Table of Contents

SUMMARY	xv
List of Figures	xxi
List of Tables	xxvii
Chapter 1: Introduction	1
1.1. Introduction to Organic Molecular Solids	1
1.2. Thermodynamics of Phase transitions	2
1.3. Behavior of Organic Molecular Solids under varying thermodynamic conditions	4
1.4. Motivation and Choice of Systems	10
1.4.1. Amino Acids.....	10
1.4.2. Metal-Organic complex <i>trans</i> -PtCl ₂ (PEt ₃) ₂	13
1.5. Layout of thesis	14
Chapter 2: Experimental Methodologies	16
2.1. Low temperature	16
2.1.1. Measurement techniques	16
2.2. High Pressure generation and measurements	23
2.3. Spectroscopic and structural characterization.....	27
2.3.1. Infrared Spectroscopy.....	27
2.3.2. Raman Spectroscopy	34
2.3.3. X-ray diffraction.....	38

2.4. Upgradation of infrared beamline	41
Chapter 3: Low Temperature Isotopic Effect in α -glycine	43
3.1. Introduction.....	43
3.2. Literature Survey.....	44
3.3. Experimental methods.....	45
3.4. Results and discussion	46
3.4.1. Low temperature behavior of <i>gly-h</i>	46
3.4.2. Hydrogen bonding network of <i>gly-h</i>	50
3.4.3. Low temperature behavior of <i>gly-d</i>	54
3.4.4. Isotopic effect on the Hydrogen bonding network	57
3.5. Orientational changes in N(H/D) ₃ torsional modes:	60
3.6. Summary	65
Chapter 4: Low Temperature Phase Transitions in L-Leucine	67
4.1. Introduction.....	67
4.2. Experimental methods.....	68
4.3. Results and discussion	69
4.3.1. Signatures of possible Phase transitions across 240 K	72
4.3.2. Hydrogen bonding network in L-Leucine below 240 K	74
4.3.3. Reorientational changes across 150 K.....	80
4.4. Summary	87
Chapter 5: Variable Temperature Studies on Metal-Organic Complex <i>trans</i> -PtCl ₂ (PEt ₃) ₂ ..	88

5.1. Introduction.....	88
5.2. Experimental details.....	90
5.3. Molecular structure of <i>trans</i> -PtCl ₂ (PEt ₃) ₂ :.....	91
5.4. Results and discussion	93
5.4.1. Spectroscopic characterization at ambient conditions.....	93
5.4.2. Low temperature Spectroscopic Studies	94
5.4.3. Probing Hydrogen bonds through stretching vibrational modes.....	102
5.5. Summary	104
Chapter 6: High Pressure Phase Transitions in <i>trans</i> -PtCl ₂ (PEt ₃) ₂ :.....	105
6.1. Introduction.....	105
6.1.1. Importance of high pressure studies in metal-organic coordination compounds.....	105
6.2. Experimental methods.....	107
6.2.1. Single Crystal and Powder X-ray Diffraction studies	107
6.2.2. Infrared spectroscopic studies	108
6.2.3. Raman spectroscopic studies	108
6.2.4. First-principles calculations.....	108
6.3. Results and Discussion	109
6.3.1. Structural study at ambient conditions	109
6.3.2. Pressure induced phase transition.....	113
6.3.3. Molecular arrangement at high pressures	125

6.3.4. High pressure behavior of metal-organic complexes	129
6.4. Summary	130
Chapter 7: Summary and Conclusions	131
7.1. Summary	131
7.2. Conclusions	131
References	134

List of Figures

Figure 1.1: Fragments of the crystal structure of the monoclinic (Upper Left) and orthorhombic (Upper Right) polymorphs of paracetamol. Relative volume changes in the monoclinic (red) and orthorhombic (blue) polymorphs of paracetamol upon cooling (Lower Left) and with increasing pressure (Lower Right) [5, 6]. (reproduced with permission).....	5
Figure 1.2: Linear strain in the low pressure polymorph of sodium oxalate upon cooling (filled symbols) and with increasing pressure (open symbols). The plots are scaled in such a way that volume changes on cooling and under pressure are the same [52]. (reproduced with permission).....	6
Figure 1.3: Comparison of changes in the cell parameter in $[\text{Co}(\text{NH}_3)_5\text{NO}_2]\text{Cl}_2$ with increasing pressure (filled symbol) and upon cooling (open symbol). The plot is scaled in such a way that the volume changes under pressure and on cooling are equal [57]. (reproduced with permission).....	6
Figure 1.4: Phase diagram of the ice-water system on the logarithmic scale of pressure [56].....	7
Figure 1.5: Structures of polymorphs of glycine (α , β , γ) upon cooling and on increasing pressures [2, 13, 68, 69, 71-73]. (reproduced with permission).....	9
Figure 2.1: Schematic of the continuous flow cryostat set up. Sample is mounted in vacuum on a heat exchanger in the cryostat, Optical access is through windows. Vapours cool the sample, then travel back from the concentric ring of the transfer line to the flow controller to the gas flow pump, from the gas flow pump to the flow meter, to the Recovery line.	18
Figure 2.2: Variation of thermal conductivity at low temperatures for commonly used materials [167].	20
Figure 2.3: Schematic of the Diamond Anvil Cell (DAC).	24
Figure 2.4: Schematic of Fourier transform infrared Spectroscopy.	29
Figure 2.5: Optical Layout of Fourier transform infrared spectrometer (BRUKER VERTEX 80V).	31
Figure 2.6: (Left) MIR spectra of normal diamond (red spectrum) and Type IIa diamond (blue spectrum) recorded using Bruker IFS125 instrument. [187] (Right) Schematic diagram of infrared microspectroscopy for high pressure measurements.	33
Figure 2.7: Experimental station of the low temperature set-up coupled to Fourier transform infrared spectrometer at BL-06, IR beamline, INDUS-1, RRCAT, Indore, India.	34
Figure 2.8: Schematic diagram of Raman scattering (Left – Stoke Raman inelastic scattering, Middle – Rayleigh elastic scattering, and Right – Anti-Stokes Raman inelastic scattering).	35
Figure 2.9: Optical layout of the Triple stage Raman spectrometer.	37
Figure 2.10: Subtractive mode configuration used in the triple stage Raman spectrometer.	37

- Figure 2.11: Schematic of low temperature sample stage set-up used with the triple stage Raman spectrometer. 38
- Figure 2.12: Schematic of IR Beamline, BL-06, at INDUS-1, RRCAT, India. [187]. 41
- Figure 2.13: 100% transmission spectra of the previous ZnSe window (red) and new ZnSe window (blue). 42
- Figure 3.1: (a) Low temperature spectra of α -glycine in the spectral range 150 – 650 cm^{-1} . Red color plots are at 4 cm^{-1} resolution using Liquid nitrogen (LN_2) and violet color plots are from the repeat measurements at 2 cm^{-1} resolution using Liquid Helium (LHe). (b) Frequency versus temperature plot in 150 – 650 cm^{-1} spectral range. Red squares represent data at 4 cm^{-1} resolution and black squares represent repeat measurement data points at 2 cm^{-1} resolution. Symbols: τ -torsional, δ -bending, γ -rocking, ω -wagging. 47
- Figure 3.2: Low temperature IR spectra of α -glycine from 700 – 3250 cm^{-1} spectral range at 1 cm^{-1} resolution using LHe cryostat. Inset shows splitting of γNH_3 and t-CH_2 modes marked with asterisk (*). Symbols: δ -bending, ν - stretching, t- twist , ω - wagging, d_s - symmetric deformation, d_{as} - asymmetric deformation, γ -rocking. 49
- Figure 3.3: Frequency versus temperature plots in (a) 690 – 1145 cm^{-1} (b) 1310 – 1630 cm^{-1} (c) 2600 – 3175 cm^{-1} spectral range for α -glycine, obtained from two different experiments at 1 cm^{-1} (black filled squares) and 2 cm^{-1} (red open squares) resolutions respectively. * denotes the appearance of new modes. Symbols: δ -bending, ν - stretching, t- twist , ω - wagging, d_s - symmetric deformation, d_{as} - asymmetric deformation. 51
- Figure 3.4: (Left) gly-*h* molecules in *ac*-planes, showing H3---O2, H4---O1 and H5---O1 bonds approximately along *c*-, *a*- and *b*- axes respectively. The network along *b*- axes has been elaborately presented in Figure 5. (Right) Variation of these hydrogen bond distances with temperature. Open and filled circles represent data estimated from two independent measurements. Also shown are the reported H---O distances in literature, with symbols: Black filled triangle – ref. [196], indigo cross mark – ref. [69], violet plus mark – ref. [197], olive star – ref. [129]. 53
- Figure 3.5: A wire-frame representation of the hydrogen bonded structure of α -glycine. The stronger hydrogen bonds lie in the *ac*-plane forming layers. These layers are connected through a weaker N1-H5---O1 hydrogen bond (dotted lines marked with H5---O1) along the *b*-axis, in a head to tail configuration forming bilayers. The adjacent bilayers are held together by the weakest C-H---O hydrogen bonds. At low temperatures, N1-H5---O1 hydrogen bonds depict the maximum strengthening. Refer Figure 4(left) for description of hydrogen bonds in the *ac*-plane (shaded sheets) which is normal to the N1-H5---O1 hydrogen bonds. 54
- Figure 3.6:(a) Low temperature IR spectra of deuterated α -glycine (gly-*d*) in the spectral range 140 – 675 cm^{-1} . (b) Frequency versus temperature plots for the corresponding modes. Symbols: τ -torsional, δ -bending, γ -rocking, ω -wagging. 55
- Figure 3.7: (a) Low temperature IR spectra of gly-*d* in the 700 – 1750 cm^{-1} range at 1 cm^{-1} resolution. * denotes splitting in t-CD_2 mode. (b) Low temperature Raman spectra of gly-*d* in 200 – 1650 cm^{-1} spectral range. Inset (left): variation of low frequency Raman modes (δCCN , τND_3 , γCOO^-) with temperature, and (right): splitting of $\text{t}(\text{CD}_2)$ below 180 K. (c) Variation of the IR and Raman peak positions of gly-*d* in the region 700 – 1600 cm^{-1} with temperature. 56
- Figure 3.8: (a) Raman and (b) IR spectra of gly-*d* in the ND and CD stretching regions at a few representative temperatures. In addition to the stretching modes, combination, overtone and self trapped modes may be

expected in this region. Grey highlighted peaks represent ND stretching modes. (c) Frequency versus temperature plots of ND and CD stretching modes, symbols: filled – IR and open – Raman modes.	59
Figure 3.9: Variation of D3---O2, D4---O1 and D5---O1 bond distances with temperature in gly- <i>d</i>	60
Figure 3.10: Structure of gly- <i>d</i> in <i>bc</i> -plane [210, 216]. Highlighted sheets are drawn to show the <i>ac</i> -planes. Upon lowering the temperature, the two strong N-H---O hydrogen bonds which form a closed ring (inset) of four molecules in the <i>ac</i> -plane get further stronger to form more compact and tightly held layers.....	60
Figure 3.11: Comparison of NH ₃ / ND ₃ torsional mode in the IR spectra of (a) gly- <i>h</i> and (b) gly- <i>d</i> at 300 K and 4.2 K.	62
Figure 3.12: Temperature variation of the "indicator" band in gly- <i>h</i> (top) and gly- <i>d</i> (bottom).	64
Figure 4.1: Ambient infrared Spectrum of powder L-Leucine in 30 – 3500 cm ⁻¹ spectral range measured using three different experimental/ instrumental parameters to cover the complete frequency range: Blue - 30-275 cm ⁻¹ , Red - 120-600 cm ⁻¹ , Black - 500-3500 cm ⁻¹	69
Figure 4.2: Two L-Leucine molecules (<i>Leu</i> -A and <i>Leu</i> -B) in the asymmetric unit along with the notation of different atoms.	72
Figure 4.3: (a) Temperature dependent variation of IR peaks in the 115-600 cm ⁻¹ spectral range. The dashed line shows the evolution of new peaks at low temperature. (b) Frequency versus temperature plot of peak positions in the 160-550 cm ⁻¹ region. The error bars are within the size of the symbols.	73
Figure 4.4: (a) Temperature dependent variation of IR spectra in the 650-1300 cm ⁻¹ spectral range. Dashed lines show the evolution of new peaks at low temperature. (b) Frequency versus temperature plot of peak positions in the 650-1300 cm ⁻¹ region.....	73
Figure 4.5: (a) Temperature dependent variation of IR spectra in the 1280-1675 cm ⁻¹ spectral range. The dashed line shows the evolution of new peaks at low temperature. (b) Frequency versus temperature plot of peak positions in the 1300-1630 cm ⁻¹ region.....	74
Figure 4.6: (a) Temperature dependent variation of IR spectra of L-leucine in the NH and CH stretching region in the 2000-3300 cm ⁻¹ spectral range. The dashed line shows the evolution of N-H stretching peaks at low temperatures. (b) Frequency versus temperature plot of the IR peak positions in the 2565-3080 cm ⁻¹ spectral range.	75
Figure 4.7: Hydrogen bonding in the two L-Leucine molecules (hydrophobic chains have been omitted for clarity) (a) in the <i>ac</i> -plane: <i>Leu</i> -A molecule having amino group (N1-H2/ H3/ H4) with two hydrogen bonds in the <i>ac</i> -plane (N1-H4---O3 and N1-H3---O3) along <i>c</i> - and <i>a</i> - axes respectively. <i>Leu</i> -B molecule having amino group (N2-H15/ H16/ H17) with three hydrogen bonds in the <i>ac</i> -plane (N2-H16---O1, N2-H17---O1 and N2-H17---O2). (b) Along <i>b</i> -direction: <i>Leu</i> -A and <i>Leu</i> -B molecules with hydrogen bonds N1-H2---O2 and N2-H15---O4 respectively. (c) Bonding details of the bifurcated hydrogen bond.	77
Figure 4.8:(a) Temperature dependent variation of IR peak positions in 30-90 cm ⁻¹ spectral range. (b) Frequency versus temperature plot of IR peak at 70 cm ⁻¹ wavenumber.	81

- Figure 4.9: Full width at half maximum (FWHM) of (C_3C_4) torsion mode, *i.e.*, $\tau(C_3C_4)$ at 107 cm^{-1} , in the temperature range $300 - 4.3\text{ K}$. Inset: Fitted IR spectrum of L-Leucine at 300 K in $80 - 160\text{ cm}^{-1}$ spectral range. 83
- Figure 5.1: *trans*-PtCl₂(PEt₃)₂ molecule with central Platinum atom (Silver), Chlorine atom (green), Carbon atom (Grey) and Hydrogen atom (white). 92
- Figure 5.2: Schematic of the bonding arrangements in the molecular units of *trans*-PtCl₂(PEt₃)₂ (distances and angles not to scale). The white orbitals along x&y axes correspond to $d_{x^2-y^2}$ (empty) and green corresponds to d_{xy} (filled) orbital of Pt. The lone pair of electron from P atom goes to empty $d_{x^2-y^2}$ orbital of Pt (straight arrows) and the electron from d_{xy} orbital of Pt goes to empty antibonding σ^* orbital of P-C (curved arrows). 92
- Figure 5.3: (a) FT-Raman and (b) FT-IR spectra of *trans*-PtCl₂(PEt₃)₂ at ambient conditions. γ – out of plane bend, δ – in-plane bend, ν_s – symmetric stretch, ν_{as} – asymmetric stretch, ω – wagging, d_{as} – asymmetric deformation, d_s – symmetric deformation. 94
- Figure 5.4: (Left to Right) FT-Raman spectra of *trans*-PtCl₂(PEt₃)₂ in the region $50-460\text{ cm}^{-1}$. New peaks emerged at low temperature have been marked as asterisk (*). 95
- Figure 5.5: Low temperature spectra of *trans*-PtCl₂(PEt₃)₂ (a) Raman (spectral range : $5-220\text{ cm}^{-1}$) and (b) IR (spectral range : $140-220\text{ cm}^{-1}$) spectra. 96
- Figure 5.6: (a) Low temperature Raman spectra of *trans*-PtCl₂(PEt₃)₂ in the $210 - 650\text{ cm}^{-1}$ region. (b) Variation of Raman active modes at low temperatures in the $10 - 650\text{ cm}^{-1}$ spectral range. Dotted vertical lines are drawn at 130 and 180 K . Open circles represent new mode emerging at low temperatures. Symbols: δ = in-plane bending, γ = out-of-plane bending, and ν = stretching vibration. 97
- Figure 5.7: (a) Low temperature IR spectra of *trans*-PtCl₂(PEt₃)₂ in the $220 - 650\text{ cm}^{-1}$ spectral region. Dashed lines indicate new peaks emerging at low temperatures. (b) Variation of IR peak positions at low temperatures in the $160 - 640\text{ cm}^{-1}$ spectral range. Dotted vertical lines are drawn at 130 and 180 K . Open circles represent new modes appearing upon cooling. 98
- Figure 5.8:(a) Low temperature IR spectra of *trans*-PtCl₂(PEt₃)₂ in the $700 - 1070\text{ cm}^{-1}$ spectral range. Dashed lines indicate new peaks evolving at low temperatures, Inset: Low temperature Raman spectra in the $1030 - 1070\text{ cm}^{-1}$ spectral range. (b) Variation of IR peak positions at low temperature in the $670 - 1050\text{ cm}^{-1}$ spectral region. Dotted vertical lines are drawn at 130 and 180 K . Open circles represent new modes emerging at low temperatures. 100
- Figure 5.9: (a) Low temperature IR spectra of *trans*-PtCl₂(PEt₃)₂ in the $1220 - 1480\text{ cm}^{-1}$ spectral range. Dashed lines indicate new peaks evolving at low temperatures. Inset: Low temperature Raman spectra of *trans*-PtCl₂(PEt₃)₂ in the $1400 - 1500\text{ cm}^{-1}$ spectral range. (b) Variation of IR peak positions at low temperatures in the $1250 - 1475\text{ cm}^{-1}$. Open circles represent new modes evolving at low temperatures. Symbols: ω = wagging, d_s = symmetric deformation, d_{as} = asymmetric deformation vibration. 101
- Figure 5.10: (a) Low temperature IR spectra of *trans*-PtCl₂(PEt₃)₂ in the $2850 - 3050\text{ cm}^{-1}$ spectral range. (b) Variation of IR modes at low temperature in the $2860 - 2970\text{ cm}^{-1}$ spectral range. Open circle symbol represent new mode emerging at low temperatures. Symbols: ν_s = symmetric stretch, ν_{as} = asymmetric stretch. 102

- Figure 5.11: (a) Low temperature Raman spectra of *trans*-PtCl₂(PEt₃)₂ in the 2850 – 3000 cm⁻¹ spectral region. (b) Variation of Raman modes in the 2860 – 2990 cm⁻¹ spectral region at low temperature. Open circle symbol represents new mode emerging upon cooling..... 103
- Figure 6.1: Unit cell of *trans*-PtCl₂(PEt₃)₂, where Et = C₂H₅. Color: Grey – Pt, Green – Cl, Violet – P, Brown– C, Pink – H atoms..... 110
- Figure 6.2: Ambient powder XRD pattern of *trans*-PtCl₂(PEt₃)₂ inside the DAC. Inset shows the picture of 2D diffraction rings..... 111
- Figure 6.3: High pressure Raman spectra of *trans*-PtCl₂(PEt₃)₂ in the spectral region 20 – 300 cm⁻¹. On the right is 100 – 275 cm⁻¹ region shown with 3X magnification and inset shows the FWHM of γ (P-Pt-Cl) mode. * denotes new peak in the lattice region and ^ denotes new shoulder peak adjacent to δ PtCl₂ mode, which emerge after the phase transition..... 115
- Figure 6.4: High pressure Raman spectra (y-offset) of *trans*-PtCl₂(PEt₃)₂ in the spectral range a) 320-470 cm⁻¹; b) 600-780 cm⁻¹. The new peaks emerged with pressure have been highlighted as guide to the eye. c) Variation of Raman modes in the spectral range 20-700 cm⁻¹, with pressure..... 116
- Figure 6.5: High pressure IR spectra (y-offset for clarity) of *trans*-PtCl₂(PEt₃)₂ in the spectral region a) 610-700 cm⁻¹ and b) 700-1100 cm⁻¹. The new peaks emerged with pressure have been marked with asterisk and highlighted as guide to the eye. 117
- Figure 6.6: High pressure (a) Raman and (b) infrared spectra of *trans*-PtCl₂(PEt₃)₂ in mid-IR region. Inset in (b) shows the peak position of ν_s CH₃ and ν_s CH₂ modes with pressure. The new peaks emerged at high pressure have been marked with *. Down arrow (\downarrow) denotes C-CH₃ rocking mode, which weakens with pressure. Numbers are pressure values in GPa, rel – pressure release. Spectra have been offset for clarity. 117
- Figure 6.7: (a) Variation of IR peak positions with pressure in *trans*-PtCl₂(PEt₃)₂ in the region (a) 630-1100 cm⁻¹ and (b) 1250-3050 cm⁻¹. Blue open circles represent new peaks emerged across 0.8 GPa..... 118
- Figure 6.8: Variation of Raman mode positions with pressure in *trans*-PtCl₂(PEt₃)₂ in the spectral range (a) 630-1120 cm⁻¹ (b) 1410-3100 cm⁻¹. The new peaks emerged during high pressure are shown with blue empty circles..... 118
- Figure 6.9: High pressure powder XRD patterns of *trans*-PtCl₂(PEt₃)₂. * denotes new peaks emerged in the high pressure phases. The enlarged views in the inset show (I) the new peak at 0.8 GPa (Phase 2); (II) peaks belonging to Phase 2 (around 6°) and Phase 3 (around 5°) at 4.7 GPa..... 120
- Figure 6.10: Variation of lattice parameters and with pressure in *trans*-PtCl₂(PEt₃)₂. The lattice parameters are fitted with Murnaghan and 3rd order Birch-Murnaghan equation of state in Phase 1 and Phase 2 respectively using EOS-Fit7 software,[305] the error bars are within the symbols. Inset shows the variation of beta angle with pressure..... 120
- Figure 6.11: Variation of unit cell volume with pressure in *trans*-PtCl₂(PEt₃)₂ fitted with Murnaghan and 3rd order Birch-Murnaghan equation of state in Phase 1 and Phase 2 respectively using EOS-Fit7 software[305], the error bars are within the symbols at all the pressures. 121

- Figure 6.12: Rietveld. refinement of *trans*-PtCl₂(PEt₃)₂ at 0.8 GPa inside DAC using GSAS-II. Inset: (Left) Enlarged view of the Rietveld refinement of XRD pattern in the region of appearance of the new peak in Phase 2, (Right) Typical 2D pattern obtained in the new phase above 0.8 GPa. 123
- Figure 6.13: Principle axes evolution with pressure in *trans*-PtCl₂(PEt₃)₂ as obtained using the software PASCAL [306]. The axis X3 coincides with the crystallographic *b*-axis, which shows the least compressibility with pressure..... 123
- Figure 6.14: Unit cells of Phase 1 (ambient) and Phase 2 (0.8 GPa) in *trans*-PtCl₂(PEt₃)₂..... 124
- Figure 6.15: Le Bail refinement of Phase 3 of *trans*-PtCl₂(PEt₃)₂ at 6.5 GPa. Inset shows the corresponding 2D pattern. 125
- Figure 6.16: Molecular structure of *trans*-PtCl₂(PEt₃)₂ (left) ambient Phase 1: $\angle\text{P-Pt-P}=180^\circ$ and $\angle\text{Cl-Pt-Cl} = 180^\circ$. (right) at 0.8 GPa in Phase 2. Molecular reorientations result in $\angle\text{P-Pt-P}=170.58^\circ$ and $\angle\text{Cl-Pt-Cl}=176.82^\circ$ in Phase 2. (Color, Pt-Silver, Cl-green, Orange-P, Dark grey-C, Light grey-H). 126
- Figure 6.17: (left) Hydrogen bonds in the structure of *trans*-PtCl₂(PEt₃)₂ at high pressures. Atom colours: Grey-Pt, Green – Cl, Purple – P, Brown – C, Pink – H. H-bonds are shown by green-pink bicolour lines. The three H-bonds are: i) intramolecular – Cl1---H-C3, nearly along the *b*-axis, ii) intermolecular – Cl2---H-C2 nearly in the *bc*-plane and iii) intermolecular – Cl1---H-C5' which connects two molecules lying in two adjacent *bc*-planes forming the three- dimensional network. Numbers are Cl---H distances in Å. (right) the extended three dimensional wire-frame structure plotted through slightly tilted *a*-axis showing the hydrogen bonded network, mimicking a possible stair-case type supramolecular assembly. 128

List of Tables

Table 2.1: Boiling temperatures of commonly used cryogenic liquids at ambient pressure (1 Atm) alongwith references.	17
Table 2.2: Emissivity of different materials.....	23
Table 2.3: Commonly used pressure transmitting media with their hydrostatic and quasi-hydrostatic pressure values alongwith references.	25
Table 3.1: Slope (-dv/dT) of frequency versus temperature plots of IR modes of gly- <i>h</i> . The modes with maximum or negative values have been highlighted.....	48
Table 3.2: Observed IR and Raman modes of gly- <i>d</i> alongwith the rate of variation of IR modes as a function of temperature.	57
Table 3.3: FWHM (in cm ⁻¹) of various modes in gly- <i>h</i> and gly- <i>d</i> at 300 K and at 4.2 K.....	62
Table 4.1: IR band positions of L-leucine observed at 300 K and 77 K and the reported vibrational assignments [118, 122, 147, 253-255]. Symbols: τ – torsion, r – rocking, ω – wagging, ν – stretching, δ – deformation, t – twist, as – asymmetric, s – symmetric.....	70
Table 4.2: Hydrogen bond parameters of <i>Leu-A</i> and <i>Leu-B</i> molecules as obtained from reference [87], along with the low temperature behavior of N-H stretching modes of both Leucine molecules.	75
Table 4.3: The fitted parameters a , b , C and E_a from equation (4.2), for the temperature dependence of FWHM of $\tau(C_3C_4)$ mode in the temperature ranges 300 – 150 K and 150 – 4.3 K.....	83
Table 6.1: Crystal structure data and refinement details of single crystal x-ray diffraction of <i>trans</i> -PtCl ₂ (PEt ₃) ₂ at ambient conditions.....	111
Table 6.2: Experimental (ambient pressure – reported (column 2) and this study (column 3)) atomic coordinates and lattice parameters of <i>trans</i> -PtCl ₂ (PEt ₃) ₂ [$P2_1/n$ (14) – space group]. The experimentally obtained structure has been submitted to CCDC (1829359) by including H-atoms refined using the riding model. To further improve structure with H-atom positions, DFT-GGA calculated (at ambient pressure) equilibrium atomic positions have also been provided in the last column, obtained by including hydrogen atoms and optimizing single crystal XRD deduced experimental coordinates, the uncertainty in unit cell volume is found to be ~ 5%. *Note: In this table, axes transformation of the single crystal structure, which has been deposited at CCDC after including H-atoms, have been carried out using PCW software for consistency in lattice parameter convention (a and c) with the reported values [264].	112
Table 6.3: Projection of the three Principle axes (X1, X2, X3) on crystallographic axes (a , b , c) in <i>trans</i> -PtCl ₂ (PEt ₃) ₂ derived using PASCAL software[306] with critical point at 0.85 GPa.....	121
Table 6.4: Variation of dihedral angles of the ethyl group attached to phosphorous atoms on the two symmetrically opposite sides of Pt atom in <i>trans</i> -PtCl ₂ (PEt ₃) ₂ molecule with pressure.....	126

Chapter 1: Introduction

1.1. Introduction to Organic Molecular Solids

Organic Molecular Solids are defined as solids which consist of molecules having carbon atom as an essential elemental species in them. The molecules in organic molecular solids are held together by multiple weak interaction forces such as Van der Waals interactions, hydrogen bonding, halogen bonding, dipole-dipole interactions etc. with conformationally flexible molecular moieties forming the 3-dimensional structure. These solids have several applications ranging from technology to bio-chemical processes, which make them an important part of science and technology. Owing to weak interactions and flexible molecular units of organic molecular solids, their structure is very sensitive to the change in thermodynamic parameters such as temperature and pressure. These parameters can be used to tune their molecular units, various interaction forces and crystal structures which can have a significant effect on its applications. For example, in the biological and biochemical processes such studies are useful in estimating force-fields and potentials which can be used to simulate different structures [1, 2]. They are also helpful in understanding the role of individual molecular orientations/conformations, distortions in the non-covalent interactions and intermolecular bonds, redistribution of electron density, and to correlate the "structure-property" relations in the formation of crystal structures. The force field calculations on small molecular organic systems can be useful in understanding of the macro-molecules such as biopolymers and proteins [1]. Thus, the understanding of individual molecular entities and their interactions provide an epitome in exploiting organic molecular crystals with huge impact on their applications in various fields such as pharmaceutical industry [3-8], molecular electronics [9-12], molecular recognition, bio-macromolecules [13-15], non-linear optical materials [16-18], crystal engineering [19], geochemistry [20], cryobiology [5, 21]

and bio-mimetic systems. The present thesis investigates two classes of organic molecular solids, *viz.*, amino acids and metal-organic systems.

Conformational flexibility of the molecular units and a network of various kinds of hydrogen bonds in the complex structures of amino acids make them an interesting as well as challenging class of organic molecular solids to study under varying thermodynamic conditions. In these systems, different molecular conformational motions are activated at different pressure/ temperature ranges and different timescales from seconds to micro-seconds [22, 23]. The study of such a molecular flexibility can be helpful in understanding the processes linked to phase transitions, polymerization and protein functionality. Another category of organic molecular solids include metal-organic complexes, where metals are held together by organic ligands which act as linkers and form 3-dimensional frameworks with applications in catalytic processes, crystal engineering, new material synthesis, gas storage and gas separation due to their porous structures [24-35]. The study of these compounds under extreme thermodynamic conditions have attained much attention due to the possibilities of realizing novel phases like supramolecular assembly, polymerization, and amorphization, which are related to their vibrational, optical and structural properties [36-40].

1.2. Thermodynamics of Phase transitions

Phase transformation is the change of the thermodynamic system from one form to another by changing any of the thermodynamic parameters such as pressure, temperature etc. They have been classified into different types depending upon the derivative state of the thermodynamic parameters, given by Ehrenfest in 1933 [41] and upon the mechanism followed during the transformation, given by Buerger in 1951 [42]. Depending upon the state of thermodynamic parameters, it is classified as the first order or second order phase transition. In the first order phase transitions, the first derivative of Gibb's free energy (G),

volume, and entropy show discontinuity at the transition point and the complete system shows a hysteresis loop. In the second order phase transition, the first derivative of Gibb's free energy, volume and entropy are continuous but the second derivative of Gibb's free energy shows discontinuous change at the transition point. These are smooth transitions as there is no time gap and no heat is absorbed or released during this transition. The Gibb's free energy is given as:

$$G = U + PV - TS \quad (1.1)$$

where, U is the internal energy, P is the pressure, V is the volume, T is the temperature and S is the entropy of the system. However, the availability of information on the change of entropy is limited by experimental techniques, therefore approach based on structural transformations (or mechanism followed during phase transformations) which in turn is based on the change in symmetry of the structure is considered. Depending upon the mechanism followed, phase transitions are classified into three categories: reconstructive, displacive, and order-disorder transitions. In the reconstructive phase transition, breaking and making of bonds occurs at the transition point which causes a new structure to be formed. This type of phase transition usually takes place deep inside the earth which causes drastic changes in the seismic properties of the earth mantle. In displacive transition, no bond breaking is required, but it involves the distortion in the bonds. The order-disorder phase transitions are further divided into two types as rotational and substitutional phase transitions. When one molecular unit rotates with respect to the rest of the molecules to causes phase transition, the process is called rotational order-disorder transition. When interchanging the positions of the atoms in a random fashion causes phase transition, it is called substitutional order-disorder phase transition.

1.3. Behavior of Organic Molecular Solids under varying thermodynamic conditions

Temperature and pressure are the two thermodynamic variables which cause isotropic and anisotropic deformation in the structure thereby causing deformation in the volume of the system and consequently change the properties of materials. Thus, variable temperature and pressure studies are helpful in understanding the structure, polymorphism, relative energies of different interactions and the behavior of hydrogen bonding network [1]. While, the main effect of pressure is to cause deformation in the electron cloud of the atoms and alter the equilibrium distance between the nuclei of the two atoms in a molecule, temperature primarily causes change in the population of energy levels for each normal mode of vibration. Therefore, the origin of deformation by both the variables may be different [43-45]. The deformation in the volume due to these variables is attributed to the anharmonic character of the potential [1]. The effect of high pressure and low temperature are generally found to be isotropic in the case of high symmetry systems such as cubic, whereas in the low symmetry systems such as monoclinic, triclinic etc., the effect may be anisotropic [46-49]. Generally, maximum and minimum compressions are observed normal and along the molecular layers respectively, which can be correlated with the anisotropy of structural distortion under varying thermodynamic conditions of temperature/ pressure [1, 50]. Thus, the emphasis of research in molecular solids is towards understanding the structural and geometrical response under different thermodynamic conditions. Also, the structural distortions in such systems under high pressure and low temperature may be same or different. For example, among the well-studied organic and metal-organic systems, the polymorphs of paracetamol [5, 51], sodium oxalate [52] etc. show similar (as shown in Figure 1.1 and Figure 1.2) and Cobalt (III) nitropentaammines [53-55], ice [56] etc. show different (as shown in Figure 1.3 and Figure 1.4) response under high pressure and low temperature conditions [15, 50, 57]. Paracetamol exists in two polymorphs as paracetamol I (monoclinic) and paracetamol II

(orthorhombic) as shown in Figure 1.1. The relative change in volume upon cooling and increasing pressure was found to be similar in both the polymorphs of paracetamol as shown in Figure 1.1.

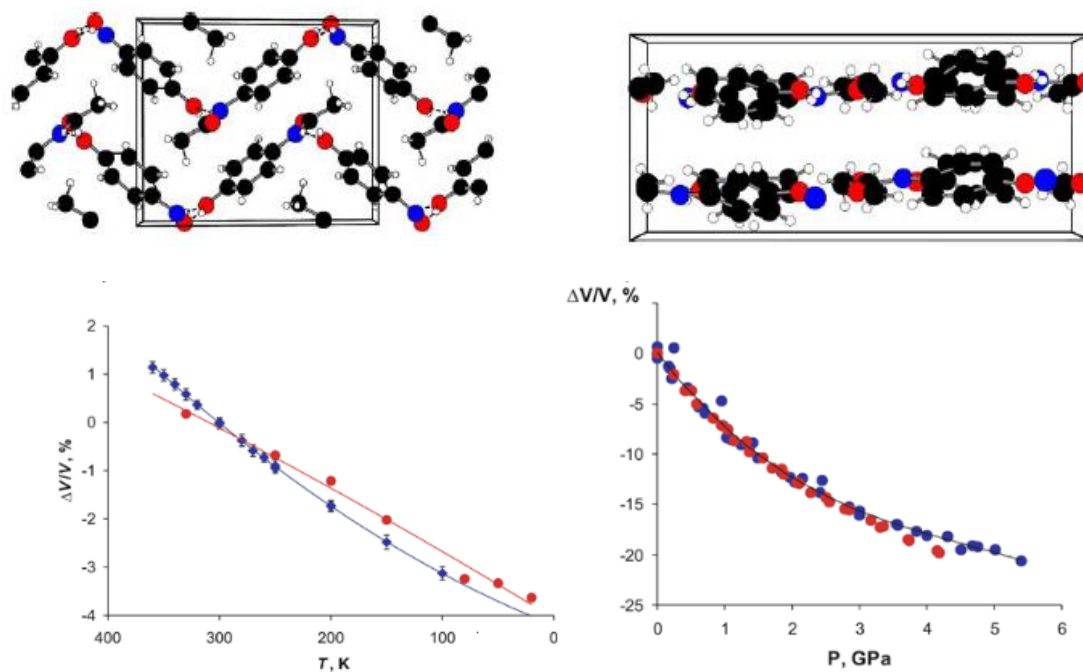


Figure 1.1: Fragments of the crystal structure of the monoclinic (Upper Left) and orthorhombic (Upper Right) polymorphs of paracetamol. Relative volume changes in the monoclinic (red) and orthorhombic (blue) polymorphs of paracetamol upon cooling (Lower Left) and with increasing pressure (Lower Right) [5, 6]. (reproduced with permission)

Similarly, the linear strain in low pressure polymorph of sodium oxalate have been found to be similar upon cooling and compression as shown in Figure 1.2. Cobalt (III) nitropentaammines depicts an example, where pressure and temperature behavior of lattice parameters are different, as shown in Figure 1.3. Thus, varied high pressure and low temperature effects are indeed a subject of extensive research for many compounds, even for the most common molecular system, *i.e.*, water ice, which possesses a range of different

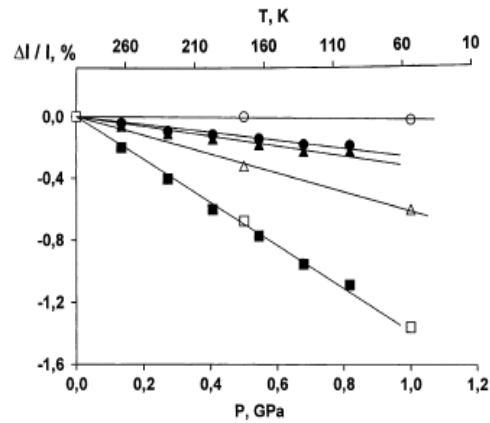


Figure 1.2: Linear strain in the low pressure polymorph of sodium oxalate upon cooling (filled symbols) and with increasing pressure (open symbols). The plots are scaled in such a way that volume changes on cooling and under pressure are the same [52]. (reproduced with permission)

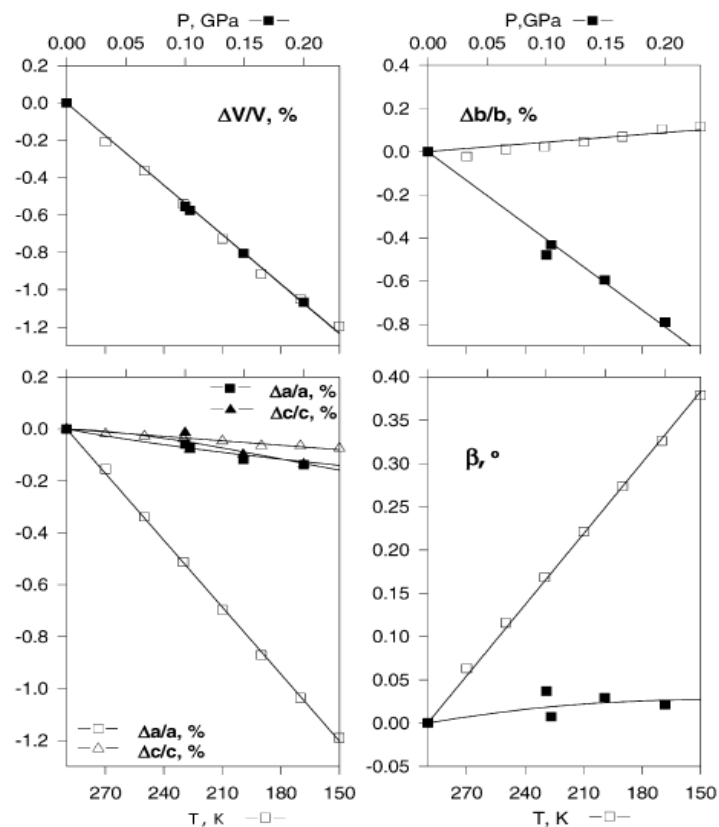


Figure 1.3: Comparison of changes in the cell parameter in $[\text{Co}(\text{NH}_3)_5\text{NO}_2]\text{Cl}_2$ with increasing pressure (filled symbol) and upon cooling (open symbol). The plot is scaled in such a way that the volume changes under pressure and on cooling are equal [57]. (reproduced with permission)

phases in the phase diagram (Figure 1.4). While, systematic cooling transforms it to ice Ih hexagonal phase, depositing vapours at very low temperatures results in cubic ice Ic phase, whereas high pressure- room temperature phase is cubic ice VII. All the phases are characterized by peculiar hydrogen bonding arrangements. Thus, the structural distortions, under varying thermodynamic conditions, can lead to phase transitions in molecular solids, which may result from drastic or sluggish modifications. In other words, the microscopic structure and properties of organic and metal-organic complexes can be tuned by varying the thermodynamic conditions which will have direct implications on their applications.

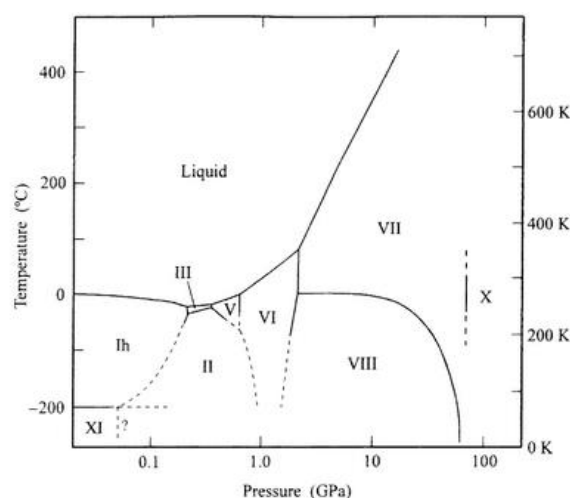


Figure 1.4: Phase diagram of the ice-water system on the logarithmic scale of pressure [56].

Further, in the hydrogen bonded organic molecular solids, the anisotropy of structural distortion can also be correlated with the directions of hydrogen bonds [15]. Hydrogen bonds, in general, are classified into three categories as strong, medium, and weak, depending on the geometry of the hydrogen bonding network, angle ($\angle A-H \cdots B$, where A is the donor, B is the acceptor and H is the hydrogen atom) and enthalpy associated with it. The geometry of hydrogen bond can be varied by changing the thermodynamic parameters or by changing the

chemical environment. However, the energy required to manipulate a hydrogen bond is very small as compared to covalent bonds [58]. The compressibility of hydrogen bonds depends on several factors such as strength of bonds, packing of molecules and other interactions in the crystal structure. These studies help us to understand various properties of hydrogen bonds and estimate its various interaction potentials. Under compression, in addition to change in inter-atomic separations, a change in the rotation of the molecular units can also occur, thereby having a complex effect on the hydrogen bonding network, which may also result in reversible or irreversible phase transitions. The effect of change in hydrogen bonding arrangement can be studied by probing various bond lengths, dihedral and torsional angles and also by studying the spectroscopic signatures of the material under respective thermodynamic conditions. Infact, various correlation plots and equations have been reported that correlate the pressure/ temperature induced change of the hydrogen bonds with the shift in the corresponding covalent bond vibrational stretching frequency [59-64]. Many amino acids have been studied at elevated pressures which result in subtle changes or drastic phase transitions [65-67]. For example, the simplest amino acid, glycine, crystallizes in three polymorphs α , β and γ depending on the ability to crystallize in different crystal lattices. The transformations among the polymorphs of glycine upon cooling and compression have been summarised in Figure 1.5. Under pressure, in crystalline α -glycine with space group $P2_1/n$, no phase transition has been observed upto 23 GPa with maximum compression is along the longest N-H---O hydrogen bond and expansion in the direction of shortest N-H---O hydrogen bond [13, 68]. β -glycine with space group $P2_1/a$, undergoes phase transition to a new phase called $\beta'(\delta)$ -phase at only 0.76 GPa [69], whereas γ -glycine with space group $P3_1$ undergoes a phase transition to new ζ -phase with space group Pn above 0.62 GPa [69] and the minimum compression is along the shortest hydrogen bond [13]. At low temperatures, β -glycine undergoes second order phase transition upon cooling to 252 K to β'' phase, with maximum

contraction along the b -direction and slight expansion along the direction close to the c -axis [70], whereas in the other polymorph, *i.e.*, α -glycine, no phase transition was observed upon cooling with the maximum contraction along the b -direction [70]. However, the anisotropy of structural distortion upon cooling α -glycine has considerable effect on its hydrogen bonding network which is still not understood. Comparative studies on glycine isotopes would be useful to understand such effects.

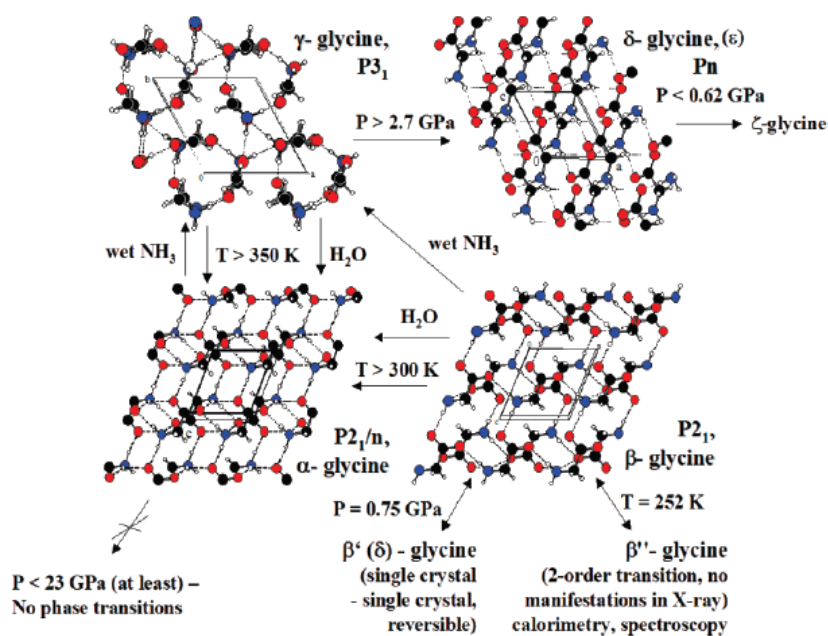


Figure 1.5: Structures of polymorphs of glycine (α , β , γ) upon cooling and on increasing pressures [2, 13, 68, 69, 71-73]. (reproduced with permission)

Another amino acid, L-serine I undergoes phase transitions to L-serine II and III forms in the same space group ($P2_12_12_1$) and the phase transitions are found to be due to conformational changes of the side chain which eventually changes the hydrogen bonding network [74-76]. Similar phase transition was observed for L-cysteine I to L-cysteine II and IV upon compression [77]. However, for the racemates of these amino acids, no phase transition was

observed for DL-serine under compression even upto 8.6 GPa [74], whereas for DL-cysteine I, phase transition was observed at very low pressures of 0.1 GPa to DL-cysteine II [78]. The difference in the behavior of different amino acid polymorphs under compression is due to varying response of constituent molecular orientations before and after phase transitions. Among the variable temperature studies, temperature induced phase transitions have been observed for L-cysteine and DL-cysteine, keeping the symmetry of space group intact [78-80]. The phase transition in L-cysteine has been depicted by subtle changes in the lattice parameters around 240 K [81]. Upon further lowering the temperature to 70 K, it showed ordering of the thiol groups and the changes in the conformations of the side chains [82, 83]. However, in DL-Cysteine, a phase transition has been observed around 206 K which is accompanied by the change in the torsional angles and re-arrangement of the hydrogen bonding network [80]. Similarly, in L-serine and DL-serine, the phase transitions were observed due to re-orientational changes in the side chain accompanied by the change in the hydrogen bonding network upon cooling [84, 85]. In yet another amino acid, L-Leucine, the temperature induced phase transitions are highly debated [86, 87] and contradictory reports exist on phase transition.

1.4. Motivation and Choice of Systems

In the present thesis, some representative amino acid and metal-organic systems have been studied, which are described below.

1.4.1. Amino Acids

Amino acids are the basic building blocks of proteins and are responsible for the existence of life on earth [88-91]. Alterations in vibrational and structural properties of amino acids by changing thermodynamic conditions is a fascinating field due to its several advantages in piezoelectricity [92-94], non-linear optics [95, 96], pharmaceuticals [97, 98] etc. The amino

acids are broadly classified into two types as “essential” and “non-essential”. Non-essential amino acids are created in the body few examples are glycine, cysteine, serine etc., whereas, essential amino acids are not created by the body for example Leucine etc. They play an important role in protein flexibility and bio-macromolecules. The detection of amino acids in interstellar regions has also generated much interest to understand their properties under varying conditions so as to obtain crucial information on the origin of life [99-106]. The crystal structures of amino acids are formed by connecting zwitterions of its molecules in the head to tail form via hydrogen bonds forming chains, helical or 3-dimensional structures [107]. The conformational changes of molecular fragments in amino acids can be correlated with the structural phase transitions [76, 78]. All the amino acids exist as a neutral molecule in the gaseous state and in the zwitterionic form in the solid and liquid state. In the present thesis, the isotopes of the simplest amino acid glycine in the solid phase at various low temperatures down to 4.2 K have been investigated. Another complex amino acid L-Leucine has also been studied under low temperature in order to understand the role of alterations of different molecular moieties in stabilizing such systems and also to probe the possible phase transitions.

a) α -glycine and deuterated α -glycine

Glycine is the simplest and the only achiral amino acid. It is a major component in macromolecular complexes of living organisms and has important applications in biomaterials. The search and study of glycine and H₂O/ CO₂ ices [99, 100, 108-110], is therefore a prime research area to probe molecular assemblies and trace life in extra-terrestrial regions where thermodynamic conditions are drastically varied [99-106]. It can serve as an archetype system where weak interactions play a decisive role for the structure stabilization. The crystal structure of glycine was first suggested in 1931 in the pioneering works of J. D. Bernal as

monoclinic with lattice parameters $a = 5.04 \text{ \AA}$, $b = 12.1 \text{ \AA}$, $c = 5.41 \text{ \AA}$ and $\beta = 111^\circ 38'$ containing four molecules in a unit cell with $P2_1/n$ space group [111]. In α -glycine, zwitterions are linked via hydrogen bonds N-H...O in double anti-parallel layers with Van der Waal interactions [107]. In the following decades, several studies have been carried out on glycine polymorphs using theory [112-116], infrared [115, 117-122], Raman [123-126], nuclear magnetic resonance (NMR) [113, 127, 128] spectroscopy, and powder/single crystal x-ray/neutron diffraction [13, 69, 107, 129, 130] with improvements in the computational and experimental techniques in order to provide finer details on the microscopic properties of its various ionic forms. Though, it has been studied by various methods for nearly a century now, systematic variable temperature/ pressure studies have been carried out in the last two decades only. Further, glycine complexes have been used for ferroelectric and non-linear applications [43, 131, 132]. The substitution of deuterium in place of hydrogen has vastly improved the properties of glycine complexes in the field of pyroelectric detectors [133-135], pharmaceutical industry [136-139] and drug metabolic processes. Due to various consequences of deuteration, several studies have been carried out to understand the isotopic effect under varying thermodynamic conditions which help to understand its physico-chemical behavior for its various applications. Thus, in order to have explicit understanding of the properties of glycine and its deuterated analogue and the behavior of hydrogen bonding network, low temperature spectroscopic studies on α -glycine and deuterated α -glycine in a wide temperature and spectral range have been carried out.

b) L-Leucine

L-Leucine ($C_6H_{13}NO_2$) is an “essential” aliphatic amino acid with wide applications in organic non-linear optical (NLO) materials due to its ultra-fast response time and high optical damage threshold to laser radiation owing to large electronic delocalization in π - π^* orbitals

[95, 140]. At ambient conditions, it crystallizes in monoclinic structure with $P2_1$ space group having lattice parameters $a = 9.61(8)$ Å, $b = 5.31(8)$ Å, $c = 14.72(8)$ Å and $\beta = 86.2^\circ$ with four molecules per unit cell having two different molecules in the asymmetric unit, as determined by Harding et al. [141], and re-determined with improved precision by Coll et al. [142] using powder diffraction experiments. This compound has been studied at ambient conditions by many techniques such as IR/Raman spectroscopy [118, 122, 143-149], x-ray diffraction [141, 150], neutron diffraction [87], NMR [151, 152], proton magnetic resonance [153], and matrix isolation infrared spectroscopy [154]. It exists in zwitterionic form in the solid state. Low temperature studies have also been carried out by different techniques in order to understand the behavior of temperature induced phase transitions. However, the previously reported temperature induced phase transitions in Leucine have not been verified in the later studies. Low temperature spectroscopic studies have been carried out in order to understand the microscopic details of possible temperature induced transitions by observing the signatures of conformational flexibility of the molecular moieties and analysing the anharmonicity associated with the vibrational modes.

1.4.2. Metal-Organic complex *trans*-PtCl₂(PEt₃)₂

Among the metal-organic complexes, *trans*-dichloro bis(triethylphosphine) platinum(II) (formula: *trans*-PtCl₂(PEt₃)₂) has been investigated at low temperatures as well as under high pressure to understand and compare the origin of phase transitions. Platinum(II)-organic complexes have applications in the field of catalysis, organic light emitting diodes (OLEDs), material synthesis, pharmaceutical industry, crystal engineering and supra-molecular assemblies [155-163]. These applications have direct correlation with their properties such as molecular geometry, metal-ligand bonding and stereochemistry. *trans*-PtCl₂(PEt₃)₂ is a metal-organic complex with the centre of inversion symmetry at the platinum atom. It exhibits a square planar structure with bulkier groups (PEt₃) placed diagonally opposite to the central Pt

atom. The studies focussed on the metal – ligand bond, π -back bonding, molecular reorientations and conditions for structural transitions have drawn interest for exploiting their technological applications. Thus, detailed investigations have been carried out under variable pressure/ temperature conditions in this representative Pt(II) based metal organic complex to study the orientational modifications of molecular moieties and weak interactions like hydrogen bonds using infrared and Raman spectroscopy well corroborated with x-ray diffraction studies.

1.5. Layout of thesis

The organization of the thesis is as follows:

Chapter 2 describes the details of the methods, experimental tools and techniques. This chapter also includes the upgradation of the IR beamline facility at INDUS-1, RRCAT, Indore, India. The tools used for compression of the materials under consideration include high pressure and low temperature. The experimental techniques include Fourier transform infrared (FTIR) spectroscopy, Raman Scattering, and x-ray diffraction. **Chapter 3** reports the observation of a perceptible isotopic effect on the 3-D framework of simplest amino acid, *i.e.*, α -glycine at low temperatures down to 4.2 K which have been examined using FTIR spectroscopy and Raman Scattering [164]. **Chapter 4** presents the effect of lowering the temperature on the complex amino acid, *i.e.*, L-Leucine which has been studied using FTIR spectroscopy [165]. Here, the understanding of the role of molecular orientations to trigger the phase transitions has been investigated in L-Leucine. **Chapter 5** presents the systematic temperature dependent study on metal-organic complex, *i.e.*, *trans*-dichloro bis(triethylphosphine) platinum(II) (formula: *trans*-PtCl₂(PEt₃)₂) which has been examined using infrared and Raman spectroscopic studies. **Chapter 6** includes the detailed high pressure study on *trans*-dichloro bis(triethylphosphine) platinum(II) using infrared/ Raman

spectroscopy, x-ray diffraction and density functional theory (DFT) techniques [166]. Finally,

Chapter 7 presents the summary of the thesis.

Chapter 2: Experimental Methodologies

2.1. Low temperature

Low temperature is an important thermodynamic parameter, which generally causes decrease in the overall volume of the unit cell by reducing the thermal agitations. Cooling of the sample can be carried out by two methods, *i.e.*, by cooling down the sample to a few Kelvin of temperature using mechanical refrigerators or by liquefying the gases and use them as a coolant. The most commonly used cryogenic fluids are Liquid Nitrogen (LN₂) and Liquid Helium (LHe) which can reach temperature of 77 K and 4.2 K respectively. Other rarely used cryogenic liquids are Liquid Hydrogen (LH), Liquid Neon (LNe), Liquid Oxygen and Helium-3 (³He). The Liquid Hydrogen can reach temperature of 20.2 K. However, there is a disadvantage of using it as cryogen as it becomes explosive when mixed with air. Therefore, special arrangements and precautions are required for its venting system. As Liquid Helium has lower boiling point than that of Hydrogen, it can be used in the low temperature range. Helium-3 and Liquid Neon are very expensive, therefore, they are rarely used as cryogens. Liquid Oxygen is also rarely used as it is an oxidising agent which can cause combustion. Different gases which are used as cryogens with different boiling temperatures when liquefied are summarized in Table 2.1. The temperature of any boiling liquid can be changed by varying the applied pressure. It can be lowered by decreasing the pressure and after a particular pressure/temperature conditions, freezing point is obtained where the corresponding gas solidify [167].

2.1.1. Measurement techniques

Cryostat (*cryo* means ‘cold’ and *stat* means ‘stable’) is an apparatus which is used to cool the sample mounted within it. There are different kinds of cryostats being used so far to cool the

Table 2.1: Boiling temperatures of commonly used cryogenic liquids at ambient pressure (1 Atm) alongwith references.

Cryogenic Liquids	Boiling Temperature at Ambient Pressure (1 Atm)
³ He	3.195 [168]
⁴ He	4.230 [169]
Hydrogen	20.268 [170]
Nitrogen	77.355 [170, 171]
Neon	27.100 [172]
Oxygen	90.196 [170, 173]
Argon	87.302 [170, 174]

sample. First is the Bath Cryostat, where the sample is directly immersed in the cryogenic liquid bath and the temperature of the dewar is changed by the pump/pressure technique. By decreasing the pressure of the dewar, low temperature is obtained at which the liquid boils. The drawback of this type of cryostat is that there is stratification of temperature in the dewar with the warmer liquid at the top and colder one at the bottom and we have temperature control only at the surface. This drawback can be overcome by using resistive heaters at different vertical positions of the dewar. Another drawback of Bath Cryostat is the use of glass dewars which could be fragile, therefore, one has to replace it with metal dewars. Second type of cryostat is the Continuous Flow Cryostat as shown in Figure 2.1. Here, the sample is cooled by attaching it to the cold finger of the cryostat which is placed in a vacuum chamber and this technique uses metal dewars. The cryogenic liquid is sucked by the pump and transferred to the cryostat through transfer line which gets evaporated by the heat exchanger, and these vapours are used to cool the sample. This type of cryostat is useful in carrying out precise variable temperature studies.

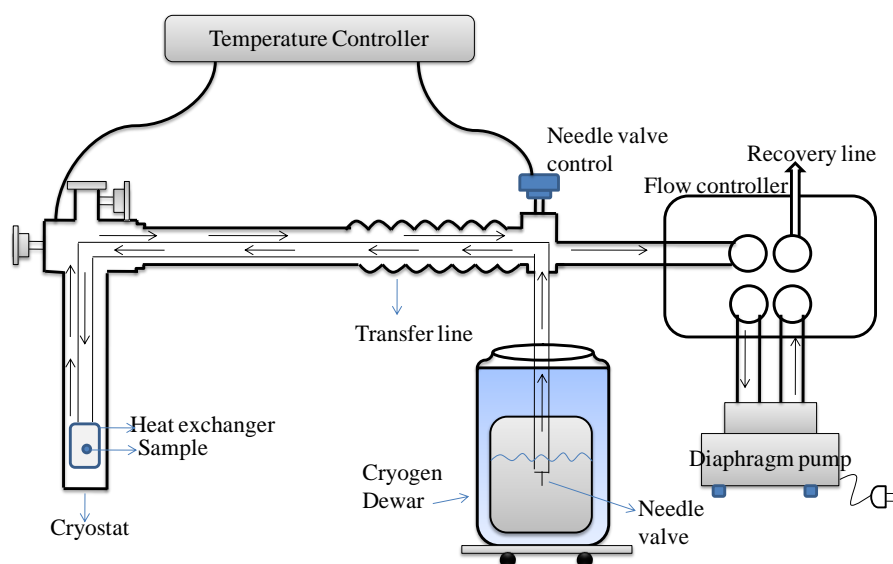


Figure 2.1: Schematic of the continuous flow cryostat set up. Sample is mounted in vacuum on a heat exchanger in the cryostat, Optical access is through windows. Vapours cool the sample, then travel back from the concentric ring of the transfer line to the flow controller to the gas flow pump, from the gas flow pump to the flow meter, to the Recovery line.

The main components for the designing of the cryostats are the cryostat outer body, sample holder, cryogen transfer tube, cryogen dewar, temperature controller, pressure gauge, and flow meter. Also proper materials should be used with appropriate contraction conditions to prevent leaks in the systems. Thus, the outer body of the cryostat should be made up of materials of low thermal conductivity, so that as temperature approaches 0 K, no heat is conducted to the cryostat. The most commonly used materials are Stainless Steel, Aluminium (Al) and Brass. These materials do not become brittle at low temperatures. The sample holder should have good thermal conductivity even at lower temperatures so that it can transfer the temperature to the sample mounted on it. The most commonly used material for making the sample holder is Copper (Cu) as it has high thermal conductivity. Heat transfer in a cryostat can take place by three processes which are conduction through solids, conduction through gases and thermal radiations. They are described as follows:

a. Heat Conduction through Solids:

Heat conduction through solids can be defined in terms of thermal conductivity. The relationship between heat flux and the temperature gradient is given by the Fourier's law [175] as:

$$q = -k(T) * \nabla T \quad (2.1)$$

where, q is the heat flux density, k is the thermal conductivity which is temperature dependent and ∇T is the temperature gradient. In 1-Dimension, equation (2.1) can be written as:

$$q = -k(T) \frac{dT}{dx} \quad (2.2)$$

The cryostat part has uniform cross-sectional area, and then we can integrate equation (2.2) as:

$$q \int_0^L \frac{dx}{A} = \int_{T_{cold}}^{T_{hot}} k(T) dT \quad (2.3)$$

where, A is the cross-sectional area and ' T_{cold} ' and ' T_{hot} ' are the temperatures at the ends of the element. When the area is constant, equation (2.3) becomes:

$$\frac{q}{A} = \frac{1}{L} \int_{T_{cold}}^{T_{hot}} k(T) dT \quad (2.4)$$

where, $\int_{T_{cold}}^{T_{hot}} k(T) dT$ term is defined as thermal conductivity integral, which is an important property of the solid materials for designing at low temperatures as the response of the solids at low temperature is different from the room temperature and L is the length of the

element. The variation of thermal conductivity with temperature for different materials is shown in Figure 2.2. In case of pure metals, the thermal conductivity varies over the entire temperature range as shown in Figure 2.2. So, in order to determine the exact value of low temperature thermal conductivity (k) of metals, we can measure low temperature electrical resistivity (ρ) from the Wiedemann-Franz law which is given as:

$$k\rho \propto T \quad \text{and} \quad k\rho = LT \tag{2.5}$$

Where, L is the Lorenz number = $2.44 \times 10^{-8} \text{ W}\Omega\text{K}^{-2}$. The equation (2.5) also explains the peak in the case of high purity metals, as the electrical conductivity decrease electron heat conduction at high temperatures.

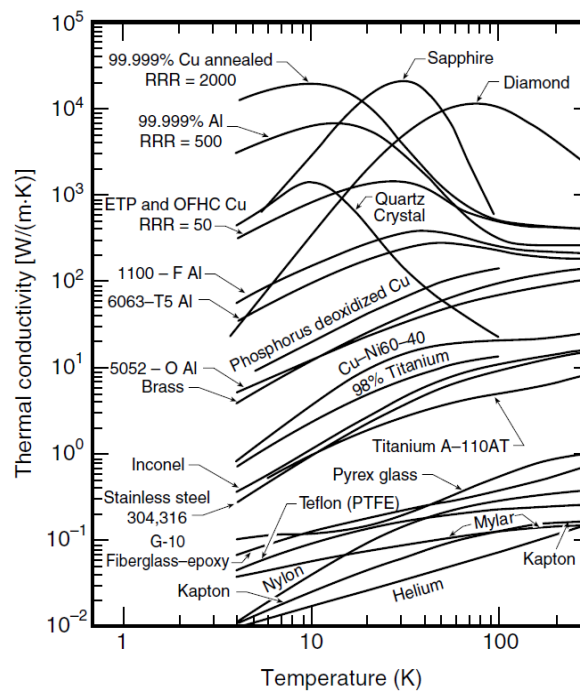


Figure 2.2: Variation of thermal conductivity at low temperatures for commonly used materials [167].

b. Heat Conduction through gases:

The heat transfer can take place by the residual gases which depend on the pressure of the gas. In the high pressure regime, the mean free path is limited by the collision of the gas molecules with each other and is inversely proportional to the pressure of the gas. The thermal conduction is, therefore, independent of pressure in this regime. The mean free path (l) is then given as [167]:

$$l = 2.87 \times 10^{-3} \frac{T^{j+1}}{P} \quad (2.6)$$

where, l is the mean free path measured in cm, T is the temperature in Kelvin and P is the pressure in Pascal. The exponent $j+1$ varies for different cryogenics; for helium (the most commonly used exchange gas), it is 1.147. At very low pressure, the gas moves from hotter region to colder region without colliding with other molecules. Therefore, thermal conduction is proportional to the number of molecules present in the system and it varies linearly with the pressure of the gas. In the normal pressure regime, the heat conduction (Q) between two plates is given as:

$$Q = \bar{k} A \frac{\Delta T}{D} \quad (2.7)$$

where, \bar{k} is the mean value of the temperature dependent thermal conductivity of the gas between two boundary temperatures, A is the surface area, D is the separation and ΔT is the temperature difference. At low pressure, the heat conduction (Q) between two concentric cylindrical rings is given as:

$$Q = r a_o P A \Delta T \quad (2.8)$$

where, r is a constant which is different for different gases, P is the pressure of the gas between two concentric rings, A is the surface area, ΔT is the temperature difference and a_o is a dimensionless number given as:

$$a_o = \frac{a_1 a_2}{\left[a_2 + \left(\frac{A_1}{A_2} \right) (1 - a_2) a_1 \right]} \quad (2.9)$$

where, a_1, a_2 the accommodation coefficients of the inner and outer are surfaces respectively and A_1, A_2 are the areas of inner and outer surfaces respectively.

c. Radiative Heat transfer:

The Radiative heat transfer (E) from a surface is given by the Stefan-Boltzmann equation as:

$$E = \sigma \epsilon A T^4 \quad (2.10)$$

where, σ is the Stephan's constant ($5.67 \times 10^{-8} \text{ Wm}^{-2} \text{ K}^{-4}$), ϵ is emissivity, A is the cross-sectional area, and T is the temperature. Emissivity is a dimensionless number which varies between 0 and 1 and for a black body ϵ is 1. The net heat exchange (ΔE) between the two surfaces is given as:

$$\Delta E = \sigma \epsilon A (T_2^4 - T_1^4) \quad (2.11)$$

where, 1 and 2 are the cold and hot surfaces respectively. The emissivity is temperature and wavelength dependent. The Radiative heat transfer in a cryostat is due to the temperature difference between various components of the cryostat and the unwanted radiations entering into it from the surrounding which may cause heating of the sample. This can be reduced by decreasing the surrounding temperature or by decreasing the surface emissivity. Therefore,

polishing of the surface with materials having low emissivity is done to reduce this effect and hence, provide good shielding from the radiation. Some of the commonly used materials which have good shielding are mentioned in Table 2.2.

Table 2.2: Emissivity of different materials

Material	Emissivity
Polished copper	0.02-0.04
Lightly oxidised copper	0.1
Highly oxidised copper	0.6
Aluminium (pure and alloys)	0.01-0.06
Highly oxidised aluminium	0.2
Gold	0.015-0.03
Ice	0.9

2.2. High Pressure generation and measurements

Pressure is defined as force per unit area ($\text{Pressure} = \text{force}/\text{area}$). Earlier, piston and cylinder were used to generate high pressure. However, due to the size constraints, limited pressure values could be achieved by this method. Then diamonds, the hardest known materials were introduced by Lawson and Tang in 1950 [176]. Later on Diamond Anvil Cells (DACs) were introduced by Weire et. al. in 1959 [177] to generate high pressures. In DACs, the pressure is applied by pushing the two diamonds towards each other with the gasket in between the two diamonds. The sample size used in DAC is very small (of the order of microns range). Therefore, very high pressures can be achieved with the DACs. The two diamonds are cut into flat parallel surfaces known as culet. These culets are aligned with respect to translation and rotation to make them concentric and parallel to each other using rocker and base plates. The rocker acts as a piston and the base plate acts as a cylinder. The two diamonds are glued on the rocker and base plate for alignment. The translational

alignment is done by matching both the diamond culets laterally by translation along the X-Y direction. The rotational alignment is done by adjusting the tilt between the two culet faces and observing the interference fringes between the two non-parallel culet faces. When the two diamonds become parallel to each other, the interference fringes disappear. The two diamonds become parallel to each other, the interference fringes disappear. The schematic of the Diamond Anvil Cell along with the gasket is shown in Figure 2.3.

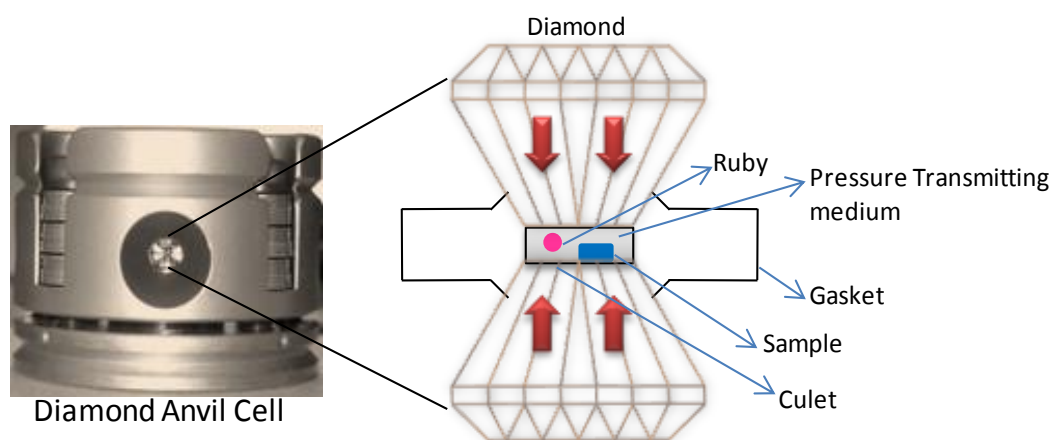


Figure 2.3: Schematic of the Diamond Anvil Cell (DAC).

The choice of the gasket material used and the hole dimensions in the gasket are one of the important deciding parameters for the highest pressure a DAC can attain. Different materials which are used as gasket are stainless steel, tungsten, rhenium, and boron epoxy. The initial thickness of the gasket is chosen nearly $\sim 200\text{-}300\ \mu\text{m}$. Then the gasket is pre-indented by placing it between the two diamonds in the DAC. The thickness of the pre-indented portion is approximately $\sim 100\ \mu\text{m}$. Then a hole is drilled either by mechanical drilling or by using spark erosion method. This hole in the gasket is known as sample chamber where a sample along with pressure marker (to estimate the pressure value) is loaded.

For high pressure experiments, uniform pressure in the sample chamber is very crucial. This is done by loading pressure transmitting medium (PTM) (for uniform or hydrostatic pressure conditions) along with the sample, which do not react or dissolve with the sample. Most commonly used PTM for high pressure experiments are 4:1 methanol:ethanol mixture and 16:3:1 methanol:ethanol:water mixture. These pressure transmitting media are hydrostatic upto a certain pressure value known as glass transition temperature. Beyond this, they become quasi-hydrostatic. Even gases can also be used as PTM which remain hydrostatic upto very high pressures (~ Mbar range). Special gas loading systems are required for loading gas in the sample chamber of the DAC. Commonly used gases are hydrogen, argon, neon and liquid helium. Table 2.3 summarizes different pressure transmitting media used with their hydrostatic and quasi-hydrostatic pressure values at ambient temperature.

Table 2.3: Commonly used pressure transmitting media with their hydrostatic and quasi-hydrostatic pressure values alongwith references.

Medium	Freezing pressure at RT (GPa)	Quasi-hydrostatic pressure range at RT (GPa)	References
4:1 Methanol:Ethanol	10.4	~20	[178, 179]
16:3:1 Methanol:Ethanol:Water	14.5	~20	[180]
Silicone oil	7	~15	[181, 182]
Hydrogen	5.7	~60	[183]
Helium	11.8	~80	[178]
Neon	4.7	~16	[178]
Nitrogen	2.4	~30	[184]

For accurate measurement of pressure value, a pressure marker is loaded in the sample chamber. Commonly used pressure markers are Gold (Au), Silver (Ag), Tungsten

(W), Platinum (Pt) and Copper (Cu), as their unit cell parameters can be obtained with static pressure conditions. Another commonly used pressure marker is Ruby ($\text{Al}_2\text{O}_3:\text{Cr}^{3+}$) which is based on the laser fluorescence method. When a laser light strikes the ruby crystal, it gets excited and undergoes a transition to Y and U bands and then they de-excite to the metastable states ($E_{1/2}$ and $E_{3/2}$) through non-radiative process. From the metastable state, they further de-excite to the ground state which gives two strong luminescence lines as R1 and R2 respectively.

$E_{1/2} \rightarrow {}^4A_2$ (R1 line at 6942 Å which is equal to 14402 cm^{-1})

$E_{3/2} \rightarrow {}^4A_2$ (R1 line at 6928.2 Å which is equal to 14432 cm^{-1})

The shift of these ruby lines with the applied pressure is used to estimate the pressure value. Even the hydrostaticity of the sample chamber can also be checked by observing the widths of these ruby lines. For hydrostatic conditions, the (R1-R2) line separation remains constant. For non-hydrostatic conditions, this distance changes as R1 line shows a prominent red shift, hence changing the distance between R1 and R2 lines. Also the peaks found to broaden up in non-hydrostatic conditions. From the pressure induced variation of volume, we can also calculate Bulk modulus (B) of the material as $B = -V(\partial P/\partial V)$, and its first derivative is given as $B' = (\partial B/\partial P)$. These zero pressure values (or almost room pressure) are denoted by $B_o = -V_o(\partial P/\partial V)_{P=0}$ and its first derivative is given as $B'_o = (\partial B/\partial P)_{P=0}$. The variation of volume with pressure is fitted with Murnaghan equation of state (EOS) [185] which is given as:

$$P(V) = \frac{B_o}{B'} \left[\left(\frac{V}{V_o} \right)^{-B'} - 1 \right] \quad (2.12)$$

This equation is used if the compression of the volume under pressure is low. For higher compression of the material, Birch-Murnaghan EOS is used which introduces a finite strain which is expanded using Taylor's series. The Birch-Murnaghan EOS of third order [186] is given as:

$$P(V) = \frac{3B_o}{2} \left[\left(\frac{V_o}{V} \right)^{\frac{7}{3}} - \left(\frac{V_o}{V} \right)^{\frac{5}{3}} \right] \left\{ 1 + \frac{3}{4} (B'_o - 4) \left[\left(\frac{V_o}{V} \right)^{\frac{2}{3}} - 1 \right] \right\} \quad (2.13)$$

where, P is the pressure, V_o is the reference volume, V is the deformed volume, B_o is the bulk modulus, and B'_o is the first derivative of the bulk modulus with respect to pressure.

2.3. Spectroscopic and structural characterization

2.3.1. Infrared Spectroscopy

For a molecule with ' N ' number of atoms, a total of ' $3N$ ' degrees of freedom are possible. Out of these ' $3N$ ' vibrations, three correspond to translational motion and three corresponds to rotational motion. The molecule is then left with ' $(3N-6)$ ' degrees of freedom which are known as normal modes of vibration of the molecule. For a linear molecule, there is no rotation about the bond axis, therefore, the molecule will have ' $(3N-5)$ ' degrees of freedom. Under the classical treatment, when electromagnetic radiations interact with the molecule, then the frequency ($\tilde{\nu}$, in wavenumber, cm^{-1}) of the bond vibration is given by:

$$\tilde{\nu} = \frac{1}{2\pi c} \sqrt{\frac{k}{\mu}} \quad (\text{cm}^{-1}) \quad (2.14)$$

where, k is the spring constant and μ is the reduced mass of the A-B bond system and c is the velocity of light (3×10^{10} cm/sec). As the vibrational energies are quantised, the energy of a vibrational state is given as:

$$E = \left(v + \frac{1}{2} \right) hc\tilde{\nu} \quad (2.15)$$

where, $h = 1.054 \times 10^{-34}$ Js, c is the velocity of light, and $\tilde{\nu}$ is the wavenumber in cm^{-1} , v is the vibrational quantum number and under harmonic approximation $\Delta v = \pm 1$ which is known as fundamental vibration. For the real systems, harmonic approximation is not applicable because there are anharmonic contributions to the potential for each vibration. Also, each vibration is not independent but coupled to other vibrations. Therefore, the selection rule under anharmonic approximation becomes $\Delta v = \pm 1, \pm 2, \pm 3, \dots$ which also contains overtone and combination modes of vibrations and the intensities also fall off rapidly.

Infrared (IR) spectroscopy is an absorption technique where infrared radiations interact with the sample. This technique provides information of the molecular vibrations associated with the molecule (bending and stretching vibrations). For a molecule to be infrared active, the necessary condition is the change of dipole moment of the molecule. The intensity (I_{IR}) of the infrared active mode is then given as:

$$I_{IR} \propto \left(\frac{\partial \mu}{\partial R} \right)^2 \quad (2.16)$$

where, μ is the dipole moment and R is the normal coordinate.

In this thesis, Fourier transform infrared (FTIR) spectroscopy has been used for the infrared measurements of the sample. The basic principle of FTIR spectroscopy is explained as follows. The infrared radiation is emitted from a source (Globar) and collimated beam of this radiation falls on the beamsplitter. It splits the beam into two parts. One is transmitted to the fixed mirror (M1) and other is reflected to the moving mirror (M2). After getting reflected back from the respective mirrors (M1 and M2) as shown in Figure 2.4, both the beams

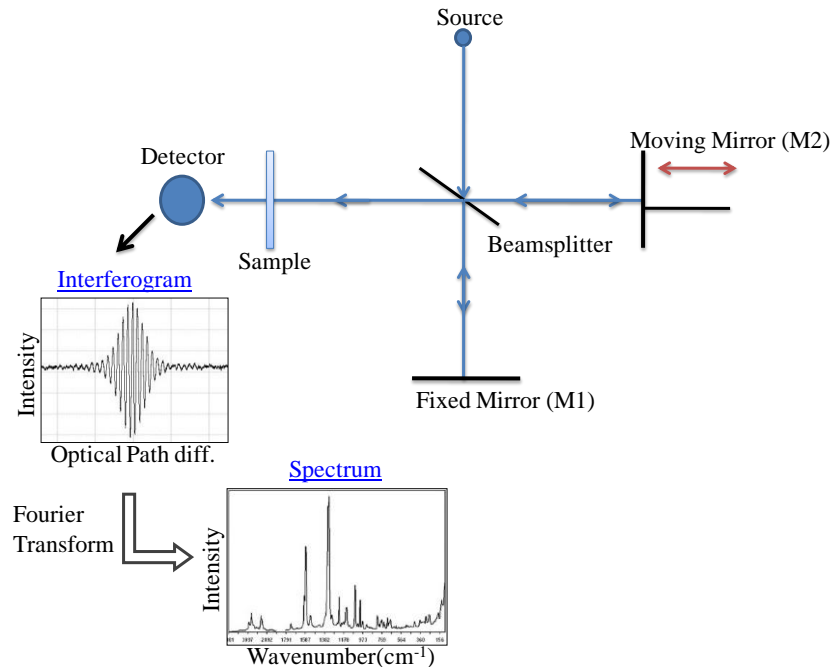


Figure 2.4: Schematic of Fourier transform infrared Spectroscopy.

recombine at the beamsplitter and interfere with each other. Depending upon the path difference (δ) between the two mirrors from the beamsplitter, constructive or destructive interference occurs. When M1 and M2 are at equal distance from the beamsplitter or the path difference is equal to the integral multiple of the wavelength, constructive interference takes place. If the path difference is half integral multiple of wavelength, destructive interference takes place. Before reaching the detector, it passes through the sample which absorbs the radiation. The interferogram, *i.e.*, intensity versus optical path difference is further Fourier transformed using algorithms to obtain the spectrum, *i.e.*, intensity versus wavenumber. The equations used for Fourier transformations of the interferogram to spectrum are as follows:

$$I(\delta) = \int_{-\infty}^{+\infty} B(\tilde{\nu}) e^{2\pi i \tilde{\nu} \delta} d\tilde{\nu} \quad (2.17)$$

And its Fourier transform as:

$$B(\tilde{\nu}) = \int_{-\infty}^{+\infty} I(\delta) e^{-2\pi i \tilde{\nu} \delta} d\delta \quad (2.18)$$

where, $I(\delta)$ is the interferogram and $B(\tilde{\nu})$ is the spectrum.

The main advantages of Fourier transform based infrared spectroscopy compared to grating based infrared spectroscopy are superior signal to noise ratio, lower acquisition time etc., which result from the following advantages:

1. Throughput (also known as Jacquinot Advantage) – all the IR radiation passes through the sample and falls on the detector.
2. Multiplex (also known as Fellgett Advantage) – all the wavenumbers of the radiation are detected at once.
3. Conne's Advantage – wavelength scale is internally calibrated by a He-Ne laser which provides accurate wavenumber information.

The infrared measurements presented in this thesis have been carried out using Bruker Vertex 80V Fourier transform based infrared (FTIR) spectrometer. The optical layout of the FTIR is shown in Figure 2.5. The infrared spectrum is divided into three regions, Far-IR (FIR), Mid-IR (MIR), and Near-IR (NIR). The FIR region spans the spectral range 10-400 cm^{-1} and is also known as lattice region which contains molecular information, lattice modes and hydrogen bond stretching vibrations. The second region is MIR region spanning spectral range 400-4000 cm^{-1} . The region 400-2000 cm^{-1} is the fingerprint region which contains information of various deformation modes of the molecule such as wagging, scissoring, twisting, torsional, bending and rocking vibrations. The region 2000-4000 cm^{-1} is a complex region as it consists of various stretching vibrations along with some overtone and combination bands. The third region, 4000-14000 cm^{-1} , is NIR. This region consists of

overtone as well as combination modes. The various components of FTIR used are briefly described below:

1. Source: It is a filament which produces radiation in the infrared region. Different sources are used in the three IR regions, defined above. Commonly used sources are mercury (Hg) lamp and globar in the FIR and MIR regions respectively. In the NIR region, tungsten lamp is used. Synchrotron radiation is another source which spans the wide spectral region from microwaves to hard x-rays. It is used for infrared measurements when high Brilliance is required.
2. Beamsplitter: Function of the beamsplitter is to split the beam into two parts, where one part of the beam is transmitted to the fixed mirror and other part is reflected to the moving mirror. Again, different regions have different beamsplitters. Commonly used beamsplitter in the FIR region is Mylar beamsplitter and in the MIR region is KBr beamsplitter. For the NIR region, CaF₂ beamsplitter is used.

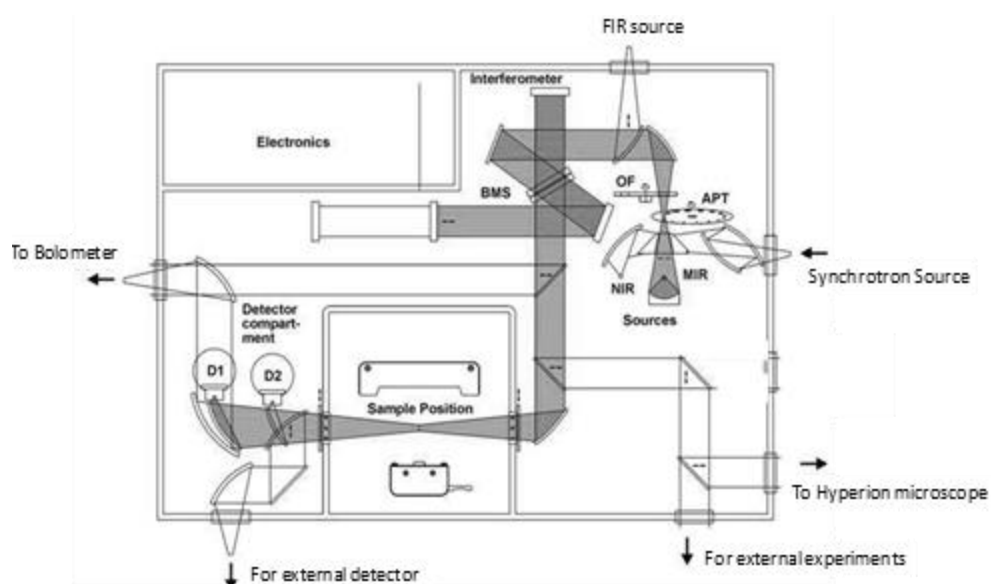


Figure 2.5: Optical Layout of Fourier transform infrared spectrometer (BRUKER VERTEX 80V).

3. Detectors: For the FIR region we have two detectors. One is known as Deuterated Tri-Glycine Sulfate detector (DTGS), which is a room temperature detector and easy to handle with sensitivity (D^* in $\text{cm.Hz}^{1/2}/\text{W}$) of the order of $\sim 2.7 \times 10^8$. Second detector is the bolometer detector which is liquid helium based and has more sensitivity (of the order of $\sim 10^{12}$) to low energy FIR radiation compared to the room temperature DTGS detector. In the MIR region, we have Mercury Cadmium Telluride (MCT) detector which is liquid nitrogen cooled with sensitivity of the order of $\sim 6.4 \times 10^{10}$. In the NIR region, InSb and Si diode detectors are used.

High Pressure infrared Spectroscopy:

Normal diamonds cannot be used for high pressure infrared measurements as these diamonds have large absorption in the MIR range. Therefore, special diamonds known as Type IIa (with no nitrogen impurities) were used for the high pressure infrared studies as they have clearer spectrum in the MIR region as shown in Figure 2.6 (Left). Infrared microscope uses special Cassegrain type of reflecting optics to minimize optical aberrations. The microscope is coupled to the FTIR instrument. The beam from FTIR instrument is focussed onto the sample through the microscope and then the transmitted beam from the sample is collected by the condenser and finally sent to the detector. The schematic diagram of infrared Microspectroscopy is shown in Figure 2.6 (Right). The spatial resolution (R) of the microscope depends upon two factors. First the incident radiation wavelength and second is the numerical aperture of the objective and condenser used and is given as:

$$R = \frac{1.22 \lambda}{(NA_{obj.} + NA_{cond.})} \quad (2.19)$$

where, NA_{obj} and NA_{cond} are the numerical apertures of objective and condenser respectively. For carrying out high pressure studies in this thesis, 15X objective has been used with 0.4 numerical aperture and working distance of 24 mm between sample and objective.

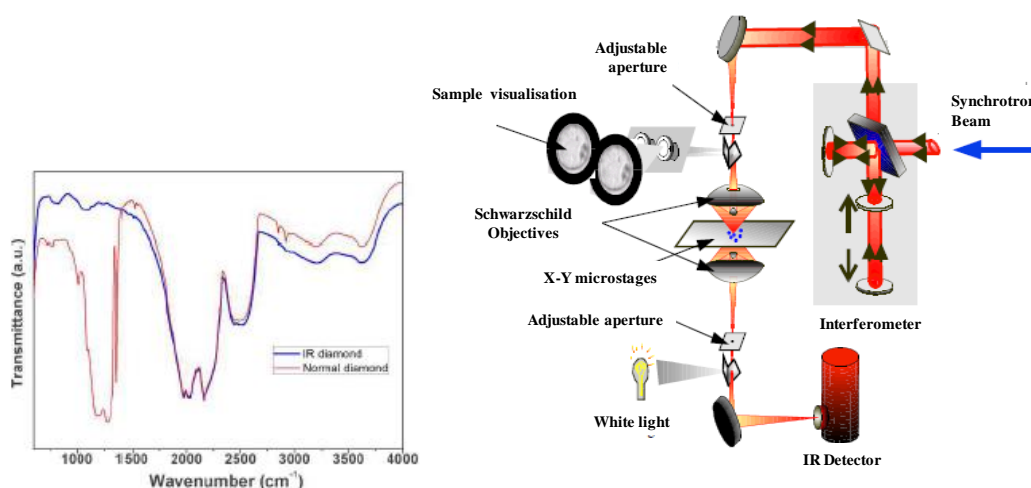


Figure 2.6: (Left) MIR spectra of normal diamond (red spectrum) and Type IIa diamond (blue spectrum) recorded using Bruker IFS125 instrument. [187] (Right) Schematic diagram of infrared microspectroscopy for high pressure measurements.

Low Temperature infrared Spectroscopy:

A continuous flow helium cryostat, Oxford Optistat CF-V was used for in-situ low temperature investigations. Figure 2.7 shows the low temperature experimental set-up installed and coupled to FTIR at BL-06, IR beamline, INDUS-1 synchrotron radiation source at RRCAT, Indore, India. The sample is mounted on the cold finger of the cryostat. The liquid cryogen is transferred from the cryogen dewar to the cryostat through the transfer line using oil free diaphragm pump. Temperature is controlled using a PID controller and helium flow is monitored using a gas flow meter calibrated for helium gas. The cryostat was mounted in the sample compartment of Bruker Vertex 80V Fourier transform infrared

spectrometer. The windows provide the optical access for the sample transmission measurement. He/N₂ vapours travel back from the concentric ring of the transfer line to the Recovery line via flow controller and gas flow pump. The temperature in this cryostat can be varied from 4.2 K to 500 K.

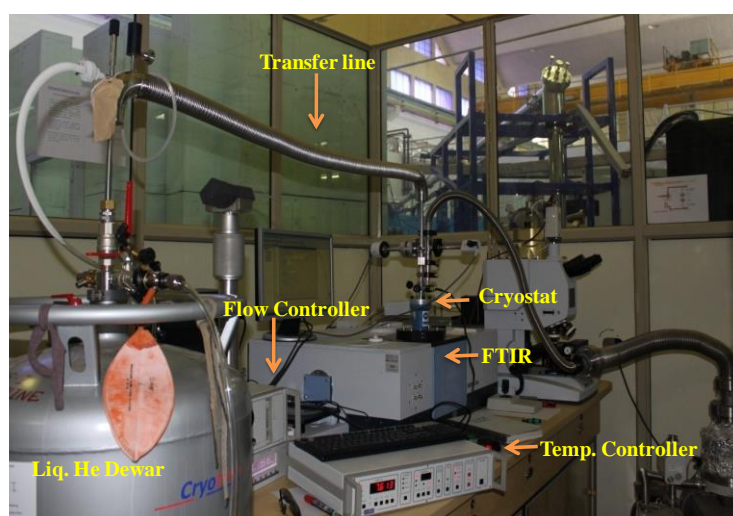


Figure 2.7: Experimental station of the low temperature set-up coupled to Fourier transform infrared spectrometer at BL-06, IR beamline, INDUS-1, RRCAT, Indore, India.

2.3.2. Raman Spectroscopy

When a monochromatic light of frequency ' ν ' is incident on the sample, it is elastically scattered by the sample. This is known as Rayleigh scattering. A very small fraction of photons (1 out of 10^6) is scattered inelastically which is referred to as Raman scattering. Therefore, it is a very weak signal. The inelastically scattered photon can have frequency higher or lower than the incident photon frequency. When the frequency is shifted lower than the incident frequency, it is known as Stokes shift (downward shift) and when the resulted

frequency is shifted to the high frequency side than the incident frequency, it is known as anti-stoke shift (upward shift). This shift is shown in Figure 2.8.

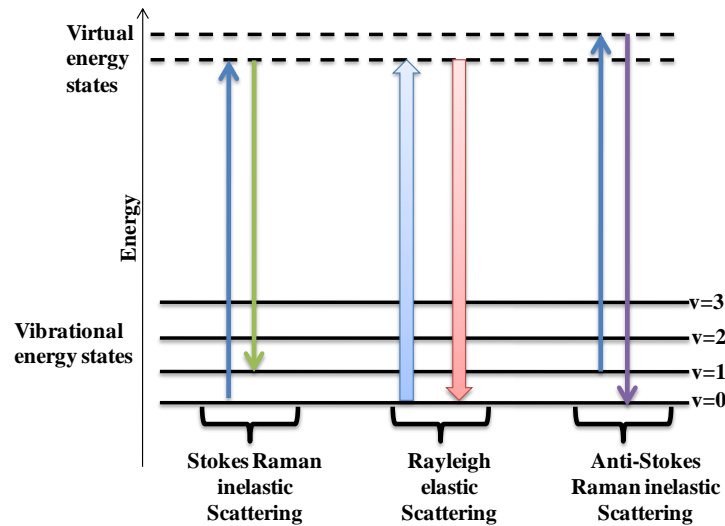


Figure 2.8: Schematic diagram of Raman scattering (Left – Stoke Raman inelastic scattering, Middle – Rayleigh elastic scattering, and Right – Anti-Stokes Raman inelastic scattering).

According to the classical theory of Raman Effect, it occurs when there is a change in the polarizability of the molecule. When the molecule is placed in the path of the static electric field, the positive charges move toward the negative pole and the negative charges move towards the positive pole of the applied electric field. This separation of positive and negative charges causes induced dipole moment and hence, the molecule becomes polarised. The induced dipole moment (μ) is given by:

$$\mu = \alpha E \quad (2.20)$$

where, α is the polarizability and E is the applied electric field. The intensity (I_{Raman}) of the Raman scattered light is proportional to the square of change in the polarizability and to the fourth power of the frequency of the laser light used, which is given as:

$$I_{Raman} \propto \left(\frac{\partial\alpha}{\partial R}\right)^2 \nu^4 \quad (2.21)$$

where, α is the polarizability, R is the normal coordinate and ν is the frequency.

High pressure Raman spectroscopy:

For recording Raman spectra at high pressure, triple stage Raman spectrometer (HORIBA Jobin Yvon's T64000) has been used in this thesis. The Raman signal is excited using 532 nm diode pump solid state laser which passes through the confocal microscope and focuses on the sample loaded in the diamond anvil cell. The optical layout of the Triple stage Raman spectrometer is shown in Figure 2.9. The inelastic scattered radiations from the sample pass to the double pre-monochromator stage which acts as a tunable filter. The first monochromator disperses the radiation. The second monochromator which is kept opposite to that of the first one, *i.e.*, the incidence angle for the second monochromator is identical to the scattered angle of the first monochromator. Therefore, the second monochromator converge the radiation and then the converged radiation passes through the third monochromator and is dispersed again. This mode of collecting the radiation is known as subtractive mode configuration and is shown in Figure 2.10. The advantage of this configuration is that it can measure very low frequencies close to the laser wavelength ($< 5 \text{ cm}^{-1}$) regardless of which wavelength of the laser used. The dispersed radiation from the third monochromator is collected by the liquid nitrogen cooled charge coupled device (CCD) detector.

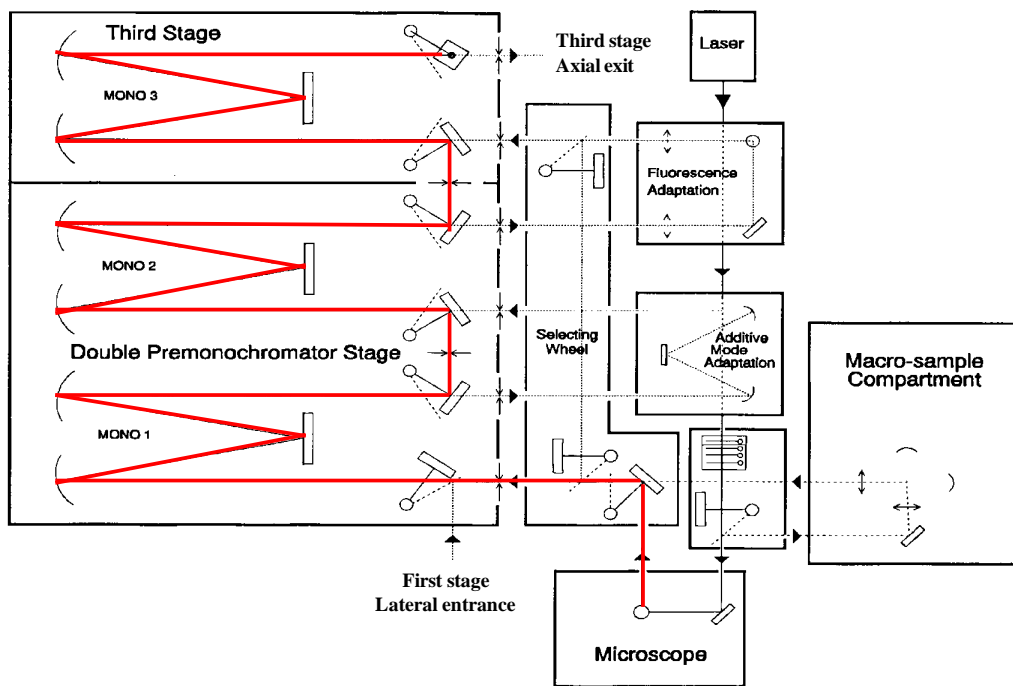


Figure 2.9: Optical layout of the Triple stage Raman spectrometer.

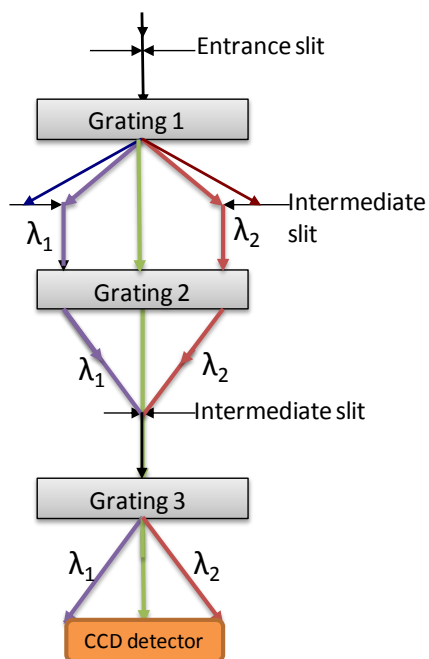


Figure 2.10: Subtractive mode configuration used in the triple stage Raman spectrometer.

Low temperature Raman spectroscopy:

The Triple stage Raman spectrometer (HORIBA Jobin Yvon's T64000) fitted with Linkam stage THMS600 was used for the low temperature Raman measurements. The schematic of the low temperature sample stage set-up used is shown in Figure 2.11. The Linkam stage is mounted at the focus point of the confocal microscope of the Raman system. The stage is connected to the temperature controller which controls the flow rate of the cryogenic liquid (liquid nitrogen) and measures the temperature at the sample. The sample stage and the top window of the Linkam stage are purged with the nitrogen gas so as to avoid condensation at the sample. The nitrogen gas is recycled through the pump and warmed for purging purpose.

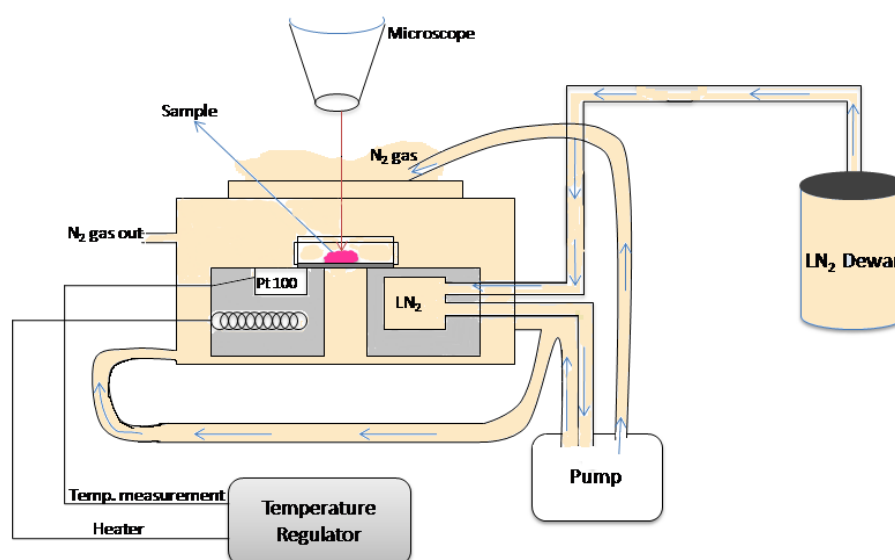


Figure 2.11: Schematic of low temperature sample stage set-up used with the triple stage Raman spectrometer.

2.3.3. X-ray diffraction

X-ray diffraction is a non-destructive technique where the x-ray radiation interacts with the electron cloud of the atoms. When x-rays hit the crystal, each atom acts as a diffraction

centre. As the x-rays have shorter wavelengths, they are scattered by adjacent atoms and the scattered x-rays interfere constructively or destructively with each other. When the path difference between the scattered rays is an integral multiple of wavelength (λ), then diffraction takes place. The diffraction condition is given by Bragg's law as:

$$2d \sin\theta = n\lambda \quad (2.22)$$

where, d is the interplanar distance between the two consecutive planes, θ is the angle of incidence made with respect to plane and λ is the wavelength of the x-rays used and n is the order of diffraction. X-ray diffraction from crystalline solids was discovered by Max von Laue in 1912. A crystal is made up of lattice plus basis, *i.e.*, there is a periodic arrangement of atoms in the planes and the distance between consecutive planes is defined by parameter d . The Bragg's condition given by equation (2.22) can be easily applied to the systems with high symmetry such as cubic, tetragonal etc. However, this equation becomes complex when applied to low symmetry systems and does not provide exact information of the intensity from the electrons in a unit cell. Therefore, we consider reciprocal space which provides complete information on the orientation of the planes with respect to the axes as well as interplanar spacing. The diffraction condition in the reciprocal space is given as:

$$K \cdot \hat{G} = \frac{1}{2} G \quad (2.23)$$

Where, G is the vector in the reciprocal space, \hat{G} is the unit vector, and K is the radius of the sphere which intersects with the point in the reciprocal lattice for diffraction condition to be satisfied. This sphere is known as Ewald sphere. The diffraction equation (2.22) can be used under two different variant forms. First is the Angle Dispersive X-Ray Diffraction (ADXRD). Here, the wavelength (λ) is fixed using a monochromator, d is unknown and angle (θ) is

scanned. So, for a particular angle, as λ is known, d can be calculated. Second variant is the Energy Dispersive X-Ray Diffraction (EDXRD). Here, we have variable λ , d is unknown and angle (θ) is fixed. The structural characterization of the samples in this thesis has been carried out using the ADXRD mode.

High pressure x-ray diffraction:

Laboratory x-ray sources have two major limitations. Firstly, they have x-ray radiation dominated by the characteristics of the anode being used. Secondly, the flux is limited which further reduces when needed to focus on the small same size in DAC (in microns range). The synchrotron radiation source overcomes these limitations and provides additional advantages such as naturally collimated beam.

When the charged particles are relativistically accelerated in a radial direction (acceleration is perpendicular to velocity), the electromagnetic radiation emitted in the tangential direction is known as Synchrotron Radiation. The properties of synchrotron radiation which are useful in the high pressure experiments are as follows:

1. Broad spectrum – any wavelength can be used for the experiments by the user.
2. High flux – atoms with weak scattering such as organic materials can also be measured.
3. Highly collimated beam – it can be easily focused on the small sample size for example the sample chamber of DAC which is in microns range.

The high pressure x-ray diffraction measurements in this thesis were carried out at the Indus-2 Synchrotron radiation source at BL-11, ECXRD beamline, RRCAT, Indore, India.

2.4. Upgradation of infrared beamline

In addition to the research works, I was also involved in the development works related to the upgradation of the infrared beamline at the Indus-1 synchrotron radiation source in India. The infrared radiation from the synchrotron source can be used to carry out spectroscopic studies. The advantage of using synchrotron source over laboratory source is high brilliance and naturally collimated beam. The schematic of the IR Beamline, BL-06, at INDUS-1 is shown in Figure 2.12.

The infrared radiation is reflected to mirror M1 (Gold coated) after which the beam collimation is carried out in the vertical direction. After mirror M1, a pair of ZnSe windows are used to separate the storage ring UHV with the high vacuum in the beamline.

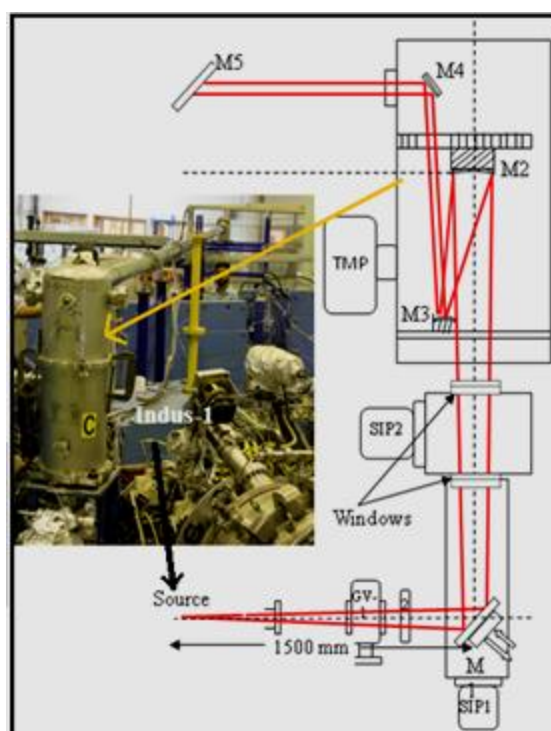


Figure 2.12: Schematic of IR Beamline, BL-06, at INDUS-1, RRCAT, India. [187]

In order to enhance the optical transmittance, laser grade ZnSe windows had been installed in the beamline. However, such windows are generally optimized for a single wavelength, which was 10 micron in the present case, and thus result in a drop in signal transmittance at some other wavelengths. I was involved in the installation of new broad band coated ZnSe windows, which provide more than 90% transmission in the complete mid-IR range, *i.e.*, 600-5000 cm^{-1} . The 100% transmission lines obtained from previous ZnSe windows has been shown in Figure 2.13 (red spectrum) which have good signal to noise ratio only in some intermediate regions. With the new windows, the signal to noise ratio shows an increase in the complete mid-IR region, as shown by the blue plot in Figure 2.13.

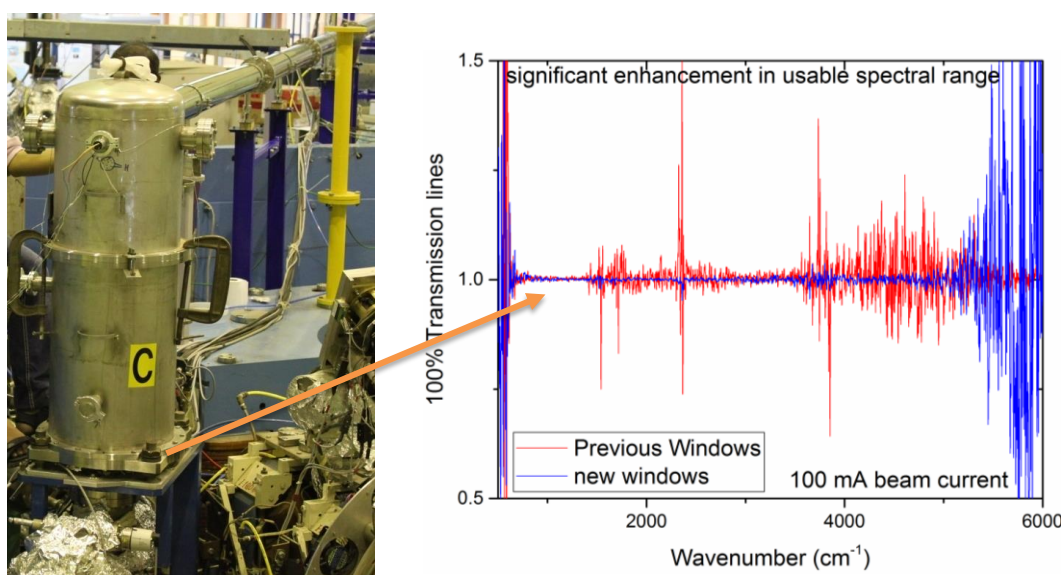


Figure 2.13: 100% transmission spectra of the previous ZnSe window (red) and new ZnSe window (blue).

Chapter 3: Low Temperature Isotopic Effect in α -glycine

3.1. Introduction

Glycine, the simplest and the only achiral amino acid, crystallizes in three polymorphic forms in the solid state [13, 107, 129]. With important applications in bio-materials and being the major constituent of macromolecular complexes, it can serve as an archetype system where weak interactions play a decisive role in structural stability. The substitution of deuterium for hydrogen has helped in improving the properties of glycine complexes in the applied fields of pyroelectric detectors [133-135], and drug metabolism in pharmacology [138, 139, 188, 189] and in basic understanding of molecular structure and vibrational frequencies [123, 124, 190-194]. However, considering the varied consequences of deuteration, comparative studies on isotopic effect under varying thermodynamic conditions require attention. An understanding of the molecular structure and structural response under such conditions would be helpful in predicting the physico-chemical behavior of such compounds for various applications, for example crystal engineering, lyophilisation or freeze drying of biological drugs, and pyroelectric/ non-linear properties.

At ambient conditions, the α -glycine zwitterions form head to tail linked double layers lying perpendicular to the b -axis with a weak N-H---O intra- double layer and very weak C-H---O inter- double layer hydrogen bonds with strong hydrogen bonded rings of glycine molecules in the ac -plane with monoclinic structure and $P2_1/n$ space group [107]. For external tuning of this network, high pressure provides an effective method for significant alterations of interatomic distances, whereas low temperature studies probe subtle details under homogeneous contraction (far less than the compression technique), by reducing thermal agitations, therefore providing valuable information on structural stability and the

possible reaction pathways. Though both techniques are expected to reduce the volume, the resulting molecular reorientations may sometimes lead to varying effects [43, 44].

3.2. Literature Survey

In the condensed phase, α -glycine exists in zwitterionic form ($\text{NH}_3^+\text{CH}_2\text{COO}^-$) in contrast to the neutral ($\text{NH}_2\text{CH}_2\text{COOH}$) gas form [195]. In 1980 and 2000, electron density studies were reported on α -glycine (zwitterionic) at 120 K [196] and at 23 K [197] respectively, which provided the N---O distances of hydrogen bonds. Subsequently, in 2003, low temperature single crystal x-ray diffraction studies of all the polymorphs ascertained the absence of polymorphic transformations and provided evidences of N---O distance shortening implying strengthening of N-H---O hydrogen bonds [70]. The values of H---O distances are however at variance in various papers at ambient conditions, which were also provided at 120 K by Legros et al. [196]. It is worth noting that, spectroscopy has emerged as a powerful tool to understand the protonic motions in organic molecular solids and can provide complimentary information to the structural studies at varying thermodynamic conditions [106, 198-201]. Several correlation plots between covalent bond stretching frequencies and the corresponding hydrogen bonded lengths deduced from several compounds for various kinds of hydrogen bonds have been provide in the literature [59-64].

The first systematic variable temperature Raman study of α -glycine in the temperature range 83 – 360 K were reported in 2005, which showed splitting of NH_3 torsional and CO_2 rocking modes [202]. The IR measurements in the range 600 – 7800 cm^{-1} were reported for all glycine polymorphs in the temperature range 93 – 433 K by Chernobai et al. in 2007 highlighting different polymorphic behavior [203]. Raman spectroscopy in the low frequency spectral range ($< 200 \text{ cm}^{-1}$) suggested that the changes in the vibrational modes of glycine polymorphs with the “dynamical transition” and conformational changes observed in

biomolecules around 200 – 250 K by monitoring the deviations in anharmonicity [204]. The dynamical transition phenomenon has also been explored by Bordallo et al. using inelastic neutron scattering in the temperature range 5 – 300 K focussing on the NH₃ reorientational transitions upon cooling [205]. These authors, in corroboration with NMR reports [127, 128], described the freezing of NH₃ reorientations below 150 K. Such changes may be reflected in NH₃ torsional vibrations, but the only systematic IR study (up to 93 K) carried out so far did not cover the corresponding spectral range [203], though prior works had noted the emergence of a shoulder mode upon cooling [206].

Interestingly, in contrast to the hydrogenated glycine (henceforth *gly-h*), the behavior of ND₃ reorientations in deuterated glycine (*gly-d*) was found to be different in deuteron magnetic resonance studies at low temperatures [207]. Unfortunately, low temperature studies are very limited for *gly-d*. The reports available in literature describe the low frequency vibrational mode assignments at 85 K for fully deuterated [208] and in the mid-IR regions at 18 K for N-deuterated compound [209]. The most recent works on glycine deal with the high pressure structural properties of *gly-d* [210], for which no systematic low temperature study could be found. Thus, to unambiguously establish the differences, if any, in the properties of glycine and its deuterated analogue, [106, 205, 211-214], detailed low temperature spectroscopic studies on *gly-h* and *gly-d* have been carried out in the widest temperature (4.2 – 300 K at close steps of ~10 K) and spectral range (140 – 4000 cm⁻¹) reported so far.

3.3. Experimental methods

Gly-h (with 99.5% purity) and deuterated α -glycine (*-d₅*, *i.e.*, all hydrogen atoms replaced with deuterium) of aldrich with 98 atom % D (D isotopic purity) were used for the low temperature IR and Raman studies. All the IR measurements were carried out in the

experimental station of the IR beamline installed at Indus-1 in India using continuous flow liquid Helium (LHe) cryostat, Oxford Optistat CF-V in the transmission mode from 300 K to 4.2 K. Temperature was controlled using PID controller and helium flow was controlled using a gas flow meter calibrated for helium gas. The cryostat was mounted in the sample compartment of Bruker Vertex 80V FTIR spectrometer. For the MIR-region (400– 4000 cm^{-1}), the spectra were recorded at a resolution of 2 cm^{-1} using LHe and the repeat measurements were carried out on freshly prepared pellets at 1 cm^{-1} spectral resolution using Globar source. For the FIR region (140 – 700 cm^{-1}) with Mercury (Hg) lamp as a source, spectra were recorded at 4 cm^{-1} resolution using LN_2 and the repeat measurements were carried out using LHe at 2 cm^{-1} resolution. A total of 100 scans were coadded in all the sample as well as background measurements. Low temperature Raman measurements were carried out using micro Raman spectrometer (Renishaw, UK, Model Invia). The spectra were recorded using 514 nm laser excitation. Temperature dependent measurements from 300 K to 80 K were carried out using a heating and cooling microscope stage (Linkam THMS 600).

3.4. Results and discussion

3.4.1. Low temperature behavior of *gly-h*

As α -glycine is an extensively studied compound, its vibrational modes as well as ambient structural parameters are well known, as reported by many techniques such as IR/ Raman spectroscopy [64, 115, 121-126, 206, 209, 215] and x-ray/ neutron diffraction [107, 111, 129, 130, 216-218] studies respectively. In the present study, we have taken the mode assignments and hydrogen bond parameters [196] from the published reports, which have also been verified by the examination of high pressure [15, 21, 68] as well as low temperature [21, 202, 206, 209] [and present work] behaviors of vibrational modes of glycine and its deuterated analogue in the Raman and infrared spectra.

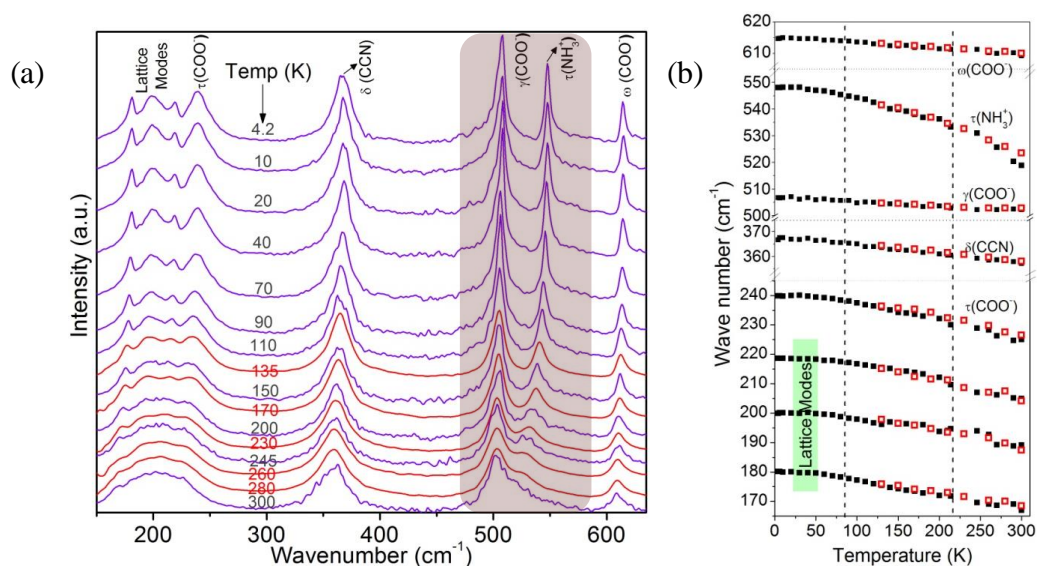


Figure 3.1: (a) Low temperature spectra of α -glycine in the spectral range 150 – 650 cm^{-1} . Red color plots are at 4 cm^{-1} resolution using Liquid nitrogen (LN_2) and violet color plots are from the repeat measurements at 2 cm^{-1} resolution using Liquid Helium (LHe). (b) Frequency versus temperature plot in 150 – 650 cm^{-1} spectral range. Red squares represent data at 4 cm^{-1} resolution and black squares represent repeat measurement data points at 2 cm^{-1} resolution. Symbols: τ -torsional, δ -bending, γ -rocking, ω -wagging.

Figure 3.1(a) shows the far infrared spectra of α -glycine at various temperatures from room temperature to 4.2 K. Figure 3.1(b) and Table 3.1 describe the low temperature behavior of the corresponding modes. All the modes show a reduction in peak width and stiffening upon lowering the temperature due to thermal contraction. The distinctly visible feature in this frequency range is the marked evolution of τ - NH_3 (torsional) mode ($\sim 523 \text{ cm}^{-1}$) upon cooling, which is buried inside the broad and stronger γ - CO_2 (rocking) mode (502 cm^{-1}) at room temperatures, with a consistent rise in relative intensity up to the lowest temperature measured. The emergence of τ - NH_3 mode on cooling accompanied with a remarkably large rate of stiffening ($\sim 30 \text{ cm}^{-1}$ shift up to 4.2 K) is a definitive signature of reorientation of glycine NH_3 groups leading to stronger N-H...O hydrogen bonds [70]. A reasonably large rate of stiffening has also been observed for τ - CO_2 (224 cm^{-1}) mode as compared to the other

Table 3.1: Slope ($-\frac{d\tilde{\nu}}{dT}$) of frequency versus temperature plots of IR modes of gly-*h*. The modes with maximum or negative values have been highlighted.

Modes	Assignment(cm^{-1})	$(-\frac{d\tilde{\nu}}{dT})$ (cm^{-1}/K) of IR modes		
	Infrared	300 – 210 K	210 – 80 K	80 – 4.2 K
Lattice Mode	167	0.043	0.047	0.024
Lattice mode	189	0.042	0.035	0.017
Lattice Mode	204	0.054	0.061	0.011
$\tau(\text{COO}^-)$	224	0.083	0.063	0.021
$\delta(\text{CCN})$	359	0.046	0.030	0.015
$\gamma(\text{COO}^-)$	502	0.010	0.024	0.036
$\tau(\text{NH}_3^+)$	523	0.169	0.065	0.047
$\omega(\text{COO}^-)$	609	0.022	0.023	0
$\delta(\text{COO}^-)$	697	0.025	0.017	0.008
$\nu(\text{CC})$	893	0.021	0.015	0.005
$\gamma(\text{CH}_2)$	912	0.034	0.032	0.017
$\nu_{\text{as}}(\text{CN})$	1032	0.007	0.016	0.010
$\gamma(\text{NH}_3^+)$	1111	0.033	0.023	0.061
$\gamma(\text{NH}_3^+)$	1129	0.034	0.031	0.010
$\tau(\text{CH}_2)$	1310	0.026	0.003	0.008
$\omega(\text{CH}_2)$	1333	0.011	0.004	0.010
$\nu_{\text{s}}(\text{COO}^-)$	1411	0.019	0.017	0.007
$\delta(\text{CH}_2)$	1444	0.013	0.008	0.004
$d_{\text{s}}(\text{NH}_3^+)$	1504	0.026	0.008	0
$d_{\text{s}}(\text{NH}_3^+)$	1523	0.013	0.019	0
$\nu_{\text{as}}(\text{COO}^-)$	1592	0	0	0
$d_{\text{as}}(\text{NH}_3^+)$	1610	0.031	0.018	0.005
$\nu(\text{NH})$	2618	-0.025	-0.036	0.004
$\nu(\text{NH})$	2904	-0.021	-0.028	-0.030
$\nu_{\text{s}}(\text{CH})$	2978	0.002	0	0
$\nu_{\text{as}}(\text{CH})$	3007	0	0	0
$\nu(\text{NH})$	3168	-0.050	-0.080	-0.022

modes, *viz.*, δCCN (bending, 359 cm^{-1}), γCO_2 and ωCO_2 (wagging, 609 cm^{-1}). It is noteworthy that the signatures of dynamical transition, a phenomenon related to sudden increase in mean square displacement in proteins and amino acids, have been observed at $\sim 200 - 250 \text{ K}$ in glycine using inelastic neutron scattering, which could not be observed using IR spectroscopy [205]. A finer inspection using the present infrared data obtained at close temperature steps and broad spectral range is suggestive of a change in the slopes of

frequency versus temperature plots across 210 K (Table 3.1). A sudden enhancement in the relative intensity of τ -NH₃ and ν NH modes is also found below 210 K. At further lower temperatures, another change in the slopes of frequency versus temperature plots has been observed across 80 K. In the mid-infrared region, we observe systematic evolution of a weak shoulder in the γ NH₃ (rocking) mode at ~ 1130 cm⁻¹, as shown in Figure 3.2(inset). A very weak shoulder has also been observed to develop on the high frequency side of the weak t-CH₂ (twist) mode (~ 1313 cm⁻¹) which may be due to inter-molecular couplings resulting in slight modifications of the weakest C-H---O linkages between glycine bilayers (explained later). It is to be noted that, we could monitor these fine changes only on increasing the spectral resolution in order to account for the expected sharpening of the peaks at low temperatures.

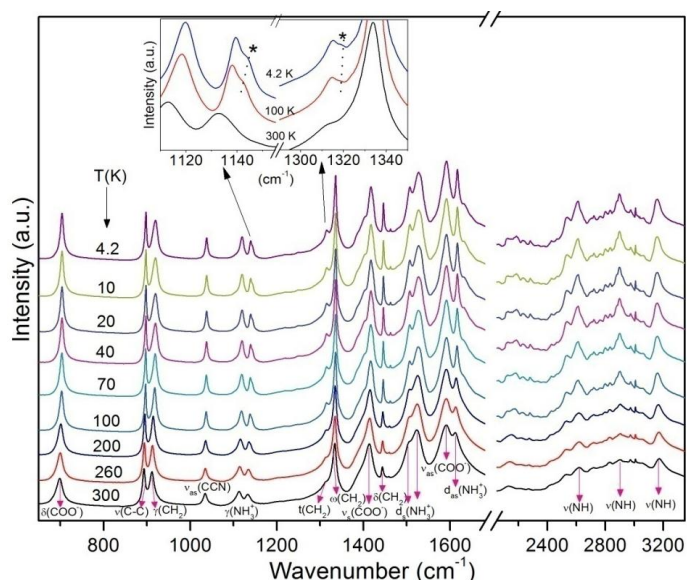


Figure 3.2: Low temperature IR spectra of α -glycine from 700 – 3250 cm⁻¹ spectral range at 1 cm⁻¹ resolution using LHe cryostat. Inset shows splitting of γ NH₃ and t-CH₂ modes marked with asterisk (*).

Symbols: δ - bending, ν - stretching, t- twist, ω - wagging, d_s - symmetric deformation, d_{as} - asymmetric deformation, γ -rocking.

3.4.2. Hydrogen bonding network of *gly-h*

The modifications in NH_3 reorientations leading to change in hydrogen bonding interactions at low temperatures are further confirmed from the behavior of N-H stretching vibrational modes lying in the region $2600 - 3200 \text{ cm}^{-1}$ (Figure 3.2). This region contains the stretching modes due to NH and CH stretching vibrations, however, the complexity enhances due to the presence of combination/ overtone modes and the self-trapped solitonic modes [219] which get stronger at lower temperatures. The three N-H stretching modes at $\sim 2618, 2904$ and 3168 cm^{-1} correspond to the three N-H---O hydrogen bonds [59]. The strongest of these hydrogen bonds (N1-H3---O2 with N---O = 2.770 \AA , H---O = 1.788 \AA and angle N-H---O = 167.2°) lies along the *c*-axis. The second most strongest hydrogen bond (N1-H4---O1 with N---O = 2.850 \AA , H---O = 1.899 \AA and angle N-H---O = 170°) lies in the *ac*-plane [69]. Together, these two hydrogen bonds bind glycine molecules in a two dimensional layered structure in the *ac*-plane. Two adjacent layers are connected by the third hydrogen bond (N1-H5---O1 \sim along *b*-axis with N---O = 3.074 \AA , H---O = 2.183 \AA and angle N-H---O = 156.4°) to form bilayers stacked normal to the *b*-axis. The bilayers are further held together by the weakest C-H---O hydrogen bonds [69]. Figure 3.3 shows the variation of N-H and C-H stretching vibrational modes as a function of temperature. Interestingly, all the three N-H stretching modes show softening upon cooling, which is an unusual observation during contraction/ compression, whereas the C-H stretching modes show a small and monotonous stiffening. This clearly implies the strengthening of all the N-H---O hydrogen bonds at low temperatures, which is consistent with the previous studies on α - glycine carried out at a few temperatures [203]. The present data also shows that subtle structural reorientations take place across 210 K and 80 K, which result in a stronger hydrogen bonded low temperature structure, as indicated from the change in the rate of variation of vibrational modes across these temperatures (Table 3.1). Such a red shift in stretching frequencies due to the formation or strengthening of

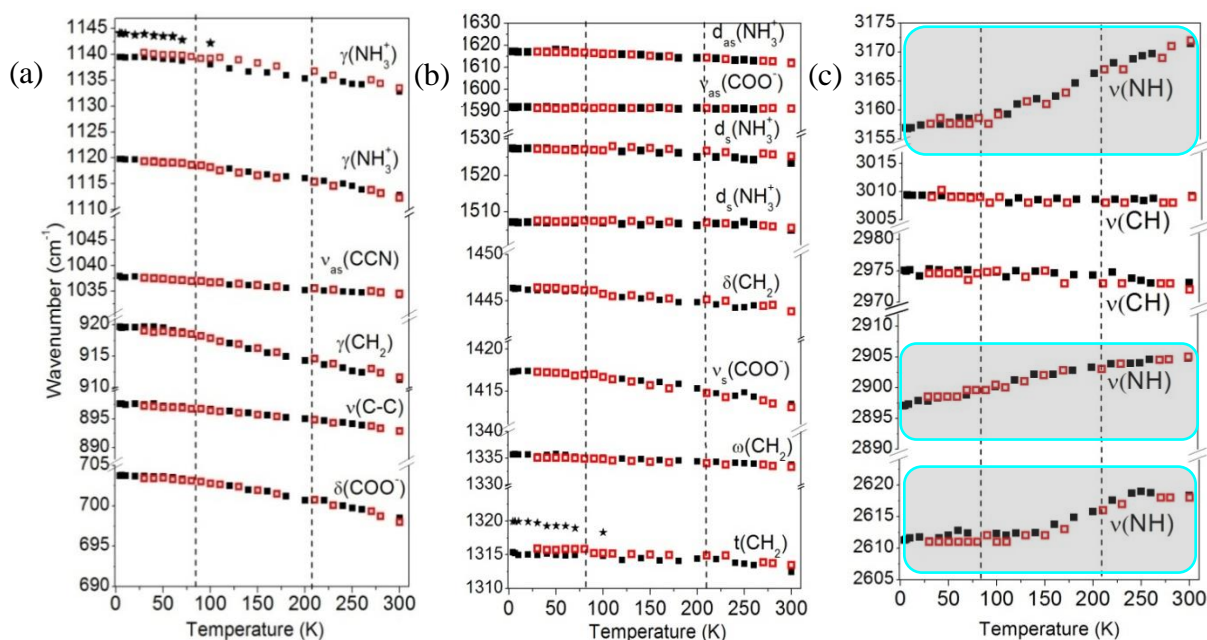


Figure 3.3: Frequency versus temperature plots in (a) 690 – 1145 cm^{-1} (b) 1310 – 1630 cm^{-1} (c) 2600 – 3175 cm^{-1} spectral range for α -glycine, obtained from two different experiments at 1 cm^{-1} (black filled squares) and 2 cm^{-1} (red open squares) resolutions respectively. * denotes the appearance of new modes. Symbols: δ - bending, ν - stretching, t - twist, ω - wagging, d_s - symmetric deformation, d_{as} - asymmetric deformation.

hydrogen bonds is an established fact [106, 199]. Change in H---O bond distance can also be estimated from the measured covalent bond stretching frequency using the well documented correlation plots and empirical relations, for a range of compounds as well as hydrogen bonds [59, 61, 63, 64, 220-224]. Though various correlation curves have been reported in the last 80 years, for different donor/ acceptor systems or ionic states, all of them show a similar qualitative trend upon the change in bond distance. A recently reported empirical relationship for various molecular systems including glycine by Rozenberg et al. [60, 225, 226], has also been used here in an attempt to estimate the change in hydrogen bond strength in gly-*h*:

$$\log(\Delta\tilde{\nu}) = - 1.97 - 6.1 \log(r) \quad (3.1)$$

where, $\Delta\tilde{\nu}$ is the change in stretching frequency relative to the free molecule (in cm^{-1}) and r is the H---O distance measured in nm . Figure 3.4(right) shows the estimated H---O bond distances the three N-H---O hydrogen bonds in glycine. While the absolute values can only be confirmed using structural techniques, the trend of their variation from room temperature to 4.2 K reveals that the two strong hydrogen bonds depict small (N1-H3---O2) and almost negligible (N1-H4---O1) reduction in H---O distances at low temperatures. In comparison, the moderately strong N1-H5---O1 hydrogen bond shows a drastic reduction in H---O distance, at a remarkable rate of decrease from ambient to ~ 80 K (0.02×10^{-3} nm/K) followed by a slightly lesser rate up to 4.2 K and therefore significant strengthening. This also corroborates with the structural report at room temperature and 23 K (see Figure 3.4right), predicting a larger reduction of this bridging distance (N1-H5---O1 nearly along the b -axis) in the weakest of the three N-H---O hydrogen bonds than the strong ones which form closed rings in the ac -plane [70, 197]. Such a strengthening of the hydrogen bond which acts as a bridge to form the bilayers, shows a similar qualitative behavior as often observed for hydrogen bonds (*e.g.*, in ice) under compression. Recently, it has been shown that the hidden force responsible for the hydrogen bond dynamics under such extreme conditions is the electrostatic interaction between the lone pair of acceptor atom and the covalently bonded electronic cloud [109, 110, 227-229].

While the strengthening of hydrogen bond, in general, upon cooling can also be explained using this model, the isotopic effect (*i.e.*, replacing H by D) may also alter the dynamics, which has been discussed in the next section. These observations indicate that the difference between the hydrogen bond strengths, *i.e.*, within the layers in the ac -plane and those connecting the layers along the b -axis, reduces on cooling. This implies that the bilayers are more compact/ strongly bound and isolated from one another at low temperatures. The variation of C-H stretching frequency also indicates that the weak inter-bilayer C-H---O

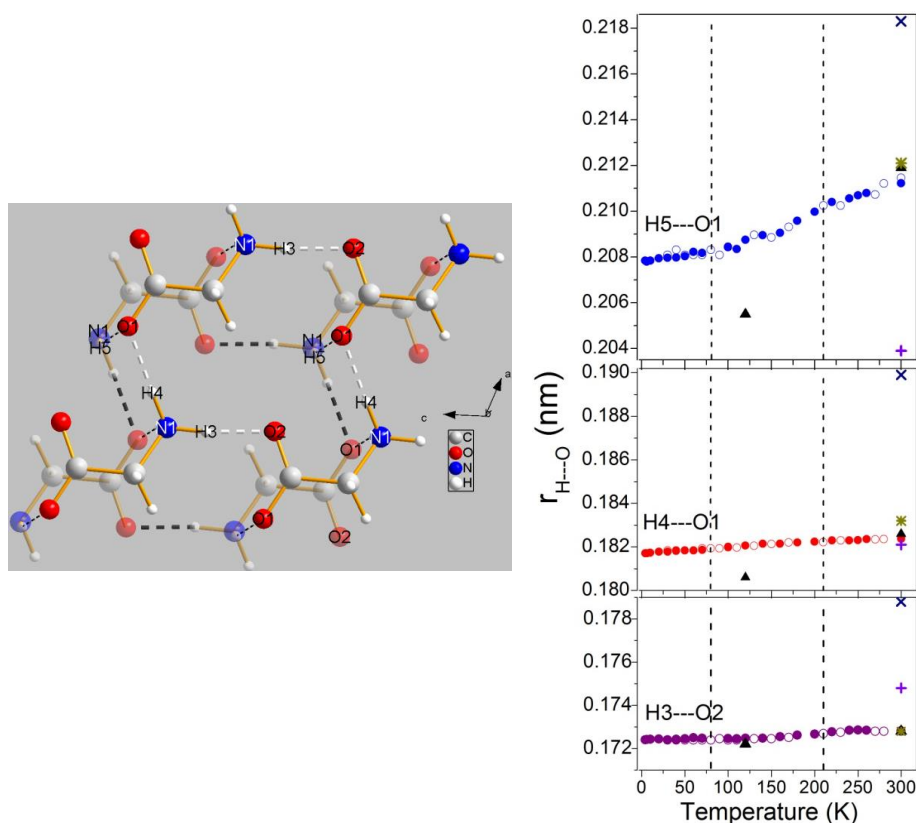


Figure 3.4: (Left) gly-*h* molecules in *ac*-planes, showing H3---O2, H4---O1 and H5---O1 bonds approximately along *c*-, *a*- and *b*- axes respectively. The network along *b*- axes has been elaborately presented in Figure 5. (Right) Variation of these hydrogen bond distances with temperature. Open and filled circles represent data estimated from two independent measurements. Also shown are the reported H---O distances in literature, with symbols: Black filled triangle – ref. [196], indigo cross mark – ref. [69], violet plus mark – ref. [197], olive star – ref. [129].

hydrogen bonds may not get much strengthened, even at low temperatures. These changes depict this compound as a supramolecular assembly of head to tail linked glycine molecules (through N1-H5---O1 nearly along the *b*-axis), which are connected to other adjacent molecules in the *ac*-plane through N1-H4---O1 and N1-H3---O2 as shown in Figure 3.4(left) and Figure 3.5. Such an assembly of glycine molecules with infinite spread in the *ac*-plane and a finite depth of two molecules are stacked along the *b*-axis.

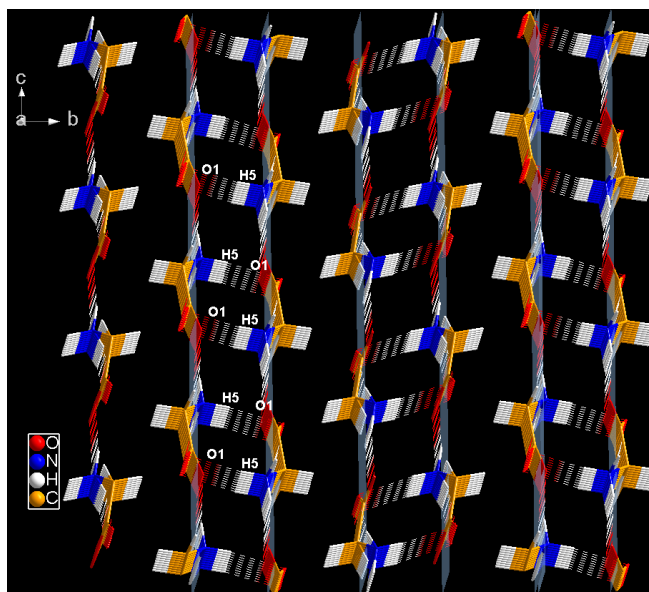


Figure 3.5: A wire-frame representation of the hydrogen bonded structure of α -glycine. The stronger hydrogen bonds lie in the ac -plane forming layers. These layers are connected through a weaker N1-H5---O1 hydrogen bond (dotted lines marked with H5---O1) along the b -axis, in a head to tail configuration forming bilayers. The adjacent bilayers are held together by the weakest C-H---O hydrogen bonds. At low temperatures, N1-H5---O1 hydrogen bonds depict the maximum strengthening. Refer Figure 4(left) for description of hydrogen bonds in the ac -plane (shaded sheets) which is normal to the N1-H5---O1 hydrogen bonds.

3.4.3. Low temperature behavior of $gly-d$

Figure 3.6(a) and (b) show the far infrared spectra ($150 - 675 \text{ cm}^{-1}$) and the temperature dependence of IR active modes for deuterated α -glycine ($gly-d$), which clearly demonstrate a distinct isotopic behavior for this simplest amino acid. Unlike in $gly-h$ where $\tau\text{-NH}_3$ mode depicts the maximum shift in frequency as well as increase in intensity, the weak $\tau\text{-ND}_3$ mode (expected near 348 cm^{-1}) [217], merged with δCCN mode (331 cm^{-1}) at ambient conditions, does not show any signs of strengthening at low temperatures. Infact, $\tau\text{-ND}_3$ is among the least affected modes and even at 4.2 K, the two peaks are not well resolved making it difficult to distinguish between them. These two peaks were analysed using Gaussian as well as Gaussian plus Lorentzian fits. While all the modes, including the lattice modes, show a small,

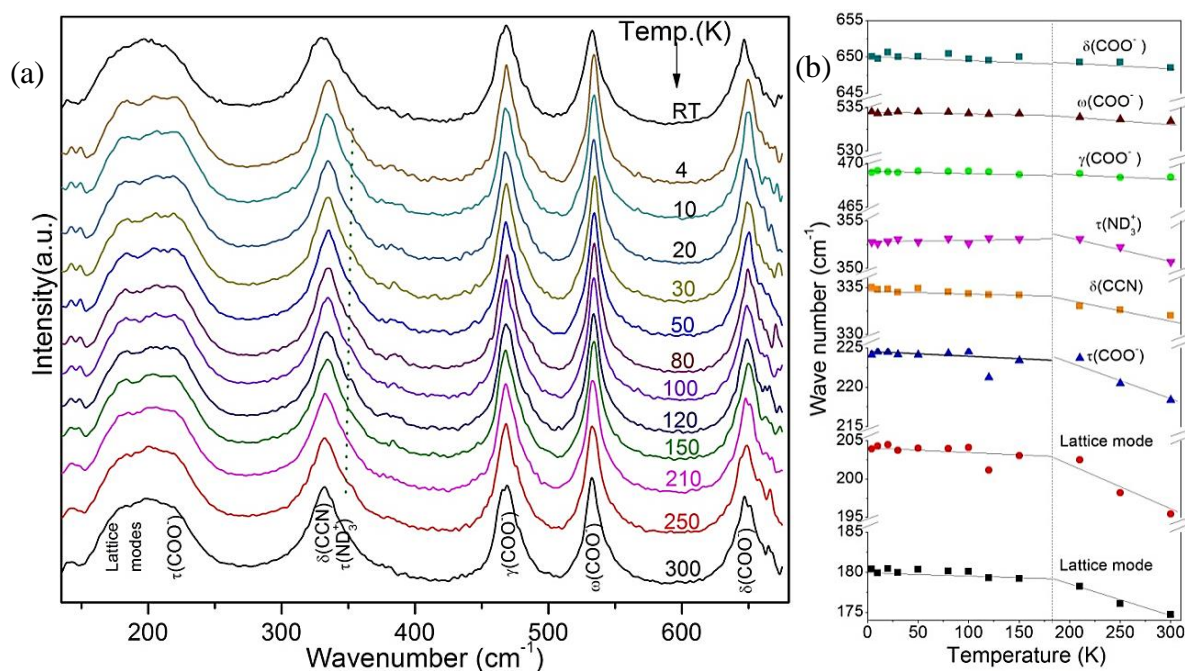


Figure 3.6:(a) Low temperature IR spectra of deuterated α -glycine (gly-*d*) in the spectral range 140 – 675 cm^{-1} . (b) Frequency versus temperature plots for the corresponding modes. Symbols: τ -torsional, δ -bending, γ -rocking, ω -wagging.

general stiffening and peak sharpening at low temperatures, a closer inspection reveals slope change in the frequency versus temperature plots across 180 K, which have been presented in Table 3.2. The modes observed in the mid infrared spectra show similar changes (Figure 3.7a). We also observe the emergence of a weak shoulder on the higher frequency side of t- CD_2 mode (1015 cm^{-1}) upon cooling (Figure 3.7a), as in gly-*h*.

In order to verify these observations on τ - ND_3 and other modes, we carried out the complementary Raman spectroscopic studies, which showed similar changes for the Raman active modes at low temperatures, (as shown in Figure 3.7(b) and Figure 3.7(c)). The broadening observed in the t- CD_2 Raman mode ($\sim 1020 \text{ cm}^{-1}$) at lower temperatures may be due to a new mode emerging at this frequency, as also in the IR spectra and in gly-*h*, consistent with some inter-molecular couplings due to slight modifications in the C-D---O

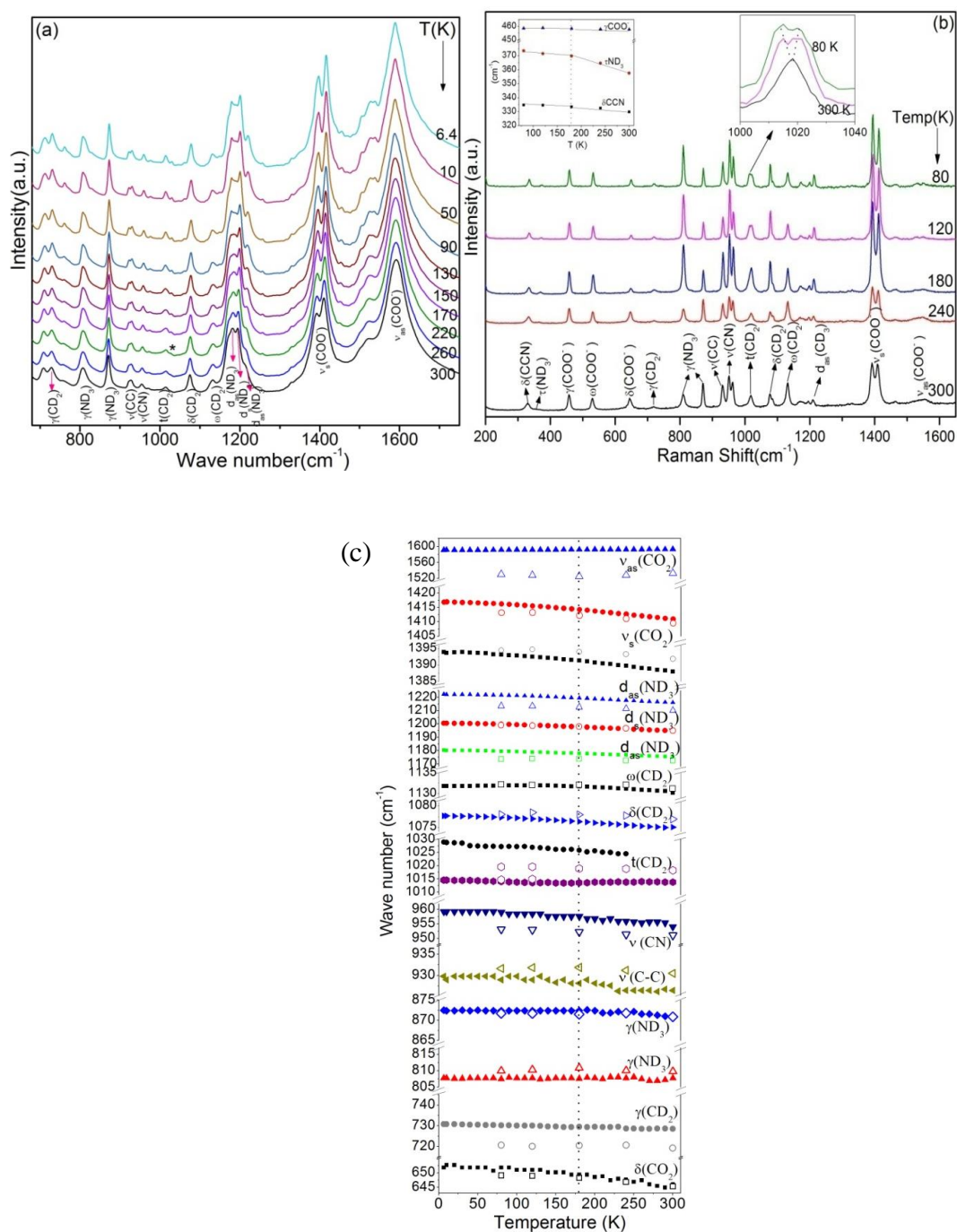


Figure 3.7: (a) Low temperature IR spectra of gly-*d* in the 700 – 1750 cm⁻¹ range at 1 cm⁻¹ resolution. * denotes splitting in t-CD₂ mode. (b) Low temperature Raman spectra of gly-*d* in 200 – 1650 cm⁻¹ spectral range. Inset (left): variation of low frequency Raman modes (δCCN , τND_3 , γCOO^-) with temperature, and (right): splitting of t(CD₂) below 180 K. (c) Variation of the IR and Raman peak positions of gly-*d* in the region 700 – 1600 cm⁻¹ with temperature.

linkages. Further, the two γ -ND₃ Raman modes near 800 – 900 cm⁻¹ depict an intensity reversal upon cooling. No other unusual low temperature behavior was observed.

Table 3.2: Observed IR and Raman modes of gly-*d* alongwith the rate of variation of IR modes as a function of temperature.

Modes	Assignment		(-(d $\bar{\nu}$ /dT)) (cm ⁻¹ /K) of IR modes	
	Infrared	Raman	300 – 180 K	180 – 4.2 K
Lattice mode	174		0.034	0.001
Lattice Mode	195		0.053	0.007
τ (COO ⁻)	218		0.034	0.004
δ (CCN)	330	330	0.022	0.005
τ (ND ₃)	350	353	0.015	0
γ (COO ⁻)	468	455	0.001	0
ω (COO ⁻)	533	528	0.006	0
δ (COO ⁻)	648	643	0.034	0.022
γ (CD ₂)	728	722	0.008	0.005
γ (ND ₃)	806	807	0.010	0.001
γ (ND ₃)	871	867	0.010	0
ν (CC)	926	928	0.020	0.005
ν (CN)	953	951	0.029	0.011
t (CD ₂)	1013	1019	-0.002	0.004
δ (CD ₂)	1075	1080	0.011	0.008
ω (CD ₂)	1130	1128	0.014	-0.001
d_{as} (ND ₃)	1175	1178	0.017	0.017
d_s (ND ₃)	1194	1199	0.036	0.014
d_{as} (ND ₃)	1216	1207	0.030	0.014
ν_s (COO ⁻)	1388	1389	0.023	0.014
ν_s (COO ⁻)	1411	1407	0.026	-0.002
ν_{as} (COO ⁻)	1592	1553	0.022	0.004
ν (ND)	2061	2058	-0.100	-0.002
ν (CD)	2182	2182	0.001	0
ν (ND)	2229	2228	-0.052	-0.005
ν (CD)	2264	2264	0.009	0
ν (ND)	2352	2333	0.001	-0.032

3.4.4. Isotopic effect on the Hydrogen bonding network

The above observations indicate that the hydrogen bonds in gly-*d* may depict a different effect of cooling than that shown by gly-*h*. Thus, to understand the nature of hydrogen bonds, we studied the N-D stretching modes and used them to estimate the change

in the strengths of hydrogen bonds at low temperatures. Interestingly, in *gly-d*, the stretching mode corresponding to the strongest N1-D3---O2 hydrogen bond (along *c*-axis) shows a significant softening on cooling up to 180 K, whereas the stretching mode corresponding to the second strongest N1-D4---O1 hydrogen bond (in the *ac*-plane) depicts a discontinuous shift to lower frequency across 180 K in addition to small softening (Figure 3.8(c)). Both these modes show relatively negligible reduction at further lower temperatures. In complete contrast, the N-D stretching mode at 2352 cm⁻¹ corresponding to the N1-D5---O1 hydrogen bond along the *b*-axis, shows nearly no change up to 180 K, followed by softening upon further lowering the temperature.

It is known that the substitution of hydrogen (H) by deuterium (D) depicts a noticeable change along the longest hydrogen bond in α -glycine (approximately along *b*-axis) [69, 210] and the prominent N-D---O hydrogen bond distances have been shown as D3---O2 ~ 1.740 Å, D4---O1 ~ 1.821 Å and D5---O1 ~ 2.131 Å [210] at 0.2 GPa. The temperature induced variation in these D---O distances as obtained from the empirical correlation given by equation (3.1) have been plotted in Figure 3.9.

Figure 3.9 shows that the distance D5---O1 remains nearly constant (in fact a slight increase is noticed on close inspection) on lowering the temperature up to 180 K, implying weakening (or no prominent change) of the hydrogen bond which binds the bilayers, below which it starts strengthening. Such a difference in *gly-d* than that observed in *gly-h* may be due to the difference in energies of the two hydrogen bonds, *viz.*, the increase of barrier height and potential well separations upon deuteration due to increased reduced mass [230]. This may be the reason that the two isotopes initially depict different behavior upon cooling. However as the temperature is lowered down to 180 K, the D5---O1 hydrogen bond starts strengthening and follows a similar trend, which can be explained using the electrostatic

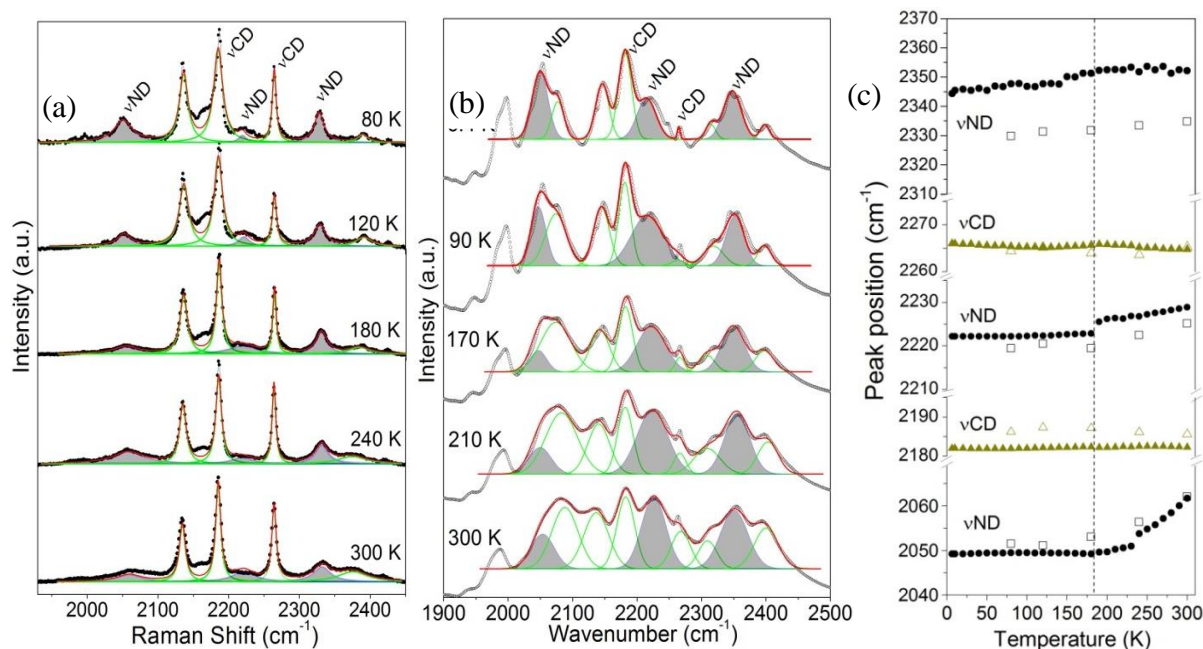


Figure 3.8: (a) Raman and (b) IR spectra of gly-*d* in the ND and CD stretching regions at a few representative temperatures. In addition to the stretching modes, combination, overtone and self trapped modes may be expected in this region. Grey highlighted peaks represent ND stretching modes. (c) Frequency versus temperature plots of ND and CD stretching modes, symbols: filled – IR and open – Raman modes.

model, as discussed earlier [109, 110, 227-229]. On the other hand, the stronger hydrogen bonds forming the layers in the *ac*-plane are strengthened on cooling down to 180 K, below which the structure is almost stable. Further, the discontinuous shift in D4---O1 and a noticeable change in the slope of D3---O2 suggest molecular reorientations within the layers leading to different temperature effects below 180 K. These observations imply that the temperature induced variations in gly-*d* are opposite to those in gly-*h* on cooling from room temperature to 180 K. Below 180 K, both the isotopes show similar behavioral change at lower temperatures. Hence, in the case of gly-*d*, the low temperature structure can be described as denser infinite layers in the *ac*-plane stacked along the *b*-axis, *i.e.*, a relatively simple layered structure as shown in Figure 3.10.

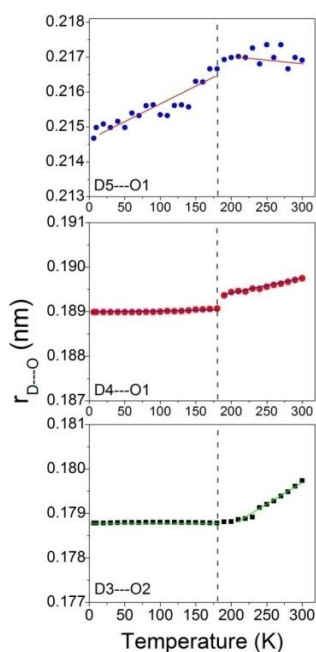


Figure 3.9: Variation of D3---O2, D4---O1 and D5---O1 bond distances with temperature in gly-*d*.

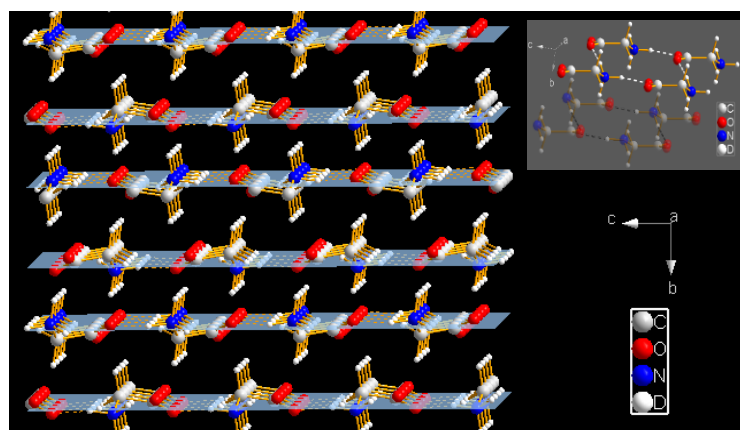


Figure 3.10: Structure of gly-*d* in *bc*-plane [210, 216]. Highlighted sheets are drawn to show the *ac*-planes. Upon lowering the temperature, the two strong N-H---O hydrogen bonds which form a closed ring (inset) of four molecules in the *ac*-plane get further stronger to form more compact and tightly held layers.

3.5. Orientational changes in N(H/D)₃ torsional modes:

A possible explanation of this varying structural behavior in the two isotopes at low temperatures can be drawn from the corroboration of these results with the nuclear magnetic resonance studies. The hydrogen bonding network in gly-*h* is governed by the motion of the

amino group of the molecules, in particular the rotation of the NH_3 entity with respect to the skeletal chain. EPR experiments have confirmed that the NH_3 group freely rotates at room temperature and all the three protonic positions are equivalent [231-234]. The corresponding torsional vibrational mode shows extremely weak IR activity. However, at low temperatures the protons are somewhat locked at their positions and merely rotate about their average positions [205, 231]. Thus, NH_3 group vibrates only moderately about the C-N axis at low temperatures. The systematic restriction of the free rotation of NH_3 group would result in the strengthening of hydrogen bonds, which is consistent with our observations on the stretching modes as well as a clear and pronounced evolution of the torsional mode as the temperature is lowered. This also highlights the importance of the intra-bilayer N1-H5---O1 hydrogen bonds in stabilizing the structural framework at varying thermodynamic conditions. However, unlike in *gly-h*, the N1-D5---O1 hydrogen bonds are not strengthened in *gly-d* upon cooling down to 180 K. This is again consistent with the fact from deuteron NMR that, although the protonic motion would also be slowed down in *gly-d*, they may not get locked upon cooling [235]. Infact, even at room temperature, the rate of reorientation of ND_3 group (in *gly-d*) is different from the NH_3 group (in *gly-h*) [113, 207, 235]. The earlier neutron scattering (NS) studies on *gly-h* have indicated that NH_3 torsional potential is anharmonic [217, 218]. Subsequently in 2008, Bordallo et al. reported an increase in the harmonic character below 150 K using inelastic NS studies [205]. These results remained the only information on the anharmonicity of the torsional vibrations, as the signature of the torsional mode is very weak in IR and Raman spectra at ambient conditions [205]. As the effects of change in anharmonicity may also be reflected in the peak widths of the vibrational modes, we have shown here a comparison of vibrational peaks lying in the region of the torsional mode in Figure 3.11 and Table 3.3.

The FWHM of τNH_3 mode decreases very rapidly upon cooling upto 150 K, below which the

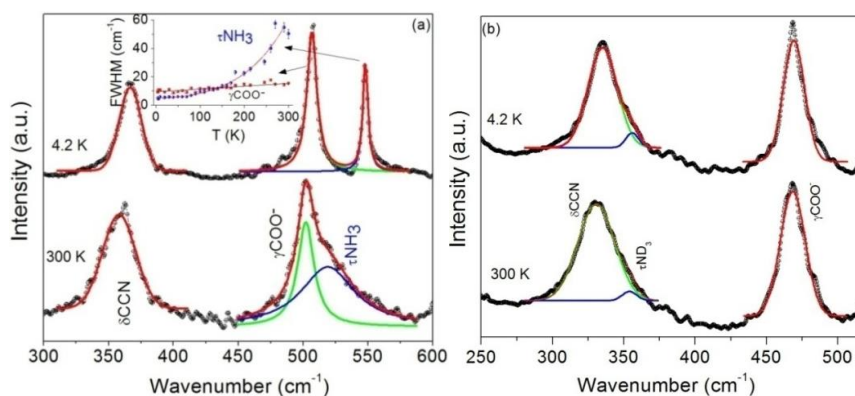


Figure 3.11: Comparison of NH_3/ND_3 torsional mode in the IR spectra of (a) *gly-h* and (b) *gly-d* at 300 K and 4.2 K.

rate of decrease reduces. The FWHM could be fitted using a combination of exponential and linear functions, which indicates a change in anharmonicity accompanied with subtle reorientational changes [236-238]. Thus, the changes observed in *gly-h*, like freezing of protonic position and distinct change in anharmonicity could not be inferred in the case of *gly-d*. The other vibrations lying in this region, *viz.*, δCCN and γCO_2 showed nearly the same behavioral changes for *gly-h* and *gly-d*. It has also been reported that the greater anharmonicity in glycine (*gly-h*) at room temperature as compared to other compounds like alanine is due to unequal strengths of the three hydrogen bonds [239]. The reduction in the difference of hydrogen bond strengths at low temperatures is therefore consistent with an increase in the harmonic character.

Table 3.3: FWHM (in cm^{-1}) of various modes in *gly-h* and *gly-d* at 300 K and at 4.2 K.

Modes	FWHM (cm^{-1}) - <i>gly-h</i>		FWHM (cm^{-1}) - <i>gly-d</i>	
	300 K	4.2 K	300 K	4.2 K
δCCN	25.67	17.12	25.95	20.61
$\tau \text{NH}_3/\text{ND}_3$	50.22	4.87	12.31	10.70
γCOO^-	15.35	9.36	17.63	15.14

Lastly, it is worth presenting the low temperature behavior of a characteristic band of medium intensity around 2100 cm^{-1} , found in amino acids, which was earlier assigned as NH stretching vibration by Koegel et al. [240] and later a bending vibration by Leifer et al. [241]. However, since 1964, when Krishnan et al. noted that this is a combination of NH_3 deformation and NH_3 torsional modes and is present only in the zwitterionic forms, it has been used as an "indicator band" for the identification of the zwitterionic form [125]. This band, *i.e.*, the $\delta\text{NH}_3 + \tau\text{NH}_3$ combination band has been observed at 2130 cm^{-1} in the spectrum of *gly-h* (Figure 3.2) and the corresponding band in *gly-d* is observed at 1522 cm^{-1} (Figure 3.7(a)). The temperature variation of these bands has been shown in Figure 3.12. While in *gly-h* this band shows a stiffening of nearly 60 cm^{-1} up to 4.2 K, in *gly-d* a relatively smaller shift of $\sim 20\text{ cm}^{-1}$ has been observed.

Thus, we observe that the amino group vibrational modes associated with hydrogen bonding, *viz.*, stretching, torsional and combinations show a lower shift in *gly-d* as compared to that in *gly-h* upon cooling. However, upon compression, the high pressure Raman spectra, reported for these isotopes under quasi- as well as non-hydrostatic conditions up to 23 GPa and 20 GPa for *gly-h* [68] and *gly-d* [242] respectively, have shown a general stiffening of the torsional modes and nearly similar shifts in the stretching modes. While subtle structural rearrangements have been reported at $\sim 3\text{ GPa}$, no structural phase transition was observed [68, 242]. The high pressure single crystal x-ray diffraction studies on *gly-h* up to 6.2 GPa have shown the least compressibility along the *c*-axis, whereas *b*-axis showed the maximum compressibility [69]. For *gly-d*, x-ray diffraction studies have been reported upto $\sim 8.7\text{ GPa}$ and no phase transition was observed in this case too [210]. Noticeably, at high pressures, the strongest hydrogen bond ($\text{H3/D3} \cdots \text{O2}$) weakens in both *gly-h* and *gly-d* (deduced from $\text{O} \cdots \text{H/D}$ distances) [69, 210]. The weakest of the three, *i.e.*, $\text{N1-H5/D5} \cdots \text{O1}$ approximately along the *b*-axis, remains almost unaffected in *gly-h*, whereas it strengthens in *gly-d* [69, 210] upon

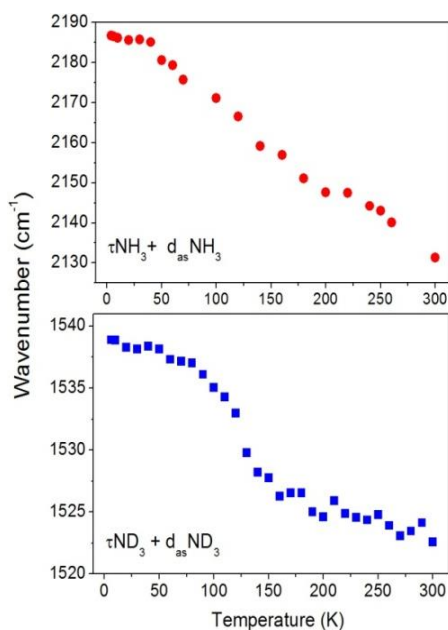


Figure 3.12: Temperature variation of the "indicator" band in gly-*h* (top) and gly-*d* (bottom).

compression. The most prominent effect was however shown by the intermediate H4/D4---O1 hydrogen bond which strengthens in both the isotopes under pressure [69, 210]. Thus, it is clear that the high pressure and low temperature behavior of the three dimensional hydrogen bonded framework is not identical for both gly-*h* and gly-*d*. Thus, it would be interesting to explore the phase diagram of this simplest, hydrogen bond stabilized, amino acid system, in lines similar to the simplest hydrogen bonded system, ice [228].

Among the simple amino acids, the low temperature studies on L-alanine, the smallest chiral amino acid shows lattice instability at 220 K due to a strong dynamic Jahn-Teller effect, whereas its deuterated analogue depicts a structural transition at 170 K due to geometrical changes, presumably because of the Ubbelohde effect [211]. In general, it is presumed that deuteration leads to profound effects primarily on vibrational frequencies (due to mass effect) and some scaling in hydrogen bonding interactions (*e.g.* due to Ubbelohde effect) [243], whereas the crystal structure and the relative strengths within the three

dimensional network of hydrogen bonds can be affected and the isotopes are believed to follow similar [244] or different [44, 192] behavior under varying conditions depending on the local environment. It is also known that deuteration may result in increase in transition temperature in the case of a temperature induced phase transition [192, 245].

The present results point out the varying behavior of *gly-h* and *gly-d* at low temperatures. The hydrogen bond lengths in *gly-h* show nearly monotonous changes upon cooling as compared to *gly-d* where the changes are relatively discontinuous at 180 K. These changes in the hydrogen bonding network of *gly-d* may also lead to some structural changes at lower temperatures as observed for some other hydrogen bonded compounds upon deuteration [246-250]. This evokes a need for systematic and comparative low temperature structural studies on the various isotopic analogues of amino acids, considering the vast range of isotopic applications in structure determination, pharmacy and biophysics.

3.6. Summary

Our variable temperature studies indicate that isotope effects may play a significant role in the properties of glycine, the simplest amino acid. Among the three N-H...O hydrogen bonds in *gly-h*, the strongest one, nearly along the *c*-axis, shows the least compression upon cooling, whereas the weakest one, nearly along the *b*-axis shows a drastic reduction. An opposite behavior has been observed for the deuterated isotope when cooled down to 180 K. The behavior of NH₃ torsional mode supports these observations which shows pronounced sharpening accompanied with a large rate of stiffening upon cooling in *gly-h*, which corroborate well with the reports of reduction in its anharmonic character. In contrast, the torsional mode in *gly-d* does not show noticeable changes on cooling. These observations imply a relatively compact and isolated three dimensional bilayered structure of *gly-h* at low

temperatures in comparison to a much strongly held two dimensional layered structure of gly-
d stacked along the *b*-axis.

Chapter 4: Low Temperature Phase Transitions in L-Leucine

4.1. Introduction

The motions of constituent molecular moieties in amino acids are responsible for major alterations in vibrational, structural and physical properties. Such motions take place at different time scales [23] and can be activated under specific temperature/pressure conditions, which may vary for different compounds [22, 23]. The studies on these aspects, *viz.*, activation of particular motions is important for understanding the protein flexibility which can cause change in the protein functionality and peptide linkages.

L-Leucine ($C_6H_{13}NO_2$) is an “essential” aliphatic amino acid with wide applications in organic non-linear optical (NLO) materials [95, 140]. However, the structural behavior of L-Leucine at low temperatures is not well understood. Thus, the monitoring of various molecular group movements can be exploited to throw light on its possible structural response upon cooling. In this regard, spectroscopic studies would be ideal to probe such changes occurring in the lattice scale in the complex L-Leucine molecular structure.

Among the reported structural studies, the low temperature single crystal XRD data recorded by Gorbitz & Dalhus in 1996 at 120 K showed no phase transition in L-Leucine [150]. However, in 2011, Filho et al. reported two phase transitions at around 150 K and 275 K using calorimetry and Raman spectroscopic studies [86]. Their neutron scattering results pointed out the changes associated with the backbone hydrophobic chain. But, the powder XRD data were not suitable for atomic refinement in order to confirm structural phase transitions, though Le-bail refinement indeed showed the anomalous behavior of monoclinic beta (β) angle between these two temperatures [86]. In 2016, Binns et al. carried out a single crystal neutron diffraction study, extracting detailed parameters at two temperatures of 300 K

and 120 K [87]. Surprisingly, this study again indicated the absence of any low temperature phase transition and highlighted the urgent need for further studies on this compound in view of the importance of this essential amino acid. This necessitated a closer inspection of changes in the constituent molecular conformations and fine monitoring of the trend of hydrogen bonding motifs, which stabilize the structural framework, at varying temperatures.

Infrared spectroscopy is a powerful technique which can provide clear and complementary information on the reorientation dynamics of various molecular units [15, 106, 199, 201, 251, 252]. In addition, it can also provide significant details of the N-H stretching modes, thereby giving vital insights into the stability of hydrogen bonding network [252]. Thus, to find the signatures and microscopic mechanism of the possible phase transitions upon cooling, along with the analysis of anharmonicity and orientational changes, systematic LT-FTIR spectroscopy on powder L-Leucine has been carried out in a wide spectral range of 30 – 3500 cm^{-1} .

4.2. Experimental methods

Powder L-Leucine was purchased from SRL (Sisco Research Laboratories Pvt. Ltd.) with 99% extra pure CHR. The low temperature IR measurements were carried out at the experimental station of IR beamline facility at Indus-1 in India using continuous flow cryostat, Oxford Optistat CF-V in the transmission mode with temperature varying from 300 K to 4.2 K using liquid nitrogen (LN_2) and liquid helium (LHe) as the cryogens. In the MIR range (500 – 4000 cm^{-1}), sample was dispersed in the CsI and spectra were recorded using KBr beamsplitter and LN_2 cooled MCT detector at 4 cm^{-1} resolution with temperature varied from 300 to 66 K using LN_2 as cryogen. For the FIR region (from 30 – 300 cm^{-1}), sample was dispersed in the polyethylene matrix and the spectra were recorded using Mylar beamsplitter, Hg source and FIR-DTGS detector at 2 cm^{-1} with temperature varied from 300 K to 4.3 K

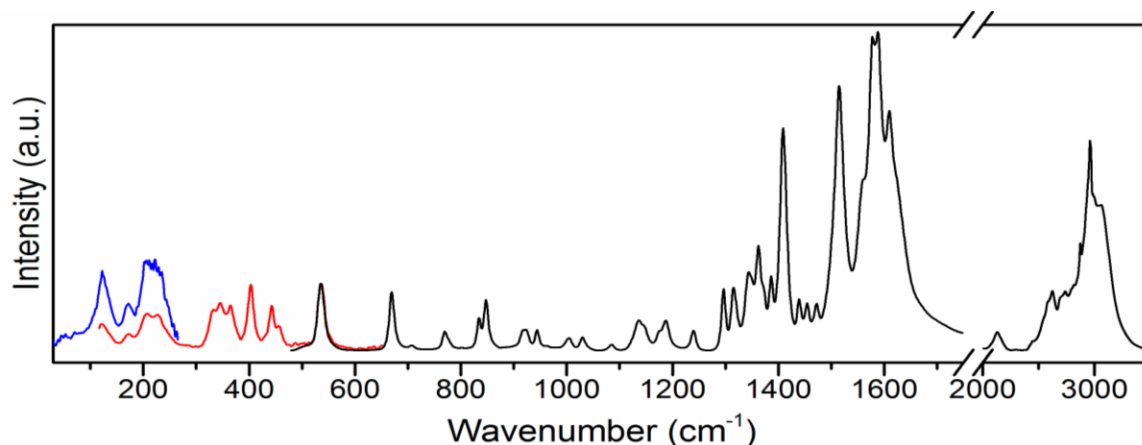


Figure 4.1: Ambient infrared Spectrum of powder L-Leucine in 30 – 3500 cm^{-1} spectral range measured using three different experimental/ instrumental parameters to cover the complete frequency range: Blue - 30-275 cm^{-1} , Red - 120-600 cm^{-1} , Black - 500-3500 cm^{-1} .

using LHe cryogen. Repeat measurements were carried out in FIR (180 – 600 cm^{-1}) region using the sample dispersed in CsI matrix at 4 cm^{-1} resolution with temperature varying from 300 K to 77 K using LN_2 . The overlapping region of the independent experiments shows excellent reproducibility as shown in Figure 4.1. For background correction, all the experiments were carried out using bare CsI/polyethylene pellets at the respective temperature points. A total of 100 scans were coadded in all the sample as well as background measurements.

4.3. Results and discussion

The infrared spectrum of powder L-Leucine has been collected at room temperature (300 K) in the 30 – 3500 cm^{-1} spectral range using three different experimental/instrumental parameters in order to cover the entire frequency range as shown in Figure 4.1. The IR peak positions along with the reported vibrational assignments [118, 122, 147, 253-255] at 300 K and their observed values at 77 K are listed in Table 4.1. The asymmetric unit of L-Leucine consists of two molecules (hereafter, *Leu-A* and *Leu-B*) which differ from each other in respect of conformations and bond lengths as shown in Figure 4.2.

Table 4.1: IR band positions of L-leucine observed at 300 K and 77 K and the reported vibrational assignments [118, 122, 147, 253-255]. Symbols: τ – torsion, r – rocking, ω – wagging, ν – stretching, δ – deformation, t – twist, as – asymmetric, s – symmetric.

IR frequency (cm ⁻¹) (This study)		Ref. [253]	Ref. [254]	Ref. [122]	Ref. [255]	Ref. [118]	Ref.[147]
300 K	77 K						
45	47			Translational mode		Hydrogen bond modes	
52	56	$\tau(\text{NH}_3)$, $\tau(\text{CH}_3), \delta\text{CH}$		Translational mode		Hydrogen bond modes	
70	71	$\tau(\text{NH}_3)$, $\tau(\text{CH}_3), \tau\text{COO}$		$\tau(\text{C}_2\text{C}_3)$		Hydrogen bond modes	
109	107	$\tau(\text{CH}_3)$, $\tau(\text{NH}_3), \tau\text{CH}_2$, $\tau(\text{COO}^-)$		$\tau(\text{C}_3\text{C}_4)$			
123	127			Rotational mode/ $\tau(\text{CO}_2)/$ $\tau(\text{C}_3\text{C}_4)$		Hydrogen bond modes	
136	138			$\tau(\text{CO}_2)/\tau(\text{C}_3\text{C}_4)$			
170	180			$\tau(\text{CO}_2)$		Hydrogen bond modes	
206	207	$r(\text{NH}_3), \delta(\text{CCN})$, $\tau(\text{CH}_3)$		$\tau(\text{C}_5\text{H}_3)$		Hydrogen bond modes	
227	229	$\delta\text{CH}_2, \omega\text{CH}_3$		$\tau(\text{C}_2\text{C}_3\text{C}_4)/\text{rot}$		COO^- vibration	
-	244						
332	329	$\delta(\text{CCN}), \delta\text{CCC}$		$\delta(\text{C}_5\text{C}_4\text{C}_6)$		CCN deformation	
343	343	$\delta\text{CH}, \delta\text{CCN}$		$\delta(\text{C}_5\text{C}_4\text{C}_6)$	Skeletal deformation	CCN deformation	
364	366	$r(\text{COO}^-)$, $\delta(\text{CCN})$			Skeletal deformation	CCN deformation	
402	403		CCC+CCN deformation	$\delta(\text{C}_3\text{C}_4\text{C}_5)$	Skeletal deformation	NH_3 modes	
442	443			$\delta(\text{C}_3\text{C}_4\text{C}_6)$		NH_3 modes	
455	457	$\delta(\text{CH})(\text{CH}_3)_2$			Skeletal deformation		
-	519						
535	539		$r(\text{CO}_2)$	$\rho(\text{CO}_2)$	$r\text{CO}_2$	CO_2 rock/bend/wag	$\omega(\text{COO}^-)$, $\delta(\text{CCN})$, $\delta(\text{COO}^-)$
668	672		$\delta(\text{CO}_2)$	$\delta(\text{CO}_2)$	ωCO_2		$\delta(\text{COO}^-)$, $\delta(\text{CCN}), \omega(\text{COO}^-)$
707	-		$\omega(\text{CO}_2)$				
769	768		C-CO+CO stretching		δCO_2		$r(\text{CH}_2)$
775	776						

Low Temperature Phase Transitions in L-Leucine

834	834		v(CC)				r(CH ₂)
847	849	δ(COO ⁻),v(C C),v(CN)	r(CH ₂)				δCOO ⁻ , vCC,vCN
917	920		r(CH ₃)+v(C C)				
924	928	r CH ₃ , v CC					
944	943						
962	961	vCCN, vCC	r(CH ₃)				vCCN, vCC
1004	1002 1009	rNH ₃ , rCH ₃ , vCC					r(NH ₃) , v(CC), r(CH ₃)
1030	1035	vCN	v(CN)				v(CN)
1084	1086		r(CH ₃)				
-	1133						
1135	1143	rCH ₃ , vCC, δCCN	r(NH ₃)				r(CH ₃), v(CC), δ(CCN)
1146	1158						
1175	1178		v(CC)				r(NH ₃), δ(CH)
1186	1191	r(NH ₃), δCH					
1239	1240	r(NH ₃), tCH ₂ , rCH ₃ , vC- COO ⁻					r(NH ₃)
1296	1294						t(CH ₂)
1315	1313 1223		CH+NH bending				δ(CH)
1343	1345						ω(CH ₂)
1362	1363		δ _s (CH ₃)				
1371	1372	v _s (COO ⁻), δ _s (CH ₃)					δ _s (CH ₃)
1386	1386		t(CH ₂)				
1408	1413 1419		v _s (CO ₂)				δ _s (CH ₃)
1439	1438		δ _s (CH ₃)				δ(CH ₂)
	1447	New					
1454	1455		δ _{as} (CH ₃)				
1471	1473		δCH ₂				δ _{as} (CH ₃)
1514	1511 1514	δCH ₂ , δ _s (CH ₃)	δ _s NH ₃				
1558	1557 1562		v _{as} CO ₂				
1577	1580						
1588	1584	v _{as} (COO ⁻)	v _{as} CO ₂				
1608	1615		δ _{as} NH ₃				
1624	1625		δ _{as} NH ₃				
1634	1638	δ _{as} (NH ₃)					
2132	2133	Combination band					
2580	2570						
2621	2615						
2738	2739	Combination band					
2871	2872	v _s (CH ₂)					
2959	2960	v _{as} (CH ₂)					
3061	3063	v _{as} (NH ₃)					
-	3108						

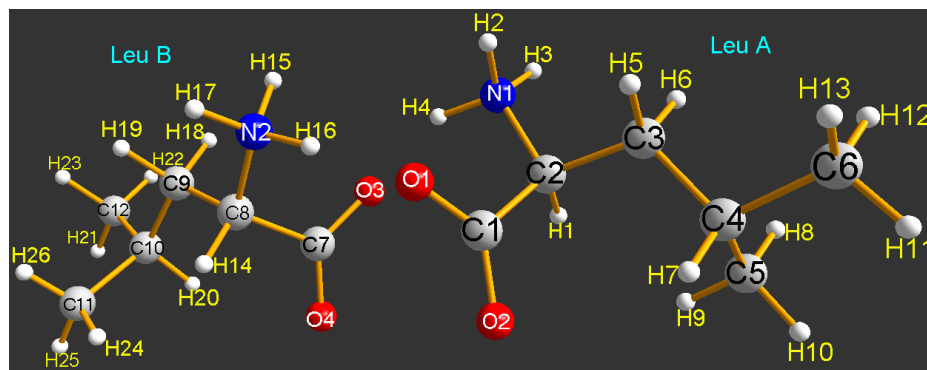


Figure 4.2: Two L-Leucine molecules (*Leu-A* and *Leu-B*) in the asymmetric unit along with the notation of different atoms.

4.3.1. Signatures of possible Phase transitions across 240 K

Upon systemic cooling of L-Leucine from room temperature, we observe significant modifications across 240 K specifically in the modes related to NH_3^+ and COO^- groups. In Figure 4.3, a new IR mode appears below 240 K at 507 cm^{-1} , which can be the out-of-plane $\gamma(\text{N-H}\cdots\text{O})$ intermolecular hydrogen bond bending mode as suggested in the INS reports [255]. This mode shows a large rate of stiffening ($0.055\text{ cm}^{-1}/\text{K}$) relative to other modes upon further cooling as shown in Figure 4.3. The modes at 1135 , 1144 cm^{-1} and 918 , 922 cm^{-1} show intensity reversal below 240 K as shown in Figure 4.4. The strong symmetric deformation, $\delta_s(\text{NH}_3)$ mode at $\sim 1514\text{ cm}^{-1}$ shows very small softening and splits below 240 K with both the components showing similar IR intensity (Figure 4.5). In contrast, the corresponding asymmetric deformation $\delta_{as}(\text{NH}_3)$ mode at $\sim 1608\text{ cm}^{-1}$ shows a noticeably large rate of stiffening ($0.031\text{ cm}^{-1}/\text{K}$) below 240 K (Figure 4.5). The symmetric stretching $\nu_s(\text{COO}^-)$ mode at 1408 cm^{-1} splits and the corresponding asymmetric stretching $\nu_{as}(\text{COO}^-)$ mode at 1587 cm^{-1} shows softening behavior below 240 K (Figure 4.5). All the above observations imply a phase transition at 240 K which may be caused due to a change in the hydrogen bonding interactions between NH_3^+ and COO^- groups in L-Leucine. The definitive signatures

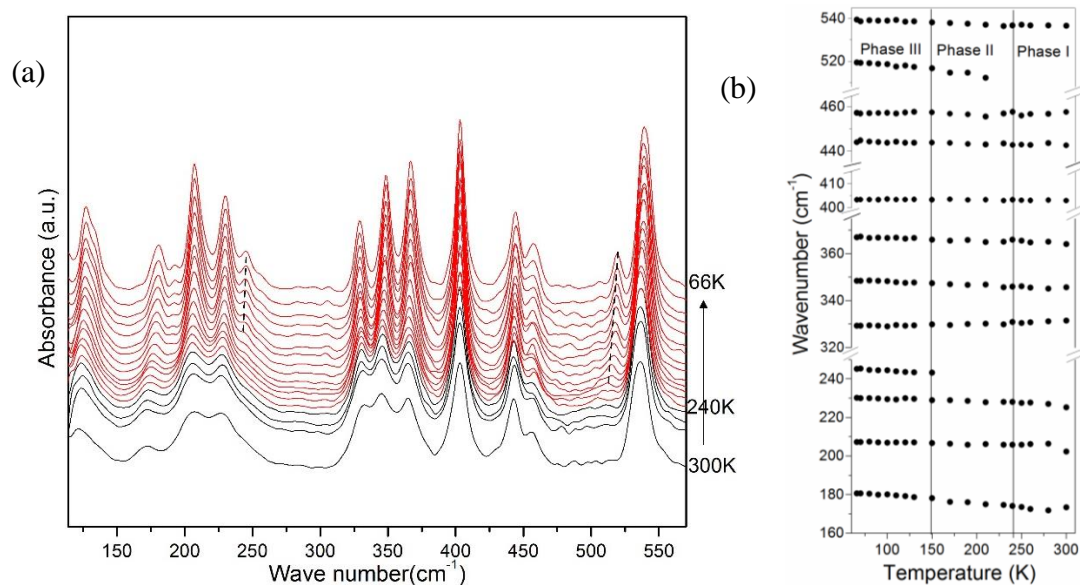


Figure 4.3: (a) Temperature dependent variation of IR peaks in the 115-600 cm⁻¹ spectral range. The dashed line shows the evolution of new peaks at low temperature. (b) Frequency versus temperature plot of peak positions in the 160-550 cm⁻¹ region. The error bars are within the size of the symbols.

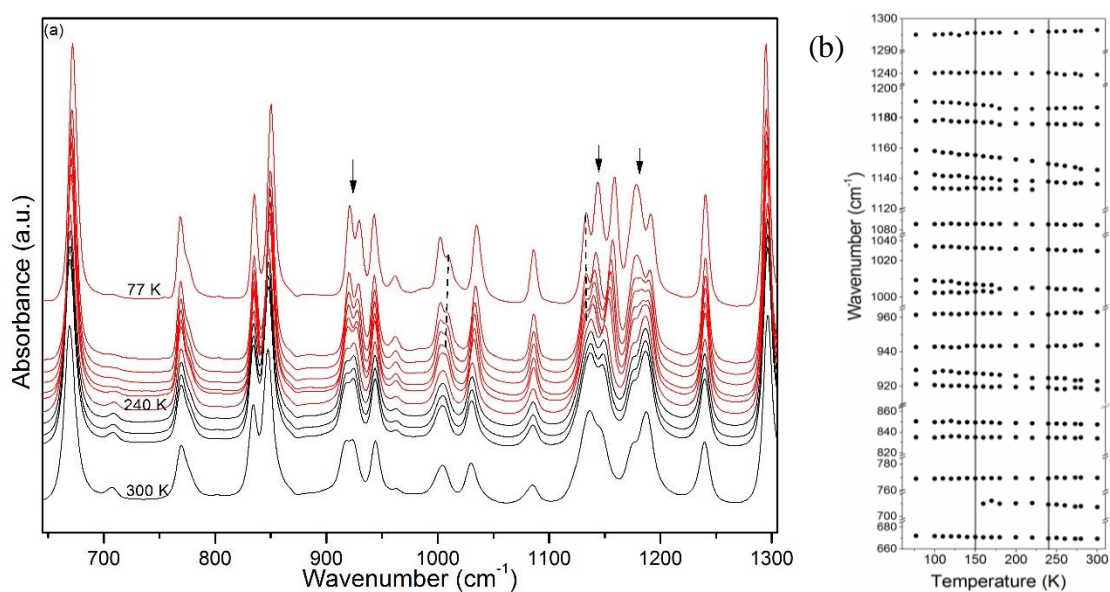


Figure 4.4: (a) Temperature dependent variation of IR spectra in the 650-1300 cm⁻¹ spectral range. Dashed lines show the evolution of new peaks at low temperature. (b) Frequency versus temperature plot of peak positions in the 650-1300 cm⁻¹ region.

of such a transition and further insights into the hydrogen bonding network can be extracted by studying the N-H stretching vibrational modes, which confirm these observations as described below.

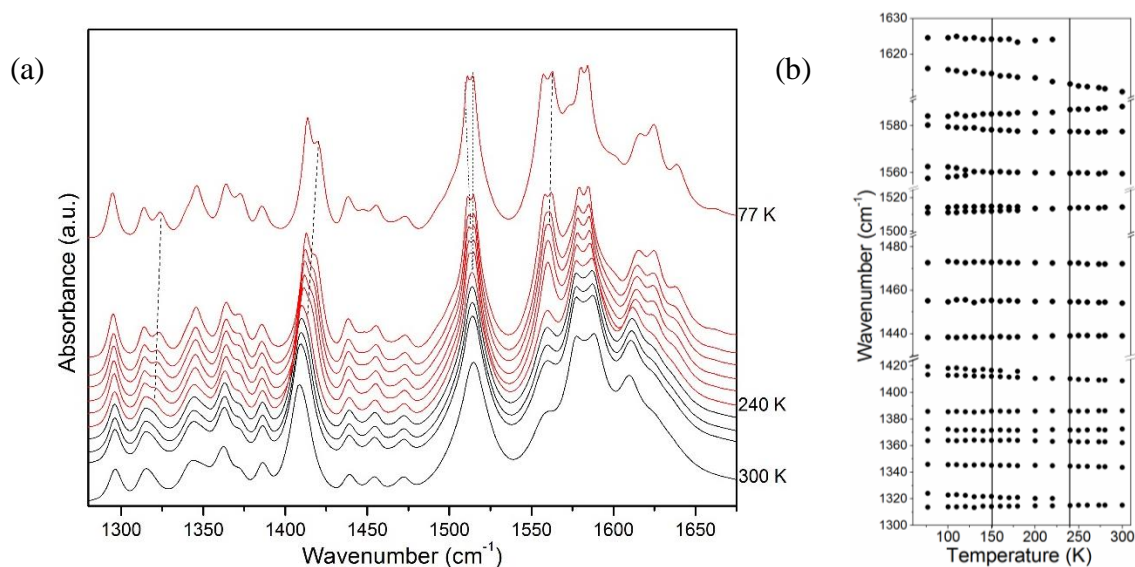


Figure 4.5: (a) Temperature dependent variation of IR spectra in the 1280-1675 cm⁻¹ spectral range. The dashed line shows the evolution of new peaks at low temperature. (b) Frequency versus temperature plot of peak positions in the 1300-1630 cm⁻¹ region.

4.3.2. Hydrogen bonding network in L-Leucine below 240 K

The asymmetric unit of L-Leucine consists of two types of molecules named as *Leu-A* and *Leu-B* (Figure 4.2). There are a total of seven N-H---O hydrogen bonds including one bifurcated hydrogen bond [87]. Out of these, 5 are in the *ac*-plane and two hydrogen bonds are approximately along the *b*-axis. In addition, there is a C-H---O hydrogen bond [87]. The bond parameters of these hydrogen bonds as reported in the recent single crystal neutron diffraction study [87] at 300 K and 120 K have been tabulated in Table 4.2. However, their

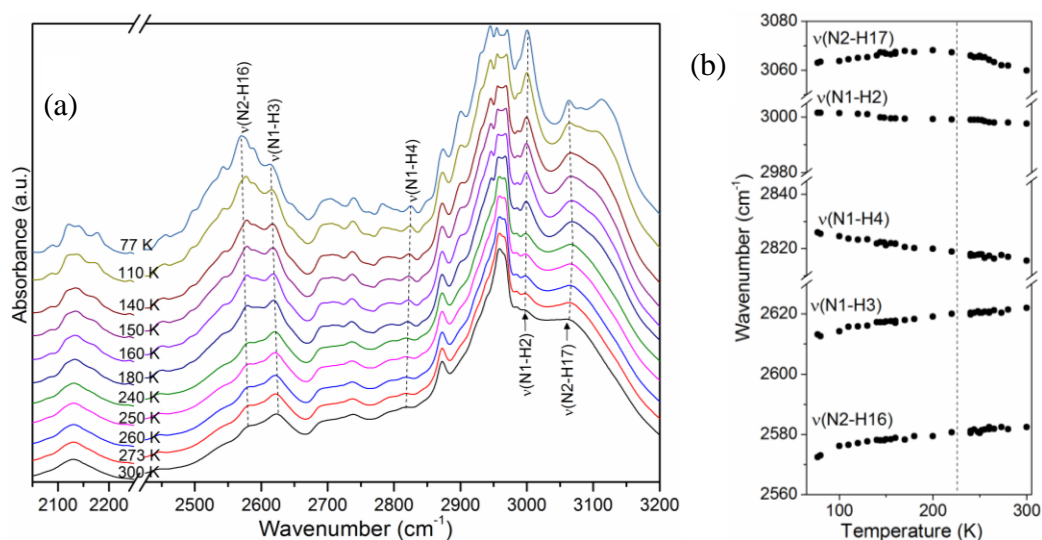


Figure 4.6: (a) Temperature dependent variation of IR spectra of L-leucine in the NH and CH stretching region in the 2000-3300 cm⁻¹ spectral range. The dashed line shows the evolution of N-H stretching peaks at low temperatures. (b) Frequency versus temperature plot of the IR peak positions in the 2565-3080 cm⁻¹ spectral range.

Table 4.2:Hydrogen bond parameters of *Leu-A* and *Leu-B* molecules as obtained from reference [87], along with the low temperature behavior of N-H stretching modes of both Leucine molecules.

Hydrogen bonds	Temp. (K)	H---O(Å)[87]	N---O(Å)[87]	Angle (°)[87]	Exp. freq., N-H (cm ⁻¹) (This study)	Behavior at LT (This Study)
N1-H2---O2	300	1.881	2.887	168.4	3000	Stiffen
	120	1.886	2.897	170.0		
N1-H3---O3	300	1.716	2.775	176.1	2623	Soften
	120	1.673	2.745	178.2		
N1-H4---O3	300	1.835	2.817	155.0	2815	Stiffen
	120	1.852	2.812	151.0		
N2-H16---O1	300	1.715	2.756	174.5	2580	Soften
	120	1.690	2.751	173.3		
N2-H15---O4	300	1.835	2.855	169.6	-	Stiffen
	120	1.836	2.860	166.8		
N2-H17---O1	300	2.071	2.952	141.8	3060	Reorientational change
	120	2.208	2.999	132.1		
N2-H17---O2	300	2.110	3.068	153.3		
	120	1.970	2.970	162.2		

behaviors in the intermediate temperature range are unclear which could give information on possible phase transitions. The spectroscopic signatures of the corresponding stretching vibrational modes can thus be exploited to understand the changes at the molecular level. The IR spectral region 2500-3000 cm^{-1} consists of the stretching vibrational modes and is shown in Figure 4.6(a). But, this region is very complex due to various overtone and combination modes apart from N-H and C-H stretching modes and the precise vibrational frequencies of N-H stretching modes are not available in the reported experimental data. Hence, in order to mark the possible assignments, we have taken help from various empirical correlation plots between N-H stretching frequencies and the corresponding N---O distances and the theoretical predictions [59, 62].

Among the three hydrogen atoms (H2, H3, H4) of the amino group of *Leu-A* molecule, two are hydrogen bonded to nearby *Leu-B* molecules nearly along the *a*- and *c*-axes respectively via their carboxyl groups, as N1-H3---O3 and N1-H4---O3, as shown in Figure 4.7(a). The bond parameters reported in the single crystal neutron diffraction studies are: (a) N1-H3---O3: N---O = 2.775(5) Å, H---O = 1.716(9) Å, $\angle\text{N-H---O} = 176.1(8)^\circ$, and (b) N1-H4---O3: N---O = 2.817(5) Å, H---O = 1.835(10) Å, $\angle\text{N-H---O} = 155.0(8)^\circ$ [87]. These correspond to inter-molecular hydrogen bonding between NH_3^+ and COO^- units. The correlation plots suggest that the N-H stretching frequencies corresponding to these hydrogen bonds are expected at around 2640 cm^{-1} and 2790 cm^{-1} respectively. We indeed observed peaks near these frequencies at 2625 cm^{-1} and 2815 cm^{-1} respectively, the features of which resemble the N-H stretching modes generally observed in the IR spectra of amino acids. Hence, the modes at 2625 cm^{-1} and 2815 cm^{-1} can be assigned to the N1-H3 and N1-H4 stretching modes respectively.

The temperature induced variations of these stretching frequencies have been plotted in Figure 4.6(b). Interestingly, N1-H3 stretching mode shows softening upon cooling which is

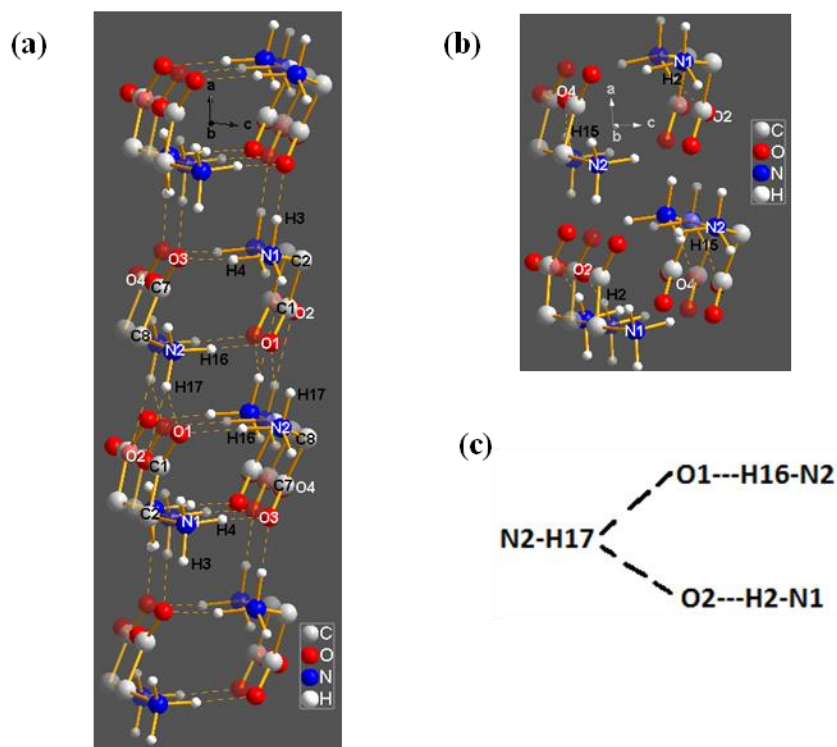


Figure 4.7: Hydrogen bonding in the two L-Leucine molecules (hydrophobic chains have been omitted for clarity) (a) in the *ac*-plane: *Leu-A* molecule having amino group (N1-H2/ H3/ H4) with two hydrogen bonds in the *ac*-plane (N1-H4---O3 and N1-H3---O3) along *c*- and *a*- axes respectively. *Leu-B* molecule having amino group (N2-H15/ H16/ H17) with three hydrogen bonds in the *ac*-plane (N2-H16---O1, N2-H17---O1 and N2-H15---O2). (b) Along *b*-direction: *Leu-A* and *Leu-B* molecules with hydrogen bonds N1-H2---O2 and N2-H15---O4 respectively. (c) Bonding details of the bifurcated hydrogen bond.

shown in Figure 4.6b. Interestingly, N1-H3 stretching mode shows softening upon cooling which represents the strengthening of H3---O3 hydrogen bond. This is also supported by the shortening of the H3---O3 hydrogen bond distance as reported by low temperature single crystal studies [87]. The other stretching frequency, *i.e.*, N1-H4 shows stiffening upon cooling, which implies weakening of H4---O3 hydrogen bond.

In the *Leu*-B molecule, the hydrogen atoms covalently bonded to nitrogen (N2) have been marked as H15, H16 and H17. The H16 hydrogen atom is connected to O1 atom of *Leu*-A molecule through N2-H16---O1 hydrogen bond along the *c*-axis, as shown in Figure 4.7(a). The second hydrogen atom (H15) forms hydrogen bond with the other *Leu*-B molecule, via, N2-H15---O4 approximately along the *b*-axis. The temperature effects on these two hydrogen bonds have been described later. Finally, the *Leu*-B molecule also forms a bifurcated hydrogen bond with carboxyl group of *Leu*-A as N2-H17---O1 and N2-H17---O2 nearly along the *a*-axis as shown in Figure 4.7(a) and Figure 4.7(c). The hydrogen bond parameters of the bifurcated bond are (a) N---O = 2.952(5) Å, H---O = 2.071(15) Å, \angle N-H---O = 141.8(11)° for N2-H17---O1, and (b) N---O = 3.068(6) Å, H---O = 2.110(10) Å, \angle N-H---O = 153.3(13)° for N2-H17---O2 [87]. In order to estimate the approximate position of the corresponding covalent N-H stretching frequency using the correlation plots, we marked the frequency value for the average of the corresponding N---O distances. This value was found to be around 3100 cm⁻¹. At close to this value, a clear peak can be found at ~ 3065 cm⁻¹ in the IR spectrum as shown in Figure 4.6(a). The assignment of this peak to the N-H stretching mode has also been confirmed from the reported Raman spectrum [86]. Interestingly, this mode stiffens upon cooling down to 240 K, after which a softening behavior has been observed. As this mode corresponds to a bifurcated hydrogen bond, this behavior may be an indication of orientational changes in the amino group of *Leu*-B molecule across 240 K. To explain this peculiar behavior, we have to study the other hydrogen bonds connected to the acceptor O1 and O2 oxygen atoms. The hydrogen bonds connected to O1 and O2 are: N2-H17---O1---H16-N2 (see Figure 4.7a) and N2-H17---O2---H2-N1 (see Figure 4.7a and Figure 4.7b) of next *Leu*-B and *Leu*-A amino groups along *c*- and *b*-axes respectively (also shown in Figure 4.7c). The N2-H16---O1 and N1-H2---O2 hydrogen bonds indeed show opposite low temperature behavior as shown in Figure 4.6. The N-H stretching frequency

corresponding to N2-H16---O1 hydrogen bond obtained from empirical correlations is around $\sim 2590 \text{ cm}^{-1}$. We observed the frequency in the IR spectrum at $\sim 2580 \text{ cm}^{-1}$. This frequency softens upon cooling as shown in Figure 4.6(b). Similarly, for the other hydrogen bond, *i.e.*, N1-H2---O2, the expected and observed N-H stretching frequencies are 2990 cm^{-1} and 2997 cm^{-1} respectively, which stiffens upon lowering the temperature as shown in Figure 4.6(b). The relative rate of strengthening of N2-H16---O1 hydrogen bond ($d\tilde{\nu}/dT$ (N2-H16) = $0.040 \text{ cm}^{-1}/\text{K}$) is higher than the rate of weakening of N1-H2---O2 hydrogen bond ($d\tilde{\nu}/dT$ (N1-H2) = $0.025 \text{ cm}^{-1}/\text{K}$) on cooling up to 240 K, whereas the rate of variations are almost similar at further lower temperatures. This is well reflected by the stiffening of the N2-H17 stretching frequency up to 240 K. However, an opposite effect is observed below 240 K, which implies that if one compares the room temperature and low temperature structures (nearly 100 K or lower), no appreciable change would be noticed in the N2-H17 bond distance. These observations provide the explanation to the reported variations in bond distances and angles at 300 and 120 K using single crystal diffraction studies [87] (also included in Table 4.2) and also explain why no change in N2-H17 bond length ($\sim 1.033 \text{ \AA}$) was found. In addition, the present studies also bring into light the significant variations due to temperature effects in the intermediate temperature range. The third hydrogen bonding of *Leu*-B molecule is via, N2-H15---O4 as shown in Figure 4.7(b). The corresponding N-H stretching frequency obtained from empirical relations is at 2938 cm^{-1} . In the IR spectra, shown in Figure 4.6, the region around $2900\text{-}2950 \text{ cm}^{-1}$ consists of several modes in addition to some shoulder peaks, which makes the unambiguous assignment of N2-H15 stretching mode difficult. However, all the modes lying in this region show stiffening behavior as the temperature is reduced. Thus, we may conclude that the N2-H15---O4 hydrogen bond weakens at low temperatures. This is in good agreement with the low temperature single crystal studies which reported elongation in the H15---O4 bond at 120 K [87].

To summarize, the stiffening behavior of N-H stretching frequencies corresponding to hydrogen bonds lying approximately along the *b*-axis (N1-H2---O2 and N2-H15---O4) upon cooling indicates an overall elongation of hydrogen bonds in this direction. The hydrogen bonds along *c*-axis show compression (N2-H16---O1) as well as elongation (N1-H4---O3) on lowering the temperature. However, the rate of elongation in the N2-H16 stretching frequency is about 0.045%, whereas the rate of reduction in the N1-H4 stretching frequency is about 0.040% upon cooling. Hence, the effect of compression may be larger than the effect of elongation along *c*-axis on lowering the temperature. Along the *a*-axis, the N1-H3 stretching mode softens upon cooling and the N2-H17 stretching mode though initially stiffens upto 240 K, also shows a softening behavior below 240 K. Therefore, there is an overall compression of hydrogen bonds along *a*-direction below 240 K. As a result, the 2-D layers in the *ac*-planes are more compact below 240 K and well separated from each other along *b*-direction (see Figure 4.7 a).

Further, the $\tau(\text{NH}_3)$ (torsional) mode ($\sim 512 \text{ cm}^{-1}$), which also provides information on hydrogen bonding, is very weak to be observed at ambient conditions (Figure 4.3). Upon cooling down to 210 K, we could clearly observe the increase in intensity of this mode and the peak position shows a large stiffening behavior (Figure 4.3a) similar to the case of α -glycine [251]. Another band linked to this mode, *i.e.*, the characteristic zwitterionic mode around 2130 cm^{-1} (indicator band): a combination of NH_3 deformation ($\sim 1608 \text{ cm}^{-1}$) and NH_3 torsional ($\sim 512 \text{ cm}^{-1}$) modes shows monotonous stiffening upon cooling.

4.3.3. Reorientational changes across 150 K

The spectral range $30\text{-}80 \text{ cm}^{-1}$ consists of three lattice modes at 45, 52, and 70 cm^{-1} which are very weak at ambient conditions (Figure 4.8a). Consistent with the reported LT- Raman studies[86], the mode at $\sim 70 \text{ cm}^{-1}$ shows a small discontinuity at around 240 K as shown in

Figure 4.8b, in addition to the emergence of a new shoulder mode across 150 K on the low frequency side, which shows softening behavior below 150 K.

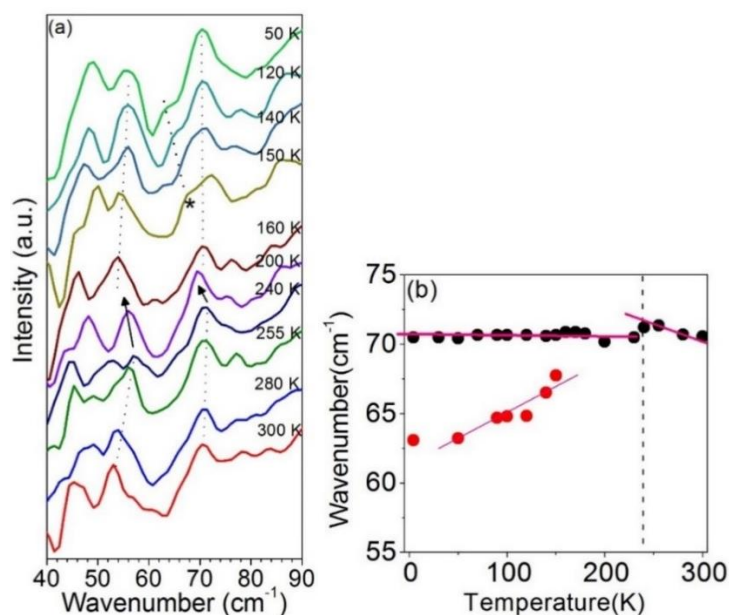


Figure 4.8:(a) Temperature dependent variation of IR peak positions in 30-90 cm⁻¹ spectral range. (b) Frequency versus temperature plot of IR peak at 70 cm⁻¹ wavenumber.

The region 90-150 cm⁻¹ consists of three modes at 107, 122 and 138 cm⁻¹ as shown in Figure 4.9 inset. The peak at 107 cm⁻¹ corresponds to torsional vibrations of $\tau(C_3C_4)$ [For notation see Figure 4.2]. We have analysed full width half maximum (FWHM) of these modes in order to understand the possibility of orientational changes associated with the hydrocarbon chain, by carrying out the Carabatos-Nedelec and Becker approach[256]. According to this approach, the displacement of an atom or molecule with the orientational disorder can be correlated with the self-diffusion process. This has been further characterized by jumping from one orientation form to another or from one potential well to another. The mean orientational correlation time (τ_R) for this jump is given as:

$$\tau_R = \tau_\infty \cdot \exp(-E_a/\bar{R}T) \quad (4.1)$$

where, τ_∞ is the relaxation time at infinite temperature, E_a is the height of the potential barrier for reorientation; \bar{R} is the Gas Constant ($8.3144 \times 10^{-3} \text{ KJ K}^{-1}\text{mol}^{-1}$) at temperature T . When $4\pi^2\nu^2\tau_R^2 \gg 1$, where, ν is the frequency of a particular phonon mode, then the expression for the temperature dependence of the FWHM (I) can be described as follows[256]:

$$\Gamma(T) = (a + bT) + C \exp(-E_a/\bar{R}T) \quad (4.2)$$

where, a , b , C and E_a are fitted parameters. The first term “ $(a + bT)$ ” (linear) in equation (4.2) describes the vibrational relaxation or anharmonicity and the second term (exponential) describes thermal reorientation mechanism of the diffuse nature of the associated modes [256]. Upon analysing the FWHM for the torsional modes, the mode at 107 cm^{-1} ($\tau(\text{C}_3\text{C}_4)$) as fitted with Gaussian function and plotted in the temperature range 300 - 4.3 K in Figure 4.9, showed an interesting behavior. Its FWHM decreases upon lowering the temperature down to 150 K as shown in Figure 4.9. The obtained parameters upon fitting the FWHM with equation (4.2) have been tabulated in Table 4.3. The activation energy, E_a , is found to be 16.3 KJ/mol, which is in good agreement with the reported NMR results[151]. Upon further cooling below 150 K, the FWHM, surprisingly, starts increasing linearly, indicating another phase transition.

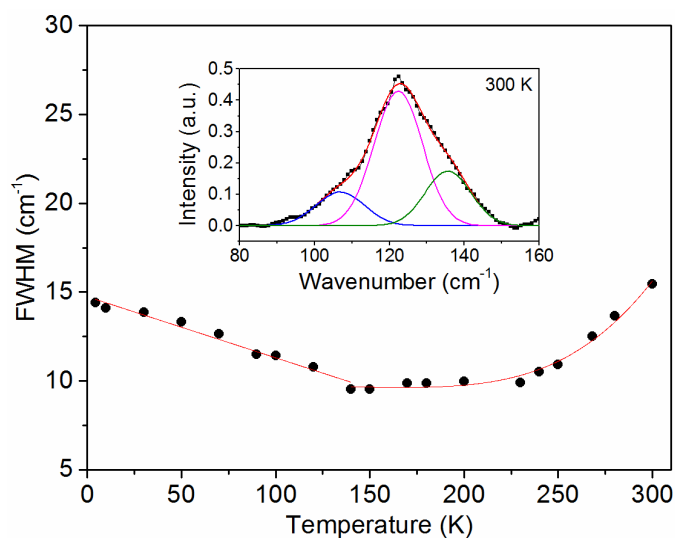


Figure 4.9: Full width at half maximum (FWHM) of (C_3C_4) torsion mode, *i.e.*, $\tau(C_3C_4)$ at 107 cm^{-1} , in the temperature range $300 - 4.3\text{ K}$. Inset: Fitted IR spectrum of L-Leucine at 300 K in $80 - 160\text{ cm}^{-1}$ spectral range.

Table 4.3: The fitted parameters a , b , C and E_a from equation (4.2), for the temperature dependence of FWHM of $\tau(C_3C_4)$ mode in the temperature ranges $300 - 150\text{ K}$ and $150 - 4.3\text{ K}$.

Fitting Parameters	T = 300 - 150 K	Error	T = 150 - 4.3 K	Error
$a\text{ (cm}^{-1}\text{)}$	9.999	1.389	14.744	0.172
$b\text{ (cm}^{-1}\text{K}^{-1}\text{)}$	-0.002	0.009	-0.034	0.002
$C\text{ (cm}^{-1}\text{)}$	4503.956	6457.101	-	-
$E_a\text{ (KJ mol}^{-1}\text{)}$	16.365	4.030	-	-

The mechanism of phase transition can be explained as follows. The high activation energy indicates a high disorder in the orientation of the branched hydrophobic chain. Below 150 K , the dominant linear dependence of FWHM of $\tau(C_3C_4)$ mode suggests a vibrational relaxation process. In other words, the negligible contribution of the exponential term implies large reduction in the activation energy. Hence, the torsional motion of $\tau(C_3C_4)$ tends to freeze and a relatively ordered configuration is obtained. It is noteworthy that the changes in the branched chains around 150 K are also supported by the reported proton magnetic studies

[153]. The decrease of activation energy at low temperatures is well supported by the exothermic peak at 150 K in the reported DSC measurements [86]. Hence, based on the results from our IR study and the reported NMR and DSC studies [86, 151], it can be concluded that the changes around 150 K are due to the hydrophobic chain in L-Leucine.

Thus, we see that there are definitive signatures of orientational changes at the molecular level related to hydrogen bonding network and the hydrophobic chains of L-Leucine which can cause preferred molecular re-arrangements and hydrogen bond reorientations upon cooling. These molecular re-arrangements may further trigger the structural phase transitions at low temperatures. However, similar molecular changes have also been observed in other amino acids which may be the necessary but not sufficient condition for the structural phase transitions to occur at low temperatures as the stability of amino acids with respect to transitions depend upon several factors such as thermal pre-history of the sample [83], size effect (sample particle size) [257], heating/cooling rates [80] etc. For example, in L-Cysteine $[(\text{NH}_3)^+\text{CH}(\text{CH}_2\text{SH})(\text{COO})^-]$ (orthorhombic, $P2_12_12_1$ space group), while DSC data did not provide signatures of phase transition, the lattice parameters depicted subtle changes around 240 K, as shown by powder XRD studies [81]. Finally, the neutron scattering technique suggested a dynamical transition around 150 K (in picosecond to nanosecond time scale range), whereas Raman scattering provided information on weak S-H...S/ S-H...O hydrogen bonds [81, 83]. Adiabatic calorimetric studies were used to show ordering of thiol groups at 70 K [82, 83] to be corroborated with signatures of transition at 30 K using single crystal XRD study [258].

However, in DL-cysteine single crystals (monoclinic, $P2_1/a$ space group), a phase transition was shown by DSC, XRD and Raman spectroscopy upon cooling down to 206 K accompanied by the change in torsion angles (rotation of the side chain) and re-arrangement

of the hydrogen bonds network [80]. The sample has been observed to show fragmentation upon cooling in phase II. On slow heating in phase II, it shows reverse transition to ambient phase at 305 K. When subjected to a second temperature cycle, the sample showed transition at ~ 245 - 230 K temperature range upon fast cooling and in the 288 - 300 K range on reverse heating to the ambient phase. Interestingly, the powder sample obtained by grinding the single crystal of DL-Cysteine with size ~ 1 μm showed no phase transition upon cooling down to 100 K, as suggested by spectroscopic, DSC and diffraction studies [257]. Similarly, different dynamics were observed for L-serine and DL-serine $[(\text{NH}_3)^+\text{CH}(\text{CH}_2\text{OH})(\text{COO})^-]$ due to diverse hydrogen bonding response to cooling as inferred from inelastic neutron and Raman scattering studies [84]. For L-serine, a transition was observed at ~ 140 K due to the reorientational change in the $-\text{CH}_2\text{OH}$ side chain of the zwitterions and no transition was observed for DL-serine [85].

Further, deuteration of sample although does not generally affect the nature of phase transition, but it has also been shown to cause the changes in the phase transition temperatures and also a different hydrogen bonding arrangement at varying thermodynamic conditions. For example, in the simplest amino acid, α -glycine $[\text{NH}_3^+\text{CH}_2\text{COO}^-]$, subtle reorientational changes in the carboxyl moieties upon cooling, lead to change in the hydrogen-bonding network at around 210 K and 180 K, with no structural phase transition at low temperatures [251]. In deuterated α -glycine, opposite behavior of hydrogen bonds were observed when cooled down to 180 K, below which similar strength of hydrogen bonds were observed as that for the hydrogenated α -glycine [251]. In another simplest chiral amino acid, L-alanine, low temperature studies showed changes around 220 K which has been attributed to the Jahn-Teller effect [259]. This was observed due to the coupling of NH_3 group with the lattice modes which lead to lattice instability around 220 K, but no structural phase transition was observed upon cooling. However, significant effects were observed on the strength of

hydrogen bonds upon deuteration of L-alanine upon cooling [211]. The N-D covalent bond lengths were elongated compared to N-H bond lengths, which causes notable increase in one of the hydrogen bond lengths (D3---O2) that link the alanine molecules into columns. Simultaneously, a new mode in the lattice region of the low temperature Raman spectra around 170 K pointed towards a structural phase transition [211]. In the D-enantiomer of alanine, *i.e.*, D-alanine, a structural phase transition was observed upon cooling [260]. Low temperature spectroscopic studies suggested change in the intensities of lattice modes and appearance of new modes below 220 K [260]. The LT neutron powder diffraction (NPD) study suggested diverse response of all the three different N-D covalent bonds for the D-alanine, whereas in L-alanine, two of the three N-D stretching modes show similar behavior [260]. This study also suggested different dynamics of hydrogen bonding network for L-alanine and D-alanine due to different crystal packing at low temperatures.

Thus we see that different molecular units are activated at different temperature and energy (time) scales which can be recorded using different techniques. This shows that detection of phase transition parameters may also be a technique dependent observation. In the case of L-Leucine, LT-FTIR spectroscopic studies have suggested changes around 240 K due to rearrangement in the hydrogen bonding network, which is well supported by the previous PMR, DSC and Raman studies [86, 153]. The change around 150 K are due to the conformational and orientational changes in the hydrophobic chains and can be corroborated with the PMR, DSC and neutron scattering results [86, 153]. Thus, in light of the conflicting reports from powder and single crystal diffraction studies, we speculate that the case of L-Leucine may be similar to that of α -glycine. In L-Leucine, preferred molecular reorientations and strengthening of 2-D layered hydrogen bonds take place across 150 K and 240 K respectively, which might result in subtle adjustment of the monoclinic angle observed in powder diffraction studies. It is imperative that a concerted analysis of spectroscopic and

high-resolution diffraction data on powder as well as single crystals of L-Leucine and other amino acids as well as their deuterated analogues would be vital to understand the trend of molecular motions and reaction pathways in such systems under varying conditions.

4.4. Summary

To summarize, the first systematic low temperature infrared spectroscopic study has been reported on L-Leucine. Notable spectral changes observed at two temperatures of ~ 150 K and ~ 240 K provide evidences of phase transitions. The transition at 150 K is governed by the hydrophobic chain where drastic changes in the FWHM of the torsional $\tau(\text{C}_3\text{C}_4)$ mode were observed. The second transition at 240 K is associated with the hydrogen bond network (between NH_3^+ and COO^- entities). The weakening of hydrogen bonds along b -axis upon lowering of temperature causes elongation along this direction, whereas a net compression, and therefore strengthening of hydrogen bonds takes place along the approximate $\sim a$ - and c -directions. Hence, owing to stronger hydrogen bonds in the ac -plane below 240 K, compact 2-D layers are formed, which are well separated from each other in the b -direction. Thus, we have observed definitive signatures of low temperature transitions at the molecular level in L-Leucine, the mechanisms of which would be helpful in understanding the physico-chemical properties of this important amino acid and harnessing its non-linear and pharmaceutical applications.

Chapter 5: Variable Temperature Studies on Metal-Organic

Complex *trans*-PtCl₂(PEt₃)₂

5.1. Introduction

Metal-organic complexes have applications in the fields of catalysis [24], drug delivery [25-30], gas storage [31, 32], and pharmacy [25, 32-35] due to their porous structure formed by organic linkers, thus attracting researchers in the fields of materials science and crystal engineering. The molecular geometry, metal-ligand bonding and directional supramolecular architecture are among the most vital physical properties of metal-organic complexes, which govern their applications and have direct correlation with their stereochemistry and lattice-scale interactions. Since their discovery, there have been several efforts to tune their structural properties by various methods in order to further improve/ optimize their capabilities which have profound effect on their applications. This tuning can be performed by modifying the size of the linking group, changing the metal salt to which linking (organic) group is attached and by altering the experimental conditions like thermodynamic parameters. Such changes cause modifications in the inter-atomic separations, which may sometimes lead to phase transitions. In this regard, the platinum (II) coordination compounds with square planar structure, which have wide range of applications, are ideal candidates to study the effects of change in thermodynamic environment.

Among the structural isomers with different ligands [261], metal complexes containing Phosphine (PR₃) ligands have attracted considerable attention due to their potential applications as catalysts and precursors in the synthesis of organic compounds in pharmaceutical industry [161]. However, a thorough understanding of the microscopic structure is essential to exploit their bonding and geometrical properties to realize useful structural frameworks. The Pt(II) complex with phosphine ligand, *i.e.*, PtCl₂(PEt₃)₂, where Et

is ethyl group (C₂H₅), exists in two isomeric structures, *cis*- and *trans*-. With bulkier groups (PEt₃) placed diagonally opposite to the central Pt atom, *trans*-isomeric structure is expected to have less steric repulsion as compared to the *cis*-isomer where PEt₃ groups lie on the same side of the central atom. The studies carried out on thermodynamic equilibrium have indicated more stability of *cis*-isomer compared to that of *trans*-PtCl₂(PEt₃)₂[262]. The interpretation of this remained ambiguous for several years, as the arguments, given for higher stability of *cis*-isomer, based on higher degree of partial double bond character of metal-ligand bonds [262, 263] were put to rest by the structural studies which showed dominant single bond character of Pt-Cl, P-C and C-C bonds [264]. Nonetheless, it is established that the strength of Pt-P bond is crucial to determine the structural stability of these compounds, which depends on various factors like the substituent in the *cis*-position to P, π -bonding etc. [264, 265]. Later, while Huheey et al. attributed the strength of Pt-P bond (in M-PR₃) to the back donation of charges from metal *d* orbitals to the 3*d* orbitals of P atom [266], subsequent studies by Xiao et al. showed that the σ^* antibonding orbitals of P-C accommodate the back donation charges from the metal atom, owing to their lower energy [267]. Since then, there have been lots of efforts to tune the π -back bonding properties for synthetic transformation [268], change in the redox potential [269], and metal reactivity [270] using chemical methods. Interestingly, a change in thermodynamic parameters provides the cleanest way to understand the effects of change in inter-atomic distances and consequently study the structural and bonding properties.

The structural tuning of *trans*- and *cis*-isomers of platinum II complexes is also of interest in the pharmacological industry, as one of the oldest drugs showing anticancer activity is cisplatin (PtCl₂(NH₃)₂) with square planar structure, but has toxic effects. The transplatin geometry, found unfavourable to interact with the DNA, primarily due to the stereochemistry [163], is relatively less toxic; which led to the use of *cis*- and *trans*- isomeric

combinations (cisplatin, oxaliplatin etc.) in chemotherapy [162]. The molecular structure and symmetry of Pt(II)-complexes, which depend upon the ligands present, are also important to determine the properties like photoluminescence quantum yield, and electroluminescence efficacy in organic LED applications [158-160].

The present thesis presents detailed investigations on square planar Pt(II) complex *trans*-PtCl₂(PEt₃)₂ under varying thermodynamic environments, *i.e.*, at low temperatures as well as high pressure conditions. We first report the low temperature studies on this compound in this chapter, which will be followed by high pressure investigations in the next chapter. Owing to the presence of organic and halide groups at a short non-bonded distance of ~ 2.7 Å at ambient conditions, it is also an interesting candidate to explore the possibility of hydrogen bond assisted supramolecular architecture in dense phases. In addition, given the importance of organic ligands in the structural stability, low temperature studies of metal organic complexes are important in light of the reports that freezing of methyl groups is associated with a dynamical phase transition [271].

In this chapter, low temperature studies on *trans*-PtCl₂(PEt₃)₂ have been reported using combined Fourier transform infrared (FTIR) and Raman spectroscopy in a wide spectral range to understand the molecular structure. The results have also been compared with the low temperature behavior of *cis*-PtCl₂(PEt₃)₂, structural isomer of this compound.

5.2. Experimental details

For the comparative studies of these isomers (*cis* and *trans*), the low frequency region of the Raman spectra of these isomers were recorded using Bruker MultiRAM FT-Raman spectrometer. The sample was excited using 1064 nm Nd:YAG laser with 100 mW power. LN₂ cooled Ge detector was used to collect the radiation scattered from the sample. A total of 100 scans were recorded at a 1 cm⁻¹ resolution in the 50-3600 cm⁻¹ spectral range. The sample

was mounted on the sample holder and was continuously cooled using liquid nitrogen for low temperature measurements. Variable infrared spectroscopic studies have been carried out on the powder sample of *trans*-PtCl₂(PEt₃)₂ from room temperature down to 4.2 K in the 140 – 3200 cm⁻¹ spectral range. The in-situ LT-IR spectra were recorded using Bruker Vertex 80V Fourier transform infrared spectrometer coupled with continuous flow cryostat. FIR spectra (140–650 cm⁻¹) were measured using Hg source, Mylar beamsplitter and FIR-DTGS detector at a resolution of 2 cm⁻¹. The MIR spectra (500–3500 cm⁻¹) measurements were carried out using thermal source with KBr beamsplitter and LN₂ cooled MCT detector at a resolution of 1 cm⁻¹. The variable LT-Raman measurements were carried out using triple stage Raman spectrograph (HORIBA JobinYvon's T64000) equipped with LN₂ cooled CCD detector. The data were recorded in the subtractive mode in the 10 – 3000 cm⁻¹ spectral range at a resolution of 4 cm⁻¹. The temperature was varied using LINK control software in the system controller from 300 K down to 77 K (THMS600 Linkam stage).

5.3. Molecular structure of *trans*-PtCl₂(PEt₃)₂:

trans-PtCl₂(PEt₃)₂ crystallize in a monoclinic structure with *P2₁/n* space group (No. 14) [264]. The molecule has square planar geometry with centre of symmetry at the platinum atom, which implies that the two chlorine atoms as well as two other PEt₃ ligands are placed diagonally opposite as shown in Figure 5.1.

The electronic configuration of Pt atom is [Xe] 4f¹⁴ 5d⁹ 6s¹. In the square planar structure, with Pt²⁺ configuration, the outermost d⁸ orbitals become non-degenerate due to the electrostatic field of ligands leaving the d_{x²-y²} orbital empty, while other four d orbitals are fully filled. In the coordinate bond between Pt and P atom, the lone pair from P is donated to this empty orbital. In the ligand PEt₃, 3p orbitals of phosphorous and p orbitals of all carbon atoms attached to the P atom form bonding (σ) and antibonding (σ*) molecular orbitals.

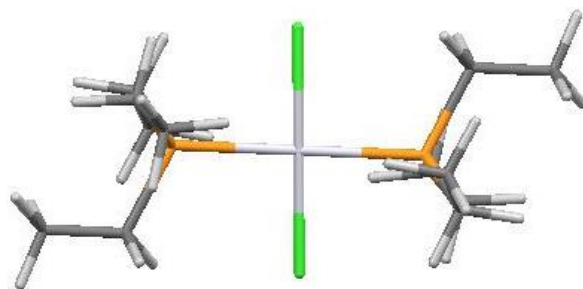


Figure 5.1: *trans*-PtCl₂(PEt₃)₂ molecule with central Platinum atom (Silver), Chlorine atom (green), Carbon atom (Grey) and Hydrogen atom (white).

While all bonding σ orbitals are completely filled, the antibonding σ^* orbitals (possessing π symmetry) are unoccupied. It is due to the relatively lower energy of σ^* molecular orbitals of P-C than the empty $3d$ orbitals of P atom that the electron density from the d_{xy} orbital of the platinum atom are back donated to σ^* , which is known as π -back bonding (Figure 5.2).

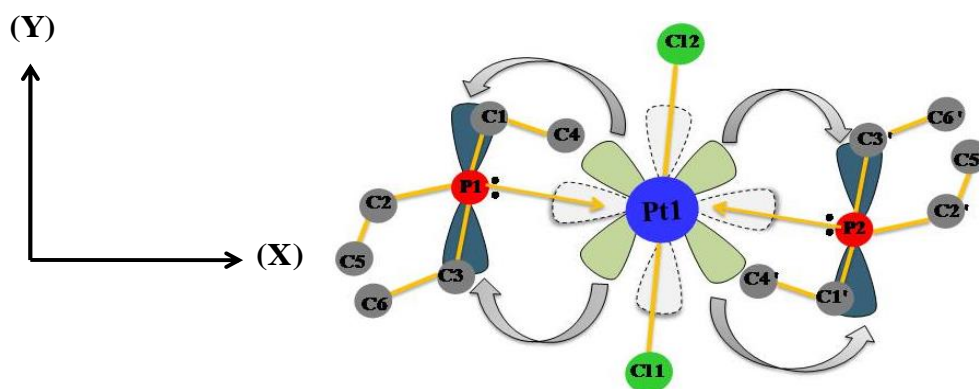


Figure 5.2: Schematic of the bonding arrangements in the molecular units of *trans*-PtCl₂(PEt₃)₂ (distances and angles not to scale). The white orbitals along x & y axes correspond to $d_{x^2-y^2}$ (empty) and green corresponds to d_{xy} (filled) orbital of Pt. The lone pair of electron from P atom goes to empty $d_{x^2-y^2}$ orbital of Pt (straight arrows) and the electron from d_{xy} orbital of Pt goes to empty antibonding σ^* orbital of P-C (curved arrows).

Thus, the bonding of phosphine ligands to metal center consists of two important components [272]. First is sigma donation from phosphorous to metal atom – forming the coordinate bond and second is the π -back bonding – which also has an influence on the strength of Pt-P bond [264, 272].

5.4. Results and discussion

5.4.1. Spectroscopic characterization at ambient conditions

The vibrational spectra (Raman and IR) of *trans*-PtCl₂(PEt₃)₂ can broadly be divided in four regions. In Figure 5.3a, the first region below 150 cm⁻¹ contains lattice vibrations. The second region 150 – 600 cm⁻¹ consists of skeletal vibrations, *i.e.*, stretching (Pt-Cl – 334 cm⁻¹ and Pt-P – 433 cm⁻¹) and deformation modes δ (P-Pt-Cl) (155 cm⁻¹), γ (P-Pt-Cl) (233 cm⁻¹), δ (Pt-Cl₂) (167 cm⁻¹) (γ - out of plane, δ - in plane bending) [273]. Third is the fingerprint region (600 – 1800 cm⁻¹) of the ligands (triethylphosphine), *i.e.*, their skeletal and deformation modes. The assignments were carried out using reported vibrational mode assignments of triethylphosphine, ethyl alcohol, metal (Pd, Ni, Pt etc.) complexes with trimethylphosphine and triethylphosphine ligands etc. [274-278]. In this region, the P-C stretching IR and Raman modes are distinctly observed at 632 cm⁻¹ and 643 cm⁻¹ respectively, whereas the C-C stretching region (~1000 cm⁻¹) is relatively complex (Figure 5.3a and Figure 5.3b). The modes observed between 700 and 800 cm⁻¹ correspond to skeletal modes of PEt₃ and CH₂ rock, whereas C-CH₃ rocking IR and Raman modes are observed at 1030 cm⁻¹ and 1047 cm⁻¹ respectively [276, 279]. Spectral range 1250 - 1500 cm⁻¹ consists of CH₂ wagging (IR – 1257 cm⁻¹, Raman – 1243 cm⁻¹), CH₃ scissoring (IR – 1412 cm⁻¹, Raman – 1421 cm⁻¹) and symmetric and asymmetric deformation modes of CH₂ and CH₃. The fourth spectral region 2800 – 3200 cm⁻¹ shows the corresponding stretching modes. The symmetric stretching (ν_s) modes lie at lower frequencies compared to the asymmetric (ν_{as}) ones. Thus, these modes are observed at: ν_s CH₃ – 2876 cm⁻¹ (Raman), 2874 cm⁻¹ (IR); ν_{as} CH₃ – 2966 cm⁻¹ (Raman), 2964

cm⁻¹ (IR); ν_s CH₂ – 2913 cm⁻¹ (Raman), 2914 cm⁻¹ (IR); ν_{as} CH₂ – 2941 cm⁻¹ (Raman), 2930 cm⁻¹ (IR), as shown in Figure 5.3a and Figure 5.3b [276].

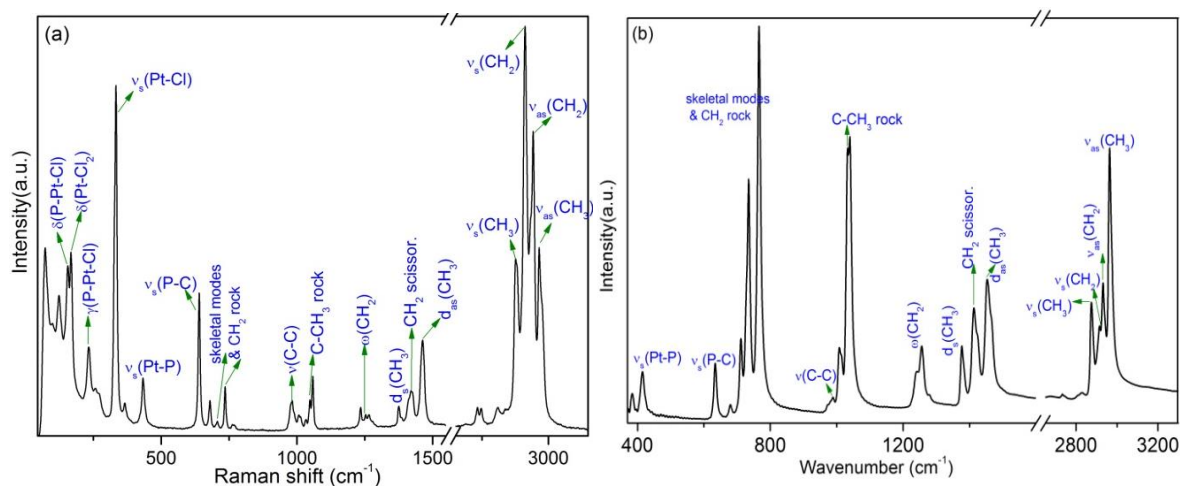


Figure 5.3: (a) FT-Raman and (b) FT-IR spectra of *trans*-PtCl₂(PEt₃)₂ at ambient conditions. γ – out of plane bend, δ – in-plane bend, ν_s – symmetric stretch, ν_{as} – asymmetric stretch, ω – wagging, d_{as} – asymmetric deformation, d_s – symmetric deformation.

5.4.2. Low temperature Spectroscopic Studies

The changes associated with the metal – ligand bonds and hence the crystal symmetry can be probed by studying the lattice and skeletal vibrational modes which are generally observed in the low frequency regions of the infrared (IR)/ Raman spectrum. Our preliminary Low temperature-FT Raman study on the structural isomers of this compound (*cis*- and *trans*-) at two temperatures of 300 K and 77 K in the spectral range 60 – 600 cm⁻¹ showed drastic alterations in the skeletal Raman modes of *trans*-isomer upon cooling as shown in Figure 5.4(Right), whereas relatively no change was detected in the spectrum of *cis*-isomer as shown in Figure 5.4. In the Raman spectra of *cis*-isomer, blue shifting and increased sharpness of the vibrational modes are the only features which are clearly visible in the spectrum upon

cooling. Except these features, there are no major changes in the two spectra and the lattice region also remains intact. However, in the *trans*-isomer, the low temperature spectra show significant changes, which have been systematically studied and presented in the following sections.

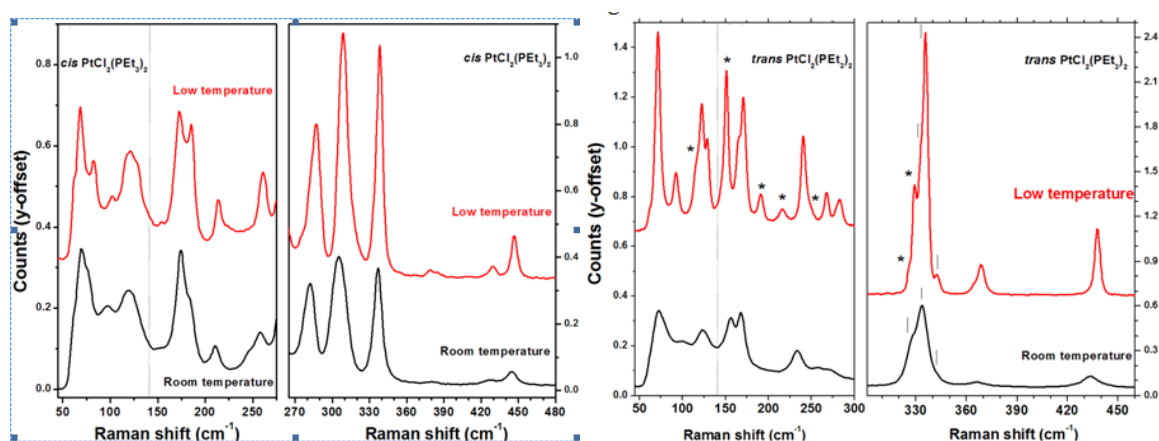


Figure 5.4: (Left to Right) FT-Raman spectra of *trans*-PtCl₂(PEt₃)₂ in the region 50-460 cm⁻¹. New peaks emerged at low temperature have been marked as asterisk (*).

a) Temperature dependent IR and Raman studies of Lattice and Skeletal vibrational modes:

Figure 5.5 represents Raman and IR spectra of *trans*-PtCl₂(PEt₃)₂ in the frequency regions below 200 cm⁻¹. Figure 5.6a represents low temperature Raman spectra in the 200 – 640 cm⁻¹ spectral range and Figure 5.6b represents the Raman peak positions versus temperature plots in the 10 – 650 cm⁻¹ spectral range. Figure 5.7a represents low temperature IR spectra in the 200 – 650 cm⁻¹ spectral range and Figure 5.7b represents the IR peak positions versus temperature plots in the 160 – 640 cm⁻¹ spectral region for *trans*-PtCl₂(PEt₃)₂. In the Raman spectra, the lattice modes at 20 and 23 cm⁻¹ show initial softening upto 173 K, followed by

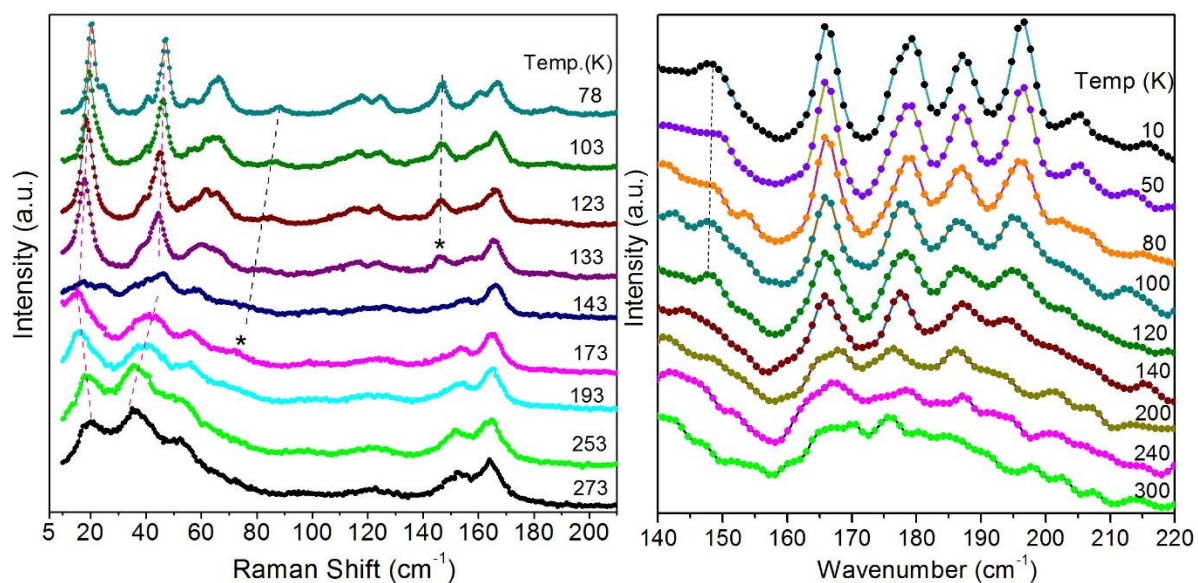


Figure 5.5: Low temperature spectra of *trans*-PtCl₂(PEt₃)₂ (a) Raman (spectral range : 5-220 cm⁻¹) and (b) IR (spectral range : 140-220 cm⁻¹) spectra.

stiffening up to 133 K as shown in Figure 5.5a and Figure 5.5b. Also, at temperatures close to 130 K, a sudden increase in intensity of lattice modes is observed as shown in Figure 5.5a. Below this temperature, the peak positions as well as intensities do not show any appreciable changes (Figure 5.5a and Figure 5.6b). New modes also appear in the Raman spectra at ~ 71 and 147 cm⁻¹ across 180 K and 130 K respectively, which stiffen upon cooling (marked with * in Figure 5.5a). Similarly, in the IR spectra, a weak feature is also observed to be emerging at ~ 147 cm⁻¹ across 130 K (Figure 5.5b). Among the skeletal modes, the δ (Pt-Cl₂) Raman as well as IR modes at 165 and 167 cm⁻¹ respectively remain almost unaltered with temperature (Figure 5.5, Figure 5.6b, Figure 5.7b). The broad band in the IR spectra which spans the region 150 – 200 cm⁻¹ is completely resolved upon cooling down to 180 K and transforms to four clear peaks at further lower temperatures (Figure 5.5b). The deformation mode γ (P-Pt-Cl), which is observed at 233 and 228 cm⁻¹ in the Raman and IR spectra respectively initially shows systematic stiffening upon cooling down to 130 K (Figure 5.6b and Figure 5.7b).

respectively). These peak positions reach a plateau at nearly 130 K, beyond which they do not show any shift. However, a new mode is clearly seen to appear around 250 cm⁻¹ in the IR spectra below 130 K (marked with * in Figure 5.7a), which strengthens at lower temperatures. The IR and Raman modes corresponding to ν (Pt-Cl) (341 and 329 cm⁻¹ respectively) and ν (Pt-P) (417 and 429 cm⁻¹ respectively) stretching vibrations show small but monotonous stiffening upon cooling, with a small change in the rate of variations across 130 K, up to the lowest temperature measured, implying systematic strengthening of the skeletal bonds (Figure 5.7b and Figure 5.6b respectively).

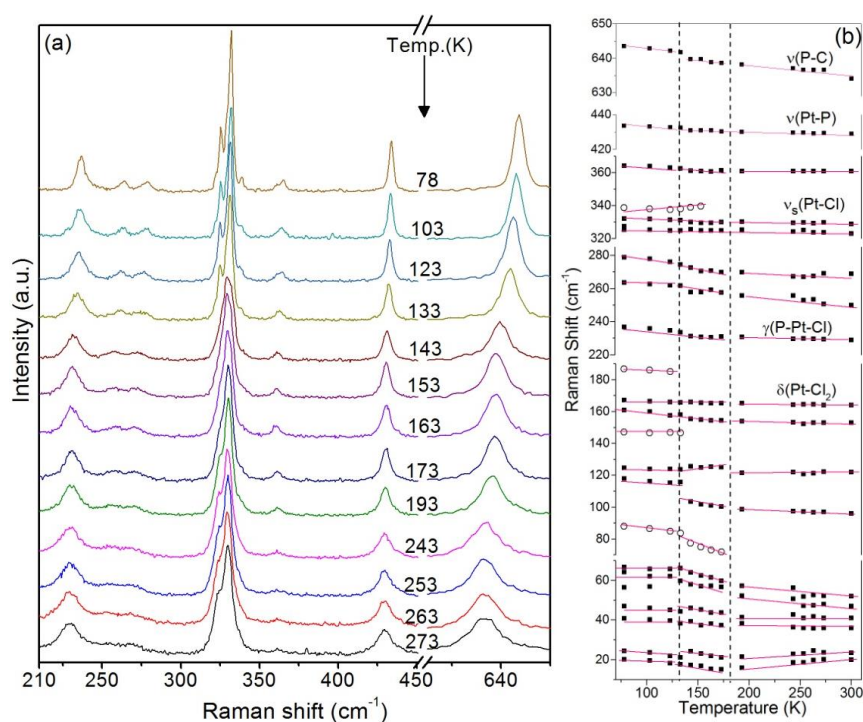


Figure 5.6: (a) Low temperature Raman spectra of *trans*-PtCl₂(PEt₃)₂ in the 210 – 650 cm⁻¹ region. (b) Variation of Raman active modes at low temperatures in the 10 – 650 cm⁻¹ spectral range. Dotted vertical lines are drawn at 130 and 180 K. Open circles represent new mode emerging at low temperatures. Symbols: δ = in-plane bending, γ = out-of-plane bending, and ν = stretching vibration.

The shoulder (333 cm⁻¹) developing on the lower frequency side of the $\nu_{as}(\text{Pt-Cl})$ (asymmetric stretching) IR mode transforms to a clear peak below 180 K and it softens upon further cooling (Figure 5.7a).

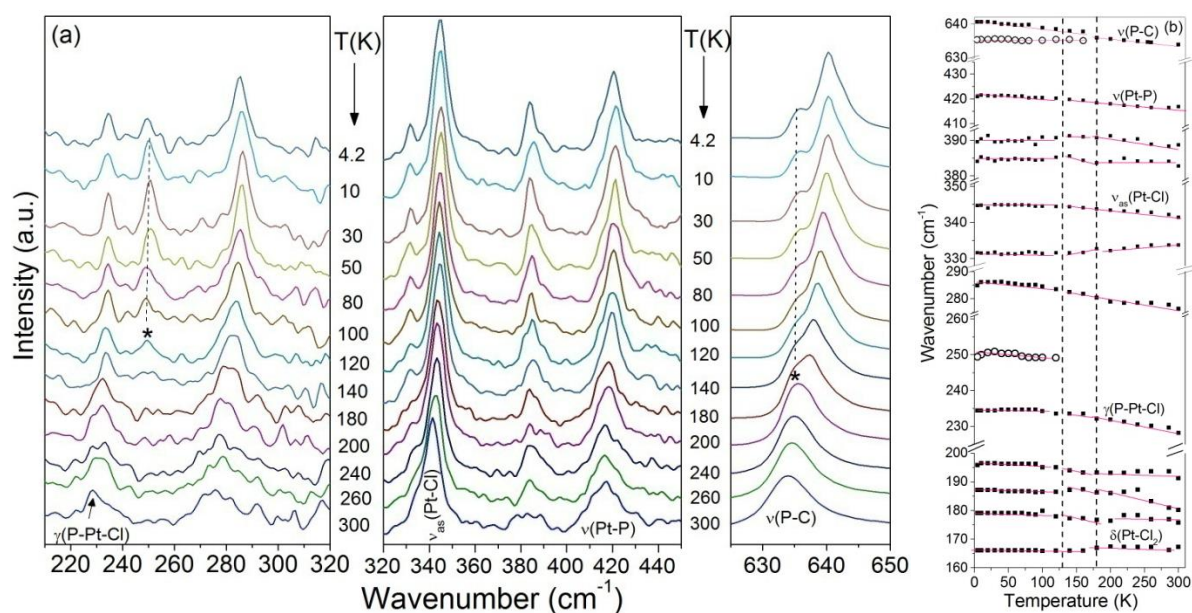


Figure 5.7: (a) Low temperature IR spectra of *trans*-PtCl₂(PEt₃)₂ in the 220 – 650 cm⁻¹ spectral region. Dashed lines indicate new peaks emerging at low temperatures. (b) Variation of IR peak positions at low temperatures in the 160 – 640 cm⁻¹ spectral range. Dotted vertical lines are drawn at 130 and 180 K. Open circles represent new modes appearing upon cooling.

In the phosphine ligand, the $\nu(\text{P-C})$ IR mode at 634 cm⁻¹ shows an increase in the rate of stiffening (~ 0.028 cm⁻¹/K below 180 K) upon cooling below 180 K with a new shoulder appearing on the low frequency side (~ 633 cm⁻¹ at 180 K), which shows small softening upon cooling, as shown in Figure 5.7a. The $\nu(\text{P-C})$ Raman mode at 632 cm⁻¹ shows stiffening behavior upon cooling in the 173-133 K temperature range (Figure 5.6b). Across 130 K, it shows discontinuous shift to a higher value. Further, most of the vibrational modes in the region 10 – 650 cm⁻¹ show slope change in the frequency versus temperature plots across 180

K and 130 K. In summary, the features like appearance of new modes in the lattice and skeletal regions, abrupt changes in the rate of variation of frequencies and change in the relative intensity of some vibrational modes in the low frequency regions of infrared and Raman spectra are clear indications of phase transition in *trans*-PtCl₂(PEt₃)₂ across 180 K and 130 K. The changes occurring in the organic ligands groups can provide further insights into the nature of these transitions.

b) Changes associated with organic ligands – IR and Raman deformation modes:

The internal vibrational modes of the organic ligands are also expected to show similar changes under temperature induced contraction [280]. Indeed, the systematic IR spectra at various temperatures in the range 4.2 – 300 K, shown in Figure 5.8 and Figure 5.9 reveal that the orientational changes associated with the organic ligand groups take place at temperatures of 180 and 130 K. The IR spectral region 700 – 800 cm⁻¹ (skeletal modes of PEt₃ and CH₂ rock), becomes complex upon cooling due to splitting and appearance of new modes across 180 K and 130 K as shown in Figure 5.8a. A new mode also appears around 1003 cm⁻¹ (near ν(C-C) IR mode) below 180 K which softens and shows a large increase in the relative intensity upon cooling, as shown in Figure 5.8a. The C-CH₃ rocking IR mode at 1032 cm⁻¹ stiffens in the 180 – 130 K temperature range, with the appearance of new shoulder (~1030 cm⁻¹) on its lower frequency side below 180 K. This new mode softens with an increase in the relative intensity upon cooling upto 4.2 K as shown in Figure 5.8a and Figure 5.8b. Below 130 K, these modes show no change upon lowering the temperature. In addition to the similar changes as in IR spectra, the distinctive feature in the Raman spectra in this region is the sudden increase in the relative intensity of C-CH₃ rocking mode at 1055 cm⁻¹ across 173 K, shown in Figure 5.8a inset.

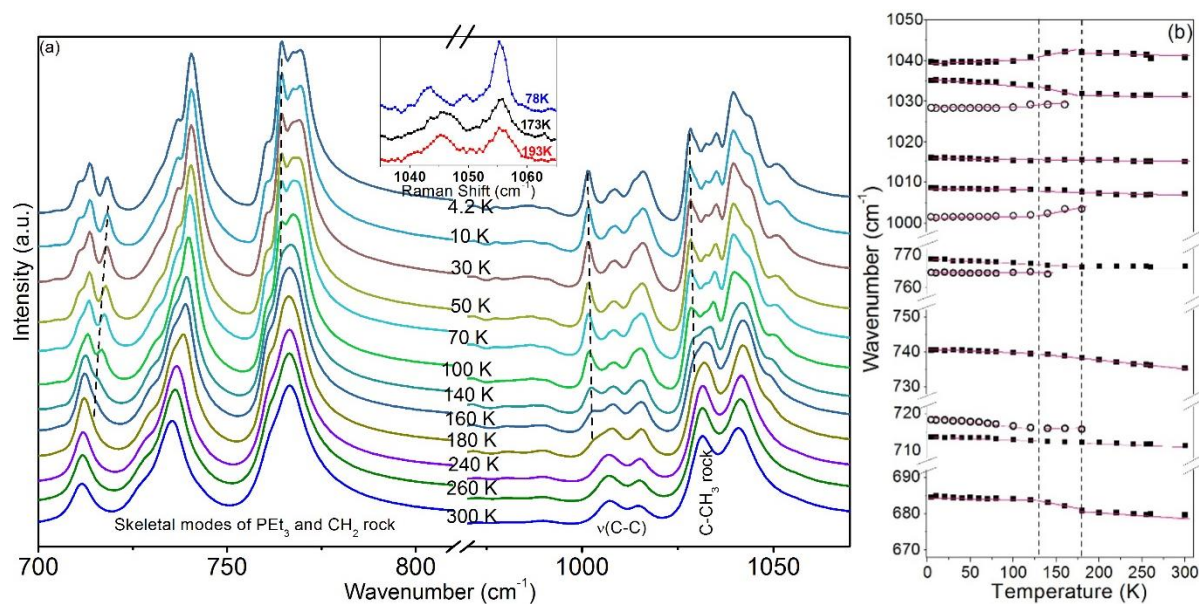


Figure 5.8:(a) Low temperature IR spectra of *trans*-PtCl₂(PEt₃)₂ in the 700 – 1070 cm⁻¹ spectral range. Dashed lines indicate new peaks evolving at low temperatures, Inset: Low temperature Raman spectra in the 1030 – 1070 cm⁻¹ spectral range. (b) Variation of IR peak positions at low temperature in the 670 – 1050 cm⁻¹ spectral region. Dotted vertical lines are drawn at 130 and 180 K. Open circles represent new modes emerging at low temperatures.

In the 1250 – 1500 cm⁻¹ spectral range, the band lying in the region of asymmetric deformation vibrations of CH₃ unit (1450 – 1500 cm⁻¹) shows splitting below 180 K in both IR and Raman spectra (Figure 5.9a). The wagging IR mode ω (CH₂) at 1260 cm⁻¹ stiffens upon cooling upto 130 K as shown in Figure 5.9. The symmetric deformation d_s (CH₃) (~1260 cm⁻¹) and asymmetric deformation d_{as} (CH₃) (~1450 cm⁻¹) IR modes soften upon cooling upto 130 K, with the appearance of a new mode on the lower wavenumber side of d_s (CH₃) below 180 K as shown in Figure 5.9a and Figure 5.9b. Upon further lowering the temperature below 130 K, these modes show no variation. The CH₂ scissoring mode (~ 1413 cm⁻¹) shows a relatively large rate of stiffening (~ 0.020 cm⁻¹/K) compared to other modes upto 130 K and below this temperature it shows no variation as shown in Figure 5.9b. This spectral region

becomes complex upon cooling due to splitting of several modes. A drastic increase in the intensity of modes, which otherwise are weak at ambient conditions, has been observed at

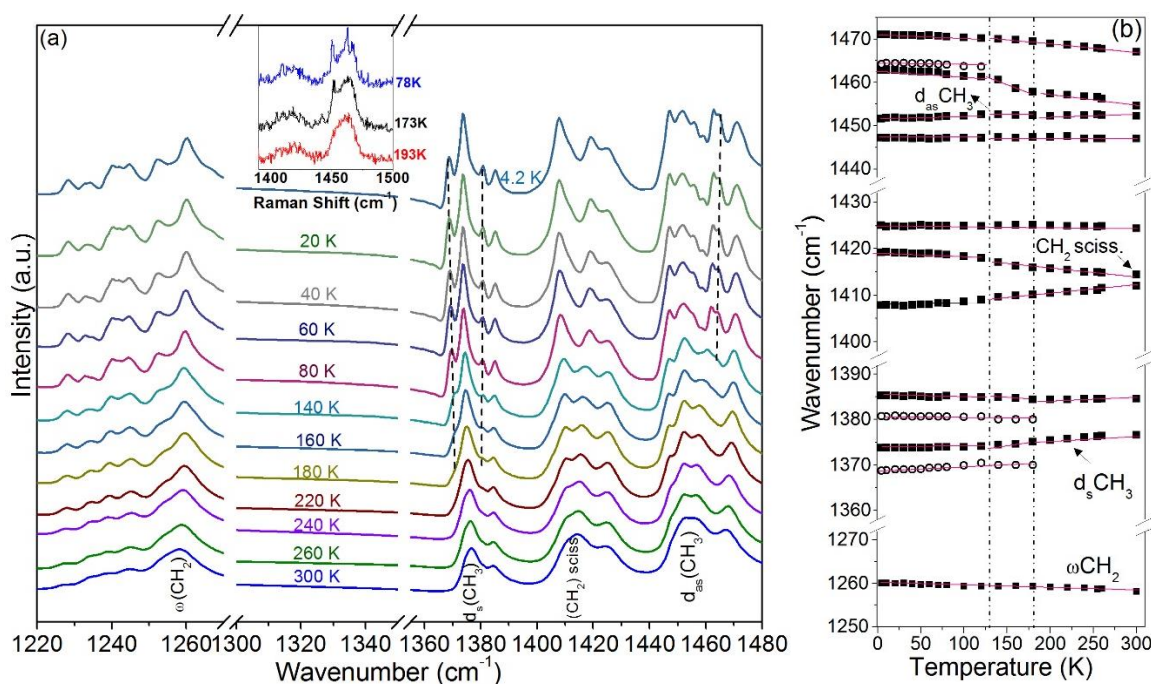


Figure 5.9: (a) Low temperature IR spectra of *trans*-PtCl₂(PEt₃)₂ in the 1220 – 1480 cm⁻¹ spectral range. Dashed lines indicate new peaks evolving at low temperatures. Inset: Low temperature Raman spectra of *trans*-PtCl₂(PEt₃)₂ in the 1400 – 1500 cm⁻¹ spectral range. (b) Variation of IR peak positions at low temperatures in the 1250 – 1475 cm⁻¹. Open circles represent new modes evolving at low temperatures. Symbols: ω = wagging, d_s = symmetric deformation, d_{as} = asymmetric deformation vibration.

low temperatures. Hence, both the IR and Raman spectra in lattice/ skeletal as well as ligand deformation regions show marked changes across 180 K and 130 K, which can be related to temperature induced phase transitions in *trans*-PtCl₂(PEt₃)₂. The stretching vibrational modes may further provide important information on the hydrogen bonding network in the structure in the low temperature phase.

5.4.3. Probing Hydrogen bonds through stretching vibrational modes

The ligand stretching region 2850 – 3050 cm⁻¹ is particularly important, as it provides information on weak non-covalent interactions like hydrogen bonds formed, via, C-H groups. At ambient conditions, *trans*-PtCl₂(PEt₃)₂ forms two short H---Cl hydrogen bonds. One is intramolecular hydrogen bond with H---Cl = 2.719 Å, C---Cl = 3.328 Å and ∠CHCl = 114.37° and the other is intermolecular hydrogen bond with H---Cl = 2.657 Å, C---Cl = 3.684 Å and ∠CHCl = 155.66° [166]. At low temperatures, the symmetric and asymmetric IR stretching vibrational peaks of CH₃ group (2874 cm⁻¹ and 2963 cm⁻¹ respectively) show small softening in the 300 – 4.2 K temperature range, with a noticeable increase in the rate of softening in 180 – 130 K temperature range, as shown in Figure 5.10b.

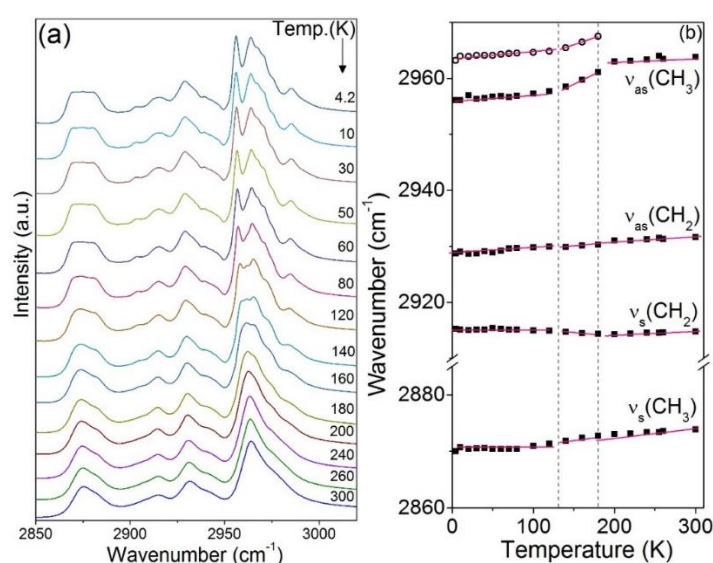


Figure 5.10: (a) Low temperature IR spectra of *trans*-PtCl₂(PEt₃)₂ in the 2850 – 3050 cm⁻¹ spectral range. (b) Variation of IR modes at low temperature in the 2860 – 2970 cm⁻¹ spectral range. Open circle symbol represent new mode emerging at low temperatures. Symbols: ν_s = symmetric stretch, ν_{as} = asymmetric stretch.

A new shoulder peak emerges close to the asymmetric stretching mode, showing a similar behavior (softening at ~ -0.100 cm⁻¹/K) and intensification relative to other modes in the 180-130 K temperature range as shown in Figure 5.10a and b. The softening behavior of CH₃ symmetric and asymmetric stretching modes in the 180 – 130 K temperature range are also verified from the Raman spectra (2875 cm⁻¹ and 2962 cm⁻¹ respectively) shown in Figure 8b. The CH₂ symmetric and asymmetric IR (2914 cm⁻¹ and 2931 cm⁻¹ respectively) and Raman (2913 cm⁻¹ and 2941 cm⁻¹ respectively) stretching modes show comparatively less changes in the complete range, except for small discontinuous shifts across 130 K (Figure 5.10b and Figure 5.11b). These observations imply preferred strengthening of the C-H---Cl hydrogen bonds through CH₃ groups in *trans*-PtCl₂(PEt₃)₂ in the low temperature phase between 180 – 130 K temperature range.

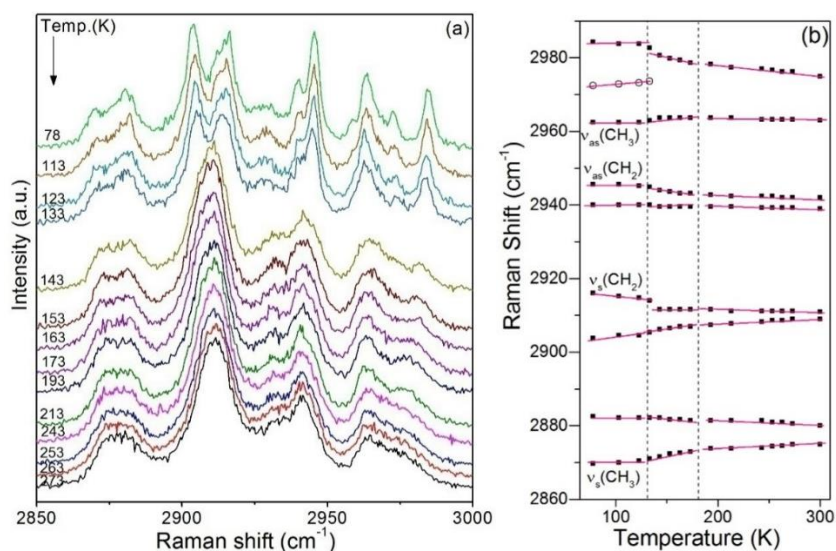


Figure 5.11: (a) Low temperature Raman spectra of *trans*-PtCl₂(PEt₃)₂ in the 2850 – 3000 cm⁻¹ spectral region. (b) Variation of Raman modes in the 2860 – 2990 cm⁻¹ spectral region at low temperature. Open circle symbol represents new mode emerging upon cooling.

Thus, based on the spectroscopic observations in the complete frequency range, upon cooling *trans*-PtCl₂(PEt₃)₂, most of the vibrational modes show change in slope around two temperatures at 180 K and 130 K. The changes around 180 K are associated with the orientational dynamics of organic ligands (phosphine triethyl), which initiate strengthening of C-H---Cl hydrogen bonds through CH₃ groups upto 130 K. Across 130 K, appearance of new modes as well as drastic increase in the intensity of some modes is observed. Finally, at further low temperatures down to 4.2 K, no new features or intensity/ peak position variations are noticed. In the skeletal modes, small changes are observed in the frequency variations of Pt-Cl deformation modes, whereas no significant effect is noticed in the stretching modes.

5.5. Summary

In summary, low temperature infrared and Raman spectroscopic studies have been carried out on *cis*- and *trans*- isomers of Pt(II) complex PtCl₂(PEt₃)₂. The *cis*-isomer is not much affected due to the temperature change, whereas the *trans*-isomer indicates lowering of structural symmetry upon cooling. Therefore, systematic low temperature studies have been carried on *trans*-PtCl₂(PEt₃)₂ using complementary FTIR and Raman spectroscopic techniques, which show significant variations in the vibrational modes associated with organic ligand moieties across 180 K and 130 K. An increase in the C-H---Cl hydrogen bonding strengths, associated with CH₃ groups, is noticed in the intermediate temperature range of 180 – 130 K. Softening of the lattice modes and appearance of new Raman modes in the lattice region across 180 K and 130 K provide a clear indication of phase transitions in this compound.

Chapter 6: High Pressure Phase Transitions in *trans*-PtCl₂(PEt₃)₂

6.1. Introduction

Similar to the low temperature behavior, the metal organic complex *trans*-PtCl₂(PEt₃)₂ shows a range of structural re-arrangements under high pressure, which have been presented in this chapter. However, interestingly, the high pressure structure is different from the low temperature structure.

6.1.1. Importance of high pressure studies in metal-organic coordination compounds

Tuning of molecular and electronic properties of Pt(II)-organic complexes have a profound effect on their applications. Such alterations can be achieved externally by varying the thermodynamic parameters such as pressure/temperature etc. which may also bring about phase transitions. Interestingly, a change in thermodynamic parameters provides the cleanest way to understand the effects of change in inter-atomic distances and consequently the structural and bonding properties, of which pressure is the most effective tool. Further, a change in inter-atomic distances is also closely associated with the tuning of non-covalent interactions, which might result in novel structural assemblies, like lamellar, stitched staircase, helical etc. as observed for some other square planar coordination complexes [281].

Though both high pressure and low temperature result in compression/ contraction of the system, the mechanism of possible phase transitions or structural relaxations in the square planar metal-organic complexes may be similar or different [43-45]. For example, in the complex [(CH₂)₃NH₂][Zn(HCOO)₃], phase transitions have been observed at low temperature as well as high pressure due to the ring-puckering motion of the cationic groups and the framework rearrangement resulting from rotations of the HCOO⁻ ions respectively [282]. In contrast, the compound *trans*-Pt(II) dithiocarbamate, which shows small variations in metal-

ligand stretching Raman modes and no variations in deformation modes at low temperatures, depicts drastic and different pressure induced changes, where a large variation of the deformation Raman modes was noted as compared to the stretching modes [283, 284].

Tidey et al. have recently reported a useful review on the high pressure properties of several coordination compounds, in particular geometrical changes occurring up to 10 GPa, which in turn can be associated with properties like negative linear compressibility, spin cross-over, magnetism, and molecular conduction [285]. Among the Pt(II) compounds, high pressure studies on the molecular wires [Pt(dmgl)₂] and [Pt(dpg)₂] (where, dmgl = dimethylglyoximate, and dpg = diphenylglyoximate) showed that the electrical and optical properties can be tuned by changing the Pt---Pt distance [286-288]. However, the simple square planar compound *trans*-PtCl₂(dimethylsulfide)₂, shows no phase transition up to 8 GPa with monotonous increase in the monoclinic β angle [289]. It is noteworthy that the compound under study, *i.e.*, *trans*-PtCl₂(PEt₃)₂ has shown significant changes in the Raman spectra upon cooling up to 77 K in contrast to no drastic spectral changes in *cis*-PtCl₂(PEt₃)₂ as described in the previous chapter of this thesis. Also, the presence of organic and halide groups at a short non-bonded distance of ~ 2.7 Å at ambient conditions, makes it an interesting candidate to explore the possibility of hydrogen bond assisted supramolecular architecture. Prompted with these two ideas, detailed high pressure studies have been carried out on the square planar compound *trans*-PtCl₂(PEt₃)₂ using combined infrared (up to 11.3 GPa), Raman (up to 15.4 GPa), x-ray diffraction (up to 16.9 GPa) and density functional theory (DFT) techniques to probe the molecular as well as structural modifications. The results obtained have provided unambiguous evidences of pressure induced phase transition to a non-centrosymmetric structure which is stabilized by a three dimensional network of C-H---Cl hydrogen bonds, thus laying out the possibilities of tuning the local metal coordination

environment as well as non-covalent interactions in square planar metal-organic coordination compounds.

6.2. Experimental methods

6.2.1. Single Crystal and Powder X-ray Diffraction studies

Single crystal x-ray diffraction pattern of *trans*-PtCl₂(PEt₃)₂ was recorded at ambient conditions at BL21 (PX) beamline at Indus-2 Synchrotron, India [290]. The data were recorded on the MARdtb with automated sample changer, having a single-axis rotation goniometer and CCD detector (Rayonix MX-225) using monochromatic x-rays of wavelength 0.9794 Å. The structure file of the above measurement is available at Cambridge Crystal Data Centre (CCDC number 1829359). Powder x-ray diffraction data at high pressures were collected at Indus-2, BL-11, Indore, India, using monochromatic x-rays of wavelength 0.7265 Å [291]. High pressures were generated using Mao-Bell type of diamond anvil cell [292] using diamond anvils of culet size ~ 400 μm. Sample chamber was prepared by drilling hole of diameter ~ 250 μm in a steel gasket of thickness 250 μm pre-indented to a thickness of 90 μm. Finely ground sample of *trans*-PtCl₂(PEt₃)₂ was loaded in this hole along with 4:1 methanol:ethanol solution as pressure transmitting medium (PTM) and Cu as internal pressure marker. The well-known equation of state of Cu under static compression was used to determine pressure at the sample [293]. Monochromatic x-rays were focused down to 0.1 X 0.1 mm² at sample position. 2D diffraction images at different pressures were collected using MAR345 imaging plate detector and converted to 1D diffraction patterns using Fit2D software [294] which were subsequently analysed through Rietveld refinement incorporated in GSAS II software [295].

6.2.2. Infrared spectroscopic studies

The high pressure infrared studies on *trans*-PtCl₂(PEt₃)₂ were carried out using indigenously designed Diamond anvil cell (DAC) mounted on Hyperion 2000 IR microscope coupled to Bruker Vertex 80V Fourier transform infrared spectrometer. These constitute parts of infrared beamline (BL-6) facility at Indus-1, India. Powder sample dispersed in CsI, along with tiny ruby chips, was loaded into a 150 μm hole of a tungsten gasket pre-indented to a thickness of 60 μm. The IR transparent matrix of CsI also served as the pressure transmitting medium. A total of 100 scans were co-added at a resolution of 2 cm⁻¹ and the repeat measurements were carried out at 4 cm⁻¹ at each pressure in the spectral range 600 to 3600 cm⁻¹. Ruby fluorescence was measured at each pressure for pressure calibration [296]. Gaussian fit of the peaks were carried out for spectral deconvolution.

6.2.3. Raman spectroscopic studies

The high pressure Raman spectra were recorded on triple stage Raman spectrograph (HORIBA Jobin Yvon's T64000) equipped with LN₂ cooled CCD detector. The Raman signal was excited by 532 nm diode pumped solid state laser. The spectra were recorded in the range of 15 – 3200 cm⁻¹ in the subtractive mode, at a resolution of 4 cm⁻¹. Finely ground sample of *trans*-PtCl₂(PEt₃)₂ crystal along with tiny chips of ruby was loaded into a tungsten gasket in a hole of ~ 120 μm diameter drilled in pre-indented gasket (60 μm) without PTM [68, 199, 297, 298].

6.2.4. First-principles calculations

The electronic structure calculations on *trans*-PtCl₂(PEt₃)₂ were performed using spin-polarized plane wave based density functional theory (DFT) at 0 K as implemented in Vienna Ab-initio Simulation Package (VASP) [299, 300]. The electron ion interactions were described by Projector Augmented Wave (PAW) [301] formalism which includes Pt (*s*¹*d*⁹),

Cl (s^2p^5), P (s^2p^3), C (s^2p^2) and H (s^1) valence states. The exchange-correlation potential as parameterized using Perdew-Burke-Ernzerhof (PBE) [302] form within the generalized gradient approximation (GGA) was used. The unit cell of *trans*-PtCl₂(PEt₃)₂ structure contains 94 atoms and the integration over the Brillouin zone was carried out on a 7×3×3 k-point mesh (22 k-points in the irreducible Brillouin zone) generated using the Monkhorst–Pack scheme [303]. A cutoff energy (E_{cutoff}) of 400 eV for the plane wave basis set was used and the above choice of E_{cutoff} and k-point mesh was sufficient for energy convergence to less than 0.1 meV/atom. The initial atomic coordinates for optimization of the ambient structure were taken from our single crystal x-ray diffraction experiment at ambient conditions. The total energy of *trans*-PtCl₂(PEt₃)₂ unit cell was optimized with respect to volume, shape and atomic positions as permitted by the space group symmetry of the crystal structure. The structural relaxation was performed using the conjugate gradient algorithm until the residual forces and stresses in the equilibrium geometry were of the order of 0.01 eV/Å and 0.01 GPa, respectively. The final calculation of total electronic energy were performed using the tetrahedron method with Blöchl corrections [301].

6.3. Results and Discussion

6.3.1. Structural study at ambient conditions

As the ambient structural parameters of *trans*-PtCl₂(PEt₃)₂, reported in 1966 [264], show some ambiguity in the ligand structures, synchrotron based x-ray diffraction studies have been carried out on the single crystal of this compound. *trans*-PtCl₂(PEt₃)₂ has been reported to crystallize in a monoclinic structure with $P2_1/n$ (Space Group No. 14) space group [264] (a setting of the space group $P2_1/c$) as shown in Figure 6.1. The refinement details are presented in Table 6.1. The refined lattice parameters at ambient conditions are found to be $a = 10.9937(7)$ Å, $b = 11.5227(10)$ Å, $c = 7.4499(5)$ Å, $\beta = 93.302(6)^\circ$, which are in close agreement with the earlier reported values [264].

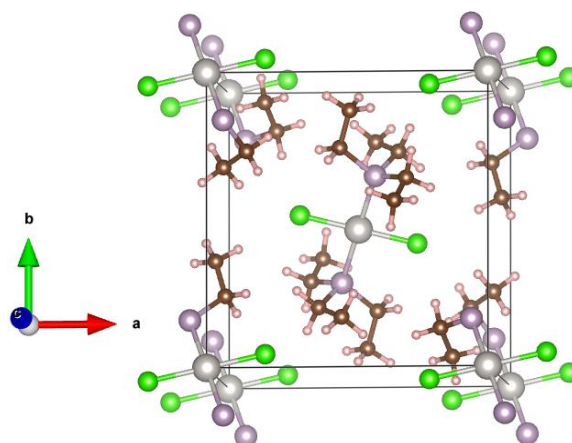


Figure 6.1: Unit cell of *trans*-PtCl₂(PEt₃)₂, where Et = C₂H₅. Color: Grey – Pt, Green – Cl, Violet – P, Brown– C, Pink – H atoms.

The non-bonded Pt-Pt distance at ambient conditions is ~ 7 Å. In addition, the present study also provides precise atomic coordinates and structural parameters for this compound at ambient conditions as shown in Table 6.2. However, the positional refinement of hydrogen atoms (not available in literature as well) was not good using the experimental data. As these may enable finer investigations of inter-atomic interactions like hydrogen bonding, the hydrogen atoms were initially generated using ‘Avogadro’ software package (<https://avogadro.cc/>) and the structure was optimized using DFT with the initial structure obtained from our single crystal studies. The theoretically optimized equilibrium atomic positions at ambient pressure, including the Wyckoff positions of hydrogen atoms, have also been presented in Table 6.2. The ambient lattice parameters obtained using powder x-ray diffraction of *trans*-PtCl₂(PEt₃)₂ measured inside the diamond anvil cell, as shown in Figure 6.2, are also consistent with the single crystal studies. From Rietveld refinement using GSAS-II software, the values are found to be $a = 11.0048(15)$ Å, $b = 11.5167(11)$ Å, $c = 7.4802(07)$ Å, $\beta = 93.483(9)^\circ$. These studies were then extended to find the structural details at higher pressures.

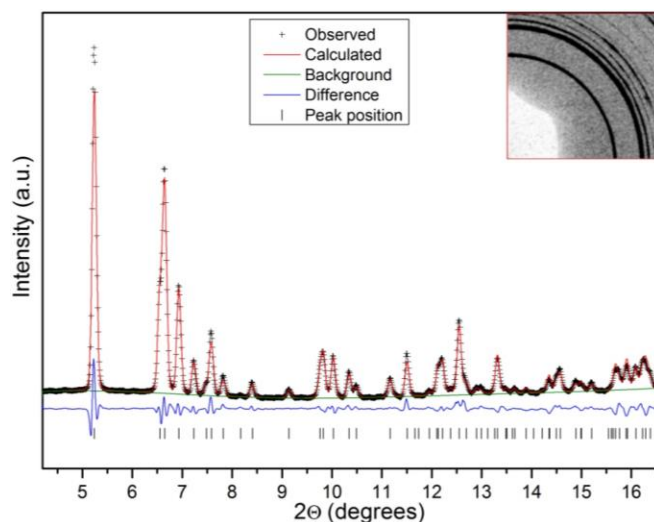


Figure 6.2: Ambient powder XRD pattern of *trans*-PtCl₂(PEt₃)₂ inside the DAC. Inset shows the picture of 2D diffraction rings

Table 6.1: Crystal structure data and refinement details of single crystal x-ray diffraction of *trans*-PtCl₂(PEt₃)₂ at ambient conditions.

Empirical formula	C ₁₂ H ₃₀ P ₂ Cl ₂ Pt
Formula weight	472.06
Temperature (K)	300
Crystal system, Space group	Monoclinic, <i>P</i> 2 ₁ / <i>n</i>
<i>a</i> , <i>b</i> , <i>c</i> (Å)	7.4499(5), 11.5227(10), 10.9937(7)
α, β, γ (°)	90, 93.302(6), 90
Volume(Å ³)	942.17(12)
Z	2
ρ_{calc} (g/cm ³)	1.7705
μ /mm-1	12.061
F(000)	475.3
Crystal size (mm ³)	0.1 × 0.2 × 0.2
Radiation	synchrotron ($\lambda = 0.9794$ Å)
2 θ range for data collection (°)	10.14 to 65.18
Index ranges	-7 ≤ <i>h</i> ≤ 7, -10 ≤ <i>k</i> ≤ 10, -11 ≤ <i>l</i> ≤ 11
Reflections collected	6786
Independent reflections	1091 [R _{int} = 0.1368, R _{sigma} = 0.0562]
Goodness-of-fit on F ²	1.032
Final R indexes [<i>I</i> > 2 σ (<i>I</i>)]	R1 = 0.0484, wR2 = 0.1702
Final R indexes [all data]	R1 = 0.0505, wR2 = 0.1601
Largest diff. peak/hole / e (Å ⁻³)	1.26/-1.61

Table 6.2: Experimental (ambient pressure – reported (column 2) and this study (column 3)) atomic coordinates and lattice parameters of *trans*-PtCl₂(PEt₃)₂ [*P2₁/n* (14) – space group]. The experimentally obtained structure has been submitted to CCDC (1829359) by including H-atoms refined using the riding model. To further improve structure with H-atom positions, DFT-GGA calculated (at ambient pressure) equilibrium atomic positions have also been provided in the last column, obtained by including hydrogen atoms and optimizing single crystal XRD deduced experimental coordinates, the uncertainty in unit cell volume is found to be ~ 5%. *Note: In this table, axes transformation of the single crystal structure, which has been deposited at CCDC after including H-atoms, have been carried out using PCW software for consistency in lattice parameter convention (*a* and *c*) with the reported values [264].

Atom (wyckoff positions)	Experimental positions [264]			Experimental position (this study) (single crystal X-ray diffraction) (without H atoms)			Equilibrium atomic positions optimized using DFT-GGA calculations (this study)		
Pt (2a)	0.5000	0.5000	0.5000	0.0000	0.0000	0.0000	0.0000	0.0000	0.0000
Cl (4e)	0.6980	0.4549	0.4604	0.7001	0.4539	0.4593	0.7054	0.4531	0.4666
P (4e)	0.4295	0.3314	0.3676	0.5705	0.6687	0.6373	0.5703	0.6709	0.6399
C 1 (4e)	0.3024	0.3623	0.1814	0.4556	0.7547	0.7441	0.4530	0.7596	0.7483
C 2 (4e)	0.3581	0.4299	0.0675	0.4970	0.8763	0.8120	0.4926	0.8819	0.8047
C 3 (4e)	0.3848	0.2393	0.6155	0.8578	0.2628	0.0251	0.8607	0.2656	0.0323
C 4 (4e)	0.4460	0.1930	0.5425	0.3054	0.3508	0.1870	0.3055	0.3479	0.1792
C 5 (4e)	0.5391	0.2797	0.2040	0.5424	0.8050	0.3250	0.5459	0.8087	0.3168
C 6 (4e)	0.5076	0.1158	0.1829	0.3330	0.4338	0.0460	0.3351	0.4350	0.0268
H 1 (4e)							0.4174	0.9267	0.8730
H 2 (4e)							0.5740	0.8828	0.9019
H 3 (4e)							0.5154	0.9339	0.6820
H 4 (4e)							0.3727	0.7605	0.6482
H 5 (4e)							0.4230	0.7096	0.8695
H 6 (4e)							0.2823	0.2618	0.1202
H 7 (4e)							0.2256	0.3773	0.2555
H 8 (4e)							0.3527	0.5211	0.0881
H 9 (4e)							0.4167	0.4102	0.9508
H 10(4e)							0.2585	0.4430	0.9211
H 11(4e)							0.4752	0.8639	0.3765
H 12(4e)							0.5922	0.8600	0.2117
H 13(4e)							0.4979	0.7358	0.2457
H 14(4e)							0.8143	0.3384	0.9581
H 15(4e)							0.7887	0.2132	0.0950
Lattice parameters									
<i>a</i> (Å)	11.00±0.02			10.9937(7)*			10.861		
<i>b</i> (Å)	11.52±0.02			11.5227(10)			11.541		
<i>c</i> (Å)	7.49±0.01			7.4499(5)*			7.134		
β (°)	93°0'±15'			93.302(6)			92.796		
Volume (Å ³)	947.832			942.17(12)			893.158		

6.3.2. Pressure induced phase transition

6.3.2.1. Spectroscopic studies:

Figure 6.3 and Figure 6.4 show the high pressure Raman spectra of *trans*-PtCl₂(PEt₃)₂ in 20 – 300 cm⁻¹ and 320 – 780 cm⁻¹ regions, respectively. The high pressures IR spectra in the region 600 – 1100 cm⁻¹ and 1100 – 3200 cm⁻¹ have been shown in Figure 6.5 and Figure 6.6b respectively, whereas the Raman spectra in the region 720 – 3200 cm⁻¹ at various pressures are plotted in Figure 6.6a. The pressure induced variations in the peak positions of IR and Raman active modes have been shown in Figure 6.7, Figure 6.8 and Figure 6.4c. The spectroscopic studies, depicting various changes in spectral features, *viz.*, emergence of new modes, and change in the rate of variation of vibrational modes are suggestive of structural modifications taking place at pressures up to ~ 0.9 GPa and ~ 4.9 GPa, as explained below.

We observe discontinuous shift in the peak positions of lattice modes (Figure 6.4c) across ~ 0.9 GPa and ~ 4.9 GPa, accompanied with emergence of new modes, for example at ~ 32 cm⁻¹ as shown by an asterisk (*) in Figure 6.3. In fact, the mode lying at higher frequency side of this mode (at ~ 30 cm⁻¹) also seems to emerge only above 0.6 GPa, however, the spectral data at still lower frequencies could not be obtained to trace its origins.

These features are a clear indication of change in the crystalline structure upon compression. The evolution of molecular skeletal region under high pressure supports this possibility. In the skeletal region of such centro-symmetric compounds, the symmetric stretching (ν_s) Raman mode appears with significantly higher intensity compared to the asymmetric stretching mode (ν_{as}) and vice versa in the IR spectrum [278]. Therefore, in *trans*-PtCl₂(PEt₃)₂, the single intense Raman band at 334 cm⁻¹ at ambient pressure corresponds to the ν_s (Pt-Cl) mode (Figure 5.3a of chapter 5). The corresponding ν_{as} (Pt-Cl) mode is observed at ~ 339 cm⁻¹ in the IR spectrum, *i.e.*, at ~ 5 cm⁻¹ higher value [273]. As

shown in Figure 6.4a and Figure 6.4c, the $\nu_s(\text{Pt-Cl})$ Raman mode splits above 0.9 GPa and the new mode appears at nearly 5 cm^{-1} higher frequency. Thus, it is possible that the new mode may be the one which is IR active at ambient conditions. We should also note that the *cis*-isomer, with no centre of symmetry, is characterized by two Pt-Cl stretching frequencies in both IR as well as Raman spectra [276]. Therefore, the splitting of Pt-Cl Raman mode can be attributed to a change in symmetry of this compound across 0.9 GPa.

Among the three deformation modes, the $\delta(\text{Pt-Cl}_2)$ mode (167 cm^{-1}) also shows the emergence of a shoulder peak at higher frequency side at higher pressures (marked by ^ in Figure 6.3 expanded view) and $\gamma(\text{P-Pt-Cl})$ mode (233 cm^{-1}) shows a pronounced increase in width above 0.9 GPa (Figure 6.3 inset). The $\delta(\text{P-Pt-Cl})$ mode (155 cm^{-1}) depicts an increase in relative intensity above 0.9 GPa, which can be correlated to a change in angular orientations. The other stretching mode, $\nu(\text{Pt-P}_2)$ at 433 cm^{-1} shows a monotonous increase in peak position and width with pressure.

Further, we observe splitting in the P-C stretching Raman mode (643 cm^{-1}) at 0.9 GPa and the new mode appears on the lower frequency side as shown in Figure 6.4b. Consistently, the corresponding IR mode (632 cm^{-1}) also splits near this pressure and the new mode emerges on the higher frequency side as shown in Figure 6.5a. A one to one correspondence (from Figure 6.7, Figure 6.8, Figure 6.4c) between IR and Raman modes provides an interesting structural insight. At 0.9 GPa, the $\nu\text{P-C}$ Raman mode stiffens up to 646 cm^{-1} and the new mode appears at 640 cm^{-1} at this pressure. In the corresponding IR spectra, at 0.8 GPa, the position of $\nu\text{P-C}$ mode is 639 cm^{-1} and the new mode appears at 645 cm^{-1} .

The above observations imply that the principle of mutual exclusion of IR and Raman modes is no more valid at high pressures, *i.e.*, the molecular inversion symmetry is lifted. Thus, at pressures above 0.9 GPa, Raman active modes can be observed in the IR spectra and

vice versa. These modifications/ reorientations in the molecular units may further lead to structural phase transition, which is discussed in the next section.

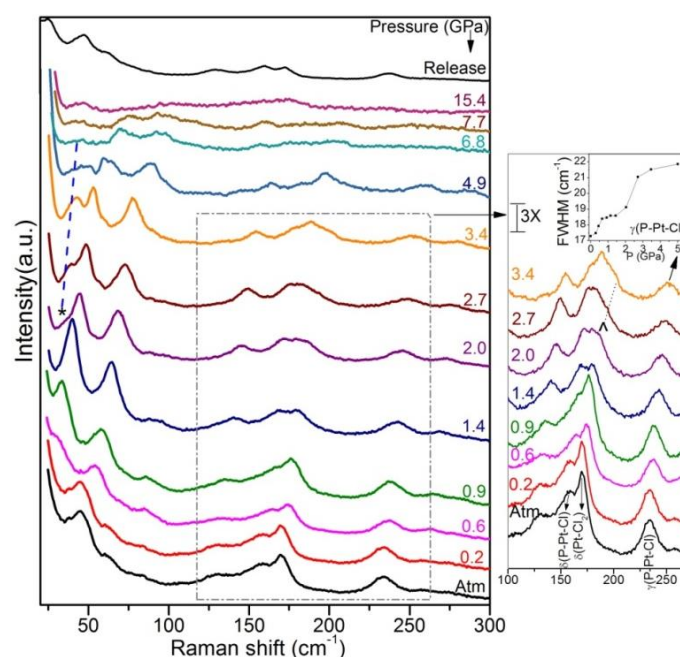


Figure 6.3: High pressure Raman spectra of *trans*-PtCl₂(PEt₃)₂ in the spectral region 20 – 300 cm⁻¹. On the right is 100 – 275 cm⁻¹ region shown with 3X magnification and inset shows the FWHM of γ (P-Pt-Cl) mode. * denotes new peak in the lattice region and ^ denotes new shoulder peak adjacent to δ PtCl₂ mode, which emerge after the phase transition.

The signatures of these molecular reorientations, resulting in the non-equivalence of the two phosphine (P-(CH₂CH₃)₃) ligands on either side of Pt-atom, are clearly visible in the spectral features of organic groups, thus verifying the above inferences. As shown in Figure 6.5 and Figure 6.6b, new modes are found to emerge and the slope of frequency versus pressure plots (Figure 6.7 and Figure 6.8) changes for most of the modes across 0.9 GPa. These changes, observed in the deformation (700 – 1600 cm⁻¹) and stretching (2800 – 3200 cm⁻¹) regions of the organic groups, are listed sequentially in the following two paragraphs.

Among some prominent changes, peak broadening/ appearance of new shoulder peaks

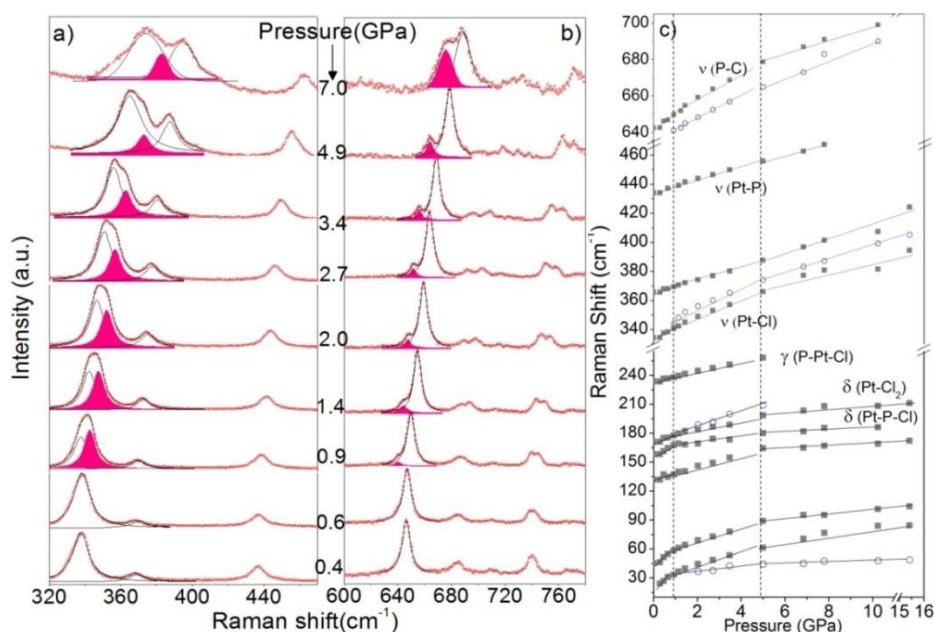


Figure 6.4: High pressure Raman spectra (y-offset) of *trans*-PtCl₂(PEt₃)₂ in the spectral range a) 320-470 cm⁻¹; b) 600-780 cm⁻¹. The new peaks emerged with pressure have been highlighted as guide to the eye. c) Variation of Raman modes in the spectral range 20-700 cm⁻¹, with pressure.

has been noticed in the $\nu(\text{C-C})$, *i.e.*, 1000 cm⁻¹ region above 0.8 GPa. The intensity of C-CH₃ rocking Raman mode at 1047 cm⁻¹ reduces above 0.9 GPa and the mode becomes very weak after 5 GPa (Figure 6.6a). The high pressure trends of Raman active modes in the region 1300 – 1400 cm⁻¹ could not be probed as they are swamped by the strong diamond mode, but the corresponding infrared behavior could be studied. The CH₂ wagging, CH₃ deformation and CH₂ scissoring IR modes at 1257 cm⁻¹, 1375 cm⁻¹ and 1413 cm⁻¹, respectively show stiffening with pressure. This is accompanied with the emergence of new modes adjacent to these modes at 1268 cm⁻¹, 1286 cm⁻¹ and 1404 cm⁻¹ above 0.8 GPa. In fact, nearly all the modes in the fingerprint region are blue shifted upon compression and most of these depict a slope change across 0.8 GPa and ~ 4.9 GPa (Figure 6.7, Figure 6.8 and Figure 6.4c). In 2800 – 3200 cm⁻¹ range, the IR and Raman $\nu_s\text{CH}_3$ modes, depicting a weak shoulder at ambient

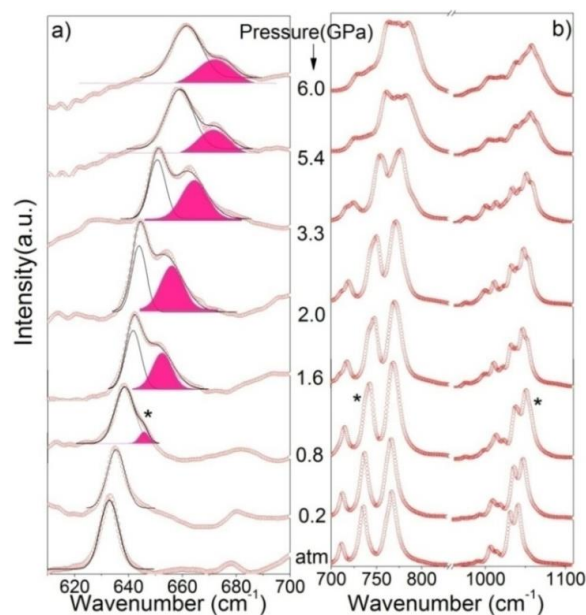


Figure 6.5: High pressure IR spectra (y-offset for clarity) of *trans*-PtCl₂(PEt₃)₂ in the spectral region a) 610-700 cm⁻¹ and b) 700-1100 cm⁻¹. The new peaks emerged with pressure have been marked with asterisk and highlighted as guide to the eye.

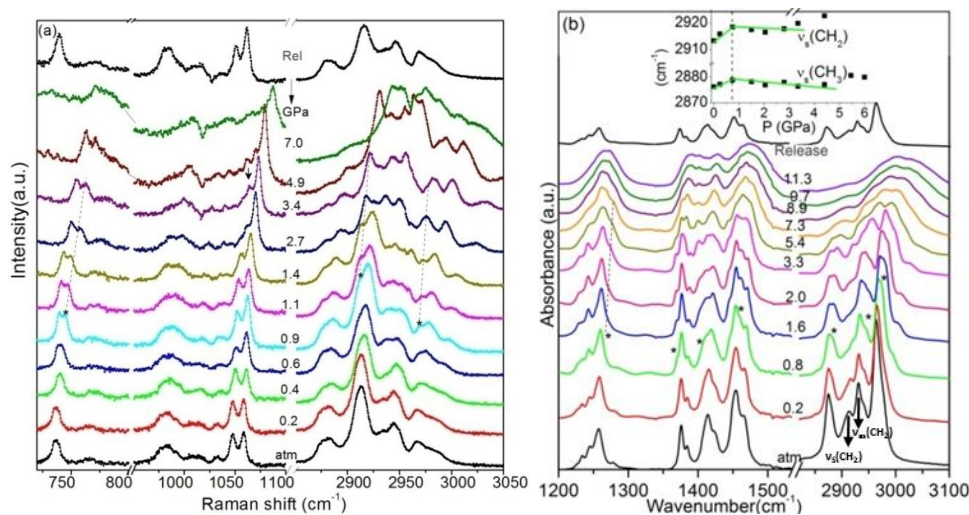


Figure 6.6: High pressure (a) Raman and (b) infrared spectra of *trans*-PtCl₂(PEt₃)₂ in mid-IR region. Inset in (b) shows the peak position of ν_s CH₃ and ν_s CH₂ modes with pressure. The new peaks emerged at high pressure have been marked with *. Down arrow (\downarrow) denotes C-CH₃ rocking mode, which weakens with pressure. Numbers are pressure values in GPa, rel – pressure release. Spectra have been offset for clarity.

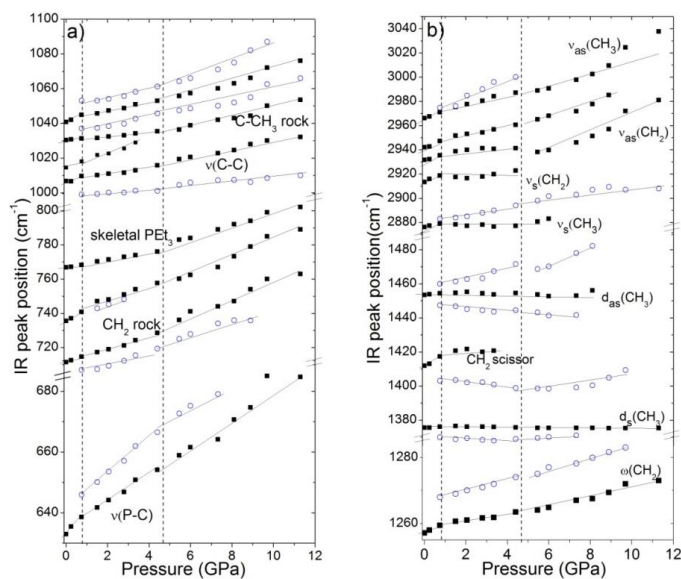


Figure 6.7: (a) Variation of IR peak positions with pressure in *trans*-PtCl₂(PEt₃)₂ in the region (a) 630-1100 cm⁻¹ and (b) 1250-3050 cm⁻¹. Blue open circles represent new peaks emerged across 0.8 GPa.

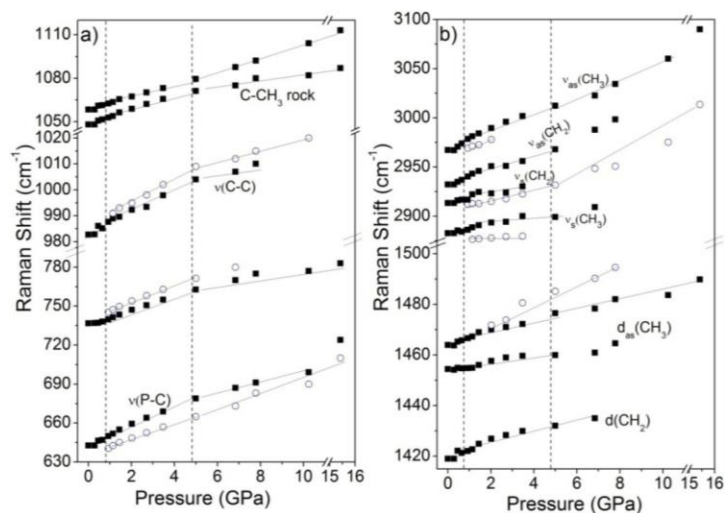


Figure 6.8: Variation of Raman mode positions with pressure in *trans*-PtCl₂(PEt₃)₂ in the spectral range (a) 630-1120 cm⁻¹ (b) 1410-3100 cm⁻¹. The new peaks emerged during high pressure are shown with blue empty circles.

pressure, show two clear peaks above 0.9 GPa (Figure 6.6). New peaks also appear adjacent to the ν_{as}CH₃ modes at high pressures. While the relative intensity of ν_sCH₂ IR mode at 2914

cm⁻¹ decreases with pressure (Figure 6.6b), the intensity of $\nu_{\text{as}}\text{CH}_2$ mode at 2930 cm⁻¹ remains unaffected. Similar changes in intensity are noted for the CH₃ group stretching modes. Such an effect of pressure on the intensity of stretching vibrations in the IR spectra have also been observed in some other square planar coordination complexes like PdCl₂[S(CH₃)₂]₂, PtCl₂[S(CH₃)₂]₂, PtBr₂(NH₃)₂, PtBr₂(TeEt₂)₂ etc., and therefore this can well be a characteristic feature of this class of compounds [304].

6.3.2.2. X-ray diffraction studies:

High pressure x-ray diffraction patterns of *trans*-PtCl₂(PEt₃)₂ have been shown in Figure 6.9 at various representative pressures. The XRD patterns show no qualitative change up to a pressure of 0.8 GPa and therefore these were Rietveld refined up to this pressure using the ambient monoclinic phase (Phase 1) with $P2_1/n$ space group (No. 14) having two formula units per unit cell ($Z=2$). The variations of lattice parameters a , b , c , β and unit cell volume, thus obtained, have been shown in Figure 6.10 and Figure 6.11 respectively, which show that the crystal b -axis (the approximate direction of Pt-P bonds) depicts the least compressibility. The pressure induced variations of lattice parameters have been fitted using Murnaghan equation of state using EOS-Fit7 software. The bulk modulus and first pressure derivative of Phase 1 of *trans*-PtCl₂(PEt₃)₂ have been found to be 5.8(2) GPa and 6.2(1) respectively. As the pressure is increased to 0.8 GPa, a new diffraction peak has been found to emerge at $2\theta \sim 5.9^\circ$, which signifies structural transition at this pressure (Figure 6.9). For $P \geq 0.8$ GPa and up to 4.7 GPa (Phase 2), the diffraction patterns could be better indexed using monoclinic phase with $P2_1$ space group (non – centrosymmetric). The starting model for the refinement of Phase 2 was taken from Phase 1(space group – $P2_1/n$) by transforming the axes and atomic coordinates of Phase 1 using PCW software. Pawley refinement was carried out on the diffraction pattern at 0.8 GPa where diffraction peaks were indexed with monoclinic $P2_1$

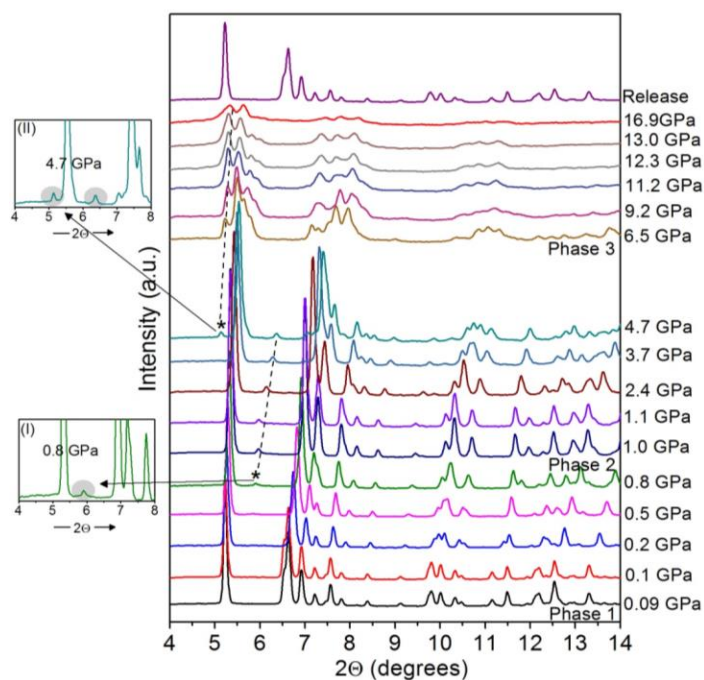


Figure 6.9: High pressure powder XRD patterns of *trans*-PtCl₂(PEt₃)₂. * denotes new peaks emerged in the high pressure phases. The enlarged views in the inset show (I) the new peak at 0.8 GPa (Phase 2); (II) peaks belonging to Phase 2 (around 6°) and Phase 3 (around 5°) at 4.7 GPa.

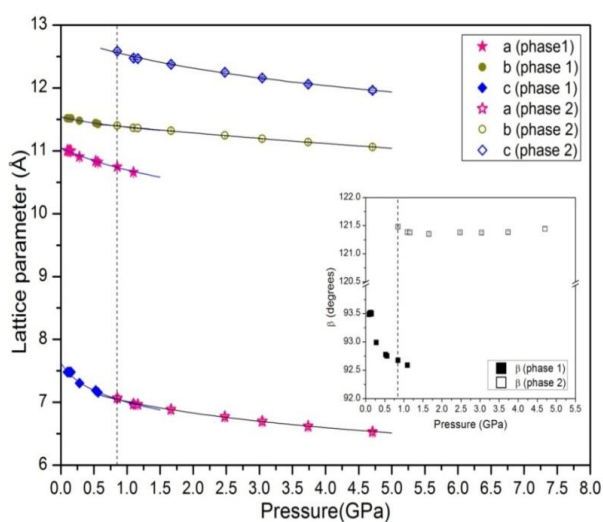


Figure 6.10: Variation of lattice parameters and with pressure in *trans*-PtCl₂(PEt₃)₂. The lattice parameters are fitted with Murnaghan and 3rd order Birch-Murnaghan equation of state in Phase 1 and Phase 2 respectively using EOS-Fit7 software,[305] the error bars are within the symbols. Inset shows the variation of beta angle with pressure.

space group, a subgroup of $P2_1/c$, another setting of initial space group $P2_1/n$. This indicates the occurrence of a group-subgroup type of phase transition across 0.8 GPa.

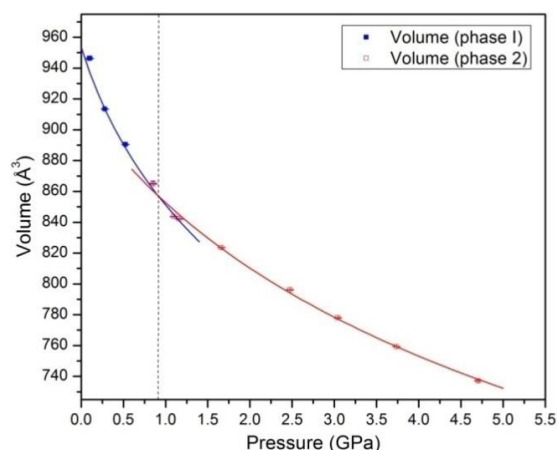


Figure 6.11: Variation of unit cell volume with pressure in *trans*-PtCl₂(PEt₃)₂ fitted with Murnaghan and 3rd order Birch-Murnaghan equation of state in Phase 1 and Phase 2 respectively using EOS-Fit7 software[305], the error bars are within the symbols at all the pressures.

Table 6.3: Projection of the three Principle axes (X1, X2, X3) on crystallographic axes (*a*, *b*, *c*) in *trans*-PtCl₂(PEt₃)₂ derived using PASCAL software[306] with critical point at 0.85 GPa.

Principle axes (Xn)	Compressibility K (TPa ⁻¹)	Error in Compressibility σK (TPa ⁻¹)	Projection of Xn on the unit cell axes		
			<i>a</i>	<i>b</i>	<i>c</i>
Phase 1					
X1	48.8612	4.8884	-0.1425	-0.0000	0.9898
X2	25.9522	2.4928	0.9298	0.0000	0.3681
X3	11.4934	1.0713	0.0000	-1.0000	0.0000
Phase 2					
X1	17.3035	0.4974	0.9919	-0.0000	0.1268
X2	10.6181	0.3504	-0.5115	0.0000	-0.8593
X3	7.3500	0.1454	0.0000	-1.0000	0.0000

Subsequently, structure was solved with rigid body method using Monte Carlo/Simulated Annealing (MC/SA) as implemented in GSAS-II software [295]. Finally, Rietveld refinement was performed on thus obtained structure with restraints on bond lengths and bond angles using GSAS-II, as shown in Figure 6.12.

In order to obtain precise information on fractional coordinates of the lighter atoms such as carbon and hydrogen in Phase 2, the refined structure at 0.8 GPa, obtained from XRD, was used to carry out DFT calculations at the same pressure. Atomic positional relaxations were performed using the conjugate gradient algorithm until the residual forces were of the order of 0.01 eV/Å. Rietveld refinement was again carried out using the relaxed structure obtained from the calculations, which matches with Figure 6.12. The structure of Phase 2, thus obtained has been also been deposited in the Cambridge Crystal Data Centre (CCDC number 1829688). The principle axes evolution with pressure as obtained using PASCAL software [306] have also been plotted in Figure 6.13, where X3 principle axis coincides with the crystallographic *b*-axis, which also shows the least compressibility with pressure as shown in Table 6.3. The obtained lattice parameters imply transformation relation between Phase 1 and Phase 2 as $a \rightarrow c$, $b \rightarrow b$ and $c \rightarrow (-a-c)$ (Figure 6.14). Thus, the lattice parameters at 0.8 GPa are found to be $a = 7.0671(41)$ Å, $b = 11.4004(10)$ Å, $c = 12.585(12)$ Å, $\beta = 121.476(12)^\circ$ and $V = 864.75(23)$ Å³ and their pressure induced variations in this high pressure phase (Figure 6.10 and Figure 6.11) have been fitted using 3rd order Birch-Murnaghan EOS. The values of B_0 and B' in Phase 2 have been obtained as 11.6(9) GPa and 5.3(4) respectively.

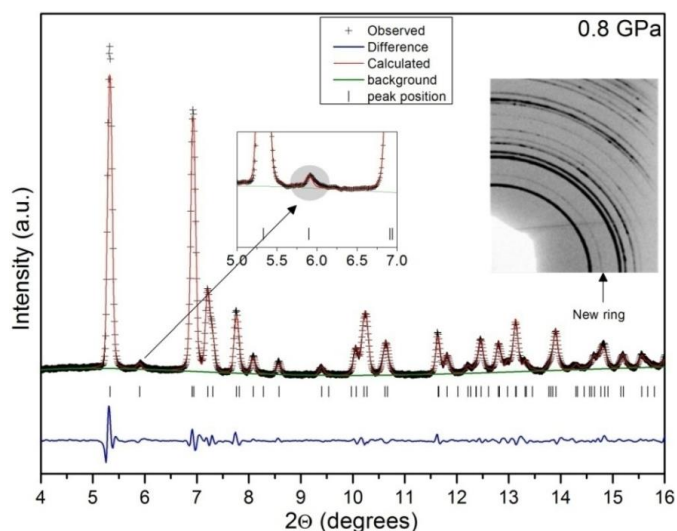


Figure 6.12: Rietveld refinement of *trans*-PtCl₂(PEt₃)₂ at 0.8 GPa inside DAC using GSAS-II. Inset: (Left) Enlarged view of the Rietveld refinement of XRD pattern in the region of appearance of the new peak in Phase 2, (Right) Typical 2D pattern obtained in the new phase above 0.8 GPa.

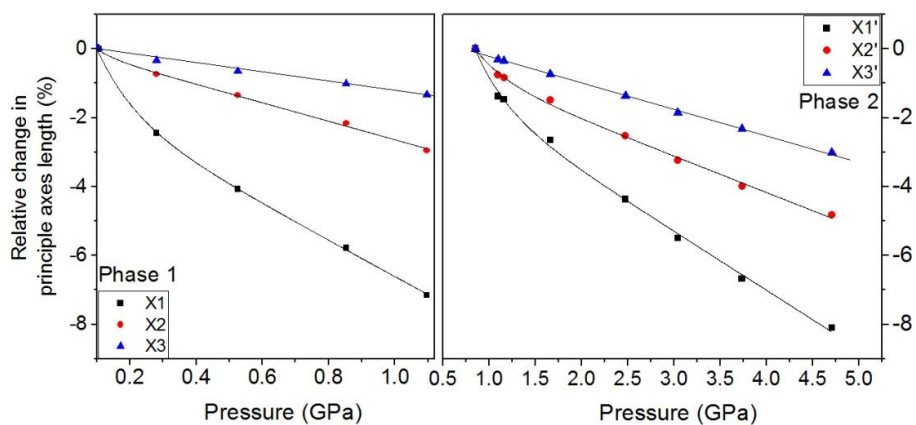


Figure 6.13: Principle axes evolution with pressure in *trans*-PtCl₂(PEt₃)₂ as obtained using the software PASCAL [306]. The axis X3 coincides with the crystallographic *b*-axis, which shows the least compressibility with pressure

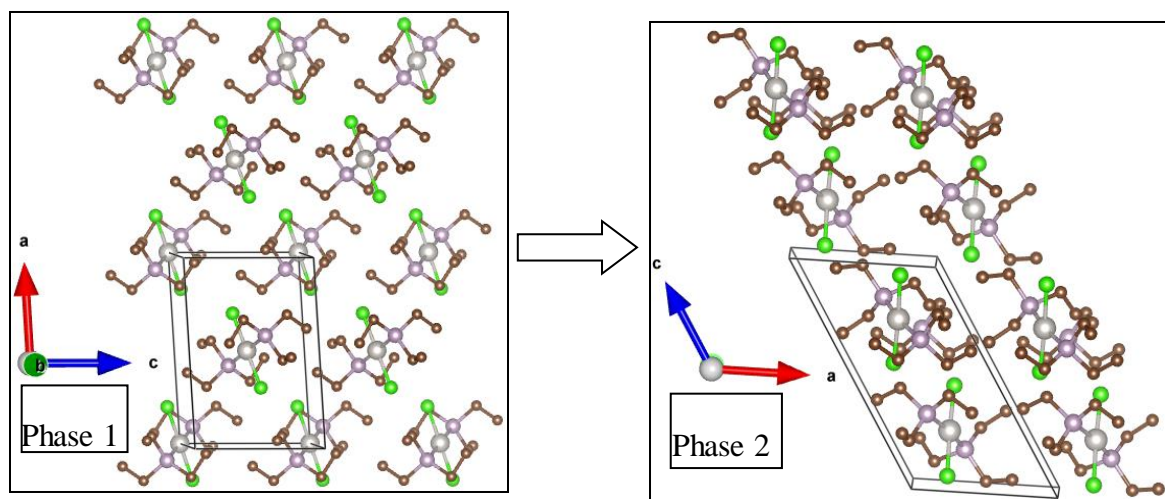


Figure 6.14: Unit cells of Phase 1 (ambient) and Phase 2 (0.8 GPa) in *trans*-PtCl₂(PEt₃)₂.

The features emerged in the second phase vanish at 4.7 GPa and newer peaks (for example at $2\theta \sim 5^\circ$) were found to emerge at this pressure, which suggests another phase transition. This new phase (Phase 3) could be indexed in the same space group, however with a supercell having lattice parameters a and c transformed to thrice and twice of those in Phase 2 respectively. Due to the overlapping of the peaks in the Phase 3, only Le Bail refinement could be carried out (Figure 6.15). Thus, we find $a = 20.1216(8) \text{ \AA}$, $b = 10.8357(7) \text{ \AA}$, $c = 24.1393(5) \text{ \AA}$ and $\beta = 122.46^\circ$ (volume, $V = 4440.89 \text{ \AA}^3$) at 6.5 GPa with this methodology. Based on density considerations, Phase 3 should have at least six formula units in a unit cell. At still higher pressures in Phase 3, the diffraction patterns tend to become complex due to peak broadening, appearance of several new peaks, especially at low 2θ values and splitting in some of the peaks (see Figure 6.9). The profiles of XRD patterns above 9 GPa are predominantly broad and tend to be nearly flat as compared to those at lower pressures. The ambient structure could be retrieved upon the release of pressure.

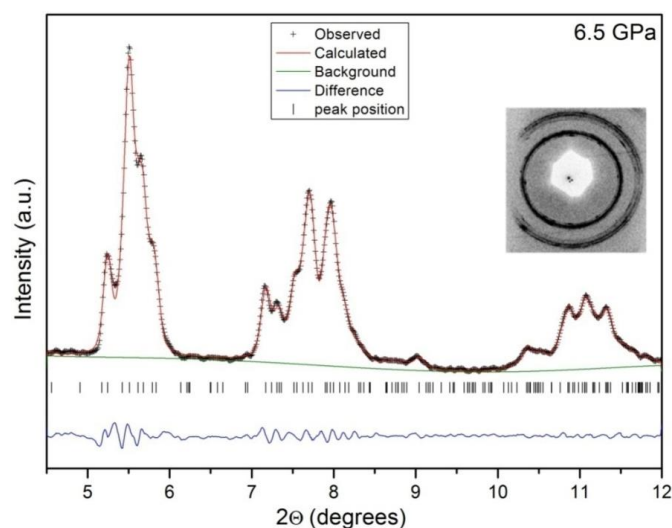


Figure 6.15: Le Bail refinement of Phase 3 of *trans*-PtCl₂(PEt₃)₂ at 6.5 GPa. Inset shows the corresponding 2D pattern.

6.3.3. Molecular arrangement at high pressures

The x-ray diffraction results corroborate well with the observations from spectroscopic studies, *i.e.*, *trans*-PtCl₂(PEt₃)₂ depicts a structural phase transition to a non-centrosymmetric phase above 0.8 GPa. Figure 6.16 show the basic molecular units of PtCl₂L₂ (L = PEt₃ ligand) present in the structures of Phase 1 and Phase 2 respectively, deduced from x-ray diffraction results. Due to the presence of molecular inversion symmetry, at ambient pressure, the Cl atoms are placed diagonally opposite to each other with $\angle\text{Cl-Pt-Cl} = 180^\circ$ and similarly the P atoms. However, subsequent to phase transition, we find $\angle\text{P-Pt-P} = 170.58^\circ$ and $\angle\text{Cl-Pt-Cl} = 176.82^\circ$ in Phase 2. In the PEt₃ ligands, two of the three ethyl groups (connected to a P-atom on one side of Pt) show subtle reorientations to show small dissimilarities in bond lengths and angles with those connected to the other P atom on the symmetrically opposite side of Pt. Noticeably, the reorientational changes observed in the third ethyl group are significantly different on the two sides of the Pt atom. In other words, the C-C entity of this third ethyl group shows significant reorientations preferentially on one side of the central Pt- atom. This

could be verified by monitoring the change in various Pt-P-C-C dihedral angles (Table 6.4). Thus, the changes observed in these ligand orientations are drastic as compared to no appreciable changes in the metal-ligand bond lengths which may lie within the error bars.

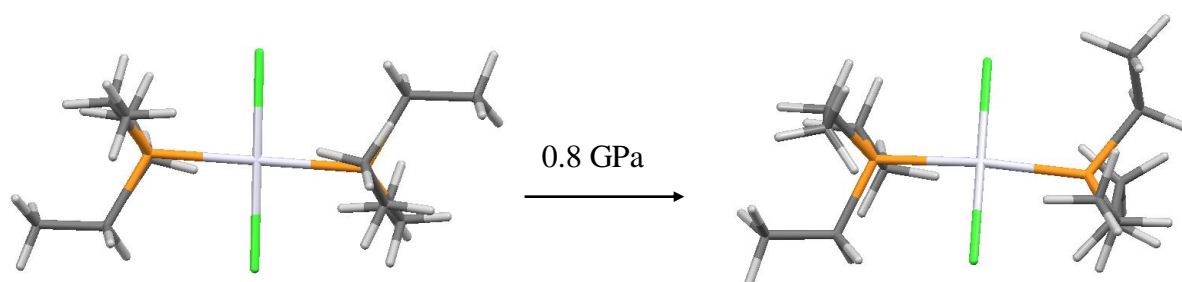


Figure 6.16: Molecular structure of *trans*-PtCl₂(PEt₃)₂ (left) ambient Phase 1: \angle P-Pt-P=180° and \angle Cl-Pt-Cl = 180°. (right) at 0.8 GPa in Phase 2. Molecular reorientations result in \angle P-Pt-P=170.58° and \angle Cl-Pt-Cl=176.82° in Phase 2. (Color, Pt-Silver, Cl-green, Orange-P, Dark grey-C, Light grey-H).

These observations imply the lifting of molecular inversion symmetry, the signatures of which are precisely reflected in the observed changes in IR and Raman vibrational modes, as discussed in previous sections. Note that the two PEt₃ ligands in the *trans*-positions to Pt compete for the same *d*-orbital of Pt atom, which results in lower stability of *trans*- compared to the *cis*- isomer.

Table 6.4: Variation of dihedral angles of the ethyl group attached to phosphorous atoms on the two symmetrically opposite sides of Pt atom in *trans*-PtCl₂(PEt₃)₂ molecule with pressure.

Dihedral Angles of ethyl groups (°)	Ambient pressure		0.8 GPa	
	One side	Other side	One side	Other side
Pt-P-C1-C4	52.67°	52.67°	62.42°	56.23°
Pt-P-C2-C5	63.81°	63.81°	62.89°	81.90°
Pt-P-C3-C6	170.95°	170.95°	160.59°	57.64°

Thus, the molecular reorientations leading to non-equivalent PEt₃ entities would imply

different π -back bonding on the two opposite sides of Pt-atom. This implies that pressure can be a useful tool for tuning π -back bonding properties, which is a subject of interest for catalysis and phase transformation applications.

Another interesting effect of pressure is the strengthening of weakly interacting forces, which arise due to shortening of non-bonded atomic distances as a result of molecular reorientations. At ambient conditions, the shortest Cl---H distances are: i) intramolecular – C3-H---Cl with Cl---H = 2.719 Å, C---Cl = 3.328 Å and $\angle\text{CHCl} = 114.37^\circ$; ii) intermolecular – C6-H---Cl with Cl---H = 2.657 Å, C---Cl = 3.684 Å and $\angle\text{CHCl} = 155.66^\circ$. Subsequent to phase transition, because of reorientations in molecular geometries, *viz.*, chlorine and phosphine ligands, the shortest distances between non-bonded atoms are also modified. In Phase 2, there are as many as three hydrogen bonds for which the Cl---H distances become less than 2.6 Å, thus forming moderate and strong hydrogen bonds as shown in Figure 6.17(left). These C-H---Cl hydrogen bonds are (at 0.8 GPa): i) intermolecular with Cl---H = 2.465 Å, C---Cl = 3.339 Å and $\angle\text{CHCl} = 135.73^\circ$, ii) intermolecular with Cl---H = 2.568 Å, C---Cl = 3.64311 Å and $\angle\text{CHCl} = 164.47^\circ$ and iii) intramolecular with Cl---H = 2.531 Å, C---Cl = 3.287 Å and $\angle\text{CHCl} = 125.06^\circ$. Note that the sum of van der Waals radii for hydrogen and chlorine atoms equals 2.95 Å and the criterion adopted to characterize long, intermediate and short hydrogen bonds is reported as H---Cl ≥ 2.95 , 2.52 – 2.95 and ≤ 2.52 Å respectively [307-309].

The spectroscopic signatures of ethyl groups indeed support the formation of stronger hydrogen bonds in Phase 2. As shown in the inset of Figure 6.6b, the CH₃ (2876 cm⁻¹) and CH₂ (2913 cm⁻¹) stretching vibrational modes cease to stiffen (even depicting a small softening) in the high pressure phase. The formation of such a hydrogen bonded structure in *trans*-PtCl₂(PEt₃)₂ has been shown in Figure 6.17(right), which is similar to the stitched stair-

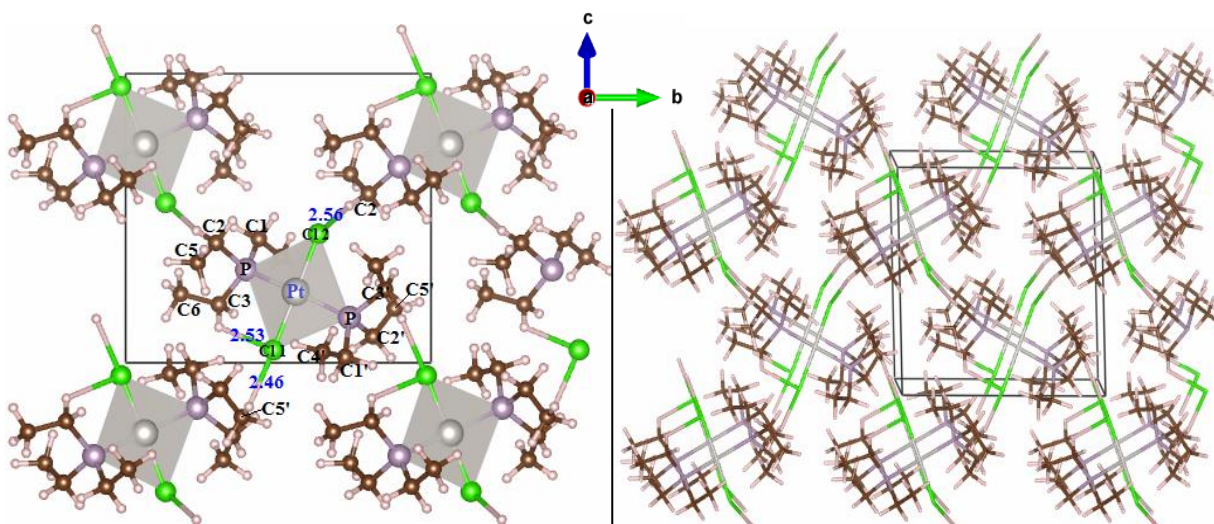


Figure 6.17: (left) Hydrogen bonds in the structure of *trans*-PtCl₂(PEt₃)₂ at high pressures. Atom colours: Grey- Pt, Green – Cl, Purple – P, Brown – C, Pink – H. H-bonds are shown by green-pink bicolour lines. The three H-bonds are: i) intramolecular – Cl1---H-C3, nearly along the *b*-axis, ii) intermolecular – Cl2---H-C2 nearly in the *bc*-plane and iii) intermolecular – Cl1---H-C5' which connects two molecules lying in two adjacent *bc*-planes forming the three-dimensional network. Numbers are Cl---H distances in Å. (right) the extended three dimensional wire-frame structure plotted through slightly tilted *a*-axis showing the hydrogen bonded network, mimicking a possible stair-case type supramolecular assembly.

case structure observed for the supramolecular synthon *trans*-octahedral [(L¹)₂CoCl₂].4H₂O, where the H---Cl distance corresponding to the C-H---Cl hydrogen bond lies in the range 2.4–2.8 Å [281]. These inferences are also supported by pronounced broadening in the C-H stretching regions of IR and Raman spectra (Figure 6.6). In addition, the broad signatures in the XRD patterns at higher pressures may also be the result of these structural changes. It is noteworthy that the C-H---Cl hydrogen bonds play important role in the applications concerning molecular recognition processes [310] and crystal engineering [155] as these directional forces control the size of molecular assemblies [157, 311]. Such studies on weak interactions between organic and non-organic systems may also be helpful in predicting the complexation behavior of simple organic moieties under extreme geophysical conditions [106, 199, 312, 313].

6.3.4. High pressure behavior of metal-organic complexes

As far as high pressure studies on Pt(II) complexes is concerned, a strong pressure dependence of luminescence properties have been observed which are linked to change in closely lying Pt-Pt distances leading to destabilization of molecular orbitals and even an insulator to metallic transition [36-40]. However, compounds with large Pt-Pt distances have also shown a change in such properties, which is predicted to be due to the interactions with organic ligands [39, 288, 314]. The studies on trigonal pyramidal (MX₃), square planar/tetrahedral (MX₂Y₂), and trigonal bipyramidal (MX₂Y₃) ~~etc.~~ complexes, where M=Pt, Pd, Co, Zn; X=halogen and Y=ligand like S(CH₃)₂, (C₇H₈), (C₆H₇N)₂ ~~etc.~~ (other than halogen), have primarily concentrated on the change in relative intensity of symmetric and asymmetric metal-halogen vibrational modes [315, 316]. In yet another Pt-complex, PtCl₂([9]aneS₃), a phase transition to a polymer chain was observed at 4.2 GPa [317]. Thus, the present studies provide evidences of molecular structure, *i.e.*, metal-ligand bonding and ligand orientations, playing a crucial role in local as well as overall structure determination which can be probed by a concerted treatment of spectroscopic and diffraction studies.

The studies carried out on other metal-coordination complexes (metal – Cu, Ni, Fe, Pd etc.) have revealed that pressure tuning may offer significant modifications in some favoured interactions [289, 318-322]. For example, the Pd(II) compound PdCl₂(1,4,7-trithiacyclononane) shows a phase transition at 4.6 GPa to form a one-dimensional chain [323], whereas the Co(II) compound [Co(NH₃)₅NO₂]Cl shows anisotropic distortion under pressure leading to selective rotation of one NH₃ unit to form N-H---Cl and N-H---O hydrogen bonds [15, 53, 324, 325]. Among some other compounds, Ru₃(CO)₁₂ exhibits the properties of soft solids with a bulk modulus of only 6.6 GPa [297], whereas the organic salt of [SbCl₅]_n²ⁿ⁻ shows significant contraction in an intermolecular Sb---Cl hydrogen bond at pressures as low as 0.55 GPa and the doubling of crystal *a*-axis at 1 GPa [326-330].

Thus, the extreme sensitivity of the molecular structure triggering various changes in *trans*-PtCl₂(PEt₃)₂ under pressure demonstrates the use of thermodynamic parameters to tune the Pt-ligand interactions and the hydrogen bonding motifs between different molecular units, without the introduction of a foreign element into the structure. Such studies can be exploited to study other technologically and biologically important compounds in this class, where stereo-isomerism plays important role in the physical and chemical properties.

6.4. Summary

To summarize, *trans*-PtCl₂(PEt₃)₂ has been studied under high pressure using infrared and Raman spectroscopic techniques combined with x-ray diffraction studies, which have also been corroborated with first principles DFT calculations. The XRD studies provide evidences of pressure induced phase transition in *trans*-PtCl₂(PEt₃)₂ at 0.8 GPa, where the space group changes from *P2₁/n* to *P2₁*, implying a non-centrosymmetric high pressure phase. Splitting of various skeletal and ligand stretching modes and the emergence of IR active modes in the Raman spectra and vice versa also point to the loss of molecular inversion symmetry at ~ 0.8 GPa. This may result in diverse interactions between metal atom and P-C ligands on either side of Pt. The pressure induced reorientation of ethyl groups of the ligand brings them in close proximity with the nearby chlorine atoms, thus forming inter- and intra-molecular C-H...Cl hydrogen bonded supramolecular network. Upon further compression, another phase transition has been indicated at pressures above 4.7 GPa. All the changes are found to be reversible upon the release of pressure. These results show that any changes in molecular orientation/ π -back bonding and weak inter-molecular interactions affect the three dimensional network and stereo-electronic properties, which consequently would influence the vast range of applications of Pt(II) complexes.

Chapter 7: Summary and Conclusions

7.1. Summary

The organic molecular solids have several applications ranging from technology to biochemical processes. These applications are governed by the microscopic properties like interatomic distances, electronic cloud distributions, intermolecular interactions, and molecular conformational flexibility of different molecular units within a structure, which makes them an interesting subject of study. Their applications can be enhanced/ optimized by varying the thermodynamic parameters such as pressure, temperature etc.

In this thesis, the role of re-orientations of different molecular moieties for structural stabilization and tuning of weak interactions like hydrogen bonding in controlling the phase behavior of organic molecular solids under varying thermodynamic conditions of high pressure/ low temperature has been investigated. The materials under investigation have been classified into two classes. First category of systems is amino acids, *viz.*, α -glycine, deuterated α -glycine and L-Leucine in the solid form. In the second category, the metal-organic coordination complex *trans*-dichloro bis(triethylphosphine) platinum(II) (*trans*-PtCl₂(PEt₃)₂) has been studied.

7.2. Conclusions

Systematic studies on the simplest and the most fundamental amino acid, glycine and its deuterated analogue under low temperature conditions using vibrational spectroscopic techniques have been carried out. A perceptible isotopic effect has been observed in the 3D-hydrogen bonded framework of α -glycine upon cooling. The primary effect responsible for this effect is the varied response of NH₃ and ND₃ torsional modes, resulting in diverse effect on their respective hydrogen bonding networks upto 180 K. Below this temperature, similar qualitative trends have been noticed on the effect of temperature on hydrogen bonds for the

two isotopes. This causes the formation of a stronger 3-dimensional bilayered assembly of glycine molecules in the hydrogenated α -glycine, whereas relatively stable 2-dimensional layered structure forming strong hydrogen bonded sheets in the *ac*-plane have been observed in the deuterated α -glycine.

Upon increasing the chain of the hydrocarbons in amino acids, flexibility of molecular moieties/ fragments plays a crucial role in depicting structural response to varying environments. In this regard, a complex amino acid, L-Leucine having a hydrophobic branched chain has been studied at variable temperatures using infrared spectroscopy. This study throws light on the importance of re-orientations in different molecular fragments, which may even result in phase transitions. The changes around 240 K have been associated with the orientational changes in the amino groups (NH_3 moieties). This transition causes strengthening of the hydrogen bonds in the *ac*-plane forming 2-D sheets, well separated from each other in the *b*-direction. The second transition around 150 K was found to be associated with the orientational changes in the hydrophobic chain which were depicted by a drastic change in the FWHM of torsional vibrations of (C_3C_4) group. The studies will be helpful in settling the long standing debates on the possibility of temperature induced phase transitions in L-Leucine.

Another class of molecular organic solids include metal-organic complexes. The compound *trans*-dichloro bis(triethylphosphine) platinum (II) [formula:*trans*- $\text{PtCl}_2(\text{PEt}_3)_2$] has been studied in this class under varying thermodynamic conditions of low temperature and high pressure. This complex has phosphine triethyl groups attached to the metal centre. The re-orientation of these triethyl chains play an important role in triggering the phase transitions in this complex upon changing the thermodynamic parameters. Upon cooling *trans*- $\text{PtCl}_2(\text{PEt}_3)_2$, the orientational changes of the phosphine triethyl ligands causes preferred strengthening of the C-H---Cl hydrogen bonds through CH_3 units, in the temperature range 180-130 K. The drastic change in the intensity, appearance of new modes in the lattice region, and slope

change of many vibrational modes across 180 K and 130 K are the signatures of phase transition.

Temperature and pressure are the thermodynamic variables which cause reduction in the volume of the material under consideration, but the origin of phase transitions under such conditions may be different or similar. Our detailed high pressure studies on the same metal-organic complex, *trans*-dichloro bis(triethylphosphine) platinum (II), showed phase transition from centrosymmetric to non-centrosymmetric structure (space group changes from $P2_1/n$ to $P2_1$) at a pressure of about 0.8 GPa. Combined investigations using vibrational spectroscopy [IR and Raman] and XRD studies well corroborated with DFT calculations confirmed this phase transition. Importantly, the study highlighted that the orientational changes of a specific phosphine-organic ligand group lead to the structural phase transition in this compound. Another phase transition was observed upon further compression upto ~ 4.7 GPa, forming a supercell above this pressure. These orientational changes bring phosphine ligands in close proximity of Cl atoms of the adjacent molecules, which cause overall strengthening of inter- and intra-molecular C-H...Cl hydrogen bonds, resulting in a stitched staircase hydrogen bond assisted supramolecular assembly in the high pressure phase. It is noteworthy that the nature of pressure and temperature induced phase transitions in *trans*-PtCl₂(PEt₃)₂ is different, since no signatures of loss of inversion symmetry were noticed at low temperatures.

We hope that the case studies presented in this thesis pave the way towards better understanding of fundamental systems like glycine, framing a general trend of hydrogen bonding networks in amino acids under varying conditions and utilization of thermodynamic parameters as well as molecular motions to harness the properties of technologically important organic systems, other macro-molecular systems such as proteins and for their molecular modelling.

References

- (1).Boldyreva, E. V., High-pressure studies of the hydrogen bond networks in molecular crystals. *Journal of molecular structure* **2004**, *700*, 151-155.
- (2).Boldyreva, E. V.; Ivashetskaya, S. N.; Sowa, H.; Ahsbahs, H.; Weber, H.-P., Effect of hydrostatic pressure on the γ -polymorph of glycine. 1. A polymorphic transition into a new δ -form. *Zeitschrift für Kristallographie-Crystalline Materials* **2005**, *220*, 50-57.
- (3).Shakhtshneider, T.; Boldyreva, E.; Vasilchenko, M.; Ahsbahs, H.; Uchtmann, H., Anisotropy of crystal structure distortion in organic molecular crystals of drugs induced by hydrostatic compression. *Journal of Structural Chemistry* **1999**, *40*, 892-898.
- (4).Boldyreva, E.; Boldyrev, V., *Reactivity of molecular solids*. Wiley: 1999; Vol. 3.
- (5).Wilson, C., Variable temperature study of the crystal structure of paracetamol (p-hydroxyacetanilide), by single crystal neutron diffraction. *Zeitschrift für Kristallographie-Crystalline Materials* **2000**, *215*, 693-701.
- (6).Boldyreva, E.; Shakhtshneider, T.; Ahsbahs, H.; Sowa, H.; Uchtmann, H., Effect of high pressure on the polymorphs of paracetamol. *Journal of thermal analysis and calorimetry* **2002**, *68*, 437-452.
- (7).Rodríguez-Spong, B.; Price, C. P.; Jayasankar, A.; Matzger, A. J.; Rodríguez-Hornedo, N. r., General principles of pharmaceutical solid polymorphism: A supramolecular perspective. *Advanced drug delivery reviews* **2004**, *56*, 241-274.
- (8).Schultheiss, N.; Newman, A., Pharmaceutical cocrystals and their physicochemical properties. *Crystal growth and design* **2009**, *9*, 2950-2967.
- (9).Walz, J.; Ulrich, K.; Port, H.; Wolf, H. C.; Wonner, J.; Effenberger, F., Fulgides as switches for intramolecular energy transfer. *Chemical physics letters* **1993**, *213*, 321-324.
- (10).Gilat, S. L.; Kawai, S. H.; Lehn, J. M., Light-triggered molecular devices: Photochemical switching of optical and electrochemical properties in molecular wire type diarylethene species. *Chemistry—A European Journal* **1995**, *1*, 275-284.
- (11).Kawai, S. H.; Gilat, S. L.; Ponsinet, R.; Lehn, J. M., A dual-mode molecular switching device: Bisphenolic diarylethenes with integrated photochromic and electrochromic properties. *Chemistry—A European Journal* **1995**, *1*, 285-293.
- (12).Irie, M., Diarylethenes for memories and switches. *Chemical Reviews* **2000**, *100*, 1685-1716.
- (13).Boldyreva, E.; Ahsbahs, H.; Weber, H.-P., A comparative study of pressure-induced lattice strain of α - and γ -polymorphs of glycine. *Zeitschrift für Kristallographie-Crystalline Materials* **2003**, *218*, 231-236.

- (14).Boldyreva, E., Molecules in strained environment. In *High-pressure crystallography*, Springer: 2004; pp 495-512.
- (15).Boldyreva, E. V., High-pressure-induced structural changes in molecular crystals preserving the space group symmetry: Anisotropic distortion/isosymmetric polymorphism. *Crystal engineering* **2003**, *6*, 235-254.
- (16).Aravindan, A.; Srinivasan, P.; Vijayan, N.; Gopalakrishnan, R.; Ramasamy, P., A comparative study on the growth and characterization of nonlinear optical amino acid crystals: L-alanine (la) and L-alanine alaninium nitrate (laan). *Spectrochimica Acta Part A: Molecular and Biomolecular Spectroscopy* **2008**, *71*, 297-304.
- (17).Ramasamy, G.; Meenakshisundaram, S., Studies on amino acid picrates: Crystal growth, structure and characterization of a new nonlinear optical material L-isoleucinium picrate. *Optik-International Journal for Light and Electron Optics* **2014**, *125*, 4422-4426.
- (18).Vijayan, N.; Rajasekaran, S.; Bhagavannarayana, G.; Ramesh Babu, R.; Gopalakrishnan, R.; Palanichamy, M.; Ramasamy, P., Growth and characterization of nonlinear optical amino acid single crystal: L-alanine. *Crystal growth & design* **2006**, *6*, 2441-2445.
- (19).Boldyreva, E., High pressure and supramolecular systems. *Russian chemical bulletin* **2004**, *53*, 1369-1378.
- (20).Peterson, E.; Horz, F.; Chang, S., Modification of amino acids at shock pressures of 3.5 to 32 gpa. *Geochimica et cosmochimica acta* **1997**, *61*, 3937-3950.
- (21).Boldyreva, E., Combined x-ray diffraction and raman spectroscopy studies of phase transitions in crystalline amino acids at low temperatures and high pressures: Selected examples. *Phase Transitions* **2009**, *82*, 303-321.
- (22).Ringe, D.; Petsko, G. A., The 'glass transition' in protein dynamics: What it is, why it occurs, and how to exploit it. *Biophysical Chemistry* **2003**, *105*, 667-680.
- (23).ZAvodszky, P.; Kardos, J.; Svingor, Á.; Petsko, G. A., Adjustment of conformational flexibility is a key event in the thermal adaptation of proteins. *Proceedings of the National Academy of Sciences* **1998**, *95*, 7406-7411.
- (24).Ruano, D.; Díaz-García, M.; Alfayate, A.; Sánchez-Sánchez, M., Nanocrystalline m-mof-74 as heterogeneous catalysts in the oxidation of cyclohexene: Correlation of the activity and redox potential. *ChemCatChem* **2015**, *7*, 674-681.
- (25).Allan, P. K.; Wheatley, P. S.; Aldous, D.; Mohideen, M. I.; Tang, C.; Hriljac, J. A.; Megson, I. L.; Chapman, K. W.; De Weireld, G.; Vaesen, S., Metal-organic frameworks for the storage and delivery of biologically active hydrogen sulfide. *Dalton Transactions* **2012**, *41*, 4060-4066.
- (26).Cattaneo, D.; Warrender, S. J.; Duncan, M. J.; Castledine, R.; Parkinson, N.; Haley, I.; Morris, R. E., Water based scale-up of cpo-27 synthesis for nitric oxide delivery. *Dalton Transactions* **2016**, *45*, 618-629.

- (27).Chavan, S.; Bonino, F.; Valenzano, L.; Civalleri, B.; Lamberti, C.; Acerbi, N.; Cavka, J. H.; Leistner, M.; Bordiga, S., Fundamental aspects of h₂s adsorption on cpo-27-ni. *The Journal of Physical Chemistry C* **2013**, *117*, 15615-15622.
- (28).Chavan, S.; Vitillo, J. G.; Groppo, E.; Bonino, F.; Lamberti, C.; Dietzel, P. D.; Bordiga, S., Co adsorption on cpo-27-ni coordination polymer: Spectroscopic features and interaction energy. *The Journal of Physical Chemistry C* **2009**, *113*, 3292-3299.
- (29).Dietzel, P. D.; Panella, B.; Hirscher, M.; Blom, R.; Fjellvåg, H., Hydrogen adsorption in a nickel based coordination polymer with open metal sites in the cylindrical cavities of the desolvated framework. *Chemical Communications* **2006**, 959-961.
- (30).Glover, T. G.; Peterson, G. W.; Schindler, B. J.; Britt, D.; Yaghi, O., Mof-74 building unit has a direct impact on toxic gas adsorption. *Chemical Engineering Science* **2011**, *66*, 163-170.
- (31).McKinlay, A.; Eubank, J.; Wuttke, S.; Xiao, B.; Wheatley, P.; Bazin, P.; Lavalley, J.-C.; Daturi, M.; Vimont, A.; De Weireld, G., Nitric oxide adsorption and delivery in flexible mil-88 (fe) metal-organic frameworks. *Chemistry of Materials* **2013**, *25*, 1592-1599.
- (32).McKinlay, A. C.; Allan, P. K.; Renouf, C. L.; Duncan, M. J.; Wheatley, P. S.; Warrender, S. J.; Dawson, D.; Ashbrook, S. E.; Gil, B.; Marszalek, B., Multirate delivery of multiple therapeutic agents from metal-organic frameworks. *APL Materials* **2014**, *2*, 124108.
- (33).Hinks, N. J.; McKinlay, A. C.; Xiao, B.; Wheatley, P. S.; Morris, R. E., Metal organic frameworks as no delivery materials for biological applications. *Microporous and Mesoporous Materials* **2010**, *129*, 330-334.
- (34).Miller, S. R.; Alvarez, E.; Fradcourt, L.; Devic, T.; Wuttke, S.; Wheatley, P. S.; Steunou, N.; Bonhomme, C.; Gervais, C.; Laurencin, D., A rare example of a porous ca-mof for the controlled release of biologically active no. *Chemical Communications* **2013**, *49*, 7773-7775.
- (35).Rojas, S.; Wheatley, P. S.; Quartapelle-Procopio, E.; Gil, B.; Marszalek, B.; Morris, R. E.; Barea, E., Metal-organic frameworks as potential multi-carriers of drugs. *CrystEngComm* **2013**, *15*, 9364-9367.
- (36).Wenger, O. S.; García-Revilla, S.; Güdel, H. U.; Gray, H. B.; Valiente, R., Pressure dependence of pt (2, 2'-bipyridine) cl₂ luminescence. The red complex converts to a yellow form at 17.5 kbar. *Chemical physics letters* **2004**, *384*, 190-192.
- (37).Takeda, K.; Shirotani, I.; Yakushi, K., Pressure-induced insulator-to-metal-to-insulator transitions in one-dimensional bis (dimethylglyoximato) platinum (ii), pt (dmg) 2. *Chemistry of materials* **2000**, *12*, 912-916.
- (38).Shirotani, I.; Inagaki, Y.; Utsumi, W.; Yagi, T., Pressure-sensitive absorption spectra of thin films of bis (diphenylglyoximato) platinum (ii), pt (dpg) 2: Potential application as an indicator of pressure. *Journal of Materials Chemistry* **1991**, *1*, 1041-1043.
- (39).Yersin, H.; Riedl, U., Extreme pressure-induced shifts of emission energies in m[au(cn)₂] and m₂[pt(cn)₄]... Nh₂o. Compounds with low-dimensional and metal-metal interactions. *Inorganic Chemistry* **1995**, *34*, 1642-1645.

- (40).Pelletier, Y.; Reber, C., Luminescence spectroscopy and emitting-state properties of pd (scn) 42-in crystals. *Inorganic Chemistry* **2000**, *39*, 4535-4541.
- (41).Ehrenfest, P., Leiden comm. Suppl. No. 75b: 1933.
- (42).Buerger, M., A new approach to crystal-structure analysis. *Acta Crystallographica* **1951**, *4*, 531-544.
- (43).Choudhury, R. R.; Poswal, H.; Chitra, R.; Sharma, S. M., Pressure induced structural phase transition in triglycine sulfate and triglycine selenate. *The Journal of chemical physics* **2007**, *127*, 154712.
- (44).Boldyreva, E. V.; Kolesnik, E. N.; Drebuschak, T. N.; Ahsbahs, H.; Beukes, J. A.; Weber, H.-P., A comparative study of the anisotropy of lattice strain induced in the crystals of l-serine by cooling down to 100 k or by increasing pressure up to 4.4 gpa. *Zeitschrift für Kristallographie-Crystalline Materials* **2005**, *220*, 58-65.
- (45).Boldyreva, E. V.; Kolesnik, E. N.; Drebuschak, T. N.; Sowa, H.; Ahsbahs, H.; Seryotkin, Y. V., A comparative study of the anisotropy of lattice strain induced in the crystals of dl-serine by cooling down to 100 k, or by increasing pressure up to 8.6 gpa. A comparison with l-serine. *Zeitschrift für Kristallographie-Crystalline Materials* **2006**, *221*, 150-161.
- (46).Krishnan, R.; Srinivasan, R.; Devanarayanan, S., Thermal expansion of crystals. Oxford: 1979.
- (47).Hazen, R. M.; Finger, L. W., *Comparative crystal chemistry: Temperature, pressure, composition and the variation of crystal structure*. J. Wiley: 1982.
- (48).Batsanov, S., Fizicheskie metody [sledovaniya neorganicheskikh materialov (physical methods in inorganic material science). Moscow: Nauka: 1981.
- (49).Ledbetter, H., Thermal expansion and elastic constants. *International Journal of Thermophysics* **1991**, *12*, 637-642.
- (50).Boldyreva, E. V., High-pressure studies of the anisotropy of structural distortion of molecular crystals. *Journal of Molecular Structure* **2003**, *647*, 159-179.
- (51).Boldyreva, E.; Shakhtshneider, T.; Vasilchenko, M.; Ahsbahs, H.; Uchtmann, H., Anisotropic crystal structure distortion of the monoclinic polymorph of acetaminophen at high hydrostatic pressures. *Acta Crystallographica Section B: Structural Science* **2000**, *56*, 299-309.
- (52).Boldyreva, E.; Shakhtshneider, T.; Ahsbahs, H.; Sowa, H.; Uchtmann, H., Effect of pressure on the crystals of sodium oxalate: Anisotropic structural distortion and a polymorphic transition. *Russian J. Struct. Chem* **2002**, *43*, 107-113.
- (53).Boldyreva, E. V.; Ahsbahs, H.; Naumov, D. Y.; Kutoglu, A., Pentaamminenitrocobalt (iii) dichloride at pressures of 0.24, 0.52, 1.25, 1.91 and 3.38 gpa. *Acta Crystallographica Section C: Crystal Structure Communications* **1998**, *54*, 1378-1383.

- (54).Boldyreva, E. V.; Ahsbahs, H.; Uchtmann, H.; Kashcheeva, N., Effects of pressure on the two polymorphs of [co (nh₃) 5no₂] i₂: The anisotropy of lattice distortion and a phase transition. *International Journal of High Pressure Research* **2000**, *17*, 79-99.
- (55).Boldyreva, E.; Kivikoski, J.; Howard, J. A., Distortion of crystal structures of some coiii ammine complexes. Ii. Distortion of crystal structures of [co (nh₃) 5no₂] x₂ (x= cl, br) on cooling. *Acta Crystallographica Section B* **1997**, *53*, 405-414.
- (56).Petrenko, V. F.; Whitworth, R. W., *Physics of ice*. OUP Oxford: 1999.
- (57).Boldyreva, E. V.; Naumov, D. Y.; Ahsbahs, H., Distortion of crystal structures of some coiii ammine complexes. Iii. Distortion of crystal structure of [co (nh₃) 5no₂] cl₂ at hydrostatic pressures up to 3.5 gpa. *Acta Crystallographica Section B* **1998**, *54*, 798-808.
- (58).Dunitz, J. D., Weak intermolecular interactions in solids and liquids. *Molecular Crystals and Liquid Crystals Science and Technology. Section A. Molecular Crystals and Liquid Crystals* **1996**, *279*, 209-218.
- (59).Krishnan, R.; Krishnan, K. In *Influence of the hydrogen bond on the nh stretching frequencies in amino-acids*, Proceedings of the Indian Academy of Sciences-Section A, Springer: 1964; pp 11-19.
- (60).Rozenberg, M.; Loewenschuss, A.; Marcus, Y., An empirical correlation between stretching vibration redshift and hydrogen bond length. *Physical Chemistry Chemical Physics* **2000**, *2*, 2699-2702.
- (61).Nakamoto, K.; Margoshes, M.; Rundle, R., Stretching frequencies as a function of distances in hydrogen bonds. *Journal of the American Chemical Society* **1955**, *77*, 6480-6486.
- (62).Pimentel, G. C.; Sederholm, C. H., Correlation of infrared stretching frequencies and hydrogen bond distances in crystals. *The Journal of Chemical Physics* **1956**, *24*, 639-641.
- (63).Fuller, W., Hydrogen bond lengths and angles observed in crystals. *The Journal of Physical Chemistry* **1959**, *63*, 1705-1717.
- (64).Edsall, J. T.; Scheinberg, H., Raman spectra of amino acids and related compounds v. Deuterium substitution in the amino group. *The Journal of Chemical Physics* **1940**, *8*, 520-525.
- (65).Boldyreva, E. V., High-pressure studies of crystalline amino acids and simple peptides. *High Pressure Bioscience and Biotechnology* **2007**, *1*, 28-46.
- (66).Katrusiak, A., High-pressure x-ray diffraction studies of organic crystals. *High Pressure Science and Technology* **1990**, *4*, 496-498.
- (67).Katrusiak, A., High-pressure x-ray diffraction studies on organic crystals. *Crystal Research and technology* **1991**, *26*, 523-531.
- (68).Murli, C.; Sharma, S. M.; Karmakar, S.; Sikka, S., A-glycine under high pressures: A raman scattering study. *Physica B: Condensed Matter* **2003**, *339*, 23-30.

- (69).Dawson, A.; Allan, D. R.; Belmonte, S. A.; Clark, S. J.; David, W. I.; McGregor, P. A.; Parsons, S.; Pulham, C. R.; Sawyer, L., Effect of high pressure on the crystal structures of polymorphs of glycine. *Crystal growth & design* **2005**, *5*, 1415-1427.
- (70).BOLDYREVA, E.; DREBUSHCHAK, T.; SHUTOVA, E., Structural distortion of the α , β , and γ polymorphs of glycine on cooling. *Zeitschrift für Kristallographie* **2003**, *218*, 366-376.
- (71).Goryainov, S.; Kolesnik, E.; Boldyreva, E., A reversible pressure-induced phase transition in β -glycine at 0.76 gpa. *Physica B: Condensed Matter* **2005**, *357*, 340-347.
- (72).Boldyreva, E.; Ivashevskaya, S.; Sowa, H.; Ahsbahs, H.; Weber, H. In *Effect of high pressure on the crystalline glycine: A new high-pressure polymorphic modification formation*, Doklady Akademii Nauk, 2004; pp 358-361.
- (73).Goryainov, S.; Boldyreva, E.; Kolesnik, E., Raman observation of a new (ζ) polymorph of glycine? *Chemical Physics Letters* **2006**, *419*, 496-500.
- (74).Kolesnik, E.; Goryainov, S.; Boldyreva, E. In *Different behavior of l-and dl-serine crystals at high pressures: Phase transitions in l-serine and stability of the dl-serine structure*, Doklady Physical Chemistry, Springer: 2005; pp 169-172.
- (75).Moggach, S. A.; Allan, D. R.; Morrison, C. A.; Parsons, S.; Sawyer, L., Effect of pressure on the crystal structure of l-serine-i and the crystal structure of l-serine-ii at 5.4 gpa. *Acta Crystallographica Section B: Structural Science* **2005**, *61*, 58-68.
- (76).Boldyreva, E.; Sowa, H.; Seryotkin, Y. V.; Drebushchak, T.; Ahsbahs, H.; Chernyshev, V.; Dmitriev, V., Pressure-induced phase transitions in crystalline l-serine studied by single-crystal and high-resolution powder x-ray diffraction. *Chemical physics letters* **2006**, *429*, 474-478.
- (77).Moggach, S.; Parsons, S.; Allan, D., High-pressure crystallographic study of l-cysteine, the route to a new polymorph. *Acta Crystallographica Section A: Foundations of Crystallography* **2004**, *60*, s251-s251.
- (78).Minkov, V. S.; Krylov, A. S.; Boldyreva, E. V.; Goryainov, S. V.; Bizyaev, S. N.; Vtyurin, A. N., Pressure-induced phase transitions in crystalline l-and dl-cysteine. *The Journal of Physical Chemistry B* **2008**, *112*, 8851-8854.
- (79).Paukov, I.; Kovalevskaya, Y.; Boldyreva, E., Low-temperature thermodynamic properties of dl-cysteine. *Journal of thermal analysis and calorimetry* **2009**, *100*, 295-301.
- (80).Minkov, V. S.; Tumanov, N. A.; Kolesov, B. A.; Boldyreva, E. V.; Bizyaev, S. N., Phase transitions in the crystals of l-and dl-cysteine on cooling: The role of the hydrogen-bond distortions and the side-chain motions. 2. Dl-cysteine. *The Journal of Physical Chemistry B* **2009**, *113*, 5262-5272.
- (81).Bordallo, H. N.; Boldyreva, E. V.; Fischer, J.; Koza, M. M.; Seydel, T.; Minkov, V. S.; Drebushchak, V. A.; Kyriakopoulos, A., Observation of subtle dynamic transitions by a combination of neutron scattering, x-ray diffraction and dsc: A case study of the monoclinic l-cysteine. *Biophysical chemistry* **2010**, *148*, 34-41.

- (82).Paukov, I. E.; Kovalevskaya, Y. A.; Drebuschak, V. A.; Drebuschak, T. N.; Boldyreva, E. V., An extended phase transition in crystalline l-cysteine near 70 k. *The Journal of Physical Chemistry B* **2007**, *111*, 9186-9188.
- (83).Paukov, I.; Kovalevskaya, Y.; Boldyreva, E., Low-temperature thermodynamic properties of l-cysteine. *Journal of Thermal Analysis and Calorimetry* **2008**, *93*, 423-428.
- (84).Bordallo, H. N.; Kolesov, B. A.; Boldyreva, E. V.; Juranyi, F., Different dynamics of chiral and racemic (l-and dl-) serine crystals: Evidenced by incoherent inelastic neutron and raman scattering. *Journal of the American Chemical Society* **2007**, *129*, 10984-10985.
- (85).Kolesov, B.; Boldyreva, E., Difference in the dynamic properties of chiral and racemic crystals of serine studied by raman spectroscopy at 3– 295 k. *The Journal of Physical Chemistry B* **2007**, *111*, 14387-14397.
- (86).Facanha Filho, P. F.; Jiao, X.; Freire, P. T.; Lima Jr, J. A.; Dos Santos, A. O.; Henry, P. F.; Yokaichiya, F.; Kremner, E.; Bordallo, H. N., Structure–property relations in crystalline l-leucine obtained from calorimetry, x-rays, neutron and raman scattering. *Physical chemistry chemical physics* **2011**, *13*, 6576-6583.
- (87).Binns, J.; Parsons, S.; McIntyre, G. J., Accurate hydrogen parameters for the amino acid l-leucine. *Acta Crystallographica Section B: Structural Science, Crystal Engineering and Materials* **2016**, *72*, 885-892.
- (88).Aubrey, A.; Cleaves, H. J.; Chalmers, J. H.; Skelley, A. M.; Mathies, R. A.; Grunthaner, F. J.; Ehrenfreund, P.; Bada, J. L., Sulfate minerals and organic compounds on mars. *Geology* **2006**, *34*, 357-360.
- (89).Bernstein, M. P.; Dworkin, J. P.; Sandford, S. A.; Cooper, G. W.; Allamandola, L. J., Racemic amino acids from the ultraviolet photolysis of interstellar ice analogues. *Nature* **2002**, *416*, 401.
- (90).Caro, G. M.; Meierhenrich, U.; Schutte, W.; Barbier, B.; Segovia, A. A.; Rosenbauer, H.; Thiemann, W.-P.; Brack, A.; Greenberg, J., Amino acids from ultraviolet irradiation of interstellar ice analogues. *Nature* **2002**, *416*, 403.
- (91).Gerakines, P. A.; Hudson, R. L., Glycine's radiolytic destruction in ices: First in situ laboratory measurements for mars. *Astrobiology* **2013**, *13*, 647-655.
- (92).Iitaka, Y., The crystal structure of γ -glycine. *Acta Crystallographica* **1961**, *14*, 1-10.
- (93).Iitaka, Y., The crystal structure of β -glycine. *Acta Crystallographica* **1960**, *13*, 35-45.
- (94).Lemanov, V.; Popov, S.; Pankova, G., Piezoelectric properties of some crystalline amino acids and their complexes. *Solid State Physics (Fiz. Tv. Tela)* **2002**, *44*, 1840-1846.
- (95).Adhikari, S.; Kar, T., Bulk single crystal growth and characterization of l-leucine—a nonlinear optical material. *Materials Chemistry and Physics* **2012**, *133*, 1055-1059.
- (96).Rieckhoff, K. E.; Peticolas, W. L., Optical second-harmonic generation in crystalline amino acids. *Science* **1965**, *147*, 610-611.

- (97).Han, Q.; Yang, R.; Li, J.; Zhang, Y.; Wang, C., Synthesis of leucine micro/nanocrystals for pharmaceutical applications. *CrystEngComm* **2011**, *13*, 6157-6162.
- (98).Boldyreva, E., Crystalline amino acids: A link between chemistry. *Materials Science and Biology*, In: *Boyens JCA, Ogilvie JF, editors. Models, Mysteries, and Magic of Molecules. Netherlands: Springer* **2007**, 167-192.
- (99).Bell, J. F.; Calvin, W. M.; Ockert-Bell, M. E.; Crisp, D.; Pollack, J. B.; Spencer, J., Detection and monitoring of h₂o and co₂ ice clouds on mars. *Journal of Geophysical Research: Planets* **1996**, *101*, 9227-9237.
- (100).Knacke, R.; McCorkle, S.; Puetter, R.; Erickson, E.; Krätschmer, W., Observation of interstellar ammonia ice. *The Astrophysical Journal* **1982**, *260*, 141-146.
- (101).Sharma, A.; Scott, J. H.; Cody, G. D.; Fogel, M. L.; Hazen, R. M.; Hemley, R. J.; Huntress, W. T., Microbial activity at gigapascal pressures. *Science* **2002**, *295*, 1514-1516.
- (102).Witze, A., Vibrant pluto seen in historic fly-by. *Nature* **2015**, *523*, 389.
- (103).Brack, A.; Pillinger, C. T., Life on mars: Chemical arguments and clues from martian meteorites. *Extremophiles* **1998**, *2*, 313-319.
- (104).Otake, T.; Taniguchi, T.; Furukawa, Y.; Kawamura, F.; Nakazawa, H.; Kakegawa, T., Stability of amino acids and their oligomerization under high-pressure conditions: Implications for prebiotic chemistry. *Astrobiology* **2011**, *11*, 799-813.
- (105).Maté, B.; Rodriguez-Lazcano, Y.; Gálvez, Ó.; Tanarro, I.; Escribano, R., An infrared study of solid glycine in environments of astrophysical relevance. *Physical Chemistry Chemical Physics* **2011**, *13*, 12268-12276.
- (106).Bhatt, H.; Mishra, A.; Murli, C.; Verma, A. K.; Garg, N.; Deo, M.; Sharma, S. M., Proton transfer aiding phase transitions in oxalic acid dihydrate under pressure. *Physical Chemistry Chemical Physics* **2016**, *18*, 8065-8074.
- (107).Albrecht, G.; Corey, R. B., The crystal structure of glycine. *Journal of the American Chemical Society* **1939**, *61*, 1087-1103.
- (108).Ioppolo, S.; Van Boheemen, Y.; Cuppen, H.; Van Dishoeck, E.; Linnartz, H., Surface formation of co₂ ice at low temperatures. *Monthly Notices of the Royal Astronomical Society* **2011**, *413*, 2281-2287.
- (109).Sun, C. Q.; Zhang, X.; Zheng, W., The hidden force opposing ice compression. *Chemical Science* **2012**, *3*, 1455-1460.
- (110).Zhang, X.; Chen, S.; Li, J., Hydrogen-bond potential for ice viii-x phase transition. *Scientific Reports* **2016**, *6*, 37161.
- (111).Bernal, J., The crystal structure of the natural amino acids and belated compounds. *Zeitschrift für Kristallographie-Crystalline Materials* **1931**, *78*, 363-369.
- (112).Chaudhuri, P.; Canuto, S.; Provasi, P. F., Nmr spin-spin coupling constants in hydrogen-bonded glycine clusters. *International Journal of Quantum Chemistry*, e25608-n/a.

- (113).Aliev, A. E.; Mann, S. E.; Rahman, A. S.; McMillan, P. F.; Corà, F.; Iuga, D.; Hughes, C. E.; Harris, K. D., High-resolution solid-state 2h nmr spectroscopy of polymorphs of glycine. *The Journal of Physical Chemistry A* **2011**, *115*, 12201-12211.
- (114).Lund, A. M.; Pagola, G. I.; Orendt, A. M.; Ferraro, M. B.; Facelli, J. C., Crystal structure prediction from first principles: The crystal structures of glycine. *Chemical physics letters* **2015**, *626*, 20-24.
- (115).Gupta, V. D.; Singh, R. D., Low frequency spectra of glycine. *Chemical Physics Letters* **1970**, *5*, 218-220.
- (116).Stepanian, S.; Reva, I.; Radchenko, E.; Rosado, M.; Duarte, M.; Fausto, R.; Adamowicz, L., Matrix-isolation infrared and theoretical studies of the glycine conformers. *The Journal of Physical Chemistry A* **1998**, *102*, 1041-1054.
- (117).Grenie, Y.; Lassegues, J. C.; Garrigou-Lagrange, C., Infrared spectrum of matrix-isolated glycine. *The Journal of Chemical Physics* **1970**, *53*, 2980-2982.
- (118).Matei, A.; Drichko, N.; Gompf, B.; Dressel, M., Far-infrared spectra of amino acids. *Chemical Physics* **2005**, *316*, 61-71.
- (119).Barth, A., The infrared absorption of amino acid side chains. *Progress in biophysics and molecular biology* **2000**, *74*, 141-173.
- (120).Husain, S. K.; Hasted, J. B.; Rosen, D.; Nicol, E.; Birch, J. R., Fir spectra of amino acids and related molecules. *Infrared Physics* **1984**, *24*, 201-208.
- (121).Ramnarine, R.; Sherman, W. F.; Chunnillal, C. J., Ir-active lattice modes of α -glycine and deuterio- α -glycine. *Microchimica Acta* **1988**, *95*, 353-355.
- (122).Trivella, A.; Gaillard, T.; Stote, R. H.; Hellwig, P., Far infrared spectra of solid state aliphatic amino acids in different protonation states. *The Journal of chemical physics* **2010**, *132*, 03B609.
- (123).Takeda, M.; Iavazzo, R. E. S.; Garfinkel, D.; Scheinberg, I. H.; Edsall, J. T., Raman spectra of amino acids and related compounds. IX. Ionization and deuterium substitution in glycine, alanine and β -alanine^{1,2,3}. *Journal of the American Chemical Society* **1958**, *80*, 3813-3818.
- (124).Ghazanfar, S. A. S.; Myers, D. V.; Edsall, J. T., Raman spectra of carbon-deuterated glycine in various ionic forms. *Journal of the American Chemical Society* **1964**, *86*, 3439-3444.
- (125).Krishnan, R.; Sankaranarayanan, V.; Krishnan, K., Raman and infra-red spectra of amino acids. *Journal of the Indian Institute of Science* **2013**, *55*, 66.
- (126).Stenback, H., On the raman spectra of solid natural α -glycine and solid 15n-substituted α -glycine. *Journal of Raman Spectroscopy* **1976**, *5*, 49-55.
- (127).Kromhout, R.; Moulton, W., Nuclear magnetic resonance: Structure of the amino group i. *The Journal of Chemical Physics* **1955**, *23*, 1673-1679.

- (128).Gu, Z.; Ebisawa, K.; McDermott, A., Hydrogen bonding effects on amine rotation rates in crystalline amino acids. *Solid state nuclear magnetic resonance* **1996**, *7*, 161-172.
- (129).Jönsson, P.-G.; Kvick, Å., Precision neutron diffraction structure determination of protein and nucleic acid components. Iii. The crystal and molecular structure of the amino acid α -glycine. *Acta Crystallographica Section B: Structural Crystallography and Crystal Chemistry* **1972**, *28*, 1827-1833.
- (130).Marsh, R. E., A refinement of the crystal structure of glycine. *Acta Crystallographica* **1958**, *11*, 654-663.
- (131).Kobayashi, Y.; Sawada, S.; Furuta, H.; Endo, S.; Deguchi, K., Ferroelectric tgs ((nh₂ch₂cooh) 3· h₂so₄) under high pressure. *Journal of Physics: Condensed Matter* **2002**, *14*, 11139.
- (132).Arun, K.; Jayalekshmi, S., Growth and characterization of glycinium oxalate crystals for nonlinear optical applications. *OPTOELECTRONICS AND ADVANCED MATERIALS – RAPID COMMUNICATIONS* **2008**, *2*, 701 - 706.
- (133).Matyjasek, K.; Czaplá, Z., Temperature dependence of polarization switching in deuterated glycine phosphite single crystals. *Phase Transitions* **2013**, *86*, 161-166.
- (134).Nayeem, J.; Wakabayashi, H.; Kikuta, T.; Yamazaki, T.; Nakatani, N., Ferroelectric properties of deuterated glycine phosphite. *Ferroelectrics* **2002**, *269*, 153-158.
- (135).Ivanov, V. V.; Kolysheva, M. V.; Klevtsova, E. A., On the relaxation of macroscopic polarization in dtgs crystals. *Ferroelectrics* **2000**, *238*, 65-72.
- (136).Schmidt, C., First deuterated drug approved. Nature Publishing Group: 2017.
- (137).Mullard, A., Deuterated drugs draw heavier backing. Nature Publishing Group: 2016.
- (138).Timmins, G. S., Deuterated drugs: Where are we now? *Expert opinion on therapeutic patents* **2014**, *24*, 1067-1075.
- (139).Kržan, M.; Vianello, R.; Maršavelski, A.; Repič, M.; Zakšek, M.; Kotnik, K.; Fijan, E.; Mavri, J., The quantum nature of drug-receptor interactions: Deuteration changes binding affinities for histamine receptor ligands. *PloS one* **2016**, *11*, e0154002.
- (140).Basu, S., A review of nonlinear optical organic materials. *Industrial & Engineering Chemistry Product Research and Development* **1984**, *23*, 183-186.
- (141).Harding, M. M.; Howieson, R., L-leucine. *Acta Crystallographica Section B: Structural Crystallography and Crystal Chemistry* **1976**, *32*, 633-634.
- (142).Coll, M.; Solans, X.; Font-Altaba, M.; Subirana, J., Structure of L-leucine: A redetermination. *Acta Crystallographica Section C* **1986**, *42*, 599-601.
- (143).Herlinger, A. W.; Wenhold, S. L.; Long, T. V., Infrared spectra of amino acids and their metal complexes. Ii. Geometrical isomerism in bis (amino acidato) copper (ii) complexes. *Journal of the American Chemical Society* **1970**, *92*, 6474-6481.

- (144).Shotts, W.; Sievers, A., The far-infrared properties of polyamino acids. *Biopolymers: Original Research on Biomolecules* **1974**, *13*, 2593-2614.
- (145).Jenkins, A. L.; Larsen, R. A.; Williams, T. B., Characterization of amino acids using raman spectroscopy. *Spectrochimica Acta Part A: Molecular and Biomolecular Spectroscopy* **2005**, *61*, 1585-1594.
- (146).Linder, R.; Nispel, M.; Häber, T.; Kleinermanns, K., Gas-phase ft-ir-spectra of natural amino acids. *Chemical physics letters* **2005**, *409*, 260-264.
- (147).Wolpert, M.; Hellwig, P., Infrared spectra and molar absorption coefficients of the 20 alpha amino acids in aqueous solutions in the spectral range from 1800 to 500 cm⁻¹. *Spectrochimica Acta Part A: Molecular and Biomolecular Spectroscopy* **2006**, *64*, 987-1001.
- (148).Derbel, N.; Hernández, B.; Pflüger, F.; Liquier, J.; Geinguenaud, F.; Jaïdane, N.; Ben Lakhdar, Z.; Ghomi, M., Vibrational analysis of amino acids and short peptides in hydrated media. I. L-glycine and l-leucine. *The Journal of Physical Chemistry B* **2007**, *111*, 1470-1477.
- (149).Dokmaisrijan, S.; Lee, V. S.; Nimmanpipug, P., The gas phase conformers and vibrational spectra of valine, leucine and isoleucine: An ab initio study. *Journal of Molecular Structure: THEOCHEM* **2010**, *953*, 28-38.
- (150).Görbitz, C.; Dalhus, B., Redetermination of l-leucine at 120k. *Acta Crystallographica Section C* **1996**, *52*, 1754-1756.
- (151).Hollingsworth, M. D.; Cyr, N., High resolution solid-state nmr spectra of leucine: A re-examination. *Journal of the Chemical Society, Chemical Communications* **1990**, 578-580.
- (152).Prasad, S.; Clark, T. M.; Sharma, R.; Kwak, H.-T.; Grandinetti, P. J.; Zimmermann, H., A combined 17o rapt and mq-mas nmr study of l-leucine. *Solid state nuclear magnetic resonance* **2006**, *29*, 119-124.
- (153).Andrew, E.; Hinshaw, W.; Hutchins, M.; Sjöblom, R.; Canepa, P., Proton magnetic relaxation and molecular motion in polycrystalline amino acids: II. Alanine, isoleucine, leucine, methionine, norleucine, threonine and valine. *Molecular Physics* **1976**, *32*, 795-806.
- (154).Stepanian, S. G.; Ivanov, A. Y.; Adamowicz, L., Conformational composition of neutral leucine. Matrix isolation infrared and ab initio study. *Chemical Physics* **2013**, *423*, 20-29.
- (155).Sarma, J. A.; Desiraju, G. R., The role of cl. Cntdot.. Cntdot.. Cntdot. Cl and ch. Cntdot.. Cntdot.. Cntdot. O interactions in the crystal engineering of 4-. Ang. Short-axis structures. *Accounts of Chemical Research* **1986**, *19*, 222-228.
- (156).Desiraju, G. R., Hydrogen bridges in crystal engineering: Interactions without borders. *Accounts of chemical research* **2002**, *35*, 565-573.
- (157).Steiner, T., The hydrogen bond in the solid state. *Angewandte Chemie International Edition* **2002**, *41*, 48-76.

- (158).Lai, S. L.; Tong, W. Y.; Kui, S. C.; Chan, M. Y.; Kwok, C. C.; Che, C. M., High efficiency white organic light-emitting devices incorporating yellow phosphorescent platinum (ii) complex and composite blue host. *Advanced Functional Materials* **2013**, *23*, 5168-5176.
- (159).Grey, J. K.; Butler, I. S.; Reber, C., Large pressure-induced increase in luminescence intensity for the [pd (scn) 4] 2-complex. *Journal of the American Chemical Society* **2002**, *124*, 9384-9385.
- (160).Grey, J. K.; Butler, I. S.; Reber, C., Pressure-induced enhancements of luminescence intensities and lifetimes correlated with emitting-state distortions for thiocyanate and selenocyanate complexes of platinum (ii) and palladium (ii). *Inorganic chemistry* **2003**, *42*, 6503-6518.
- (161).Ananikov, V. P.; Gayduk, K. A.; Starikova, Z. A.; Beletskaya, I. P., Ni (acac) 2/phosphine as an excellent precursor of nickel (0) for catalytic systems. *Organometallics* **2010**, *29*, 5098-5102.
- (162).Kaur, T.; Borse, V.; Sheth, S.; Sheehan, K.; Ghosh, S.; Tupal, S.; Jajoo, S.; Mukherjea, D.; Rybak, L. P.; Ramkumar, V., Adenosine a1 receptor protects against cisplatin ototoxicity by suppressing the nox3/stat1 inflammatory pathway in the cochlea. *Journal of Neuroscience* **2016**, *36*, 3962-3977.
- (163).Jena, S. L. a. P., *Bulletin of American Physical Society* **2011**, *56*.
- (164).Bajaj, N.; Bhatt, H.; Murli, C.; Vishwakarma, S.; Chitra, R.; Ravindran, T.; Deo, M., Perceptible isotopic effect in 3d-framework of α -glycine at low temperatures. *Spectrochimica Acta Part A: Molecular and Biomolecular Spectroscopy* **2018**, *204*, 495-507.
- (165).Bajaj, N.; Bhatt, H.; Vishwakarma, S.; Deo, M. N., Orientational adaptations leading to plausible phase transitions in l-leucine at low temperatures: Revealed by infrared spectroscopy. *The Journal of Physical Chemistry B* **2019**.
- (166).Bajaj, N.; Bhatt, H.; Pandey, K. K.; Poswal, H. K.; Arya, A.; Ghosh, P.; Deo, M., Phase transition in metal-organic complex *trans*-ptcl2(pet3)2 under pressure—insights of molecular and crystal structure. *CrystEngComm* **2018**.
- (167).Ekin, J., *Experimental techniques for low-temperature measurements: Cryostat design, material properties and superconductor critical-current testing*. Oxford university press: 2006.
- (168).Sydoriak, S.; Roberts, T.; Sherman, R., The 1962 he3 scale of temperatures, ii. Derivation. *J. Res. Natl. Bur. Stand.(US) A* **1964**, *68*, 559-565.
- (169).McCarty, R. D.; Arp, V. D., A new wide range equation of state for helium. In *Advances in cryogenic engineering*, Springer: 1990; pp 1465-1475.
- (170).Younglove, B. A. *Thermophysical properties of fluids. I. Argon, ethylene, parahydrogen, nitrogen, nitrogen trifluoride, and oxygen*; NATIONAL STANDARD REFERENCE DATA SYSTEM: 1982.
- (171).Span, R.; Lemmon, E. W.; Jacobsen, R. T.; Wagner, W.; Yokozeki, A., A reference equation of state for the thermodynamic properties of nitrogen for temperatures from 63.151

to 1000 k and pressures to 2200 mpa. *Journal of Physical and Chemical Reference Data* **2000**, 29, 1361-1433.

(172).Katti, R.; Jacobsen, R.; Stewart, R.; Jahangiri, M., Thermodynamic properties of neon for temperatures from the triple point to 700 k at pressures to 700 mpa. In *Advances in cryogenic engineering*, Springer: 1986; pp 1189-1197.

(173).Schmidt, R.; Wagner, W., A new form of the equation of state for pure substances and its application to oxygen. *Fluid Phase Equilibria* **1985**, 19, 175-200.

(174).Tegeler, C.; Span, R.; Wagner, W., A new equation of state for argon covering the fluid region for temperatures from the melting line to 700 k at pressures up to 1000 mpa. *Journal of Physical and Chemical Reference Data* **1999**, 28, 779-850.

(175).Kreith, F.; Black, W. Z., *Basic heat transfer*. Harper & Row New York: 1980.

(176).Lawson, A.; Tang, T. Y., A diamond bomb for obtaining powder pictures at high pressures. *Review of Scientific instruments* **1950**, 21, 815-815.

(177).Weir, C.; Lippincott, E.; Van Valkenburg, A.; Bunting, E., Infrared studies in the 1-to 15-micron region to 30,000 atmospheres. *J. Res. Natl. Bur. Stand. A* **1959**, 63, 55-62.

(178).Piermarini, G.; Block, S.; Barnett, J., Hydrostatic limits in liquids and solids to 100 kbar. *Journal of Applied Physics* **1973**, 44, 5377-5382.

(179).Otto, J.; Vassiliou, J.; Frommeyer, G., Nonhydrostatic compression of elastically anisotropic polycrystals. I. Hydrostatic limits of 4: 1 methanol-ethanol and paraffin oil. *Physical Review B* **1998**, 57, 3253.

(180).Fujishiro, I. In *Viscosities and glass transition pressures in the methanol-ethanol-water system*, High Pressure Res. Ind. AIRAPT Conf. 8th, 1982; pp 608-511.

(181).Shen, Y.; Kumar, R. S.; Pravica, M.; Nicol, M. F., Characteristics of silicone fluid as a pressure transmitting medium in diamond anvil cells. *Review of scientific instruments* **2004**, 75, 4450-4454.

(182).Ragan, D. D.; Clarke, D. R.; Schiferl, D., Silicone fluid as a high-pressure medium in diamond anvil cells. *Review of scientific instruments* **1996**, 67, 494-496.

(183).Mao, H.; Bell, P., Observations of hydrogen at room temperature (25 c) and high pressure (to 500 kilobars). *Science* **1979**, 203, 1004-1006.

(184).LeSar, R.; Ekberg, S.; Jones, L.; Mills, R.; Schwalbe, L.; Schiferl, D., Raman spectroscopy of solid nitrogen up to 374 kbar. *Solid State Communications* **1979**, 32, 131-134.

(185).Murnaghan, F., Fd murnaghan, am. J. Math. 59, 235 (1937). *Am. J. Math.* **1937**, 59, 235.

(186).Birch, F., Finite elastic strain of cubic crystals. *Physical review* **1947**, 71, 809.

(187).Bhatt, H., Infrared spectroscopy of molecular solids under extreme conditions. **2016**.

- (188).Schmidt, C., First deuterated drug approved. *Nature Biotechnology* **2017**, *35*, 493.
- (189).Mullard, A., Deuterated drugs draw heavier backing. *Nature Reviews Drug Discovery* **2016**, *15*, 219.
- (190).Casati, N.; Macchi, P.; Sironi, A., Hydrogen migration in oxalic acid di-hydrate at high pressure? *Chemical communications* **2009**, 2679-2681.
- (191).Macchi, P.; Casati, N.; Marshall, W. G.; Sironi, A., The α and β forms of oxalic acid di-hydrate at high pressure: A theoretical simulation and a neutron diffraction study. *CrystEngComm* **2010**, *12*, 2596-2603.
- (192).McMahon, M.; Nelmes, R.; Kuhst, W.; Dorwarth, R.; Piltz, R.; Tun, Z., Geometric effects of deuteration on hydrogen-ordering phase transitions. *Nature* **1990**, *348*, 317.
- (193).Merz, K.; Kupka, A., Deuterium perturbs the molecular arrangement in the solid state. *Crystal Growth & Design* **2015**, *15*, 1553-1558.
- (194).Merz, K., Crystal engineering-using h/d exchange for molecular rearrangement. *British Association For Crystal Growth Annual Conference 2017* **2017**.
- (195).Rosado, M. T.; Duarte, M. L. T.; Fausto, R., Vibrational spectra of acid and alkaline glycine salts. *Vibrational Spectroscopy* **1998**, *16*, 35-54.
- (196).Legros, J.-P.; Kvick, Å., Deformation electron density of α -glycine at 120 k. *Acta Crystallographica Section B: Structural Crystallography and Crystal Chemistry* **1980**, *36*, 3052-3059.
- (197).Destro, R.; Roversi, P.; Barzaghi, M.; Marsh, R. E., Experimental charge density of α -glycine at 23 k. *The Journal of Physical Chemistry A* **2000**, *104*, 1047-1054.
- (198).Goncharov, A.; Struzhkin, V.; Somayazulu, M.; Hemley, R.; Mao, H., Compression of ice to 210 gigapascals: Infrared evidence for a symmetric hydrogen-bonded phase. *Science* **1996**, *273*, 218-220.
- (199).Bhatt, H.; Murli, C.; Mishra, A.; Verma, A. K.; Garg, N.; Deo, M.; Chitra, R.; Sharma, S. M., Hydrogen bond symmetrization in glycinium oxalate under pressure. *The Journal of Physical Chemistry B* **2016**, *120*, 851-859.
- (200).Stewart, J. W., Compression and phase transitions of solid nh_3 , sif_4 , h_2s , and cf_4 . *The Journal of Chemical Physics* **1960**, *33*, 128-133.
- (201).Bhatt, H.; Murli, C.; Garg, N.; Deo, M.; Chitra, R.; Choudhury, R. R.; Sharma, S. M., High pressure phase transformations in bis (glycinium) oxalate—an infrared absorption study. *Chemical Physics Letters* **2012**, *532*, 57-62.
- (202).Murli, C.; Thomas, S.; Venkateswaran, S.; M Sharma, S., Raman spectroscopic investigation of α -glycine at different temperatures. *Physica B: Condensed Matter* **2005**, *364*, 233-238.

- (203).Chernobai, G.; Chesalov, Y. A.; Burgina, E.; Drebushchak, T.; Boldyreva, E., Temperature effects on the ir spectra of crystalline amino acids, dipeptides, and polyamino acids. I. Glycine. *Journal of Structural Chemistry* **2007**, *48*, 332-339.
- (204).Surovtsev, N.; Malinovsky, V.; Boldyreva, E., Raman study of low-frequency modes in three glycine polymorphs. *The Journal of chemical physics* **2011**, *134*, 01B626.
- (205).Bordallo, H. N.; Boldyreva, E. V.; Buchsteiner, A.; Koza, M. M.; Landsgesell, S., Structure– property relationships in the crystals of the smallest amino acid: An incoherent inelastic neutron scattering study of the glycine polymorphs. *The Journal of Physical Chemistry B* **2008**, *112*, 8748-8759.
- (206).Fearheller, W. R.; Miller Jr, J., The infrared spectra of amino acids and some simple polypeptides to 33 cm^{-1} at room and liquid nitrogen temperatures. *Applied Spectroscopy* **1971**, *25*, 175-182.
- (207).Müller-Rowat, C.; Haeberlen, U.; Rowat, J.; Colpa, J. P., Temperature dependence of the reorientation of the nd^{3+} group in α -glycine. *Chemical Physics* **1985**, *96*, 327-332.
- (208).Andrews, B.; Torrie, B. H.; Powell, B. M., Intermolecular potentials for alpha-glycine from raman and infrared scattering measurements. *Biophysical Journal* **1983**, *41*, 293-298.
- (209).Ivanov, A.; Korolik, E.; Insarova, N.; Il'Ich, G., Application of low-temperature ir spectroscopy to the analysis of the molecular structure of glycine. *Journal of Applied Spectroscopy* **1991**, *54*, 291-294.
- (210).Shinozaki, A.; Komatsu, K.; Kagi, H.; Fujimoto, C.; Machida, S.; Sano-Furukawa, A.; Hattori, T., Behavior of intermolecular interactions in α -glycine under high pressure. *The Journal of Chemical Physics* **2018**, *148*, 044507.
- (211).de Souza, J. M.; Freire, P. T.; Bordallo, H. N.; Argyriou, D. N., Structural isotopic effects in the smallest chiral amino acid: Observation of a structural phase transition in fully deuterated alanine. *The Journal of Physical Chemistry B* **2007**, *111*, 5034-5039.
- (212).Ichikawa, M., Hydrogen-bond geometry and its isotope effect in crystals with oho bonds—revisited. *Journal of Molecular Structure* **2000**, *552*, 63-70.
- (213).Rozenberg, M.; Jung, C.; Shoham, G., Ordered and disordered hydrogen bonds in adenosine, cytidine and uridine studied by low temperature ft infrared spectroscopy. *Physical Chemistry Chemical Physics* **2003**, *5*, 1533-1535.
- (214).Rozenberg, M.; Shoham, G.; Reva, I.; Fausto, R., Low-temperature fourier transform infrared spectra and hydrogen bonding in polycrystalline l-alanine. *Spectrochimica Acta Part A: Molecular and Biomolecular Spectroscopy* **2003**, *59*, 3253-3266.
- (215).Yulei, S.; Li, W., Collective vibrational spectra of α - and γ -glycine studied by terahertz and raman spectroscopy. *Journal of Physics D: Applied Physics* **2005**, *38*, 3741.
- (216).Miao, P.; Torii, S.; Yonemura, M.; Ishikawa, Y.; Zhang, J.; Kamiyama, T. In *Structure analysis on small molecular crystal by high resolution neutron powder diffraction*, Journal of Physics: Conference Series, IOP Publishing: 2014; p 012055.

- (217).Thaper, C.; Dasannacharya, B.; Goyal, P.; Chakravarthy, R.; Tomkinson, J., Neutron scattering from glycine and deuterated glycine. *Physica B: Condensed Matter* **1991**, *174*, 251-256.
- (218).Thaper, C. L.; Sinha, S. K.; Dasannacharya, B. A., Neutron inelastic scattering by amino acids. *AIP Conference Proceedings* **1982**, *89*, 249-251.
- (219).Kolesov, B. A.; Boldyreva, E. V., Self-trapped n-h vibrational states in the polymorphs of glycine, l-and dl-alanine. *Journal of Raman Spectroscopy* **2010**, *41*, 670-677.
- (220).Novak, A., Hydrogen bonding in solids correlation of spectroscopic and crystallographic data. In *Large molecules*, Springer: 1974; pp 177-216.
- (221).Mikenda, W., Stretching frequency versus bond distance correlation of o-d (h)··· y (y=n, o, s, se, cl, br, i) hydrogen bonds in solid hydrates. *Journal of Molecular Structure* **1986**, *147*, 1-15.
- (222).Rozenberg, M. S., Ir spectra and hydrogen bond energies of crystalline acid salts of carboxylic acids. *Spectrochimica Acta Part A: Molecular and Biomolecular Spectroscopy* **1996**, *52*, 1559-1563.
- (223).Lutz, B.; van der Maas, J.; Kanters, J. A., Spectroscopic evidence for c-h··· interaction in crystalline steroids and reference compounds. *Journal of molecular structure* **1994**, *325*, 203-214.
- (224).Lutz, E.; Van der Maas, J., Hydrogen bonds in crystalline carbohydrates a variable-temperature ft-ir study. *Journal of molecular structure* **1994**, *324*, 123-132.
- (225).Rozenberg, M.; Shoham, G.; Reva, I.; Fausto, R., A correlation between the proton stretching vibration red shift and the hydrogen bond length in polycrystalline amino acids and peptides. *Physical Chemistry Chemical Physics* **2005**, *7*, 2376-2383.
- (226).Iogansen, A., Direct proportionality of the hydrogen bonding energy and the intensification of the stretching ν (xh) vibration in infrared spectra. *Spectrochimica Acta Part A: Molecular and Biomolecular Spectroscopy* **1999**, *55*, 1585-1612.
- (227).Li, J.; Ross, D., Evidence for two kinds of hydrogen bond in ice. *Nature* **1993**, *365*, 327-329.
- (228).Zhang, X.; Sun, P.; Yan, T.; Huang, Y.; Ma, Z.; Zou, B.; Zheng, W.; Zhou, J.; Gong, Y.; Sun, C. Q., Water's phase diagram: From the notion of thermodynamics to hydrogen-bond cooperativity. *Progress in Solid State Chemistry* **2015**, *43*, 71-81.
- (229).Huang, Y.; Zhang, X.; Ma, Z.; Zhou, Y.; Zheng, W.; Zhou, J.; Sun, C. Q., Hydrogen-bond relaxation dynamics: Resolving mysteries of water ice. *Coordination Chemistry Reviews* **2015**, *285*, 109-165.
- (230).Sobczyk, L.; Obrzud, M.; Filarowski, A., H/d isotope effects in hydrogen bonded systems. *Molecules* **2013**, *18*, 4467-4476.
- (231).Pauwels, E.; Verstraelen, T.; De Cooman, H.; Van Speybroeck, V.; Waroquier, M., Temperature study of a glycine radical in the solid state adopting a dft periodic approach:

Vibrational analysis and comparison with epr experiments. *The Journal of Physical Chemistry B* **2008**, *112*, 7618-7630.

(232).Collins, M.; Whiffen, D., The electron spin resonance of irradiated glycine at 77° k. *Molecular Physics* **1966**, *10*, 317-325.

(233).Sanderud, A.; Sagstuen, E., Epr and endor studies of single crystals of α -glycine x-ray irradiated at 295 k. *The Journal of Physical Chemistry B* **1998**, *102*, 9353-9361.

(234).Sagstuen, E.; Sanderud, A.; Hole, E. O., The solid-state radiation chemistry of simple amino acids, revisited. *Radiation research* **2004**, *162*, 112-119.

(235).Derbyshire, W.; Gorvin, T.; Warner, D., A deuteron magnetic resonance study of deuterated glycine. *Molecular Physics* **1967**, *12*, 299-300.

(236).Ashcroft, N.; Mermin, N., Solid state physics (philadelphia: Saunders college). *et seq* **1976**, 76.

(237).Sushchinskii, M. M., *Raman spectra of molecules and crystals*. Israel Program for Scientific Translations: 1972.

(238).Forss, S., A raman spectroscopic temperature study of nh₃⁺ torsional motion as related to hydrogen bonding in the l-alanine crystal. *Journal of Raman Spectroscopy* **1982**, *12*, 266-273.

(239).Bordallo, H. N.; Barthes, M.; Eckert, J., Vibrational dynamics of crystalline l-alanine. *Physica B: Condensed Matter* **1997**, *241*, 1138-1140.

(240).Koegel, R. J.; Greenstein, J. P.; Winitz, M.; Birnbaum, S. M.; McCallum, R. A., Studies on diastereoisomeric α -amino acids and corresponding α -hydroxy acids. V. Infrared spectra. *Journal of the American Chemical Society* **1955**, *77*, 5708-5720.

(241).Leifer, A.; Lippincott, E., The infrared spectra of some amino acids. *Journal of the American Chemical Society* **1957**, *79*, 5098-5101.

(242).Sharma, B. B.; Murli, C.; Chitra, R.; Sharma, S. M., Hydrogen-bonding interactions in fully deuterated α -glycine at high pressures. *Journal of Raman Spectroscopy* **2012**, *43*, 138-145.

(243).Ubbelohde, A., Les propriétés thermiques de la liaison hydrogène dans les cristaux. *Journal de Chimie Physique* **1949**, *46*, 429-437.

(244).Rundle, R., The deuterium effect on hydrogen bond distances in crystals. *The Journal of Chemical Physics* **1953**, *21*, 937-938.

(245).Katrusiak, A., Macroscopic and structural effects of hydrogen-bond transformations. *Crystallography Reviews* **1996**, *5*, 133-175.

(246).Ichikawa, M.; Matsuo, T., Deuteration-induced structural phase transitions in some hydrogen-bonded crystals. *Journal of molecular structure* **1996**, *378*, 17-27.

- (247).Totsuji, C.; Matsubara, T., Deuteration induced phase transition in hydrogen bond. *Solid state communications* **1998**, *105*, 731-733.
- (248).Totsuji, C.; Matsubara, T., Theory of phase transition induced by deuteration of hydrogen bond. *JOURNAL-KOREAN PHYSICAL SOCIETY* **1998**, *32*, S50-S52.
- (249).Kume, Y.; Muraoka, H.; Yamamuro, O.; Matsuo, T., Deuteration-induced phase transition in ammonium hexachloroplumbate. *The Journal of chemical physics* **1998**, *108*, 4090-4097.
- (250).Matsuo, T.; Inaba, A.; Yamamuro, O.; Onoda-Yamamuro, N., Proton tunnelling and deuteration-induced phase transitions in hydrogen-bonded crystals. *Journal of Physics: Condensed Matter* **2000**, *12*, 8595.
- (251).Bajaj, N.; Bhatt, H.; Murli, C.; Vishwakarma, S.; Chitra, R.; Ravindran, T.; Deo, M., Perceptible isotopic effect in 3d-framework of α -glycine at low temperatures. *Spectrochimica Acta Part A: Molecular and Biomolecular Spectroscopy* **2018**.
- (252).Bhatt, H.; Deo, M., A synchrotron infrared absorption study of pressure induced polymerization of acrylamide. *Spectrochimica Acta Part A: Molecular and Biomolecular Spectroscopy* **2017**, *185*, 45-51.
- (253).Groşan, C. B.; ALMĂŞAN, V., Structure and vibrational spectrum of l-leucine: A dft-pcm investigation. *CHEMIA* **2011**, 199.
- (254).Bougeard, D., Phase transition and vibrational spectra of i-leucine. *Berichte der Bunsengesellschaft für physikalische Chemie* **1983**, *87*, 279-283.
- (255).Pawlukojc, A.; Leciejewicz, J.; Natkaniec, I., The ins spectroscopy of amino acids: L-leucine. *Spectrochimica Acta Part A: Molecular and Biomolecular Spectroscopy* **1996**, *52*, 29-32.
- (256).Carabatos-Nédelec, C.; Becker, P., Order–disorder and structural phase transitions in solid-state materials by raman scattering analysis. *Journal of Raman spectroscopy* **1997**, *28*, 663-671.
- (257).Minkov, V. S.; Drebuschak, V. A.; Ogienko, A. G.; Boldyreva, E. V., Decreasing particle size helps to preserve metastable polymorphs. A case study of dl-cysteine. *CrystEngComm* **2011**, *13*, 4417-4426.
- (258).Moggach, S. A.; Clark, S. J.; Parsons, S., L-cysteine-i at 30 k. *Acta Crystallographica Section E: Structure Reports Online* **2005**, *61*, o2739-o2742.
- (259).Barthes, M.; Bordallo, H.; Denoyer, F.; Lorenzo, J.-E.; Zaccaro, J.; Robert, A.; Zontone, F., Micro-transitions or breathers in l-alanine? *The European Physical Journal B-Condensed Matter and Complex Systems* **2004**, *37*, 375-382.
- (260).Belo, E. A.; Pereira, J. E.; Freire, P. T.; Argyriou, D. N.; Eckert, J.; Bordallo, H. N., Hydrogen bonds in crystalline d-alanine: Diffraction and spectroscopic evidence for differences between enantiomers. *IUCrJ* **2018**, *5*, 6-12.

- (261).Wu, H., Metal-organic compounds of iridium (iii) and platinum (ii): Synthesis, characterization and optoelectronic applications. **2014**.
- (262).Chatt, J.; Wilkins, R., 824. The nature of the co-ordinate link. Part vi. A comparison of equilibria between cis-and trans-(met 3) 2 ptcl 2, where m= p, as, and sb. *Journal of the Chemical Society (Resumed)* **1952**, 4300-4306.
- (263).Chatt, J.; Williams, A., 677. The nature of the co-ordinate link. Part iv. Complex formation by phosphorus trifluoride. *Journal of the Chemical Society (Resumed)* **1951**, 3061-3067.
- (264).Messmer, G.-G.; Amma, E., Crystal structures and multiple bonding in trans-pt [p (c2h5) 3] 2cl2 and trans-pt [p (c2h5) 3] 2br2. *Inorganic Chemistry* **1966**, 5, 1775-1781.
- (265).Mason, R.; Meek, D. W., The versatility of tertiary phosphane ligands in coordination and organometallic chemistry. *Angewandte Chemie International Edition* **1978**, 17, 183-194.
- (266).Huheey, *J. Organic Chemistry; Harper and Row: New York* **1983**, 432-441.
- (267).Xiao, S.; Trogler, W.; Ellis, D.; Berkovich-Yellin, Z., Theoretical study of the frontier orbitals of metal-phosphine complexes. *Journal of the American Chemical Society* **1983**, 105, 7033-7040.
- (268).Khramov, D. M.; Lynch, V. M.; Bielawski, C. W., N-heterocyclic carbene– transition metal complexes: Spectroscopic and crystallographic analyses of π -back-bonding interactions. *Organometallics* **2007**, 26, 6042-6049.
- (269).Maeda, Y.; Hashimoto, H.; Kinoshita, I.; Nishioka, T., Π -back-bonding interaction depending on the bridging chain lengths of chelated n-heterocyclic carbene platinum units in heterometallic trinuclear complexes affecting their electrochemical property. *Inorganic chemistry* **2014**, 53, 661-663.
- (270).Reddy, D.; Jaganyi, D., Controlling the extent of π -backbonding in platinum (ii) terpyridyl systems: A detailed kinetic, mechanistic and computational approach. *Dalton Transactions* **2008**, 6724-6731.
- (271).Besara, T.; Jain, P.; Dalal, N. S.; Kuhns, P. L.; Reyes, A. P.; Kroto, H. W.; Cheetham, A. K., Mechanism of the order–disorder phase transition, and glassy behavior in the metal-organic framework [(ch3) 2nh2] zn (hcoo) 3. *Proceedings of the National Academy of Sciences* **2011**.
- (272).Chatt, J., The co-ordinate link in chemistry. *Nature* **1950**, 165, 637.
- (273).Chatt, J.; Leigh, G. J.; Mingos, D. M. P., Raman spectra of some tertiary phosphine complexes of rhodium, iridium, palladium, and platinum. *Journal of the Chemical Society A: Inorganic, Physical, Theoretical* **1969**, 2972-2975.
- (274).Plyler, E. K., Infrared spectra of methanol, ethanol, and rz-propanol. *Journal of Research of the National Bureau of Standards* **1952**, 48.
- (275).Kaeszi, H.; Stone, F., Infra-red spectra of some vinyl and ethyl compounds of mercury, cadmium, zinc, tin and phosphorus. *Spectrochimica Acta* **1959**, 15, 360-377.

- (276).Goggin, P.; Goodfellow, R., Identification of the stereochemistry of square planar bis-triethylphosphine complexes by infrared spectroscopy. *Journal of the Chemical Society A: Inorganic, Physical, Theoretical* **1966**, 1462-1466.
- (277).Goodfellow, R.; Evans, J.; Goggin, P.; Duddell, D., Infrared spectra (800–200 cm⁻¹) of trimethylphosphine and trimethylarsine complexes of platinum and palladium $mx\ 2\ 1\ 2$ and $m\ 2\ x\ 4\ 1\ 2$ (x= cl, br, or i). *Journal of the Chemical Society A: Inorganic, Physical, Theoretical* **1968**, 1604-1609.
- (278).Duddell, D.; Goggin, P.; Goodfellow, R.; Norton, M.; Smith, J., Vibrational spectra of some gold (i), palladium (ii), and platinum (ii) complexes with trialkylphosphines and trialkylarsines. *Journal of the Chemical Society A: Inorganic, Physical, Theoretical* **1970**, 545-564.
- (279).Clark, H.; Tsang, W., Chemistry of metal hydrides. II. Spectroscopic studies of fluorovinylplatinum (ii) derivatives. *Journal of the American Chemical Society* **1967**, *89*, 533-539.
- (280).Bhatt, H.; Deo, M.; Vishwakarma, S.; Bajaj, N.; Sharma, S. M. In *Ft-raman spectroscopy of structural isomers of pt (ii) complex ptcl2(pet3)2*, AIP Conference Proceedings, AIP Publishing: 2015; p 090045.
- (281).Balamurugan, V.; Hundal, M. S.; Mukherjee, R., First systematic investigation of c□ h·· cl hydrogen bonding using inorganic supramolecular synthons: Lamellar, stitched stair-case, linked-ladder, and helical structures. *Chemistry-a European Journal* **2004**, *10*, 1683-1690.
- (282).Mączka, M.; da Silva, T. A.; Paraguassu, W.; Ptak, M.; Hermanowicz, K., Raman and ir studies of pressure-and temperature-induced phase transitions in [(ch₂)₃nh₂][zn (hcoo)₃]. *Inorganic chemistry* **2014**, *53*, 12650-12657.
- (283).Suffren, Y.; Rollet, F.-G.; Reber, C., Raman spectroscopy of transition metal complexes: Molecular vibrational frequencies, phase transitions, isomers, and electronic structure. *Comments on Inorganic Chemistry* **2011**, *32*, 246-276.
- (284).Genre, C.; Levasseur-Thériault, G.; Reber, C., Emitting-state properties of square-planar dithiocarbamate complexes of palladium (ii) and platinum (ii) probed by pressure-dependent luminescence spectroscopy. *Canadian Journal of Chemistry* **2009**, *87*, 1625-1635.
- (285).Tidey, J. P.; Wong, H. L.; Schröder, M.; Blake, A. J., Structural chemistry of metal coordination complexes at high pressure. *Coordination Chemistry Reviews* **2014**, *277*, 187-207.
- (286).Takeda, K.; Hayashi, J.; Shirotani, I.; Fukuda, H.; Yakushi, K., Structural, optical, and electrical properties of one-dimensional bis (dimethylglyoximato) nickel (ii), ni (dmg)₂ at high pressure. *Molecular Crystals and Liquid Crystals* **2006**, *460*, 131-144.
- (287).Shirotani, I.; Hayashi, J.; Takeda, K., X-ray study with synchrotron radiation for one-dimensional complex bis (diphenylglyoximato)-platinum (ii), pt (dpg)₂ at high pressures. *Molecular Crystals and Liquid Crystals* **2005**, *442*, 157-166.

- (288).Konno, M.; Okamoto, T.; Shirotani, I., Structure changes and proton transfer between $o \cdots o$ in bis (dimethylglyoximato) platinum (ii) at low temperature (150k) and at high pressures (2.39 and 3.14 gpa). *Acta Crystallographica Section B: Structural Science* **1989**, *45*, 142-147.
- (289).Hansson, C.; Carlson, S.; Giveen, D.; Johansson, M.; Yong, S.; Oskarsson, Å., Cis/trans isomers of ptx_2l_2 (x= halogen, l= neutral ligand); the crystal structure of trans-dichlorobis (dimethyl sulfide) platinum (ii) and the pressure dependence of its unit-cell dimensions. *Acta Crystallographica Section B: Structural Science* **2006**, *62*, 474-479.
- (290).Kumar, A.; Ghosh, B.; Poswal, H.; Pandey, K.; Hosur, M.; Dwivedi, A.; Makde, R. D.; Sharma, S. M., Protein crystallography beamline (px-bl21) at indus-2 synchrotron. *Journal of synchrotron radiation* **2016**, *23*, 629-634.
- (291).Pandey, K.; Poswal, H.; Mishra, A.; Dwivedi, A.; Vasanthi, R.; Garg, N.; Sharma, S. M., Energy-dispersive x-ray diffraction beamline at indus-2 synchrotron source. *Pramana* **2013**, *80*, 607-619.
- (292).Jayaraman, A., Diamond anvil cell and high-pressure physical investigations. *Reviews of Modern Physics* **1983**, *55*, 65.
- (293).Dewaele, A.; Loubeyre, P.; Mezouar, M., Equations of state of six metals above 94 gpa. *Physical Review B* **2004**, *70*, 094112.
- (294).Hammersley, A., Fit2d: An introduction and overview. *European Synchrotron Radiation Facility Internal Report ESRF97HA02T* **1997**, *68*, 58.
- (295).Toby, B. H.; Von Dreele, R. B., Gsas-ii: The genesis of a modern open-source all purpose crystallography software package. *Journal of Applied Crystallography* **2013**, *46*, 544-549.
- (296).Mao, H.; Xu, J.-A.; Bell, P., Calibration of the ruby pressure gauge to 800 kbar under quasi-hydrostatic conditions. *Journal of Geophysical Research: Solid Earth* **1986**, *91*, 4673-4676.
- (297).Sleboznick, C.; Zhao, J.; Angel, R.; Hanson, B. E.; Song, Y.; Liu, Z.; Hemley, R. J., High pressure study of ru_3 (co) 1_2 by x-ray diffraction, raman, and infrared spectroscopy. *Inorganic chemistry* **2004**, *43*, 5245-5252.
- (298).Murli, C.; Sharma, S. M.; Kulshreshtha, S.; Sikka, S., High-pressure behavior of β -ni (oh) 2 —a raman scattering study. *Physica B: Condensed Matter* **2001**, *307*, 111-116.
- (299).Kresse, G., G. Kresse and J. Furthmüller, *phys. Rev. B* *54*, 11169 (1996). *Phys. Rev. B* **1996**, *54*, 11169.
- (300).Kresse, G.; Furthmüller, J., Efficiency of ab-initio total energy calculations for metals and semiconductors using a plane-wave basis set. *Computational materials science* **1996**, *6*, 15-50.
- (301).Blöchl, P. E., Projector augmented-wave method. *Physical review B* **1994**, *50*, 17953.

- (302).Perdew, J. P.; Burke, K.; Ernzerhof, M., Generalized gradient approximation made simple. *Physical review letters* **1996**, *77*, 3865.
- (303).Monkhorst, H. J.; Pack, J. D., Special points for brillouin-zone integrations. *Physical review B* **1976**, *13*, 5188.
- (304).Allkins, J. R.; Obremski, R. J.; Brown, C. W.; Lippincott, E. R., Effect of high pressure on the vibrational spectra of square-planar coordination compounds. *Inorganic Chemistry* **1969**, *8*, 1450-1454.
- (305).Gonzalez-Platas, J.; Alvaro, M.; Nestola, F.; Angel, R., Eosfit7-gui: A new graphical user interface for equation of state calculations, analyses and teaching. *Journal of Applied Crystallography* **2016**, *49*, 1377-1382.
- (306).Cliffe, M. J.; Goodwin, A. L., Pascal: A principal axis strain calculator for thermal expansion and compressibility determination. *Journal of Applied Crystallography* **2012**, *45*, 1321-1329.
- (307).Bondi, A., Van der waals volumes and radii. *The Journal of physical chemistry* **1964**, *68*, 441-451.
- (308).Aullón, G.; Bellamy, D.; Orpen, A. G.; Brammer, L.; Bruton, E. A., Metal-bound chlorine often accepts hydrogen bonds. *Chemical Communications* **1998**, 653-654.
- (309).Aakeröy, C. B.; Evans, T. A.; Seddon, K. R.; Pálinkó, I., The c-h... cl hydrogen bond: Does it exist? *New Journal of Chemistry* **1999**, *23*, 145-152.
- (310).Shimon, L.; Vaida, M.; Addadi, L.; Lahav, M.; Leiserowitz, L., Molecular recognition at the solid-solution interface: A relay mechanism for the effect of solvent on crystal growth and dissolution. *Journal of the American Chemical Society* **1990**, *112*, 6215-6220.
- (311).Perlstein, J., The weak hydrogen bond in structural chemistry and biology (international union of crystallography, monographs on crystallography, 9) by gautam r. Desiraju (university of hyderabad) and thomas steiner (freie universität berlin). Oxford university press: Oxford and new york. 1999. Xiv+ 507 pp. \$150. Isbn 0-19-850252-4. ACS Publications: 2001.
- (312).Spanu, L.; Donadio, D.; Hohl, D.; Schwegler, E.; Galli, G., Stability of hydrocarbons at deep earth pressures and temperatures. *Proceedings of the National Academy of Sciences* **2011**, *108*, 6843-6846.
- (313).Livengood, T.; Kostiuik, T.; Sonnabend, G.; Annen, J.; Fast, K.; Tokunaga, A.; Murakawa, K.; Hewagama, T.; Schmülling, F.; Schieder, R., High-resolution infrared spectroscopy of ethane in titan's stratosphere in the huygens epoch. *Journal of Geophysical Research: Planets* **2006**, *111*.
- (314).Levasseur-Thériault, G.; Reber, C.; Aronica, C.; Luneau, D., Large pressure-induced red shift of the luminescence band originating from nonstacked square-planar [pt (scn) 4] 2-in a novel trimetallic complex. *Inorganic chemistry* **2006**, *45*, 2379-2381.

- (315).Postmus, C.; Nakamoto, K.; Ferraro, J. R., High-pressure effect on far-infrared spectra. I. Symmetric and antisymmetric metal-halogen stretching vibrations. *Inorganic Chemistry* **1967**, *6*, 2194-2199.
- (316).Mitra, S.; Postmus, C.; Ferraro, J., Pressure dependence of long-wavelength optical phonons in ionic crystals. *Physical Review Letters* **1967**, *18*, 455.
- (317).Allan, D. R.; Bailey, D.; Bird, N.; Blake, A. J.; Champness, N. R.; Huang, D.; Keane, C. P.; McMaster, J.; Prior, T. J.; Tidey, J. P., High-pressure studies of palladium and platinum thioether macrocyclic dihalide complexes. *Acta Crystallographica Section B: Structural Science, Crystal Engineering and Materials* **2014**, *70*, 469-486.
- (318).Gould, J. A.; Rosseinsky, M. J.; Moggach, S. A., Tuning the coordination chemistry of a cu (ii) complex at high-pressure. *Dalton Transactions* **2012**, *41*, 5464-5467.
- (319).Scheins, S.; Overgaard, J.; Timco, G. A.; Stash, A.; Chen, Y. S.; Larsen, F. K.; Christensen, M.; Jørgensen, M. R.; Madsen, S. R.; Schmøkel, M. S., Pressure versus temperature effects on intramolecular electron transfer in mixed-valence complexes. *Chemistry-A European Journal* **2013**, *19*, 195-205.
- (320).Wilson, C.; Iversen, B. B.; Overgaard, J.; Larsen, F. K.; Wu, G.; Palić, S. P.; Timco, G. A.; Gerbelev, N. V., Multi-temperature crystallographic studies of mixed-valence polynuclear complexes; valence trapping process in the trinuclear oxo-bridged iron compound, [Fe₃O (O₂CC(CH₃)₃)₆ (C₅H₅N)₃]. *Journal of the American Chemical Society* **2000**, *122*, 11370-11379.
- (321).Galloway, K. W.; Moggach, S. A.; Parois, P.; Lennie, A. R.; Warren, J. E.; Brechin, E. K.; Peacock, R. D.; Valiente, R.; González, J.; Rodríguez, F., Pressure-induced switching in a copper (ii) citrate dimer. *CrystEngComm* **2010**, *12*, 2516-2519.
- (322).Prescimone, A.; Sanchez-Benitez, J.; Kamenev, K. K.; Moggach, S. A.; Warren, J. E.; Lennie, A. R.; Murrie, M.; Parsons, S.; Brechin, E. K., High pressure studies of hydroxo-bridged cu (ii) dimers. *Dalton Transactions* **2010**, *39*, 113-123.
- (323).Allan, D. R.; Blake, A. J.; Huang, D.; Prior, T. J.; Schröder, M., High pressure coordination chemistry of a palladium thioether complex: Pressure versus electrons. *Chemical Communications* **2006**, 4081-4083.
- (324).Boldyreva, E.; Kivikoski, J.; Howard, J. A., Distortion of crystal structures of some Co(III) ammine complexes. I. Distortion of crystal structure of [Co(NH₃)₅NO₂]Cl(NO₃) on cooling. *Acta Crystallographica Section B: Structural Science* **1997**, *53*, 394-404.
- (325).Boldyreva, E. V., High-pressure diffraction studies of molecular organic solids. A personal view. *Acta Crystallographica Section A: Foundations of Crystallography* **2008**, *64*, 218-231.
- (326).Bujak, M.; Angel, R. J., High-pressure-and low-temperature-induced changes in [(CH₃)₂NH(CH₂)₂NH₃][SbCl₅]. *The Journal of Physical Chemistry B* **2006**, *110*, 10322-10331.
- (327).Fisher, G. A.; Norman, N. C., The structures of the group 15 element (III) halides and halogenoanions. In *Advances in inorganic chemistry*, Elsevier: 1994; Vol. 41, pp 233-271.

-
- (328).Sobczyk, L.; Jakubas, R.; Zaleski, J., Self-assembly of sb (iii) and bi (iii) halo-coordinated octahedra in salts of organic cations. Structure, properties and phase transitions. *Polish Journal of Chemistry* **1997**, *71*, 265-300.
- (329).Bujak, M.; Zaleski, J., Synthesis of chloroantimonates (iii) with selected organic cations. X-ray studies of phase transition in ferroelectric tris (trimethylammonium) nonachlorodiantimonate (iii) at 125k. *Journal of Solid State Chemistry* **2004**, *177*, 3202-3211.
- (330).Bujak, M.; Angel, R. J., Low-temperature single crystal x-ray diffraction and high-pressure raman studies on [(ch 3) 2 nh 2] 2 [sbcl 5]. *Journal of Solid State Chemistry* **2007**, *180*, 3026-3034.